Investigation of low-energy photoelectron dynamics accelerated in terahertz light fields using a novel Velocity-Map-Imaging spectrometer

Dissertation
zur Erlangung des Doktorgrades
an der Fakultät für Mathematik,
Informatik und Naturwisschenschaften
Fachbereich Physik
der Universität Hamburg

Vorgelegt von
Martin Ranke
aus Jena

Hamburg 2019

Gutachter/innen der Dissertation:	Prof. Dr. Ulrike Frühling Priv. Doz. Tim Laarmann
Zusammensetzung der Prüfungskommission:	Prof. Dr. Ulrike Frühling Priv. Doz. Tim Laarmann Prof. Dr. Markus Drescher Prof. Dr. Franz X. Kärtner Prof. Dr. Robin Santra
Vorsitzende/r der Prüfungskommission:	Prof. Dr. Robin Santra
Datum der Disputation:	13.12.2019
Vorsitzender des Fach-Promotionsausschusses PHYSIK:	Prof. Dr. Günter Hans Walter Sigl
Leiter des Fachbereichs PHYSIK:	Prof. Dr. Wolfgang Hansen
Dekan der Fakultät MIN:	Prof. Dr. Heinrich Graener

Abstract

In this work, the dynamics of low-energy photoelectrons, generated by multiphoton ionization from near-infrared (NIR) laser pulses, in the presence of intense near single-cycle carrier-envelope phase stable Terahertz (THz) pulses, were experimentally investigated. For certain time delays between the NIR and THz pulses, a strong modulation of the photoelectron momentum distribution was observed and attributed to rescattering from the ionic core. During the rescattering process, an additional momentum was transferred to the photoelectrons leading to a higher kinetic energy in the continuum in contrast to directly emitted photoelectrons that are not rescattered.

In another experiment, the 51^{st} harmonic of the NIR laser, generated by a high-order harmonic generation source, was used to ionize $4d$ photoelectrons in Xe leading to single and double Auger decays. A dominant decay channel was a double Auger decay, where a slow Auger (SA) and a fast Auger electron are involved. The superposition with intense THz radiation led to a relative time shift between the time-dependent $4d_{5/2}$ photoelectron and the SA electron momentum distributions. This relative time shift can be explained by the Auger lifetime $\tau_{\text{AE}} > 23\,\text{fs}$ of the SA electron as well as contributions of the Eisenbud-Wigner-Smith and Coulomb-laser coupling time delays, which are pronounced at low kinetic electron energies and long streaking wavelengths.

In the both experiments, the angular momentum distribution of photoelectrons was measured by a velocity-map imaging spectrometer (VMIS) with a novel capillary gas injection. The VMIS provides high target gas densities while preserving its energy resolution and was embedded in a table-top THz streak camera.

Zusammenfassung

In der vorliegenden Arbeit wurden die Dynamiken von niedrig energetischen Photoelektronen untersucht, die durch Multiphoton-Ionisation eines nahen Infrarot (NIR)-Lasers erzeugt und in Gegenwart von intensiven phasenstabilen Terahertz (THz)-Pulsen beschleunigt wurden. Es hat sich gezeigt, dass für bestimmte Zeitunterschiede zwischen dem THz- und NIR-Puls die Impulsverteilung der Photoelektronen stark moduliert ist, was mit einer Streuung am positiven Ionenkern erklärt werden kann. Während des Streuprozesses erhalten die Photoelektronen einen zusätzlichen Impulsbetrag, sodass deren kinetische Energie im Kontinuum deutlich größer als die kinetische Energie der direkt emittierten Photoelektronen ist.
In einem weiteren Experiment wurden $4d$ Photoelektronen in Xe durch die 51. Harmonische des NIR-Lasers erzeugt, die zu einfachen und doppelten Augerzerfällen führten. Ein dominanter Augerzerfall war ein Doppel-Augerzerfall, bei dem langsame und schnelle Augerelektronen erzeugt wurden. Die Überlagerung mit intensiver THz-Strahlung führt zu einer Modulation der Elektronenimpulse. Dabei wurde ein zeitlicher Versatz zwischen den langsamen Augerelektronen und den $4d_{5/2}$ Photoelektronen gemessen. Neben der Zerfallskonstante von $\tau_{\mathrm{AE}} > 23\,\mathrm{fs}$ des langsamen Augerelektrons treten vor allem induzierte Zeitverzögerungen während des Ionisationsprozesses auf. Dabei handelt es sich um Eisenbud-Wigner-Smith und Coulomb-Laser Kopplung induzierte Zeitverschiebungen, die vor allem bei niedrigen Elektronenenergien und großen Streak-Wellenlängen auftreten.
Für die winkelaufgelösten Messungen der Elektronenimpulse wurde ein Velocity-Map Imaging Spektrometer (VMIS) mit einer neuartigen Gaszufuhr verwendet. Das VMIS liefert hohe Gasdichten im Wechselwirkungsbereich und wird als Detektor innerhalb einer laserbasierten THz-Streak-Kamera eingesetzt.

Contents

Chapter 1

Introduction

Almost 150 years ago, the photographer Eadweard Muybridge published a series of images about a horse in motion to answer the question, whether all feet of a moving horse are lifted frome ground at the same time [1]. This question was not easy to answer because it cannot be resolved by human eyes. In fact, the images showed that there are moments in which no leg of the horse touches the ground. This remarkable experimental result required a detector with a temporal resolution on the order of tens of milliseconds. A few decades later later, Harold Edgerton invented strobe photography to capture the motion of objects. For example, the transition of a bullet through an apple could be temporally resolved using a strobe camera [2]. The temporal resolution of such a device was on the order of a few microseconds. In 1960, Theodore Maiman invented the first laser, which emits monochromatic coherent light with a wavelength of $\lambda = 694\,\mathrm{nm}$ [3]. This invention in combination with the concept of chirped-pulse amplification [4] and Kerr-lens mode-locking [5] led to the development of ultrashort pulses, which can be used to study ultrafast phenomena on the natural time scale of molecules or atoms. Nowadays, extreme-ultraviolet (XUV) pulses with pulse durations as low as 43 as can be generated to investigate processes on the electronic time scale [6]. In such an experiment the pump-probe technique is often used, where a first laser pulse triggers the physical process while a second time-delayed pulse captures the resulting dynamics [7]. By varying the time-delay between both pulses a movie of the process is created and the underlying mechanisms can be investigated.

With the discovery of high-order harmonic generation (HHG), by focusing an intense NIR laser into a noble gas target to create XUV photons, a new toolbox was invented to investigate inner-shell atomic and molecular properties [8, 9]. The detection of light-induced electrons is an essential part to study atomic and molecular processes. Electron dynamics in these systems take place on a femtosecond to subfemtosecond time scale. Such ultrafast dynamics can be experimentally investigated with a light-field-driven streak camera, which is based on the principle of a conventional streak camera [10, 11]. With such a streak camera the temporal structure of a short XUV pulse is imprinted on photoelectrons, which are generated from a photocathode. These photoelectrons are deflected by a fast-varying electric field of an electrode and imaged on a fluoerescent screen, thus mapping the temporal information of the XUV pulse on a spatial coordinate. In a light-field-driven streak camera the photocathode is replaced by a target gas and a short pulse is used as a streaking-field. In a first experiment with this novel device, the pulse duration of isolated XUV pulses around 1 fs was measured and prepared the way for attosecond science [12]. Soon afterwards the temporal evolution of single attosecond pulses with resolutions down to 100 as was obtained [13–15]. A necessary condition for streaking is that the period of the electric streak field is orders of magnitude bigger than the pulse duration of the ionization field. For comparable values sidebands may occur in the spectrum [16]. The extension of the streaking principle in the femtosecond time

domain was performed on accelerator-based [17] and laser-based [18] experiments, where THz instead of NIR electric streaking-fields were used. Besides the characterization of attosecond pulses, the streaking technique is widely used to investigate ultrafast processes within atoms, such as the measurement of the lifetime of the M-shell vacancy in atomic Kr [19] or the control of real-time electron dynamics in the sub-femtosecond regime [20]. The ionization of inner-shell photoelectrons with XUV radiation can lead to nonradiative decays via Auger emission [21]. Their spectral width and kinetic energy is an intrinsic property of the atomic or molecular system. It it known from the literature that both electrons can exchange energy via post-collision-interaction when they are close enough to each other [22–25]. This leads to a modification of both electron spectra. For example, a fast Auger electron in Kr or Xe can overtake an earlier emitted photoelectron, which gives rise to an energetic chirp of the Auger spectrum. This effect was observed using a THz streak camera [26].

In many light-field streaking experiments, a time-of-flight (TOF) spectrometer is used as an electron diagnostic tool. This device measures the number of electrons as a function of the TOF, which can be transformed to the kinetic energy. Another detector is a velocity-map-imaging spectrometer (VMIS) that allows for measuring photoelectron momentum distributions. This imaging device was developed by André Eppink and David Parker and was a substantial improvement to the previously used Wiley-Mc-Laren setup [27]. A VMIS requires a symmetry axis parallel to the two dimensional detector, which is usually given by the polarization direction of the ionizing laser beam. This measurement instrument is widely used to measure targets in the gas phase but can be also used to investigate solid-state targets [28, 29]. Generally, the energy resolution of such an apparatus is worse than a TOF spectrometer but angular information is gained. The additional insertion of electrostatic lenses can significantly improve the energy resolution and makes it comparable to TOF spectrometers [30, 31]. In many experiments, where VMIS are used, the density of the target gas is very low. However, the integration of a capillary into the Repeller electrode leads to a considerable increase of the target gas density [32]. A VMIS was already utilized to study the dynamics of the photoemission in Ne and the $N_{4,5}OO$ Auger decay in Xe in an attosecond streaking experiment [33]. In another experiment, autoionization channels in atomic and molecular clusters were investigated employing THz-streaking and a VMIS [34]. Within the framework of this thesis, a VMIS with a novel capillary gas injected was developed to measure the photoelectron momentum distribution. The VMIS is capable to deliver high gas while preserving the energy resolution and is embedded into a table-top THz streak camera.

The detailed understanding of the dynamics of photoelectrons, which are generated and steered by intense laser pulses, is an important topic in strong-field laser physics. Under certain conditions, the photoelectron might come back and recombine with the parent ion, leading to non-sequential double ionization or rescatter from the ionic core. The first process, for example, is very important in HHG because it leads to the emission of coherent high-energy photons. Non-sequential double ionization was first discovered in Sr^{2+} [35] and later observed in nobles gases [36]. Rescattering processes are very important in the area of strong-field ionization. More than a decade after the first observation of above-threshold ionization (ATI) [37], the angular distribution of photoelectrons of the plateau region in the ATI spectrum [38]

could be explained by rescattering [39–41]. In the following years more attention was paid to the low-energy (LE) part of the photoelectron spectrum [42, 43]. Both experiments were carried out in the tunneling regime. Numerous theoretical models have been developed to describe strong-field tunneling ionization [43–48]. Very recently, the photoelectron momentum distribution of carbonyl sulfide was investigated with a model, which is in the intermediate regime between multiphoton and tunneling ionization [49]. One focus of this work is the experimental investigation of rescattering processes in the multiphoton regime. In contrast to other measurements, LE photoelectrons, generated by multiphoton ionization (MPI) with $0.8\,\mu m$ NIR pulses, are steered and driven back to the ionic core with carrier-envelope phase stable intense THz pulses, whose wavelength is around $385\,\mu m$. Thus, the ionization and motion of the photoelectron was separated from each other. For certain time delays between both pulses a strong modulation of the photoelectron momentum distribution was observed. The motion of the photoelectrons was treated classically to give a qualitative description of the measured effect. Due to the slow photoelectron, the Coulomb potential of the remaining ion had to be taken into account in the classical calculations. It was shown that a portion of the photoelectrons will reach a distance around 20 nm before they return and scatter from the ionic core. New questions arise from this: What is the rescattering probability of the photoelectron wavepacket with the ionic core? Can we learn something about the ionic structure? Another focus of this work is the experimental investigation of delays in photoemission. In an experiment from another group a time delay on the order of 21 as between the emission of electrons from the $2s$ and $2p$ orbital in Ne was observed using an attosecond light-field-driven streak camera [50]. The measured time delay is a function of the electron kinetic energy and therefore an intrinsic property of the system. In addition, the combination of the electric probe field with the ionic Coulomb potential modifies the time delay and is thus a measurement-induced property. This publication triggered a debate about the absolute zero time in the photoelectric effect [51, 52]. In a very recent publication, induced photoemission time delays between $2p$ and shake-up photoelectrons in Ne were measured with a light-field-driven THz camera in the femtosecond time domain [53]. In the current work, the induced time delay between a slow Auger (SA) electron of a double Auger decay in Xe and a $4d_{5/2}$ photoelectron was measured instead. Due to the long streaking wavelength, the induced time delay was also observed in the femtosecond time domain. Classical simulations showed that the Coulomb potential of the parent ion also played an important role when investigating the induced time delay.

This work is structured as follows. In chapter 2 a theoretical background is provided. Starting with the interaction of atoms in weak fields, the focus is mainly on the interaction of atoms with intense laser fields, where effects like HHG or MPI are introduced. In this chapter a general overview about THz radiation as well as principles of a light-field-driven streak camera is given. In chapter 3 the table-top THz streak camera, consisting of an HHG source, an HHG spectrometer, a THz source and a VMIS, is explained. The characterization of the commercial NIR laser, the THz generation source as well as the HHG source is covered in chapter 4. A detailed description of the VMIS is given in chapter 5. Here, the concept of velocity-map imaging is explained and the VMIS with the novel capillary gas injection is introduced. Since the VMIS was constructed from scratch, the geometry was optimized

by extensive computer simulations. At the end of this chapter, several Abel inversion algorithms are presented and compared with each other. In chapter 6 the performance of the VMIS is experimentally investigated using ATI photoelectrons from MPI with an NIR laser and $4d$ photoelectrons from single-photon ionization with XUV light.
The key results of this work are presented in 7. Here, light-induced photoelectron dynamics in Xe in the presence of THz radiation are discussed. In the first part, the dynamics of near-threshold photoelectrons, generated by the simultaneous absorption of multiple NIR photons, are experimentally investigated. In the second part, the ionization of $4d$ photoelectrons in Xe by the 51^{st} harmonic of the NIR laser triggers several single and double Auger decay channels. A dominant double Auger decay channel is observed, where a SA and fast Auger electron are involved. The focus of this part are the THz-induced dynamics of the SA and the $4d_{5/2}$ photoelectrons. In the final chapter 8 the main achievements of this work are summarized and an outlook is given.

Chapter 2

Theoretical background

The interaction of light with atoms or molecules is a very fundamental process and gives rise to new effects depending on the involved systems. Here, the basic concepts of such interactions with a special focus on intense light sources will be introduced. Depending on the intensity of the light source and the choice of the target gas, several phenomena may occur. At lower intensities the simultaneous absorption of multiple photons leads to MPI. At higher intensities the atomic Coulomb potential of atom is significantly distorted and under appropriate conditions the generated photoelectrons recombine with the parent ion resulting in HHG. Another emphasis of this chapter will be the generation and detection of coherent and intense long-wavelength radiation, the so-called THz radiation. All of these concepts form the basis of the light-field driven streak camera, which will be explained in detail in the last part of this chapter.

2.1 Atoms in weak laser fields

The absorption of a photon with an energy $\hbar\omega$ by an atom with a binding energy $E_\mathrm{B} < \hbar\omega$ leads to the emission of a photoelectron with a kinetic energy of

$$E_\mathrm{kin} = \hbar\omega - E_\mathrm{B}. \tag{2.1}$$

This effect is also known as the photoelectric effect or photoemission [54]. By measuring the kinetic energy of the photoelectron and the initial photon energy the binding energy can be calculated and thus structural properties of the matter can be revealed. For noble gases the binding energies are on the order of 10 eV for valence electrons and can be as high as a few MeV for deeply bound electrons. The probability of a photon being absorbed in a specific electronic orbit is given by the photoionization cross section σ. Numerous photoionization cross sections have been extensively studied in the literature [55].
The absorption of a photon that exceeds the binding energy of an inner-shell may lead to one of the following scenarios: (i) emission of a photoelectron or (ii) emission of a photoelectron with a shake-up process. In case (i), an inner-shell photoelectron of the energy level E_1 is released via an XUV photon (Fig. 2.1a). The singly-charged ion is in an excited state and an electron from an outer-shell, E_3, can fill this vacancy (Fig. 2.1b). The residual energy either leads to the emission of a photon or an ejection of another electron, which will leave the ionic potential if it exceeds the binding energy. The release of a secondary electron is also called Auger electron [21]. The core hole excitation has a finite lifetime τ_L to decay into a lower-energy state. For the nonradiative Auger transition, this is spectrally associated with a natural Lorentzian-like linewidth Γ. The lifetime τ_L and the linewidth Γ are related via the Heisenberg uncertainty principle

$$\tau_L \times \Gamma = \hbar, \tag{2.2}$$

where $\hbar$ is the reduced Planck constant. For example, the natural linewidth of the $3d$ orbital in Kr is 88 meV [56], which corresponds to a lifetime of 7.48 fs. In a more general case cascaded Auger electrons can be released into the continuum after the ionization of a deeply bound photoelectron [57] or multiple photoionization due to high photon fluxes may result to several Auger electrons [58].
In case (ii) the emission of a photoelectron is accompanied by an excitation of an outer-shell electron into a higher state (shake-up). Due to energy conserveration, the kinetic energy of the photoelectron is reduced according to the excited state of the shake-up electron. Therefore, additional peaks, so-called satallites, appear in the photoelectron energy spectrum and also the Auger electron will have a different intrinsic energy [55].

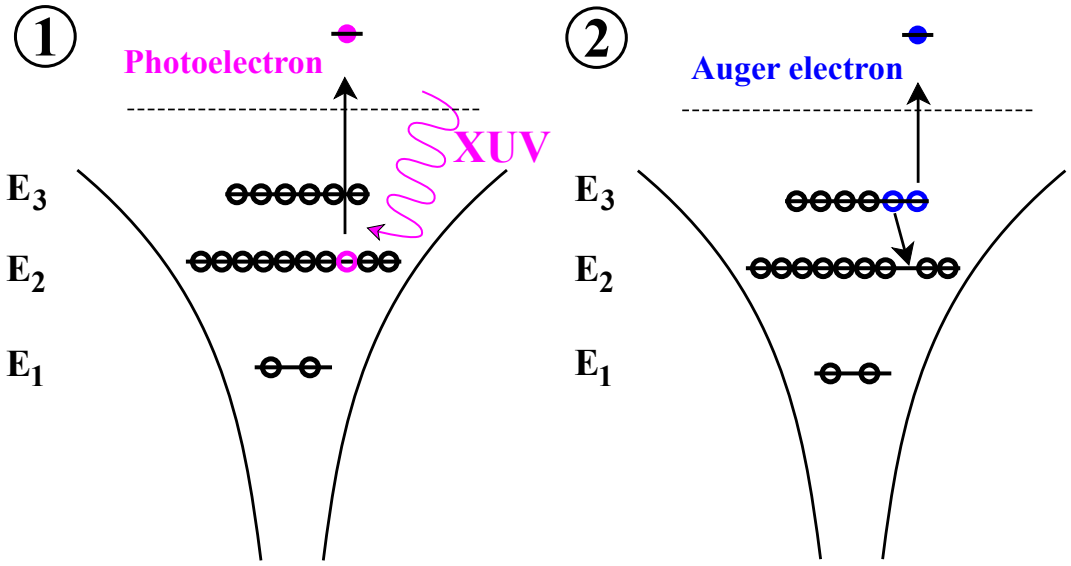

(a) Photoionization (b) Electron decay

Figure 2.1: Emission of a Photo- and Auger electron. The electron energy levels are denoted as E_1, E_2 and E_3. The dashed line represents the energetic continuum. (a) step 1, photoionization of an inner-shell electron, (b) step 2, vacancy is filled by an outer-shell electron and an Auger electron is ejected.

Note that the kinetic energies of the Auger electrons do not depend on the XUV excitation energy and consequently reflect the intrinsic electronic structure of the ion. Hence, Auger spectroscopy can be used to determine fundamental atomic and molecular properties of matter. However, if the Auger electron has a higher energy than the initial photoelectron, then a post-collision interaction will eventually take place. When the Auger electron leaves the ionic core its trajectory is determined by the positive doubly-charged ionic core. As soon as the Auger electron overtakes the slower photoelectron it will only experience the positive singly-charged ionic core and hence energy is transferred from the photoelectron to the Auger electron. The amount of transferred energy is larger the earlier the Auger electron overtakes

the photoelectron. Under certain conditions the energy distribution of the Auger electron is modified [26].

2.2 Perturbative treatment of the polarization

The interaction of an electromagnetic field $\vec{E}(\vec{r},t)$ with matter can be described by the wave equation [59]

$$\left(\Delta - \frac{1}{c^2}\frac{\partial^2}{\partial t^2}\right)\vec{E}(\vec{r},t) = \mu_0 \frac{\partial^2}{\partial t^2}\vec{P}(\vec{r},t). \tag{2.3}$$

Here, $\mu_0 = 1/\epsilon_0 c^2 = 1.257 \times 10^{-6}\,\mathrm{Vs/Am}$ is the magnetic constant, $\epsilon_0 = 8.85 \times 10^8\,\mathrm{As/Vm}$ the vacuum permittivity and $c = 3 \times 10^8\,\mathrm{m/s}$ the speed of light. This equation can be directly derived from Maxwell's equations and assumes vanishing free charges and currents. The macroscopic response function $\vec{P}(\vec{r},t)$ denotes the polarization of the medium and measures the average microscopic displacement of electrons compared to the nuclei. The polarization strongly depends on the applied electric field and can be expanded in a Taylor series (in Cartesian coordinates, $i = 1,2,3$) in the Fourier space

$$P_i = \underbrace{\epsilon_0 \chi^{(1)}_{ij} E_j}_{P_{i,L}} + \underbrace{\epsilon_0 \chi^{(2)}_{ijk} E_j E_k + \epsilon_0 \chi^{(3)}_{ijkl} E_j E_k E_l + \ldots}_{P_{i,NL}}, \tag{2.4}$$

where $\chi^{(n)}$ represents the susceptibility tensor of rank $(n+1)$. The polarization $\vec{P}$ and electric field $\vec{E}$ are a function of time and space. For clarity, these dependencies are ignored in the following. In the general case, the susceptibility tensor has off-axis elements to account for effects in an anisotropic medium. Note that a summation over the same indices is implied in Eq. (2.4). The response function $\vec{P}$ can be regarded as instantaneous with respect to the originating electric field $\vec{E}$. For instance, the nonlinear response is on the order of tens of attoseconds, which was measured with attosecond metrology [60]. The total polarization is decomposed into a linear term $P_{i,L}$ and a nonlinear term $P_{i,NL}$. Generally, the amplitude of the susceptibility tensor $\chi^{(n)}$ decreases rapidly for higher orders n. Therefore, higher nonlinear contributions only play a role for larger electric field strengths. Typical examples for second-order and third-order nonlinear effects are second-harmonic generation [61], i.e. the emission of light with the double frequency, and the optical Kerr effect [62], where the refractive index is proportional to the intensity, respectively. Note that the perturbative approach of the polarization is only valid for low intensities where the atomic Coulomb field is slightly distorted by the external electric field. In this regime the electrons are always attached to the atom. The ratio of consecutive nonlinear terms is given by [63]

$$\frac{\chi^{(n+1)}E^{n+1}}{\chi^{(n)}E^n} \approx \frac{eE_0 a_B}{\hbar\Delta} = \alpha_{\mathrm{bb}}, \tag{2.5}$$

where $\Delta = |\omega_{ik} - \omega_0|$, ω_{ik} is the transition frequency from the ground state $|i\rangle$ to a bound excited state $|k\rangle$, ω_0 the laser carrier frequency, E_0 the time-varying

electric field amplitude and a_B the Bohr radius. For small ratios $\alpha_{\mathrm{bb}} \ll 1$ the Taylor expansion in Eq. (2.4) will converge.

2.3 Atoms in intense laser fields

With the development of intense laser sources the route to investigate time-resolved atomic processes was opened. In the presence of a strong laser field with angular frequency ω_L and electric field strength E_0, a free electron with mass m_e performs an oscillating motion with an average kinetic energy of

$$U_{\mathrm{P}} = \frac{e^2 E_0^2}{4 m_e \omega_L^2}. \tag{2.6}$$

The term U_{P} is also called ponderomotive potential. In experiments it is useful to express the ponderomotive potential in terms of the peak intensity I_0 and the center wavelength λ_0:

$$U_p(eV) \approx 9.34 \times 10^{-20} \times [\lambda(\mathrm{nm})]^2 \times I_0 \left(\mathrm{W/cm^2}\right) \tag{2.7}$$

Already several decades ago, Keldysh described theoretically how an electron can leave the atomic potential in the presence of a low-frequency intense electric field [64]. By introducing the Keldysh parameter

$$\gamma = \sqrt{\frac{I_{\mathrm{P}}}{2U_{\mathrm{P}}}}, \tag{2.8}$$

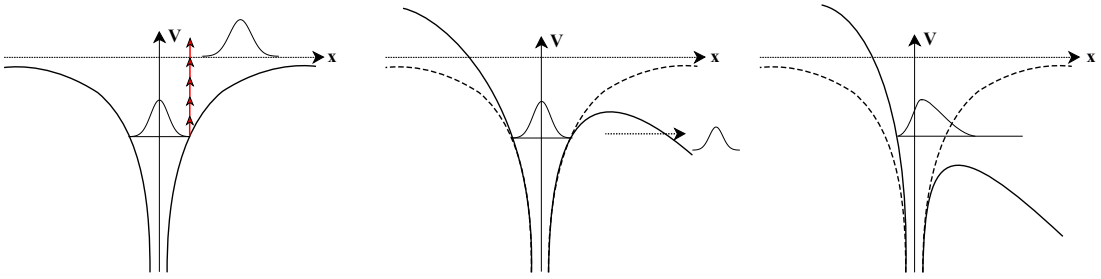

(a) Multiphoton ionization ($\gamma \gg 1$)

(b) Tunnel ionization ($\gamma \ll 1$)

(c) Barrier-suppression ionization ($I \geq I_{\mathrm{th}}$)

Figure 2.2: Sketch of possible strong field ionizations. The Coulomb potential $V(x)$ is a function of the distance x from the core and is modified in the presence of an external laser field. Depending on the Keldysh parameter and the intensity, the processes can be categorized in multiphoton, tunnel or barrier-suppression ionization. The threshold intensity I_{th} is defined in Eq. (2.10).

with I_{p} being the ionization potential, two regimes can be distinguished. For $\gamma \gg 1$ the ionization potential dominates over the ponderomotive potential and multiphoton ionization is observed, where several photons are simultaneously absorbed to

release the electron into the continuum (Fig. 2.2a). In the other case, $\gamma \ll 1$, the ionization potential is much smaller than the ponderomotive potential and the electron can tunnel out of the atomic Coulomb field (Fig. 2.2b). This case is referred to as the tunneling regime. Both regimes will be explained in detail in the following section.
At very high intensities the laser field suppresses the atomic Coulomb potential and an electron wavepacket can propagate directly into the continuum (Fig. 2.2c). In this case, the one dimensional electric potential can be classically described as a superposition of the ionic Coulomb potential and the quasistatic electric field (in atomic units) [65]:

$$V(x) = -\frac{Z}{|x|} - E_0 x, \tag{2.9}$$

where Z denotes the effective charge of the ion. The function $V(x)$ has a local maximum $x_{\max}$. Assuming that the electron has to overcome the ionization potential $I_p = V(x_{\max})$, a threshold intensity I_{th} can be calculated to

$$I_{\text{th}}\left(\text{W/cm}^2\right) = 4 \times 10^9 \frac{I_p^4(\text{eV})}{Z^2}. \tag{2.10}$$

For example, Xe has an ionization potential of $I_p = 12.1\,\text{eV}(Z = 1)$, thus the threshold intensity I_{th} is on the order of 10^{15}W/cm^2.

2.3.1 High-order harmonic generation

The discovery of HHG was very important in modern physics and led to the opportunity to directly access the electronic structure of atoms or molecules [8, 9]. In HHG, valence electrons are released by tunnel ionization, accelerated in the laser field, recombine with the parent ion and emit high-energy photons. In this highly nonlinear optical process, the interaction of an intense laser field, which is typically on the order of $10^{14} - 10^{15}\,\text{W/cm}^2$, with a target medium produces frequency-up converted extreme ultraviolet (XUV) radiation. By fulfilling the phase-matching conditions, intense XUV radiation can be generated. Nowadays, HHG is the standard approach to go beyond the femtosecond into the attosecond regime to observe electron dynamics in real time. Using a mid-infrared driving laser, energies up to 1.6 keV were already reached [66]. The shortest isolated attosecond pulse that has been measured so far with the laser-based streaking technique has a pulse duration (FWHM) of 43 as [6].
A typical spectrum in HHG consists of a superposition of odd harmonics of the driving laser field (Fig. 2.3). Due to the inversion symmetry of the target gas, even harmonics destructively interfere. Low-order harmonics form the perturbative regime where the intensity of a certain harmonic order decays exponentially. Higher harmonic orders have an equal intensity and define the plateau regime. At high energies the intensity of the harmonic radiation drastically decreases. This part of the spectrum is the so-called cut-off region. The maximum photon energy, i.e. the cut-off energy $\hbar\omega_{\max}$ obtained from HHG is given by

$$\hbar\omega_{\max} = I_\mathrm{p} + 3.17U_\mathrm{p}, \tag{2.11}$$

where I_p and U_p denote the ionization potential and the ponderomotive potential, respectively. The ponderomotive potential was introduced in Eq. (2.6). One of the first theoretical approaches to describe HHG solves the time-dependent Schrödinger equation (TDSE) numerically [67] and a slightly different prefactor of 3 instead of 3.17 in Eq. (2.11) was obtained. Further theoretical quasi-classical [68] and quantum mechanical [69] descriptions confirmed the cut-off energy. If higher photon energies are required in the experiment, then (i) a target gas with a higher ionization potential I_p, (ii) a higher electric field strength E_0 or (iii) a driving laser with a longer wavelength (since the ponderomotive potential U_p scales quadratically with the λ_L) can be used. In all cases the overall conversion efficiency will be reduced. Typical conversion efficiencies for nobles gases and a NIR driving laser are on the order of 10^{-8} (Ne) to 10^{-6} (Ar) [70]. Applying a longer wavelength λ_L reduces the HHG signal, since the harmonic yield scales with λ_L^{-6} in the plateau region and with λ_L^{-5} in the cut-off region, respectively [71]. Using a superposition of a NIR laser and its orthogonal second harmonic in He results in the highest ever measured conversion efficiency of 2×10^{-4} [72].

Semiclassical model:
HHG is qualitatively well described by the semiclassical or quasistatic 3 step model [68], which is valid, if

$$U_p \gg I_p \gg \hbar\omega_L \tag{2.12}$$

holds. This model is a single-atom response and will be described in detail in the following. The fundamental steps of HHG are tunnel ionization (Fig. 2.4b), motion of the electron wavepacket (Fig. 2.4c) and recombination with the parent ion leading to the emission of a high energy photon (Fig. 2.4d). HHG occurs every half cycle of the oscillating laser field.

Ionization:
When a strong laser field is applied to the target gas, the atomic Coulomb potential is bent and a weakly bound electron can tunnel through the finite Coulomb barrier into the continuum. In the quasistatic limit, i.e. long wavelength limit, the Keldysh parameter, according to Eq. (2.8), is zero. In this scenario the tunneling time is much shorter compared to the oscillation period of the driving electric field. The corresponding ionization rate, is described by the Ammosov-Delone-Krainov (ADK) theory [73] and for a linearly polarized electric field given by

$$\begin{aligned} W_\mathrm{ADK}(E(t)) &= |C_{n^*l^*}|^2 G_{l,m} \left(\frac{4\omega_s}{\omega_t}\right)^{2n^*-m-1} \exp\left(-\frac{4\omega_s}{3\omega_t}\right), \\ |C_{n^*l^*}|^2 &= \frac{2^{2n^*}}{n^*\Gamma(n^*+l^*+1)\Gamma(n^*-l^*)}, \\ G_{l,m} &= \frac{(2l+1)(l+|m|)!2^{-|m|}}{|m|!(l-|m|)!}, \end{aligned} \tag{2.13}$$

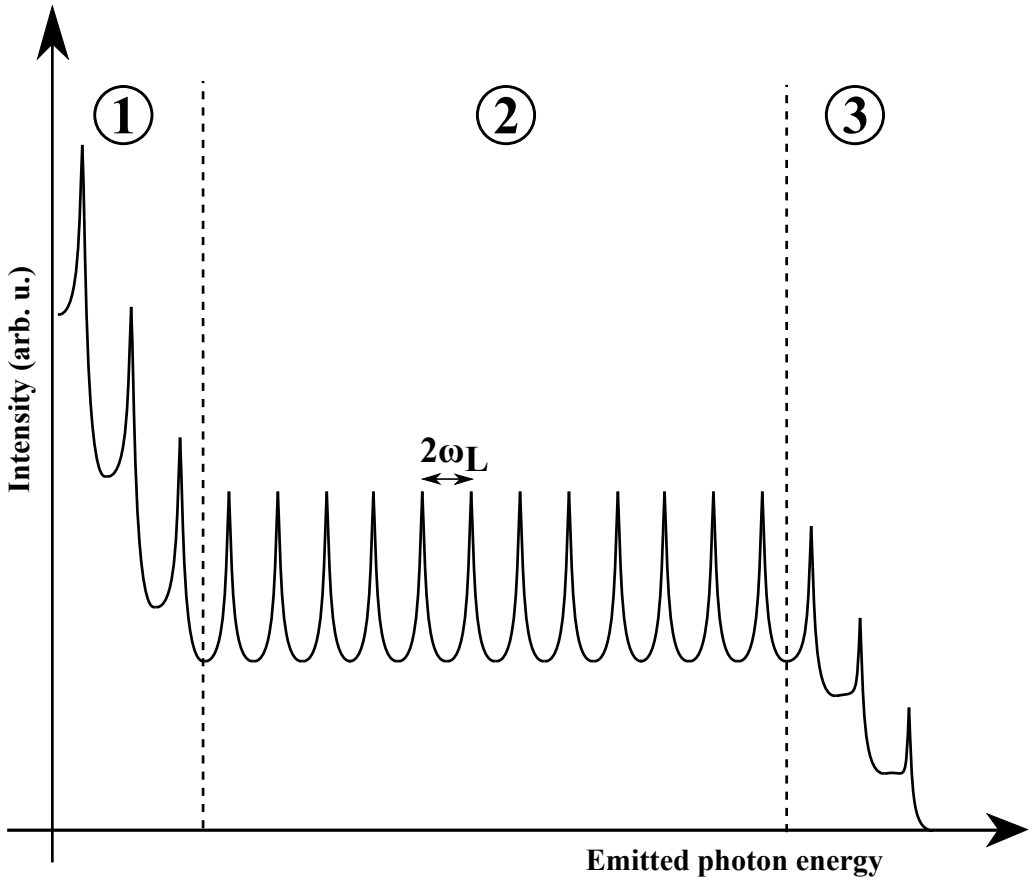

Figure 2.3: Sketch of a typcial HHG spectrum. The spacing between neighboring harmonics is $2\omega_L$. The parameter ω_L denotes the driving laser frequency. The HHG spectrum can be divided in 3 parts: (1) perturbative regime, (2) plateau regime, (3) cut-off regime.

with $\omega_s = I_p/\hbar$, $\omega_t = eE(t)/\sqrt{2m_e I_p}$, $n^* = \sqrt{I_p^h/I_p}$. The terms l and m represent the orbital quantum number and its projection. The variable I_p^h denotes the ionization potential of hydrogen and Γ is the Γ-function, whereas the electric field is described by $E(t)$. Since several energetic energy levels in an atom with different magnetic quantum numbers are occupied, the total ionization rate is given by

$$\tilde{W}_{\mathrm{ADK}}(E(t)) = \frac{1}{2l+1} \sum_{m=-l}^{l} W_{\mathrm{ADK}}(E(t)). \tag{2.14}$$

The total number of photoelectrons $N(t)$ generated with the intense electric field is formulated as

$$N(t) = N_0 \left[1 - \exp\left(- \int_{-\infty}^{t} \tilde{W}_{\mathrm{ADK}}(E(t'))dt' \right) \right], \tag{2.15}$$

where N_0 is the total number of atoms within a certain volume assuming that only one-electron ionizations take place. Note that the ADK-rates are valid only in the long wavelength limit. More accurate results are given by the Yudin-Ivanov theory,

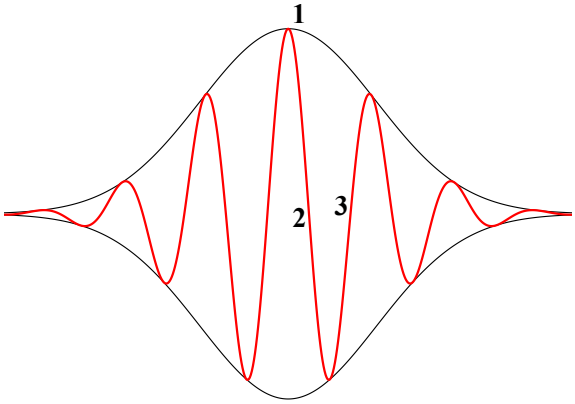

(a) Laser field

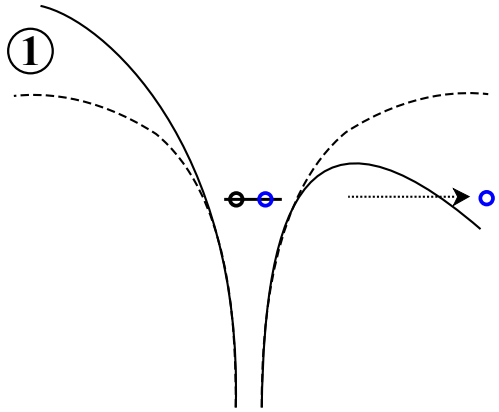

(b) Tunnel ionization

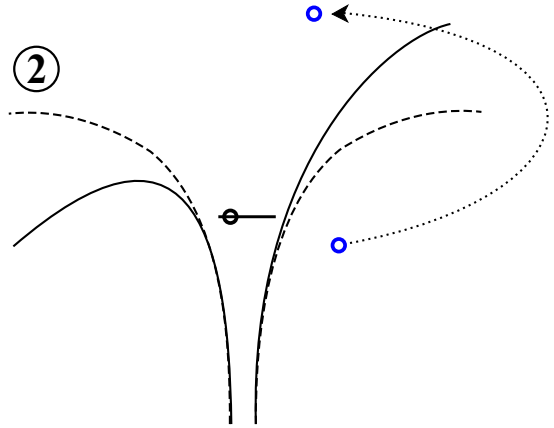

(c) Acceleration

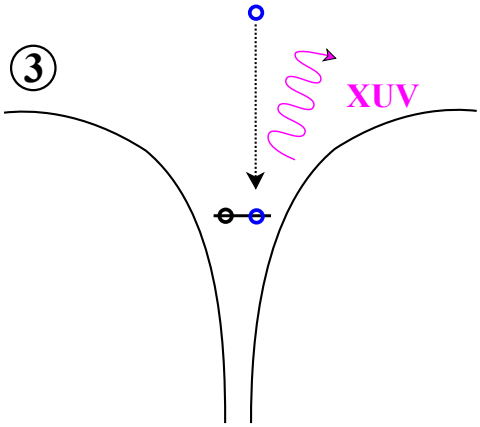

(d) Recombination and emission

Figure 2.4: Sketch of the HHG 3 step model. An intense ultrashort few-cycle laser pulse distorts the atomic Coulomb potential and an electron can tunnel into the continuum. The motion of the electron is determined by the electric laser field and, under certain conditions, might come back to the parent ion. The recombination leads to the emission of a high energy XUV photon.

which can be used if the Keldysh parameter is close to 1 [74].

Propagation of the photoelectron

The motion of the photoelectron can be described with classical mechanics. Using a linearly polarized electric laser field $E(t) = E_0 \cos(\omega_L t)$ along the x-direction as the driving force, where ω_L is the angular frequency and neglecting magnetic effects and the Coulomb potential of the remaining ion, the equation of motion is given by

$$\begin{aligned} m\ddot{x}(t) &= -eE_0 \cos(\omega_L t), \\ v_x(t) - v_{0x} &= -\frac{eE_0}{m\omega_L} \left[\sin(\omega_L t) - \sin(\omega_L t_0)\right], \\ x(t) - x_0 - v_{0x}(t - t_0) &= \frac{eE_0}{m\omega_L^2} \left[\cos(\omega_L t) - \cos(\omega_L t_0) + (t - t_0)\sin(\omega_L t_0)\right], \end{aligned} \tag{2.16}$$

where t_0 determines the ionization time. The initial position $x_0 = x(t_0)$ and initial velocity $v_{0x} = v_x(t_0)$ can be set to zero. From the condition $x(t_1) = 0$ that the electron comes back to its parent ion the return time t_1 can be calculated from the implicit formulation

$$\cos(\omega_L t_0) = \cos(\omega_L t_1) + (t_1 - t_0)\sin(\omega_L t_0). \tag{2.17}$$

Depending on the ionization time t_0, the photoelectron will either return or not return to the parent ion. During one optical laser cycle T_L the photoelectrons will only return to the core, if one of the following conditions is fulfilled:

$$\begin{aligned} 0 \leq \omega_L t_0 \leq \frac{\pi}{2} \\ \pi \leq \omega_L t_0 \leq \frac{3\pi}{2} \end{aligned} \tag{2.18}$$

In the other cases,

$$\begin{aligned} \frac{\pi}{2} < \omega_L t_0 < \pi \\ \frac{3\pi}{2} < \omega_L t_0 < \pi \end{aligned} \tag{2.19}$$

the photoelectrons will directly leave the parent ion. The first condition (2.18) in combination with a periodic driving laser field already shows that HHG occurs every half cycle. This means that there is a periodic emission of XUV photons twice per oscillation period of the electric field. In frequency-space this corresponds to an emission of every second harmonic, which already explains the harmonic spacing in the energy spectrum. The kinetic energy gained in the presence of the electric field at the recollision time t_1 is

$$E_{\text{kin}}(t_1) = \frac{m_e}{2} v(t_1)^2 = 2U_p \left[\sin(\omega_L t_1) - \sin(\omega_L t_0)\right]^2. \tag{2.20}$$

The ionization time t_0 determines the shape of the photoelectron trajectory and thus its kinetic energy $E_{\text{kin}}(t_1)$ at the recollision (Fig. 2.5a). The maximum kinetic energy of $3.17U_p$ is obtained for an initial phase $\omega_L t_0 \approx 18°$ (Fig. 2.5b). The corresponding trajectory is defined as the cut-off trajectory. All other trajectories are either long or short with respect to the cut-off trajectory (see. Tab. 2.1). For a given kinetic energy a short and a long trajectory exist. The trajectories are calculated for an intensity of $3.5 \times 10^{14}\text{W/cm}^2$, which corresponds to a maximum electric field strength of $5.1 \times 10^{10}\text{V/m}$. The maximum displacement of a photoelectron from the parent ion is on the order of 3 nm. In the classical description, photoelectrons will never come back to their initial position when circularly polarized electric light is used and thus no HHG takes place.

Recombination

When a photoelectron joins its parent ion again, the photoelectron can scatter (elastically or inelastically), liberate additional electrons (e.g. non-sequential double ionization) or recombine. In the latter case an XUV photon with energy

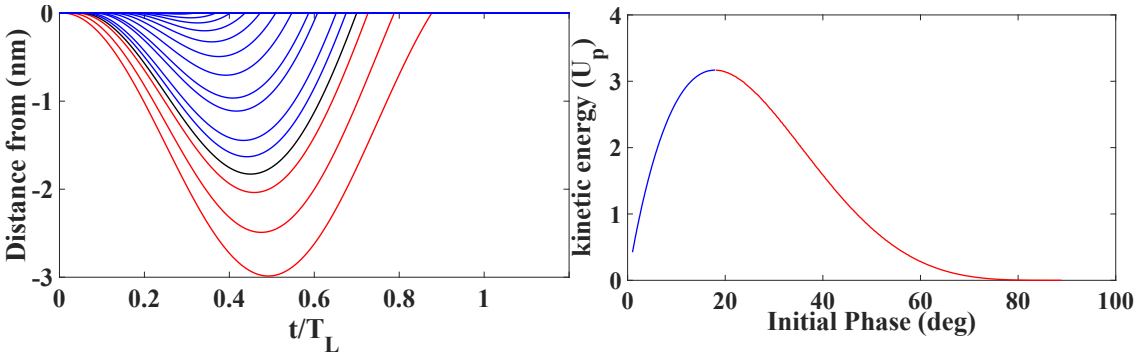

(a) Photoelectron trajectories

(b) Kinetic energy

Figure 2.5: Calculated classical photoelectron trajectories (see Eq. (2.16)) and corresponding kinetic energies (see Eq. (2.20)). Short (long) trajectories are blue (red). The cut-off trajectory has the highest kinetic energy of $3.17U_p$ (black).

Type	Ionization phase $\omega_L t_0$
cut-off trajectory	$18°$
Short trajectory	$0° \leq \omega_L t_0 < 18°$
Long trajectory	$90° \geq \omega_L t_0 > 18°$

Table 2.1: HHG trajectories and corresponding ionization phases using Eq. (2.16)

$$\hbar\omega_{\mathrm{XUV}} = I_p + E_{\mathrm{kin}} \tag{2.21}$$

is emitted. For the cut-off trajectory the highest kinetic energy of $E_{\mathrm{kin}} = 3.17U_p$ of the photoelectron is transferred to a photon and thus the cut-off energy (see Eq. (2.11)) is obtained.
A fully quantum-mechanical description of the HHG theory was given by [69] using the strong field approximation (SFA), which assumes that the Coulomb field of the parent ion during the motion of the photoelectron can be neglected. HHG theory was further generalized for elliptically polarized light where the finite extension of the electron wavepacket and quantum diffusion effects were taken into account [75]. Note that relativistic effects will play an important role provided that $2U_p > m_e c^2$ [76].
In the previous descriptions, only a single-atom response was considered. However, a macroscopic analysis of the HHG process is very important to apply this concept to experiments since HHG will take place in several atoms within the target gas volume [77] (Fig. 2.6). The following considerations are mainly taken from [63, 78]. During the propagation of XUV photons in the target gas volume, effects like absorption, dephasing and defocusing play an important role. Hence, the cut-off energy (Eq. (2.11)) is usually not reached. In the following it is assumed that HHG will take place within a gas target volume of length L_{med}.

Absorption
The energy of HHG photons is usually sufficient to excite or ionize deeply-bound

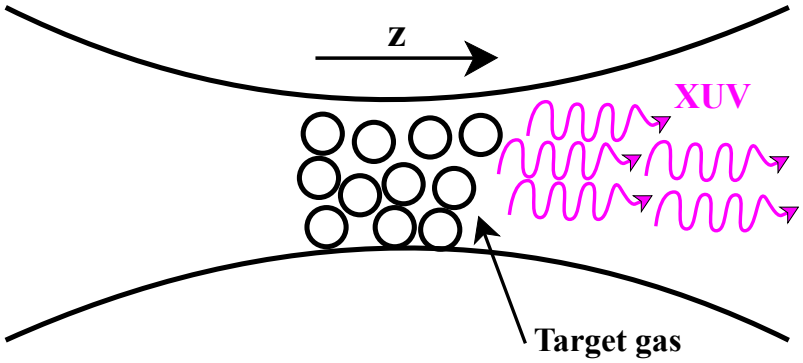

Figure 2.6: Experimental arrangement of an HHG process. The target gas is placed in the focus of a laser beam, which propagates along the z-direction. Under appropriate conditions XUV radiation will be generated.

electrons. The absorption cross-section σ_q of the harmonic order q strongly depends on the target gas and the photon energy [55]. A substantial part of the generated harmonics can be reabsorbed and thus the overall HHG efficiency is reduced. A quantitative parameter to describe reabsorption is the absorption length $L_{\text{abs}} = 1/n_a\sigma_q$, that defines the length at which the signal intensity is reduced by a factor of e. The variable n_a denotes the atomic density. As a consequence, the target gas volume should be spatially confined according to the optimum conditions and residual target gas in the vicinity should be removed to avoid reabsorption.

Dephasing

Phase-matching between the driving electric field and the generated electric field of the harmonic wave is important to achieve a high HHG output. The phase-mismatch is defined as

$$\Delta k = k_q - qk_L = \Delta k_{\text{dipole}} + \Delta k_{\text{G}} + \Delta k_{\text{disp}}, \tag{2.22}$$

where $k_L = 2\pi/\lambda_L$ and $k_q = 2\pi/\lambda_{\text{XUV}}$ are the wave numbers of the driving laser field and the generated harmonic, respectively. The term q denotes the order of the HHG radiation. In this context the coherence length

$$L_{\text{coh}} = \pi/\Delta k \tag{2.23}$$

can be defined, which is the propagation distance where the HHG yield increases monotonically. If the phase mismatch between both electric fields is high, the harmonic yield will be reduced. The main contributions for dephasing between the driving and HHG electric field are the dipole Δk_{dipole}, the geometrical Δk_{G} and the dispersive Δk_{disp} phase mismatch.
The dipole phase mismatch Δk_{dipole} along the propagation direction z is given by

$$\Delta k_{\text{dipole}} = -\alpha_q \frac{\partial I_L}{\partial z}, \tag{2.24}$$

where I_L is the laser intensity and α_q is a positive coefficient that depends on the harmonic order q. The coefficient is small (large) for short (long) trajectories.
The geometrical phase mismatch Δk_{G} for a Gaussian beam is determined by the Gouy phase and can be calculated using Eq. (A.8)

$$\Delta k_{\mathrm{G}} = -q\frac{\partial \Phi_G}{\partial z} = -q\frac{\partial}{\partial z}\left[\arctan\left(\frac{z}{z_r}\right)\right] \approx -\frac{q}{z_r}, \tag{2.25}$$

where z_r denotes the Rayleigh length. This equation is valid if the medium length L_{med} is small compared the Rayleigh length z_r.
The dispersive phase mismatch Δk_{disp} originates from the contribution of free electrons and neutral atoms within the target gas volume and can be calculated by [79]

$$\Delta k_{\mathrm{disp}} = p\left[\eta N_a r_e\left(q\lambda_L - \frac{\lambda_L}{q}\right) - \frac{2\pi(1-\eta)q}{\lambda}\Delta\delta\right]. \tag{2.26}$$

The parameter $\Delta\delta$ is the difference of the refractive indices between the harmonic and driving laser. The other variables η, N_a, p and r_e denote the ionization fraction, the atomic number density, the gas pressure and the classical electron radius, respectively.
Substituting Eqs. (2.26) and (2.25) into (2.22), a relation between the different parameters can be obtained. Experimentally, phase matching can be achieved for a given focusing geometry by varying (1) the target gas pressure, (2) the laser focus intensity or (3) the focus position. A change in the target gas pressure (1) directly changes the dispersive phase, i.e. the contribution of the free electrons and the neutral atoms. A variation of the intensity (2) changes the ionization fraction as well as the dipole phase. When the focus position with respect to the gas target volume is changed (3), all three phase contributions are influenced. In the phase-matched case, the ionization fraction is on the order of a few percent. The corresponding optimum pressure is on the order of several hundreds of mbar for a tight focusing geometry while the optimum pressures are significantly lower for loose focusing geometries.
An estimation of the photon number $N_{\mathrm{out}}^{(q)}$ per unit of time and area of the qth harmonic, which is emitted on-axis, is given by [80]

$$\begin{aligned} N_{\mathrm{out}}^{(q)} &= \frac{\omega_q}{4c\epsilon_0\hbar}\left|\int_0^{L_{\mathrm{med}}} \rho A_q(z)\exp\left(-\frac{L_{\mathrm{med}}-z}{2L_{\mathrm{abs}}}\right)\exp[i\varphi_q(z)]dz\right|^2 \\ &= \rho^2 A_q^2 \frac{4L_{\mathrm{abs}}^2}{1+4\pi^2(L_{\mathrm{abs}}^2/L_{\mathrm{coh}}^2)}\left[1+\exp\left(-\frac{L_{\mathrm{med}}}{L_{\mathrm{abs}}}\right)-2\cos\left(\frac{\pi L_{\mathrm{med}}}{L_{\mathrm{coh}}}\right)\exp\left(-\frac{L_{\mathrm{med}}}{2L_{\mathrm{abs}}}\right)\right]. \end{aligned} \tag{2.27}$$

Here, $A_q(z)$ is the amplitude of the atomic response at the harmonic frequency ω_q and $\varphi_q(z)$ is the accumulated phase at the end of the interaction volume. In the second step of Eq. (2.27) a z-independent A_q and a constant gas density ρ was assumed.
An increase of the laser intensity leads to a shift of the optimum target gas pressure towards larger values. This is a consequence of the ionization fraction η. For larger

intensities the number of free electrons increases and thus the pressure has to be raised in order to preserve the optimum ionization fraction. In general, two different regimes in the HHG process can be observed: absorption-limited and phase-matched limited. In the first case, the HHG signal is reduced when propagating through the interaction volume, since the harmonic is reabsorbed. Typically this effect occurs for the generation of lower-order harmonics. In the second case, the absorption length is significantly larger than the coherence length and the HHG signal is drastically reduced. The two conditions

$$\begin{aligned} L_{\text{med}} &= 3L_{\text{abs}} \\ L_{\text{coh}} &= 5L_{\text{abs}} \end{aligned} \tag{2.28}$$

guarantee that the overall signal is at least half the highest possible value [80].

Defocusing
The generation of free electrons strongly depends on the local intensity of the laser within the interaction volume. The largest free electron densities are reached in the center of the beam while the densities at the wings are weaker. These differences give rise to various refractive indices and thus to defocusing effects.

2.3.2 Multiphoton ionization

The multiphoton regime is characterized by a large Keldysh parameter $\gamma \gg 1$. Typically, at laser intensities on the order of $10^{13}\,\mathrm{W/cm^2}$ multiphoton ionization takes place, i.e. the simultaneous absorption of several photons $S = (N+M)$, where N is the minimum number of absorbed photons necessary to exceed the binding energy E_{b}. The variable M is the additional number of photons, which are absorbed above the ionization potential. Hence, the kinetic energy of the photoelectron is given by

$$E_{\text{kin}}(S, E_{\text{b}}) = S \cdot \hbar\omega_L - (E_{\text{b}} + U_p), \tag{2.29}$$

where ω_L is the center laser frequency. This process is also called ATI. The correction in Eq. (2.29) due to the ponderomotive potential U_p can be understood as a Stark shift and becomes important for high laser intensities. At these intensities, lower ATI peaks are suppressed. For low laser intensities, this effect is negligible. In the first ATI experiment [37], Xe was ionized and two peaks above the threshold ($N = 6$, $M_{1,2} = 0, 1 \Rightarrow S_{1,2} = 6, 7$) were observed using the second harmonic of a Nd^{3+} glass laser ($2\hbar\omega_L = 2.34\,\mathrm{eV}$). The probability to absorb multiple photons simultaneously scales nonlinearly with the laser intensity I_0 and is calculated by

$$W_{\text{MPI}} \propto \sigma_S I_0^S. \tag{2.30}$$

Hence, higher ATI peaks require higher laser peak intensities. In further experiments, which were carried out on Xe and Kr, higher ATI peaks were studied [81, 82].

The photoelectron angular distribution of an ATI process is obtained by calculating the dipole matrix element between the initial bound state and the final continuum [83, 84]. Assuming linearly polarized light and neglecting spin-orbit coupling as well as hyperfine splitting, the differential S-photoionization cross section $d\sigma^{(S)}/d\Omega$ in the dipole approximation is given by

$$\begin{aligned} \frac{d\sigma^{(S)}}{d\Omega}(\Theta) &= \frac{\sigma_{\text{tot}}}{4\pi} \sum_{j=0}^{2S} \beta_{2j} P_{2j}(\cos\Theta) \\ -1 \leq \beta_{2j} &\leq 2, \end{aligned} \tag{2.31}$$

Here, the terms P_{2j} represent the Legendre polynomials, β_{2j} are the so called anisotropy parameters and σ_{total} is the total ionization cross section. The first Legendre polynomials are given in the appendix (see section A.1). The angle Θ is defined with respect to the polarization axis. Eq. (2.31) means that $2S$ Legendre polynomials and anisotropy parameters are necessary to describe the angular distribution of any S-photoionization process. Note that only even Legendre polynomials are needed to describe the angular distribution.

2.3.3 Rescattering of photoelectrons

Both previously described processes are well defined for $\gamma \gg 1$ (multiphoton ionization) and $\gamma \ll 1$ (tunnel ionization). However, using e.g. an NIR laser system the experiments are typically carried out with intensities on the order of $10^{14}\,\text{W/cm}^2$ and the corresponding Keldysh parameter becomes comparable to unity. In this case, the low energy ATI peaks are strongly suppressed due to a large ponderomotive potential U_p. Moreover, the kinetic photoelectron spectrum shows a plateau [38], which cannot only be described with Eq. (2.29). A better description is given by the SFA, which was introduced in the previous section. Consequently, it is also possible to describe ATI processes with the 3-step model. In the presence of a strong laser field, a photoelectron is ionized, accelerated in its field and eventually comes back and rescatters with the parent ion. The trajectory of the photoelectron in the second step can be classically described with Eq. (2.16), where the Coulomb potential of the remaining ion is neglected. Depending on the ionization time t_0, the photoelectron will either directly leave or will return to the parent ion.
In the first case, the trajectories of the photoelectrons are called direct and the measured kinetic energy far away from the target volume is obtained by the time-averaged kinetic energy using Eq. (2.16)

$$E_{\text{kin}} = \frac{m}{2T_L} \int_0^{T_L} v_x^2 dt - U_p = 2U_p \sin^2(\omega_L t_0). \tag{2.32}$$

Note that for direct trajectories one of the conditions (2.19) has to be met. Obviously, the maximum kinetc energy of $2U_p$ is reached for every zero crossing of the driving electric field (Fig. 2.7a).
In the second case, the photoelectron may scatter (forward or backward) from the ionic core at time t_1 (see Eq. (2.17)). Assuming elastic scattering with an angle ϑ_0

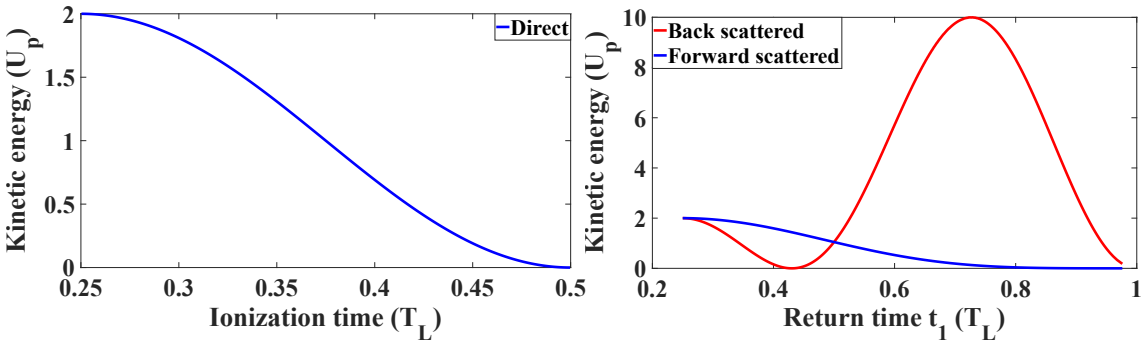

(a) Direct trajectories (b) Scattering trajectories

Figure 2.7: (a) Direct trajectories. Calculated kinetic energies of scattered photoelectrons using Eq. (2.32). (b) Scattering trajectories. Calculated kinetic energies of scattered photoelectrons using Eq. (2.34). Forward (back) scattering is described by $\vartheta_0 = 0$ ($\vartheta_0 = \pi$).

with respect to the x-axis, the velocity of the photoelectron after scattering $t \geq t_1$ is described by [40]

$$\begin{aligned} v_x &= -\frac{eE_0}{m\omega_L}\left[\sin(\omega_L t) - \sin(\omega_L t_1) + \cos\vartheta_0\left(\sin(\omega_L t_1) - \sin(\omega_L t_0)\right)\right], \\ v_y &= -\frac{eE_0}{m\omega_L}\sin\vartheta_0\left(\sin(\omega_L t_1) - \sin(\omega_L t_0)\right). \end{aligned} \tag{2.33}$$

The measured kinetic energy E_{kin} of the photoelectron with a detector far away from the target volume is given by the time-averaged kinetic energy

$$\begin{aligned} E_{\text{kin}} &= \frac{m}{2T_L}\int_0^{T_L}\left(v_x^2 + v_y^2\right)dt - U_p \\ &= 2U_p\left[\sin^2(\omega_L t_0) + 2(1-\cos\vartheta_0)\sin(\omega_L t_1)\left(\sin(\omega_L t_1) - \sin(\omega_L t_0)\right)\right]. \end{aligned} \tag{2.34}$$

Forward scattering corresponds to $\vartheta_0 = 0$ while back scattering is determined by $\vartheta_0 = \pi$. Forward-scattered photoelectrons have a maximum kinetic energy of $2U_p$ (Fig. 2.7b). On the other hand, back-scattered photoelectrons can reach kinetic energies up to $10U_p$ and they form a plateau (Fig. 2.8a). Those heights are many orders of magnitude lower than the maximum height of the spectrum and is most apparent for Xe and Ar. [40].
Another interesting feature occurs at energies well below U_p (Fig. 2.8b). At very low energies, a characteristic spike is observed and becomes dominant and broader for longer wavelengths of the driving laser. In addition, it also seems to be a universal effect, since it is measured for different atoms and molecules. SFA does not explain this peak because the Coulomb interaction between the photoelectron and the parent ion is neglected but it plays an important role for rescattered photoelectrons. Therefore, the influence of the Coulomb field has to be taken into account. A detailed review about low-energy (LE) structures can be found elsewhere [85].

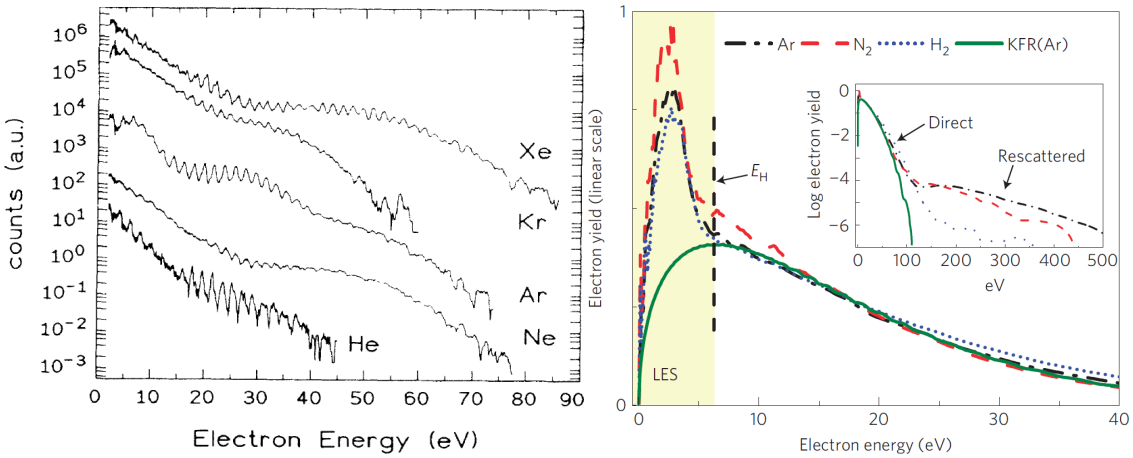

(a) ATI plateau (b) LE structure

Figure 2.8: (a) Photoelectron spectra of several noble gases. The applied intensities correspond to Keldysh parameters close to unitiy. In each spectrum a characteristic platau up to $10U_p$ is clearly visible (reprinted from [38] with permission from American Physical Society) (b) LE structure well below U_p. This features appears for any target gas and is more pronounced for higher wavelengths (reprinted from [42] with permission from SpringerNature).

2.4 Terahertz radiation

The following section is based on [86]. Terahertz (THz) radiation roughly covers the frequency spectrum between 0.1 THz and 30 THz. Especially in the past three decades, scientific and technological efforts made it possible to access this part of the electromagnetic spectrum and close the gap between the microwave and infrared region, the so-called THz gap (Tab. 2.2) . The THz spectrum is so important because many phenomena, like phonon excitation in solid states or gap sizes of superconductors are associated with these energies. Moreover, THz photons ca be used to transfer momentum to photoelectrons, which plays an essential role when using a THz-based light-field driven streak camera.

Physical property	Physical unit
Frequency f	$(0.1 - 30)$ THz
Oscillation period $T = 1/f$	$(0.03 - 10)$ ps
Wavelength $\lambda = c/f$	$(10 - 3000)$ μm
Photon energy $E = hf$	$(0.41 - 124)$ meV
Temperature $T = hf/k_B$	$(4.8 - 1440)$ K

Table 2.2: Characteristics of THz radiation [86].

2.4.1 Terahertz generation

In the following section an overview about different THz generation methods will be given. An extensive review about THz generation methods can be found elsewhere

[87].

Photoconductive antenna
A photoconductive antenna (PCA) consists of a semiconductor substrate (e.g. low-temperature grown GaAs) and a metallic electrode arrangement on the surface to apply a biased DC voltage [88]. When an ultrashort laser pulse impinges the semiconductor surface, free charge carriers are generated provided that the photon energy is higher than the semiconductor bandgap. These free charge carriers are subsequently accelerated by the applied electric field and the induced electric current I_{PC} gives rise to the emission of THz radiation

$$E_{\mathrm{THz}}(t) \propto \frac{dI_{\mathrm{PC}}}{dt}. \tag{2.35}$$

Typically, a near single-cycle pulse with a sub-ps peak width is emitted (Fig. 2.9a). This corresponds to a spectrum with a center frequency of around 1 THz (Fig. 2.9b).

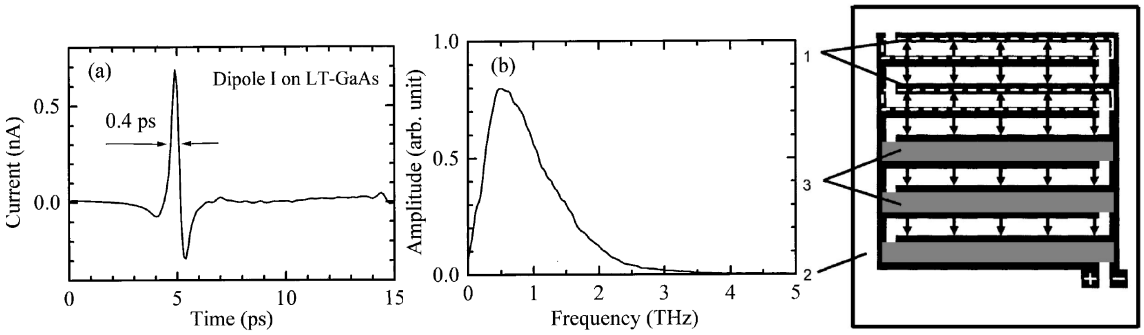

(a) Time-dependent current (b) THz spectrum (c) Electrode arrangement

Figure 2.9: (a) Time-dependent current, which produces THz radiation (see Eq. (2.35)), (b) THz spectrum (both reprinted from [89] with permission from Optical Society of America) (c) Electrode arrangement on the semiconductor substrate, 1: interdigitated finger electrodes, 2: GaAs substrate, 3: metallization block, the arrows indicate the direction of the biased electric field (reprinted from [90] with permission from AIP Publishing).

THz output scaling is often limited by saturation effects. Further developments led to a special metal-semiconductor-metal structure (Fig. 2.9c) to obtain higher THz electric fields. The interdigitated metal electrode structure is attached to the GaAs surface and every second electrode gap is blocked with another Au metallization in order to ensure an unidirectional acceleration of the free charge carriers and thus no destructive interferences of THz radiation in the far field [90]. When the biased voltage is synchronized with the ultrashort laser pulses, the thermal heat deposition can be drastically reduced and peak THz electric fields up to 3.6 MV/m are measured [91]. In this case the NIR-to-THz conversion efficiency is 2×10^{-3}.

Air-plasma-generation
Another approach to get high THz electric field strengths can be realized by focusing an intense ultrashort laser above the threshold intensity into a gas and generate

a plasma. A further nonlinear crystal is placed before the focus to generated additional second harmonic radiation. The superposition of both beams results in a coherent emission of THz radiation, which is separated by a low-pass filter [92]. This process was first described by a third-order nonlinear process, however, it was not possible to explain the measured THz field strengths. A better description was given a few years later by directly solving the TDSE [93].

Undulator-based generation
An undulator is a periodic arrangement of alternating poled magnets with a constant magnetic field B_0. Electrons with relativistic speeds $v \approx c$, rest mass m_e and charge e that enter this structure are deflected due to the Lorentz force. The movement of these electrons is perpendicular to the direction of the magnetic field and velocity and result to the emission of synchrotron radiation of wavelength

$$\lambda_{\mathrm{ph}} = \frac{\lambda_{\mathrm{u}}}{2\gamma^2}\left(1 + \frac{K^2}{2}\right). \tag{2.36}$$

Here, λ_{u} is the undulator period, $\gamma = (1 - v^2/c^2)^{-1/2}$ and $K = eB_0\lambda_{\mathrm{u}}/2\pi m_e c$ the undulator parameter. For a given undulator geometry, i.e. a fixed undulator parameter K, the emitted photon wavelength in Eq. (2.36) is tuned by changing the speed v of the accelerating electrons and THz radiation can be produced.

Optical rectification
A very important technique to generate intense table-top THz radiation is optical rectification (OR). This method is a second-order nonlinear effect and can be understood as difference-frequency mixing within a broadband initial pulse inside a nonlinear crystal. Assuming an initial Gaussian pulse with a duration of $\tau = 25\,\mathrm{fs}$ (FWHM), the time-bandwidth product [59]

$$0.441 = \tau\Delta\nu \tag{2.37}$$

yields a spectral width of $\Delta\nu = 17.6\,\mathrm{THz}$ (FWHM). This bandwidth is sufficient to generate THz pulses. Generally, the source term, i.e. the nonlinear polarization, for second-order nonlinear processes is given by Eq. (2.4):

$$P_{\mathrm{i}}^{(2)}(\omega_1, \omega_2) = \epsilon_0 \chi_{ijk}^{(2)}(\omega_1, \omega_2) E_j(\omega_1) E_k(\omega_2). \tag{2.38}$$

In the simplest case the nonlinear medium is isotropic, i.e. off-diagonal elements of the susceptibility tensor vanish. If the initial wave is a superposition of two plane waves with the same amplitude E_0 and linearly polarized along one direction [59]

$$E(\omega_1, \omega_2) = \frac{E_0}{2}\left(\exp(-i\omega_1 t) + \exp(-i\omega_2 t) + c.c.\right), \tag{2.39}$$

then only one term in Eq. (2.38) is not equal to zero and yields

$$\begin{aligned} P^{(2)}(\omega_1, \omega_2) &= \frac{\epsilon_0}{2} E_0^2 \chi^{(2)} \left[\exp(-i\omega_1 t) + \exp(-i\omega_2 t)\right]^2 + c.c. \\ &= \frac{\epsilon_0}{2} E_0^2 \chi^{(2)} [\exp(-2i\omega_1 t) + \exp(-2i\omega_2 t) \\ &\quad + \exp(-i(\omega_1 - \omega_2)t) + \exp(-i(\omega_1 + \omega_2)t) + 2 + c.c.]. \end{aligned} \tag{2.40}$$

The different contributions account for second-harmonic generation $(2\omega_1, 2\omega_2)$, sum-frequency generation $(\omega_1 + \omega_1)$, difference-frequency generation $(\omega_1 - \omega_1)$ and OR, which is a constant term. In the general case of a broadband laser pulse

$$E(t) = \frac{1}{2}\left[E_0(t)\exp(-i\omega_0 t) + c.c.\right], \tag{2.41}$$

where ω_0 and $E_0(t)$ denote the carrier frequency and the slowly-varying envelope, respectively, the propagation through a nonlinear crystal of length L yields for $z \leq L$ [94]

$$\begin{aligned} E(\omega, z) &= \frac{\mu_0 \chi^{(2)}(\omega) I_0(\omega)}{n(\omega_0)\left[\frac{c}{\omega}\left(\frac{\alpha_{\mathrm{THz}}(\omega)}{2} + \alpha_0\right)\right] + i\left[n(\omega) + n_g\right]} \times g(\omega, z) \\ g(\omega, z) &= \frac{\exp\left[-i\frac{\omega n(\omega)}{c}z\right]\exp\left[-\frac{\alpha_{\mathrm{THz}}(\omega)}{2}z\right] - \exp\left(-i\frac{\omega n_g}{c}z\right)\exp(-\alpha_0 z)}{\frac{\alpha_{\mathrm{THz}}(\omega)}{2} - \alpha_0 + i\frac{\omega}{c}\left[n(\omega) - n_g\right]}, \end{aligned} \tag{2.42}$$

where only OR is considered. Here, $\chi^{(2)}(\omega) = \chi^{(OR)}(\omega)$ is the susceptibility , $I_0(\omega)$ is the spectral intensity of the input pulse, n_g is the group index, $n(\omega)$ is the refractive index, α_0 is the absorption coefficient of the input pulse and $\alpha_{\mathrm{THz}}(\omega)$ absorption coefficient of the generated THz pulse. The consequences of this equation will be discussed in the following.

High nonlinear coefficient

Obviously, a high nonlinear coefficient $\chi^{(2)}(\omega)$ will produce a higher THz electric field (Tab. 2.3). Note that contrary to the previous assumption of an isotropic medium, the used THz crystals are generally anisotropic, which means that non-vanishing off-axis tensor elements exist. Below resonances, the susceptibility can be regarded as independent of the frequency and a contracted notation d_{il} can be introduced [59]

$$\begin{aligned} d_{\mathrm{ijk}} &= \frac{1}{2}\chi^{(2)}_{\mathrm{ijk}}, \\ d_{\mathrm{ijk}} &= d_{\mathrm{ikj}} = d_{\mathrm{il}} \end{aligned} \tag{2.43}$$

with the redefinition of the indices

jk:	11	22	33	23, 32	31, 13	12, 21
l:	1	2	3	4	5	6.

For a given nonlinear crystal and fixed geometry, the nonlinear polarization can be formulated as a scalar value d_{eff} and is usually used to describe the nonlinear effect. In the past years increased efforts were carried out to grow crystals for THz generation, especially organic crystals like DAST [95], DSTMS [96] or OH1 [97], with high d_{THz}. However, these organic crystals require a higher pump wavelength, which implies using an optical parametric amplifier (OPA) when only an 800 nm laser is

Nonlinear crystal	d_{THz}(pm/V)	$\lambda_{\mathrm{pump}}(\mu\mathrm{m})$	f_{THz}(THz)
ZnTe	64	0.84	1
GaP	24	1.0	1
$LiNbO_3$	160	0.8	1
DAST	240	1.5	3.5
DSTMS	250	1.5	3.5
OH1	280	1.35	1.5

Table 2.3: Nonlinear coefficients for crystals to generate THz radiation via optical rectification. The data was taken from [98]. Ultrashort pulses with a center wavelength λ_{pump} are used to pump the nonlinear crystal and THz radiation with a center frequency f_{THz} is expected.

available.

Intensity of pump pulse

Another prerequisite for the generation of intense THz pulses is a high intensity $I_0(\omega)$ of the input pulse at the pump wavelength. The maximum intensity, which is applied to the nonlinear crystal, is limited by its photorefractive (PR) damage threshold. Although organic crystals have the highest nonlinear coefficients, they often suffer a lower PR damage threshold in comparison to inorganic crystals like $LiNbO_3$. One way to increase the THz output would be to grow bigger crystals, which is chemically challenging. For example, there are two ways to produce $LiNbO_3$ crystals: stoichiometric or congruent growth. In the latter case much bigger crystals can be produced and they only show a slightly smaller nonlinear coefficient [99]. Furthermore, an incorporation of MgO into the crystal lattice structure gives rise to a bigger PR damage threshold [100].

Phase matching

An important aspect is phase-matching between the fundamental and THz pulse to ensure an efficient THz generation. According to Eq. (2.42), the group index n_g of the fundamental pulse has to be matched with the refractive index $n(\omega)$ of the THz pulse (Tab. 2.4). The phase matching condition is intrinsically fulfilled for the organic crystals while there is a big discrepancy for the $LiNbO_3$ crystal. Hence, there will be no phase-matching in the collinear geometry. A possible route to achieve phase-matching can be realized with a pulse-front tilt, which will be explained later. In analogy to Eq. (2.23), the coherence length L_{coh} is defined by

$$L_{\mathrm{coh}} = \frac{\pi c}{\omega \left[n(\omega) - n_g \right]}, \tag{2.44}$$

where THz absorption is neglected. The case of non-vanishing THz absorption was considered in [94]. The THz energy $E_{\mathrm{THz}}^{(\mathrm{g})}$ is generated inside a crystal with refractive index n_{THz}. Therefore, the THz energy has to be coupled out into free space causing Fresnel reflection losses. The resulting THz energy is reduced to

$$E_{\mathrm{THz}}^{(\mathrm{T})} = E_{\mathrm{THz}}^{(\mathrm{g})} \frac{(n_{\mathrm{THz}} - 1)^2}{(n_{\mathrm{THz}} + 1)^2}. \tag{2.45}$$

Nonlinear crystal	$n_g(\lambda_{\mathrm{pump}})$	n_{THz}	$\alpha_{\mathrm{THz}}\,(\mathrm{cm}^{-1})$	$f_{\mathrm{TO}}(\mathrm{THz})$
ZnTe	2.18	3.16	1.3	5.3
GaP	4.01	3.34	0.2	10.8
$LiNbO_3$	2.18	4.96	17	
DAST	2.3	2.26	20	1.1 [94]
DSTMS	2.3	2.26	15	1.0 [101]
OH1	2.33	2.28	2	1.8 [102]

Table 2.4: Properties of nonlinear crystals to generate THz radiation via optical rectification. The data was taken from the literature (see brackets) and [98].

THz absorption
The THz output spectrum is also determined by THz absorption within the nonlinear crystal. In many crystals transversal optical (TO) phonons lead to a reduction of the generated THz field (Tab. 2.4). In case of the inorganic $LiNbO_3$ crystal, a cryogenic cooling will strongly suppress the phonon-polariton coupling and therefore drastically reduce the THz absorption. The conversion efficiency can be increased by more than a factor of 3 [103].

In the previous discussions the required properties of nonlinear crystals were analyzed. The best suitable candidates seem to be organic crystals since they posses the highest nonlinear coefficients, a good phase-matching over the generation spectrum and a relatively low THz absorption coefficient. However, for efficient THz generation an OPA is required to produce pump wavelengths on the order of 1.5 μm beforehand. In this step typically a 800 nm-to-1.5 μm conversion efficiency around 50% is reached. Besides this, the amount of available laser energy is not enough to drive HHG and THz generation using an OPA at the same time. As a result, the chosen crystal is $LiNbO_3$, which is also a good choice for the generation of intense THz radiation. Another advantage of this crystal is its relatively low center frequency of the THz spectrum at 1 THz compared to the organic crystals. As will be shown in the next section, this is favorable, since the energetic shift of a photoelectron in the presence of a THz streaking field is more pronounced for lower THz frequencies. On the other hand, of course, the focus size of a THz beam gets bigger when the center frequency is lower. As already stated above, $LiNbO_3$ cannot be used in a collinear geometry because phase-matching won't be achieved (Tab. 2.4). Instead, a tilt in the pulse front has to be introduced, which is explained in the following.
A detailed explanation can be found elsewhere [104–106]. Briefly, for efficient THz generation the group velocity $v_g(\lambda_0)$ should be the same as the phase velocity v_{THz} of the THz pulse (see Eq. (2.42)), which is realized by tilting the pulse front of the pump pulse by an angle Θ. The phase-matching condition can be written as

$$v_g(\lambda_0) \cdot \cos\Theta = v_{\mathrm{THz}} \quad \Rightarrow \quad \cos\Theta = \frac{n_g}{n_{\mathrm{THz}}}. \tag{2.46}$$

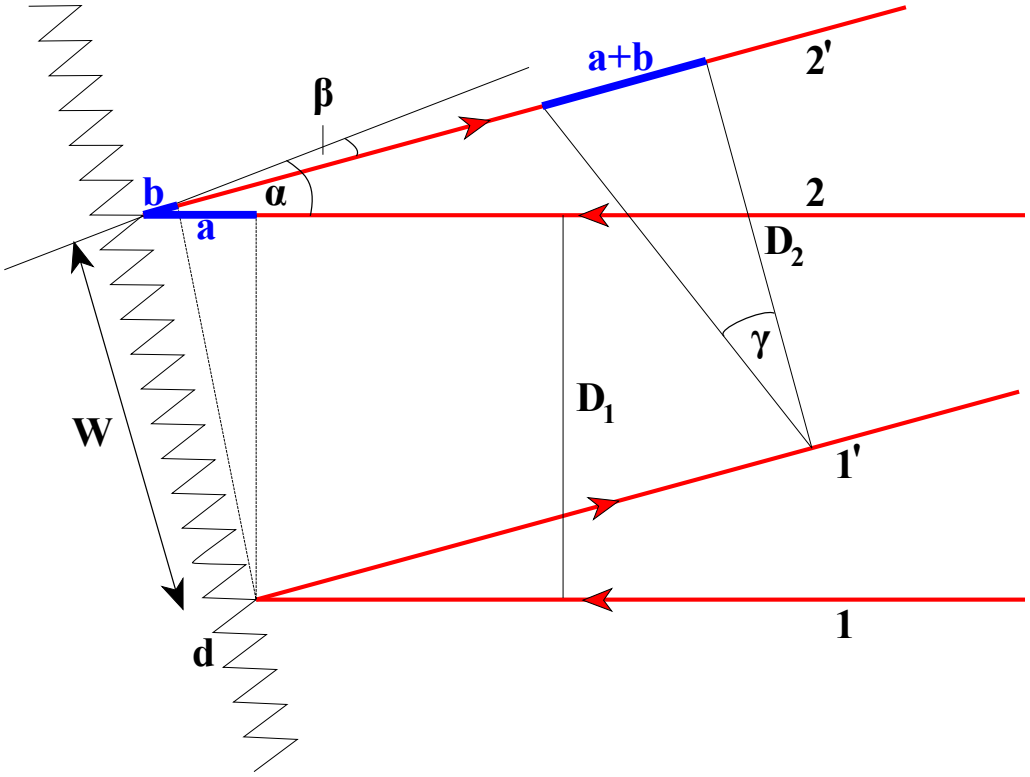

Figure 2.10: Introduction of a pulse-front tilt. A monochromatic beam (width D_1) is diffracted (width D_2) at a grating with line spacing d. Incoming and diffracted angle are α and β, respectively. The pulse-front is tilted by γ (Adapted from [104]).

The tilt angle Θ can be introduced either by a prism or grating. For ultrashort pulses, reflective optics are prefered to minimize nonlinear effects. The diffraction in the first order of a monochromatic beam of wavelength λ at a grating with line spacing d is determined by the grating equation

$$\sin\alpha + \sin\beta = \frac{\lambda}{d}, \tag{2.47}$$

where α and β denote the incoming and diffracted angle, respectively (Fig. 2.10). Obviously, a path difference of $(a+b)$ between the lower $(1 \rightarrow 1')$ and upper $(2 \rightarrow 2')$ path leads to a pulse-front tilt angle γ, which is calculated by

$$\tan\gamma = \frac{a+b}{D_2} = \frac{W(\sin\alpha + \sin\beta)}{W\cos\beta} = \frac{\lambda}{d\cos\beta}. \tag{2.48}$$

Due to the broadband pulse, the diffraction off the grating leads to an angular dispersion and an imaging setup (e.g. one lens) is necessary for a temporal and spatial overlap of the spectral components in the $LiNbO_3$ crystal. For a given demagnification M of the imaging setup, the tilt angle γ' of the pulse front within the nonlinear crystal is modified to

$$\tan\gamma' = \frac{\lambda}{M n_g \cdot d\cos\beta} \stackrel{!}{=} \tan\Theta, \tag{2.49}$$

where n_g is the group index of the pump pulse. The grating is imaged into the $LiNbO_3$ crystal with a tilt angle ϑ (Fig. 2.11a). This angle should match with the angle γ' of the pulse front to ensure a minimum pulse duration along the image [106]

$$\tan\vartheta = n_0 M \tan\beta \stackrel{!}{=} \tan\gamma', \tag{2.50}$$

where n_0 is the refractive index of the pump pulse at the center wavelength. Optimum THz generation is achieved when both conditions (Eqs. (2.49) and (2.50)) are fulfilled (Fig. 2.11b). This is possible by choosing the correct values of α, β, d and M.

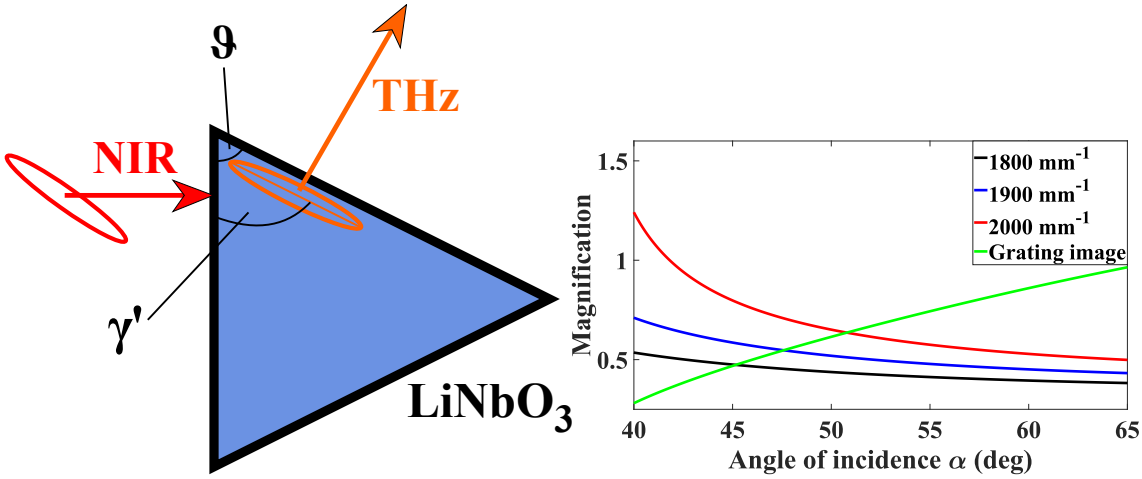

(a) Tilted-pulse-front (b) Grating conditions

Figure 2.11: (a) Tilted-pulse-front. Phase-matching requires that the pump pulse tilt angle γ' coincides with the cyrstal angle ϑ. (b) Conditions for THz generation (Eqs. (2.47), (2.49) and (2.50)). The physical propoerties were calculated for a pump pulse center wavelength of 800 nm (Tab. 2.4). Best conditions are achieved when both curves are matched.

2.4.2 Terahertz detection

The detection of THz radiation can be generally distinguished into incoherent and coherent detection.
In the first instance, the detection is based on heat deposition, which is a time-averaged detection. Since THz radiation lies in the meV energy region (Tab. 2.2), thermal noise has to be carefully suppressed for an efficient THz detection. A commonly used detector is a pyroelectric detector, which is based on the pyroelectric effect. This detector consists of a pyroelectric material with an attached electrode. An incoming THz electric field is absorbed and the increase in temperature will change the spontaneous polarization inside the pyroelectric material. This also modifies the surface charges and therefore an induced current flow can be measured [86]. Another typical detector is a bolometer where an electrical resistance strongly depends on the temperature. The sensitivity of this device is often increased by external cooling (heat sink). A third example for incoherent THz detection is a Golay cell, where absorbed energy due to THz radiation is used to increase the pressure

of a target gas within a small pneumatic chamber resulting in the deformation of a flexible mirror. The optical beam path of light, which is reflected at the flexible mirror outside the pneumatic chamber, will change and the measured deviation can be correlated with the absorbed energy.
In the second instance, the electric field $E_{\mathrm{THz}}(t)$ is directly mapped to another physical quantity enabling the simultaneous measurement of its phase and amplitude. The most prominent technique for coherent THz characterization is electro-optic (EO) sampling. The basic concept of EO sampling relies on the pump-probe technique: broadband THz radiation induces a transient birefringence inside an EO sensor crystal, which is immediately probed by an optical light pulse. The change in the refractive index leads to a modification of the polarization of the probe pulse. By varying the time delay between pump- and probe pulse, the amplitude and phase of the THz electric field can be retrieved. A typical setup to measure THz pulses is a balanced detection scheme (Fig. 2.12). Both polarization components are spatially separated with a polarizing beamsplitter and detected with two independent photodiodes. The quarter waveplate is adjusted such that in the unpumped case (i.e. no THz) the difference signal between both photodiodes vanishes. The full THz electric field $E_{\mathrm{THz}}(t)$ is directly proportional to the difference signal $\Delta I(t)$ of both photodiodes. Suitable EO sensor crystals are ZnTe or GaP (Tabs. 2.4, 2.3). For the detection of THz pulses produced by $LiNbO_3$ with a tilted-pulse-front ZnTe is preferred since it has a higher nonlinear coefficient.

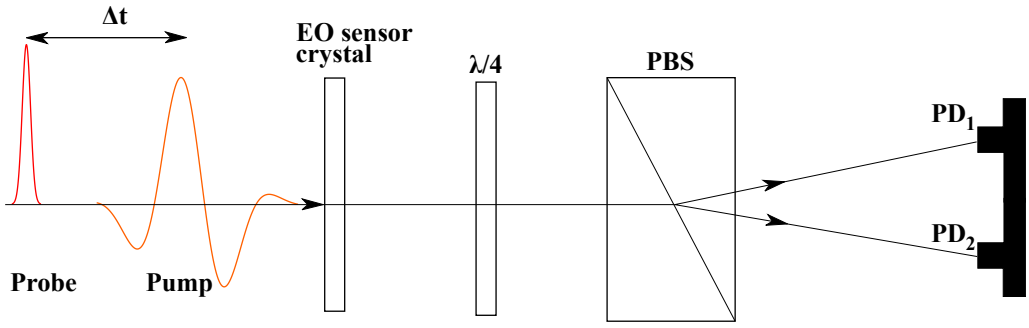

Figure 2.12: General layout of a balanced detection scheme for EO sampling. An EO sensor crystal is pumped by a THz pulse and probed by a subsequent optical pulse. The abbreviations mean time delay (Δt) , quarter waveplate ($\lambda/4$), polarizing beamsplitter (PBS), photodiode 1/2 ($\mathrm{PD}_{1/2}$).

The following theoretical description is based on [107]. The change of the refractive index induced by THz radiation can be described by the Pockels effect. Since the THz frequencies are much smaller than the optical frequencies ($\omega_{\mathrm{THz}} \ll \omega_{\mathrm{opt}}$), the electric field $E_k(\omega_2)$ in Eq. (2.38) is replaced by $E_k(0)$ and the second order nonlinear polarization reads

$$P_{\mathrm{i}}^{(2)}(\omega) = \epsilon_0 \chi_{ijk}^{(2)}(\omega, 0) E_j(\omega) E_k(0), \tag{2.51}$$

where $E_j(\omega)$ is the electric field of the optical probe pulse. Eq. (2.51) indicates that there is a close relation with OR and $E_k(\omega)$ induces a transient birefringence. ZnTe is a cubic crystal and belongs to the $\bar{4}3$m point group. The only non-vanishing electro-optic tensor element is r_{41} and the index ellipsoid is given by

$$1 = \frac{x^2 + y^2 + z^2}{n^2} + 2r_{41}E_{\mathrm{THz},1}yz + 2r_{41}E_{\mathrm{THz},2}xz + 2r_{41}E_{\mathrm{THz},3}xy, \tag{2.52}$$

where x, y, z are the coordinate axis of the crystal and n the refractive index of the center wavelength of the optical probe pulse. The components $E_{\mathrm{THz},j}\,(j = 1, 2, 3)$ of the THz electric field are defined along the x, y, z crystal axis. The mixing terms xy, xz and yz vanish after applying consecutively two coordinate transformations. Details are provided in [107]. The obtained refractive indices in the new coordinate (x'', y'') system are

$$\begin{aligned} n_{y''}(\alpha) &= n + \frac{n^3}{2} r_{41} E_{\mathrm{THz}} \left[\cos\alpha \sin^2\vartheta + \cos(\alpha + 2\vartheta)\right] \\ n_{z''}(\alpha) &= n + \frac{n^3}{2} r_{41} E_{\mathrm{THz}} \left[\cos\alpha \sin^2\vartheta - \cos(\alpha + 2\vartheta)\right]. \end{aligned} \tag{2.53}$$

The angle α is defined as the relative angle between the THz electric field and the (001) ZnTe crystal axis while φ is defined as the relative angle between the NIR electric field and the (001) ZnTe crystal axis. The resulting induced intensity ΔI is the difference between both probe polarizations and given by

$$\begin{aligned} \Delta I(\alpha, \varphi) &= I_p \sin\left[2(\phi - \vartheta)\right] \sin\left[\frac{\omega}{c} L \left(n_{y''}(\alpha) - n_{z''}(\alpha)\right)\right] \\ &= \frac{\omega n^3 E_{\mathrm{THz}} L}{2c} \left(\cos\alpha \sin(2\varphi) + 2\sin\alpha \ \cos(2\varphi)\right). \end{aligned} \tag{2.54}$$

Obviously, the THz electric field E_{THz} is directly mapped to the induced intensity ΔI for a given pair of angles α and φ. Note that ΔI modulates with both angles α and φ (Fig. 2.13). Certain combinations of α and φ even lead to a vanishing ΔI.

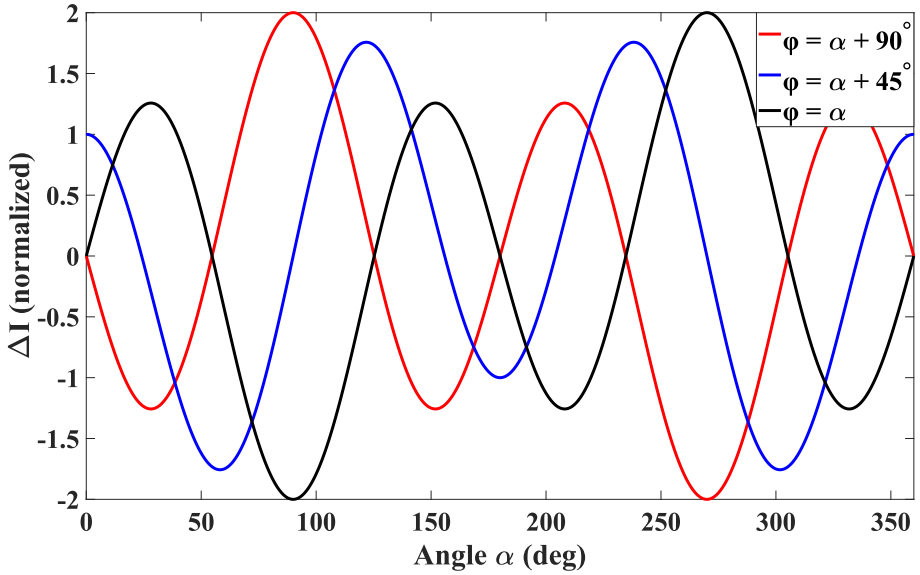

Figure 2.13: Induced intensity signal ΔI as a function of the angles α and φ (Eq. (2.53)).

2.5 Light-field-driven streak camera

The temporal structure of short XUV pulses can be characterized with a classical streak camera (Fig. 2.14). An incoming XUV pulse initiates photoelectrons, which are ejected and accelerated from a photocathode towards a fluorescent detector. The temporal profile of the XUV pulse is imprinted on the temporal structure of the released photoelectron wave package. On their path towards the detector the photoelectrons will pass a region with a fast varying voltage and will be transversely deflected due to the electric Coulomb force. If the voltage ramp up is significantly fast, the photoelectrons will be streaked, i.e. the leading edge of the electron bunch will receive a different moment transfer than the trailing edge. Consequently, the temporal information is mapped onto spatial coordinate of the fluorescent detector [10, 11]. The main limitations for the temporal resolution with this classical streak camera are:

- space-charge effects of the ejected photoelectrons from the photocathode
- energy spread of the initial photoelectrons
- rise-time δt of the applied fast-varying electric voltage
- synchronization between photoelectron wave packet and fast-varying electric voltage

The best temporal resolution down to 280 fs was achieved by reducing the electron beam size with an aperture beam stop and an additional electrostatic quadrupole lens to reduce the electron spread [108]. Further improvements led to a temporal resolution of 233 fs [109].

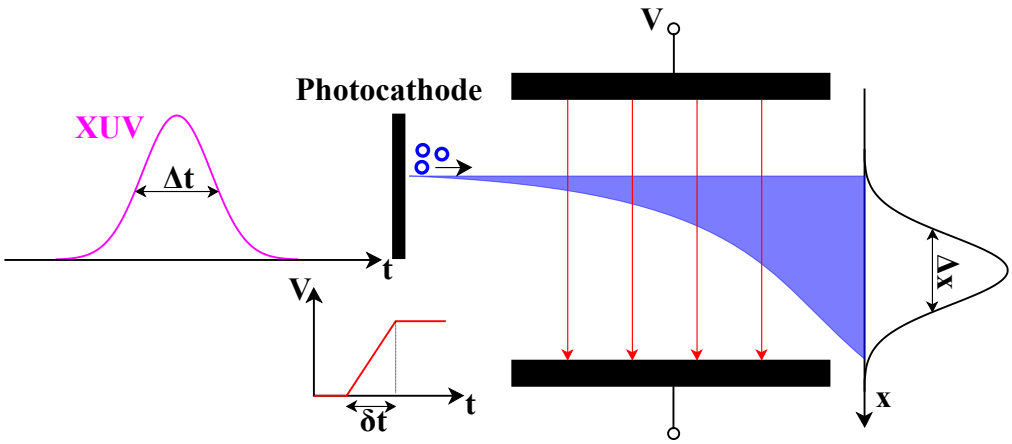

Figure 2.14: Classical streak camera. Short XUV pulses generate photoelectrons from a photocathode, which are accelerated and deflected in a fast-varying electric field before they hit a fluorescent screen. The temporal information Δt of the XUV pulse is mapped on the spatial coordinate Δx.

The natural timescale for dynamics of electrons in atoms is on the order of hundreds of attoseconds. To observe such processes even shorter XUV pulses and thus better time resolution for the temporal characterization is necessary. By replacing the photocathode with a gas target and the fast varying voltage with a fast oscillating electric light pulse the resolution of a conventional streak camera can be tremendously improved by several orders of magnitude (Fig. 2.15). With this technique many of the previously mentioned limitations can be overcome. In a typical experiment with a so-called light-field-driven streak camera the short XUV pulse is superimposed with an NIR light pulse in a noble gas. The ejected photoelectron wave packet contains the same temporal information as the initial ionizing XUV pulse. In the presence of the NIR light field, a momentum will be transferred to the photoelectrons and measured with an electron detector. The momentum transfer depends on the relative phase between both pulses. From the kinetic energy distribution the temporal profile of the XUV pulse can be retrieved. In one of the first experiments using NIR, isolated XUV pulses with a pulse duration of 1.8 fs were measured [12] getting closer to the attosecond frontier. Shortly afterwards, this barrier was broken and 650 as isolated XUV pulses were measured [13]. Nowadays, the streaking method is used to measure soft-X-ray pulses down to 43 as [6].

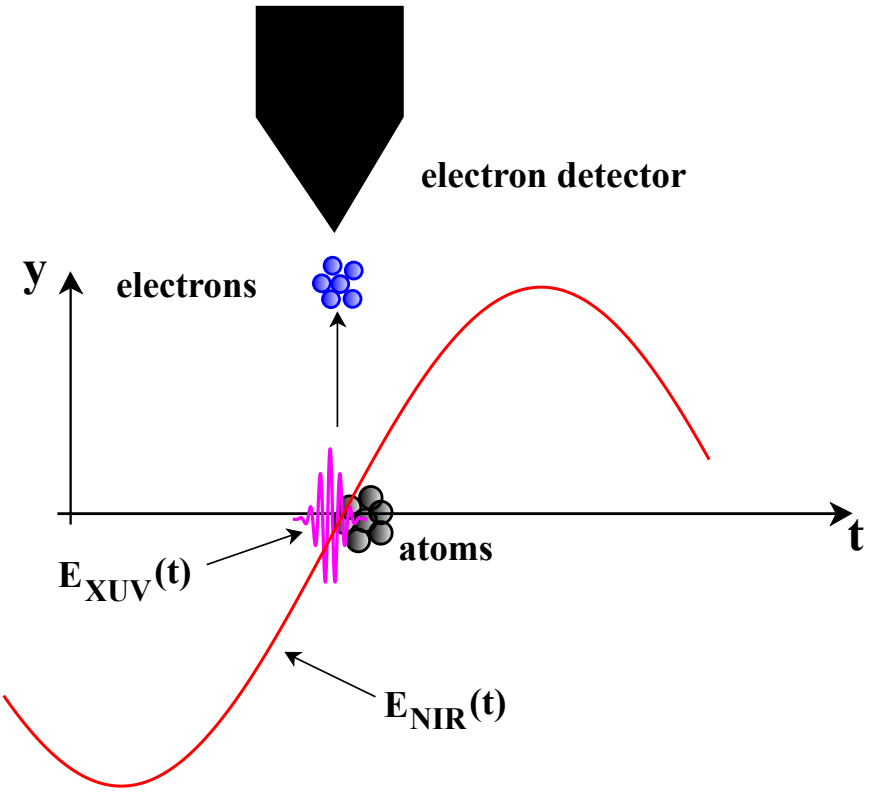

Figure 2.15: Light-field-driven streak camera. An incoming XUV pulse releases photoelectrons from a gas medium, which are accelerated by an NIR light field, whereby the momentum change depends on the ionization time. An electron detector measures the electron momentum distribution and hence the temporal information about the initial XUV pulse can be retrieved.

A brief semiclassical description of the light-field-driven streak camera will be given in the following and is mainly based on [110, 111]. If the frequency of the XUV pulse

ω_{XUV} is much larger than the frequency of the laser pulse ω_{L}, the streaking process can be divided in two parts: (1) absorption of an XUV photon and emission of a photoelectron, (2) deflection of the photoelectron. In the first step the generated photoelectron obtains a kinetic energy of

$$W_{\mathrm{kin}} = \frac{m}{2} v_0^2 = \hbar\omega_{\mathrm{XUV}} - E_{\mathrm{B}}, \tag{2.55}$$

where the variables m, v_0 and E_{B} denote the electron mass, its initial speed and the binding energy of the target gas, respectively. The influence of the NIR electric field is neglected during the ionization. In the second step, the equation of motion of the photoelectron in the presence of the NIR electric field can be described classically provided that the ponderomotive potential $U_{\mathrm{P}} = e^2 E_0^2/(4m\omega_L^2)$ is much larger than the photon energy of the NIR laser field ($U_{\mathrm{P}} \gg \hbar\omega_{\mathrm{L}}$) and the energy of the ionizing XUV photon is much larger than the ionization potential ($\hbar\omega_{\mathrm{XUV}} \gg I_{\mathrm{P}}$). Assuming a linear polarized laser along the y-direction, the electric field can be described by

$$\vec{E}_{\mathrm{L}} = \vec{E}_0(t)\cos\left(\omega_{\mathrm{L}} t + \varphi\right) \tag{2.56}$$

with a phase offset φ and the slowly-varying envelope $\vec{E}_0(t)$. The momentum transfer from the laser field to a photoelectron emitted at time t_i is given by

$$\Delta\vec{p}(t_i) = e\int_{t_i}^{\infty} \vec{E}_{\mathrm{L}}(t')dt' = e\vec{A}_{\mathrm{L}}(t_i). \tag{2.57}$$

The quantity $\vec{A}_{\mathrm{L}}$ defines the vector potential of the laser field. Thus, the photoelectron emission time t_i is mapped onto $\Delta\vec{p}(t_i)$. The final momentum of the photoelectron $\vec{p}_{\mathrm{f}} = \vec{p}_0 + \Delta\vec{p}$ (Fig. 2.16a) is equivalent to a kinetic energy of

$$\begin{aligned} W_{\mathrm{f}} &= W_0 + 2U_{\mathrm{P}}\cos 2\vartheta \sin^2\varphi_i \pm \alpha_L\sqrt{8W_0U_{\mathrm{P}}}\cos\vartheta\sin\varphi_i, \\ \alpha_L &= \sqrt{1 - \frac{2U_{\mathrm{P}}}{W_0}\sin^2\vartheta\sin^2\varphi_i}. \end{aligned} \tag{2.58}$$

The angle φ_i determines the phase of the electric laser field at time t_i while ϑ denotes the angle between the laser polarization direction and the final photoelectron momentum $\vec{p}_{\mathrm{f}}$. Typically, the electron detector is aligned such that the kinetic energy in parallel direction $W_{\parallel}$ ($\vartheta = 0$) or in perpendicular direction $W_{\perp}$ ($\vartheta = 90°$) is measured. Consequently, the final kinetic energy of Eq. (2.58) is reduced to

$$W_{\parallel} = W_0 + 2U_{\mathrm{P}}\sin^2\varphi_i \pm \sqrt{8W_0U_{\mathrm{P}}}\sin\varphi_i, \tag{2.59}$$

$$W_{\perp} = W_0 - 2U_{\mathrm{p}}\sin^2\varphi_i. \tag{2.60}$$

In many cases the ponderomotive potential U_{P} can be neglected with respect to the initial kinetic energy W_0. According to Eq. (2.60), the kinetic energy in parallel direction essentially depends on the phase φ_i while in the perpendicular direction the unperturbed kinetic energy is measured. Thus, the shift in the kinetic energy spectrum due to the electriqc laser field is

$$W_{\mathrm{streak}}(t) = \sqrt{8W_0U_{\mathrm{P}}}\sin\varphi_i = e\sqrt{\frac{2W_0}{m}}\frac{E_0}{\omega_L}\sin\varphi_i = e\sqrt{\frac{2W_0}{m}}A_L(t_i). \tag{2.61}$$

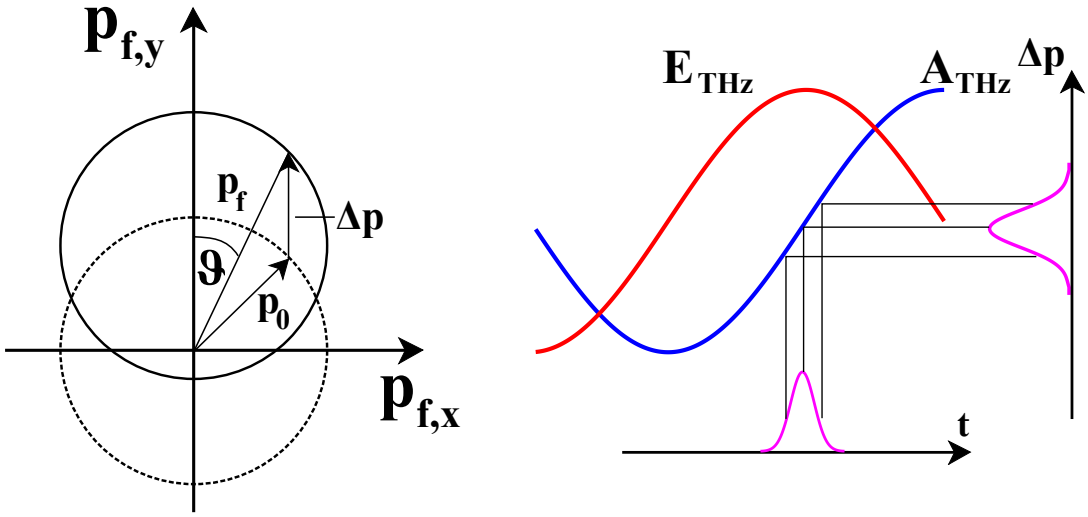

(a) Momentum transfer (b) Time-space correspondance

Figure 2.16: Principles of a light-field-driven streak camera. (a) After ionization, a strong laser field introduces a momentum transfer $\Delta\vec{p} = e\vec{A}(t_i)$ resulting in a final momentum $\vec{p}_f$. Without the laser field, a uniform momentum distribution is assumed (inspired by [110]). (b) Direct mapping of the temporal profile of the XUV pulse to a kinetic energy distribution (inspired by [112]).

By changing the time delay between the ionization time and the laser field the vector potential $A_L(t)$ of the laser can be fully reconstructed. For a time delay $\tilde{t}_i$ such that $A(\tilde{t}_i) = 0$ the kinetic energy distribution of the photoelectron wavepacket, that represents the temporal structure of the XUV pulse, is broadened and the XUV pulse duration can be extracted (Fig. 2.16b).
The fully quantum mechanical description of the streaking principle is explained in the following and is mainly based on [113], where atomic units are used.
Using the single active electron approximation, the transition of an electron from the ground state to the continuum by an electric XUV field $\vec{E}_{\mathrm{XUV}}$ can be described by the transition amplitude

$$a_v = -i \int_{-\infty}^{\infty} \vec{E}_{\mathrm{XUV}}(t)\vec{d}_{\vec{v}} \exp\left(i(W + I_p)t\right) dt, \tag{2.62}$$

where W is the kinetic energy of the photoelectron in the continuum (see Eq. (2.55)), I_p the ionization potential and $\vec{d}_{\vec{v}}$ the dipole transition matrix element. Eq. (2.62) shows that there is a direct relation between the electric XUV field $\vec{E}_{\mathrm{XUV}}$ and the photoelectron spectrum a_v. In many cases the phase and amplitude dependence of the matrix dipole element $\vec{d}_{\vec{v}}$ on the velocity $\vec{v}$ can be neglected. Far away from resonances, the temporal structure of the XUV pulse is consequently imprinted on the photoelectron wavepacket. Providing that the XUV photon energy is much larger than the ionization potential, the Coulomb potential of the ionic core can be neglected, which is essentially the SFA [69]. For a certain time delay τ between the XUV and NIR field the transition amplitude is given by

$$a_v(\tau) = -i \int_{-\infty}^{\infty} \vec{E}_{\mathrm{XUV}}(t-\tau)\vec{d}_{\vec{v}} \exp\left[i\left(I_p t - \int_t^{\infty} \frac{\vec{p}^2(t')}{2} dt'\right)\right] dt, \tag{2.63}$$

where $\vec{p}(t) = \vec{v}_0 + \int_{\infty}^{t} \vec{E}_{\mathrm{L}}(t')dt'$ is the instantaneous momentum of the photoelectron and $\vec{E}_L(t)$ the electric field of the NIR laser field. Note that the electric NIR field vanishes for $t \to \infty$ and hence the final momentum $\vec{p}_f(t) = \vec{v}_0 + \vec{A}(t)$ is the same as in the semiclassical description. Eq. (2.63) can be written as amplitude $a(\tau)$ and a phase $\phi(t)$

$$a(\tau) = -i \int_{\infty}^{\infty} \exp[i\phi(t)]\vec{d}_{\vec{v}}\vec{E}_{\mathrm{XUV}}(t-\tau)\exp[i(W+I_p)t]dt, \tag{2.64}$$

$$\phi(t) = -\int_t^{\infty} \left(\vec{v}\vec{A}(t') + \frac{\vec{A}(t')^2}{2}\right) dt'. \tag{2.65}$$

It follows that the XUV pulse mainly modifies the amplitude $a(\tau)$ while the NIR electric field essentially induces a phase modulation $\phi(t)$. In case of a periodic NIR electric field, which is described by Eq. (2.56) and $\varphi = 0$, the phase modulation reads

$$\begin{aligned}
\phi(t) &= \phi_1(t) + \phi_2(t) + \phi_3(t), \\
\phi_1(t) &= -\int_t^{\infty} U_p(t), \\
\phi_2(t) &= \frac{\sqrt{8WU_p(t)}}{\omega_{\mathrm{L}}} \cos\vartheta \cos(\omega_{\mathrm{L}} t), \\
\phi_3(t) &= -\frac{U_p(t)}{2\omega_{\mathrm{L}}} \sin(2\omega_{\mathrm{L}} t),
\end{aligned} \tag{2.66}$$

with $U_p(t) = E_0^2(t)/4\omega_{\mathrm{L}}^2$ being the ponderomotive potential. The first term $\phi_1(t)$ is slowly varying due to the fact that the envelope $\vec{E}_0(t)$ is also modulating slowly. The other two contributions $\phi_1(t)$ and $\phi_2(t)$ rapidly change since they oscillate with ω_{L} and $2\omega_{\mathrm{L}}$, respectively. The second term $\phi_2(t)$ also depends on the relative angle ϑ between laser polarization and the momentum $\vec{p}$ thus it contributes most for small ϑ. The phase is directly linked to the energy modulation ΔW of the photoelectron: $\Delta W = -\partial\phi/\partial t$. In the limit of a XUV pulse duration much shorter than the duration of the NIR pulse, the phase modulation $\phi(t)$ in Eqs. (2.65) and (2.66) can be linearly expanded leading to an energetic shift $\Delta W = W - W_0 = -\partial\phi/\partial t$. This is the same as the expression from the semiclassical description (see Eq. (2.58)). If the XUV pulse duration is comparable or longer than the pulse duration of the NIR field, interferences between different parts of the photoelectron wavepacket with the same final energy occur and lead to sidebands. A first experimental demonstration of sidebands [16] was used to characterize XUV pulses on the order of 100 fs.
The reconstruction of an XUV pulse is extensively described in [112]. In summary, the electric field of a chirped linearly polarized XUV pulse can be described as

$$E_{\mathrm{XUV}}(t) = E_{\mathrm{XUV},0} \exp\left[-a(t-t_0)^2\right] \cdot \exp\left[i\omega(t-t_0) + c(t-t_0)^2\right], \tag{2.67}$$

where $E_{\mathrm{XUV},0}$ is the amplitude of the electric field, t_0 the temporal offset and chosen such that the streaking vector potential has a zero crossing at the ionization time. The parameter a is a constant and c the linear chirp. Using Eq. (2.63) the streaked photoelectron spectrum is given by

$$S(\omega) = \left| \int_{-\infty}^{\infty} E_{\mathrm{XUV}}(t) \exp[i\phi(t)] \exp(-i\omega t) \right|. \tag{2.68}$$

For the case of $U_p \ll W_{\mathrm{kin}}$ the term $\phi_2(t)$ in Eq. (2.66) dominates and the spectral width σ_s (FWHM) of the streaked spectrum is obtained by

$$\sigma_s = \sqrt{\sigma_{us}^2 + \tau_{\mathrm{XUV}}^2 \left(s^2 \pm 4cs\right)}, \tag{2.69}$$

where $s = \partial \Delta W / \partial t$ is the streaking speed, σ_{us} the spectral width (FWHM) in the absence of the streaking field and τ_{XUV} the XUV pulse duration (FWHM). The streaking speed can be directly calculated using Eq. (2.57)

$$s = \frac{\partial}{\partial t} \left[\frac{(p_0 + \Delta p)^2}{2m} - \frac{p_0^2}{2m} \right] = -\frac{p_0 + eA_L}{m} eE_L. \tag{2.70}$$

Note that the time-dependence is implied in the vector potential $A_L(t)$ and the electric field $E_L(t)$. In many cases the initial momentum p_0 is much larger than the transferred momentum Δp and the streaking speed is reduced to

$$\tilde{s} = -\frac{p_0}{m} eE_L. \tag{2.71}$$

In the attosecond regime, a more accurate pulse characterization method is FROG-CRAP [114].

Chapter 3

Implementation of a femtosecond streak camera

In this work, a new experimental setup was designed and implemented in order to perform THz femtosecond streaking experiments using an electron imaging spectrometer. During the operation either intense NIR or weak XUV radiation is used to generate free electrons in a target gas. The design is closely related to [18] and is located on a single experimental table, accept the NIR laser system (Fig. 3.1). The experimental apparatus consists of the following parts: HHG source, HHG spectrometer, THz generation and streaking experiment. Details will be provided in the subsequent sections.

3.1 Beamline requirements

The experimental beamline has to fulfill the following requirements.

Beam transport:
The intense NIR femtosecond laser system is located in an adjacent laboratory. The laser beam propagates approximately 10 m in air before it enters the experimental setup. Therefore, the beam size has to be sufficiently large to avoid nonlinear effects and stable opto-mechanics should be used to minimize pointing jitter. In addition, the design of the femtosecond streak camera should be compact and fit on the experimental laser table.

HHG source:
A compact and efficient HHG source is necessary that operates in the pressure range of a few 100 **mbar**. An appropriate differential pumping scheme is mandatory to avoid reabsorption of HHG radiation in the vacuum chamber. In addition, the HHG source should be designed in a collinear geometry to ensure an easy transition when substituting XUV by NIR light.

HHG spectrometer:
The HHG spectrometer fulfills the following two tasks: (i) HHG separation and (ii) HHG diagnostics and steering. On the one hand, the HHG radiation has to be spatially separated from residual NIR radiation. This will be realized by a hole mirror. On the other hand, the harmonic spectrum has to be imaged with a camera after using a microchannel-plate (MCP) assembly togehter with a fluorescent screen. The spatial separation of the different harmonic colors will be realized with a grating. In addition, the desired harmonic has to be selected and guided to the experimental

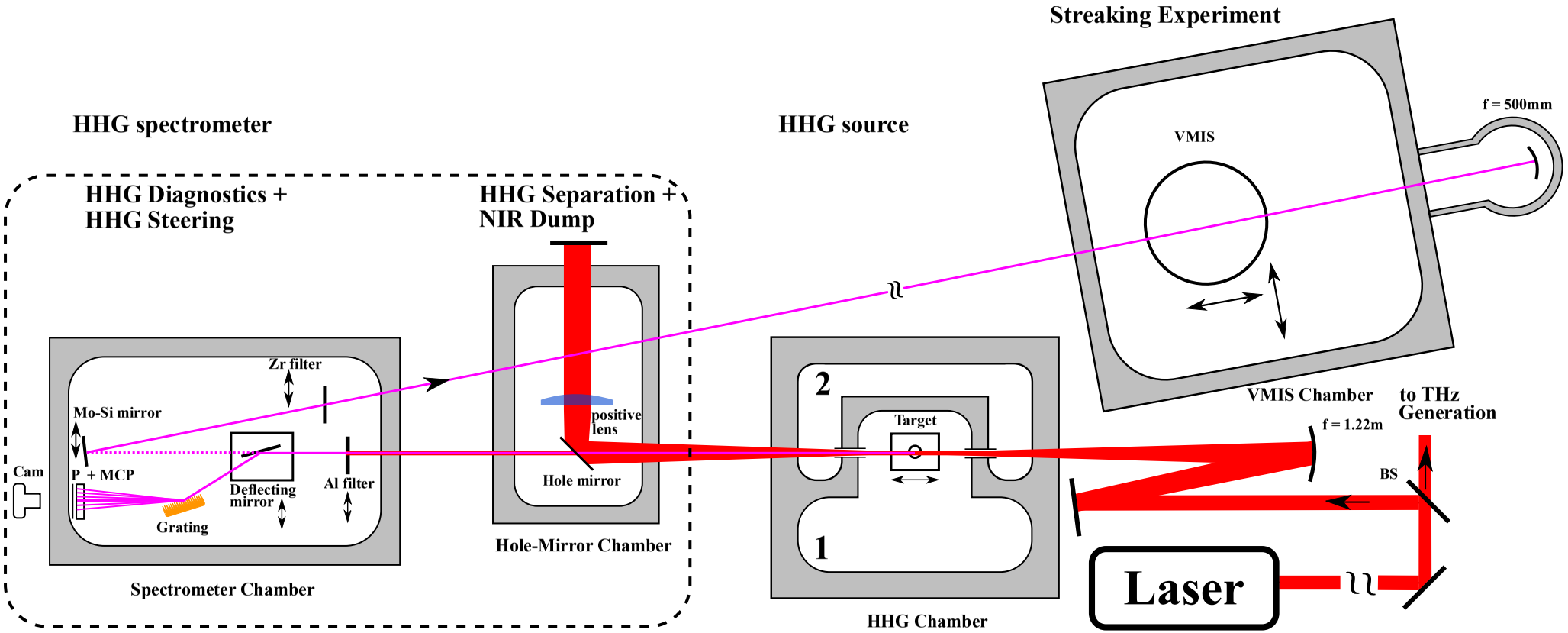

Figure 3.1: Experimental beamline

	Base pressure (10^{-7} **mbar**)	**Operating pressure** (10^{-7} **mbar**)
HHG source (1)	4.0	$\leq 4 \times 10^5$
HHG source (2)	1.5	≤ 90
HHG spectrometer	2.5	≤ 5.0
Streaking experiment	< 1.0	$50 - 80$

Table 3.1: Summary of the measured base and operating pressures at all beamline stages.

streaking chamber with appropriate multilayer mirrors.

THz source:
For the streaking experiment, intense near single-cycle THz pulses have to be generated, collimated and transported into the vacuum streaking chamber to overlap in time and space with the XUV pulses. Additionally, the Gouy-phase should not change too much over the interaction volume, i.e. the Rayleigh length should be larger than the interaction length.

Streaking experiment:
The streaking experiment has to be equipped with an electron spectrometer that measures the actual electron momentum distribution. The electron spectrometer should be designed such that a simultaneous incoupling of the NIR/XUV and THz radiation is possible.

3.2 Overview of the experimental beamline

The experimental setup is separated from the laser system in another room (Fig. 3.1). All involved vacuum chambers where made of an EN-AW-5083 aluminium alloy and CNC-machined from a single solid block in our on-site campus workshop. With the exception of the streaking chamber, that has an aluminium alloy top, all vacuum chambers have a double-stacked glass lid, which improves the visibility of the NIR beam path. The base and operating pressures of all vacuum chambers are in the high-vacuum regime (Tab. 3.1).
The laser beam is guided with 2″ plane dielectric mirrors to the experimental beamline and separated with a 50:50 beamsplitter into two parts. To avoid dispersion, the reflected part of the beam is focused with a spherical dielectric mirror (focal length $f_{\mathrm{HHG}} = 1215\mathrm{mm}$) through a 1 mm thick SiO_2 window for HHG. A small angle of incidence on the spherical mirror of approximately 5° is chosen to reduce astigmatism. The transmitted part of the beam is directed with 2″ plane dielectric mirrors to a table-top setup where the broadband NIR pulse is converted via difference-frequency mixing to THz radiation. The output THz beam is collimated and guided into the streaking chamber and superimposed together with the XUV/NIR beam in the interaction volume. A more detailed description of all experimental stages will

be given in the subsequent sections.

3.3 High-order harmonic generation source

In the HHG chamber, noble gases, such as Ar or Ne, are delivered from the bottom into a thin-walled metallic tube that is positioned on a linear manipulation stage to achieve phase-matching for the highly nonlinear process. The atoms can interact with the focused NIR for HHG. The residual gas will leave the metallic tube through small holes, made by the intense laser in the metallic surface. In steady-state, pressures up to 300 mbar in the metallic tube can be reached. Due to the high gas load and to avoid reabsorption of produced harmonics, a differential pumping scheme is implemented. The majority of the gas particles is removed by a high throughput turbomolecular pump (Edwards, STPH301C) in chamber 1. Two thin aluminium tubes, that have Kapton foils on one of their end surfaces for differential pumping purposes, connect chambers 1 and 2. The chamber 2 is equipped with another turbomolecular pump (Pfeiffer Vacuum, HiPace 300). The design and the experimental setup was supported by Thomas Gebert and Markus Pfau.

3.4 High-order harmonic generation spectrometer

The HHG spectrometer consists of two separate chambers: the spectrometer chamber and the hole-mirror chamber. Both chambers are evacuated by a single turbomolecular pump (Leybold, Turbovac 361). After the HHG, the NIR and XUV beams are co-propagating. The majority of the NIR beam is deflected by a hole mirror (hole diameter: $d = 3\,\mathrm{mm}$), collimated by a positive plano-convex lens ($f = 1\,\mathrm{m}$) and directed through a vacuum window onto a beam dump. The position of the beam also serves as a near-field monitor. The residual NIR and the co-propagating XUV beam enter the spectrometer chamber and are reflected by a plane bilayer Mo-B_4C (48 nm, 2.5 nm) 1″ mirror before they are diffracted on a blazed Au-grating that has a line spacing of 1200 lines/mm and a blaze angle of 1°. The grating is designed to diffract energies at around 80 eV with the highest efficiency. Due to the different wavelengths, the individual odd harmonics as well as the NIR beam are spatially separated and directed onto a home-built MCP detector with a diameter of $d = 40\,\mathrm{mm}$ that is equipped with a P46-phosphor screen. The visible harmonics on the phosphor screen are imaged with a camera. To avoid damage on the MCP, the angle of the grating is chosen such that the 0th order does not hit the sensitive MCP surface. For calibration, a 0.2μm thick Al filter can be magnetically flipped into the beam path to block the NIR beam completely and to introduce a sharp cut-off in the energy spectrum of the harmonics at 72.6 eV. Therefore, photon energies above this value are not transmitted (Fig. 3.2a).
After the optimization of the harmonics, the deflecting mirror can be removed from the beam path such that a single harmonic can be separated with a special Mo/Si-multilayer mirror (AXO Dresden GmbH), optimized for an angle of incidence of 6.5° (with respect to the normal). The multilayer is designed such that only the 51st

harmonic is reflected (multilayer period $d_{\mathrm{ML}} = 8.103\,\mathrm{nm}$; number of periods $N = 60$; ratio of bottom layer thickness to period $\Gamma = 0.32$). The multilayer mirror essentially operates as a bandpass filter (Fig. 3.2b). To steer the 51st harmonic into the streaking chamber, both axes of this XUV optic can be mechanically manipulated from outside the vacuum. To remove residual NIR light, a $0.2\,\mu\mathrm{m}$ thick Zr filter can be magnetically flipped into the beam path, that blocks LE photons (Fig. 3.2a). The implementation of the HHG spectrometer was supported by Sophie Walther.

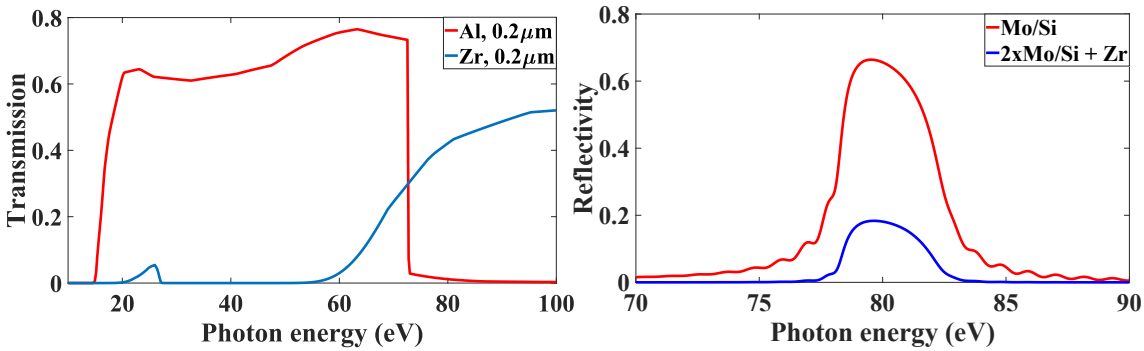

(a) Transmission (b) Reflectivity

Figure 3.2: Transmission and reflectivity of XUV optics. The raw data was taken from [115]. (a) Transmission of $0.2\,\mu\mathrm{m}$ thick metal filters, (b) Reflectivity of the used multilayer mirror(s).

3.5 Laser-based Terahertz source

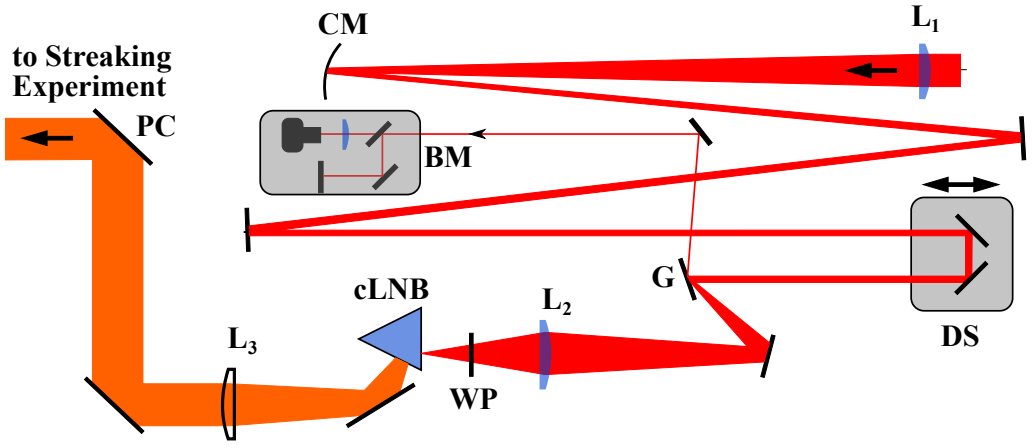

Figure 3.3: Sketch of the THz generation. L_1: focusing lens, CM: convex mirror, DS: delay stage, G: grating, L_2: achromatic lens, WP: half-waveplate, cLNB: congruent $LiNbO_3$, L_3: teflon lens, PC: 90° periscope, BM: beam monitor.

A laser-based, tilted-pulse front setup generates high THz fields using difference frequency mixing in a congruent $LiNbO_3$ (cLNB) and is placed next to the streaking chamber (Fig. 3.3). The beam size of the incoming NIR beam is reduced by a telescope, consisting of a plano-convex lens (L_1, $f_1 = 250\,\mathrm{mm}$) and a convex Au

mirror (CM, $f = -46.5\,\mathrm{mm}$). The latter element was chosen to keep the B-integral low, thus avoiding self-focusing. To vary the temporal overlap in the streaking experiment, a delay stage (DS) was placed into the NIR beam path before the beam hits the grating (G, 1800 lines/mm) that introduces a pulse front tilt in the first diffraction order. The 0th diffraction order of the grating serves as a beam monitor (BM) for the near- and far-field. The first diffraction order of the beam is subsequently imaged into a 6.0% MgO-doped cLNB by an achromatic focusing lens (L_2, $f_2 = 75\,\mathrm{mm}$). The magnification of the imaging setup and the diffracted angle off the grating were chosen such that both conditions Eqs. (2.49) and (2.50) for efficient THz generation are fulfilled. The cLNB crystal was chosen since it can be grown to a large size although it has a smaller nonlinear coefficient for THz generation in comparison to stoichiometric LNB [99]. The base of the cLNB consists of an isosceles triangle with an apex angle of $\alpha = 54°$ thus providing the opportunity to flip the crystal when damage by the NIR pump beam occurs. Note that due to the high refractive index of 4.96 (see. Tab. 2.4) in the THz range only 56% of the generated THz in the cLNB crystal is transmitted through the exit face (see Eq. (2.45)). Since Kapton has a refractive index of around 1.72 [116], a small layer of Kapton foil was taped on the exit face of the cLNB crystal to serve as a quasi anti-reflection coating. This increases the signal by approximately 10 %. Likewise, the incoming surface of the cLNB crystal has a manufactured anti-reflection coating to minimize Fresnel losses of the pump laser. A half-waveplate (WP) ensures that the polarization of the incoming beam coincides with the z-axis of the crystal. The divergent THz radiation, which is generated in the cLNB, is collimated using a plano-convex PTFE lens (L_3,$f_3 = 100\,\mathrm{mm}$) and transported with 2″ plane Cu mirrors to the streaking experiment. The THz field is s-polarized and needs to be rotated to match with the XUV field polarization. Since the THz beam has to be lifted to enter the streaking chamber, a 90° periscope is used to flip the THz field polarization. The PTFE lens was chosen because its transmission below 1.5 THz is around 90% and the majority of NIR light is blocked. The experimental setup was supported by Anastasios Dimitriou.

3.6 Streaking experiment

The streaking experiment is located in the streaking vacuum chamber and can be operated either with NIR or XUV radiation (Fig. 3.4). In the center of the chamber, a VMIS is mounted on an xyz manipulator. The spectrometer axis is tilted by $\alpha = 10°$ with respect to the breadboard normal to ensure that the linear polarizations of the XUV and THz fields are parallel to the VMIS imaging plane. A detailed description of the spectrometer will be given in chapter 5. The incoupling of the THz radiation into the vacuum chamber is realized with a 3 mm thick TOPAS window, which has a clear aperture of 45 mm. The window material was chosen because it features low THz transmission losses [116, 117] and it is also transparent in the visible range of the electromagnetic spectrum, thus providing the opportunity to use an alignment laser during the optical setup. The chamber is pumped by a single turbomolecular pump (Leybold, Turbovac 361). Due to its mechanical ball bearings, no external magnetic field is produced that might distort the electron trajectories in the VMIS. While working with XUV, a high noble gas load is injected into the HHG chamber. Due to this high gas load, the base pressure in the streaking chamber increased by

0.22×10^{-7} mbar.
In the vacuum, the THz beam, that is transmitted trough the TOPAS window, is reflected from a 2″ Cu-mirror (CM) and focused with a 2″ off-axis parabolic mirror (OAPM), which has a focal length of 101.6 mm. The chosen focal length is a compromise between a small focus size, i.e. a high THz electric field strength, and its Rayleigh length, which accounts for the Gouy-phase change within the interaction region. The generated XUV radiation propagates from below the VMIS and is reflected and focused with a Mo/Si multilayer mirror (FM) with a focal length of 500 mm through a 2 mm hole in the OAPM. When using NIR instead of XUV radiation, the metallic tube in the HHG chamber as well as the Zr filter in the spectrometer chamber are removed. Both the THz and the NIR or XUV radiation overlap in space and time in the interaction volume of the VMIS.

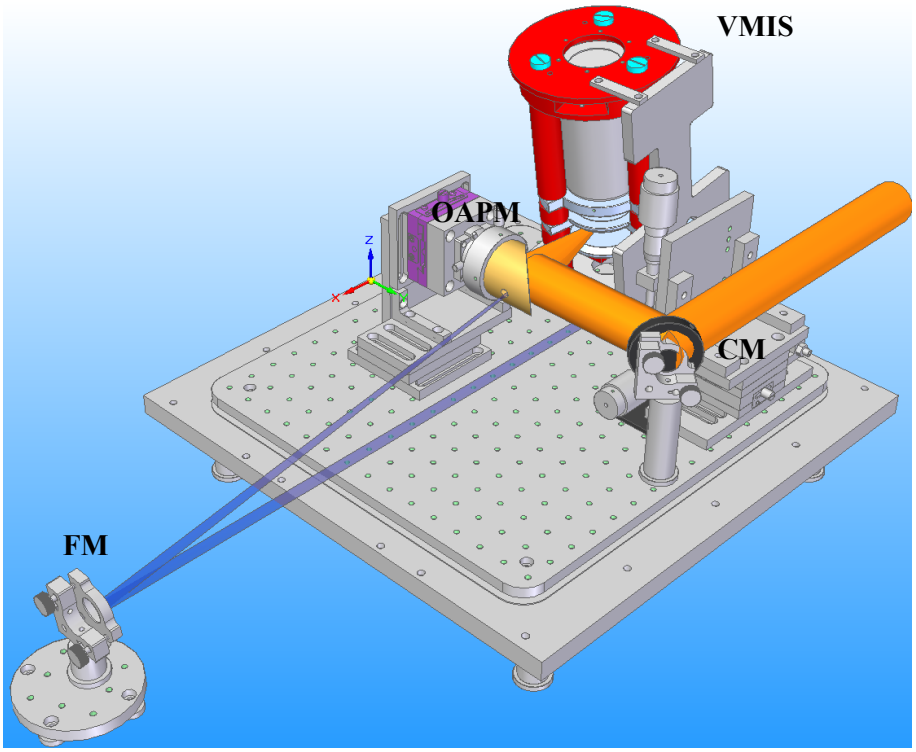

Figure 3.4: Sketch of the streaking experiment. For clarity, the chamber walls and vacuum flanges are not shown. The THz beam (orange) overlaps with the XUV beam (blue) in the interaction region of the VMIS. The THz radiation is guided with a Cu-mirror (CM) and focused with an off-axis-parabolic mirror (OAPM) with a focal length of $f = 101.6$ mm. The XUV beam is focused with a focusing mirror (FM) and a focal length of $f = 500$ mm into the interaction volume.

The XUV beam is reflected twice from a Mo/Si-multilayer mirror and separated from the co-propagating NIR field, which leads to significant reflectivity losses (Fig. 3.2b).

Chapter 4

Characterization of the coherent light sources

After the introduction of all relevant coherent light sources in the previous chapter, these sources will be now characterized. The temporal and spatial properties of these sources are important for the realization of a table-top THz streak camera. The challenge of these measurements is the use of different detectors because the involved light sources range from the THz to the XUV-regime.

4.1 Femtosecond laser system

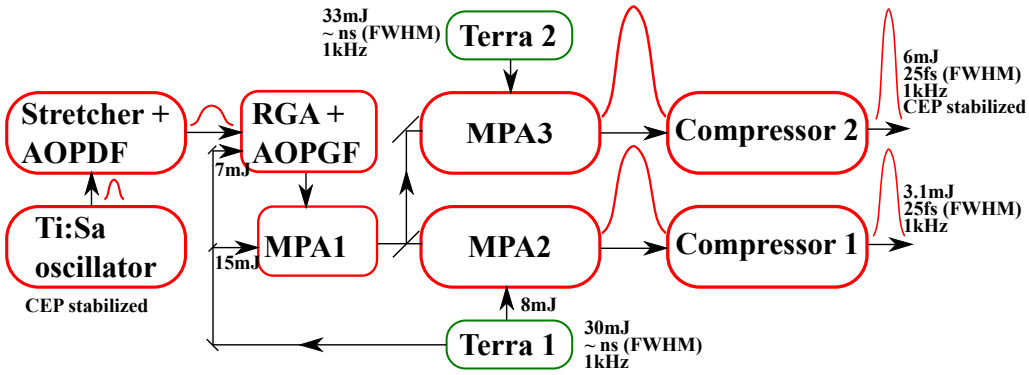

Figure 4.1: Principal layout of the AURORA laser system. The laser has two separate and independent branches with pulse energies of 3mJ and 6mJ, respectively. See text for more details.

Intense NIR pulses are generated by a femtosecond laser system (Amplitude Technologies, AURORA). The laser system is located in a different climatized laboratory to ensure a fully stabilized environment with a constant temperature of $T = (20.4 \pm 0.1)°C$ and an absolute humidity of $(7.0 \pm 0.1)\mathrm{g/m^3}$. The commercial AURORA laser system consists of several different parts, which will be shortly explained in the following (Fig. 4.1). Starting with a broadband Ti:Sa carrier-envelop-phase (CEP) stabilized oscillator (Venteon Laser Technologies, pulse duration FWHM $< 5\,\mathrm{fs}$, repetition rate $f_{\mathrm{rep}} = 80\,\mathrm{MHz}$), the pulses are amplified via the chirped pulse amplification scheme [4]. To prevent damage of the amplifier, induced by intense laser pulses, the pulse train is stretched with a pair of gratings and subsequently amplified before it gets compressed by another pair of gratings. The stretcher is equipped with an acousto-optic programmable dispersive filter (AOPDF), which allows for modification of the spectral phase and amplitude. Afterwards, the dispersed seed pulses enter the regenerative amplifier (RGA) and a

first multipass amplifier (MPA1) before the beam is divided with a beamsplitter in two independent parts. As a special feature, the RGA is additionally equipped with an acousto-optic programmable gain control filter (AOPGF) to adjust the intracavity spectral losses and consequently stop gain narrowing [118]. The two divided pulses are then separately amplified with two different multipass amplifiers (MPA2 and MPA3, respectively) and compressed with two independent grating compressors leading to strong pulses at 1 kHz repetition rate, a pulse duration of about 25 fs (FWHM), a central wavelength at $\lambda_c = 795\,\text{nm}$ and pulse energies of 3.1 mJ and 6.0 mJ, respectively. The high energy branch is additionally equipped with a feedback loop to stabilize the CEP fluctuations arising from the amplification process [119]. Only the low energy branch was used for the experiment.
In order to characterize the temporal shape of the laser pulses, a SPIDER measurement [120], which is a self-referencing technique similar to FROG [121], was carried out at the compressor exit (Fig. 4.2). The reconstruction algorithm provides the pulse shape as well group delay or group delay dispersion. The reconstructed pulse was fitted with a Gaussian function. A pulse duration of $\tau = 24\,\text{fs}$ (FWHM) was obtained from the Gaussian fit. The signal modulation in the wings of the reconstructed pulse indicates contributions of higher chirp orders.

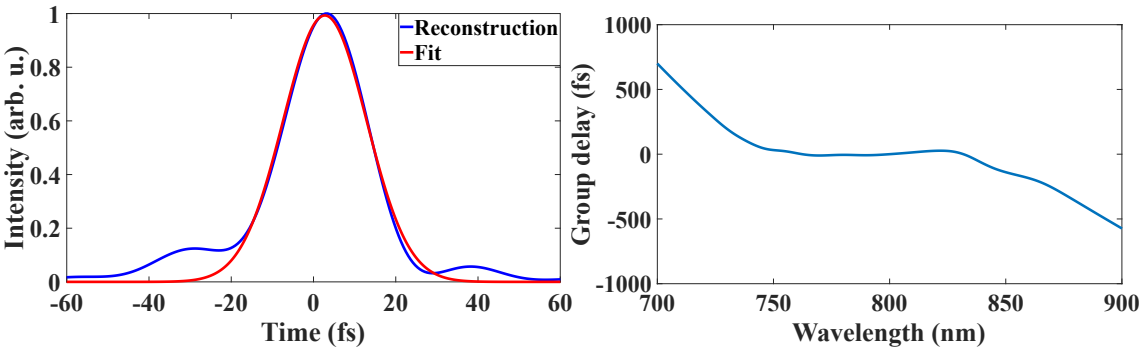

(a) Reconstructed pulse (b) Group delay

Figure 4.2: SPIDER measurements at compressor exit. (a) Pulse reconstruction, $\tau = 24\,\text{fs}$ (b) Obtained group delay in the laser emission range.

For the evaluation of the laser beam size, a knife-edge scan at the compressor exit was performed. The measurement provides the beam radii ($1/e^2$) in horizontal (X) and vertical (Y) direction (Fig. 4.3). A horizontal and vertical beam radius of $w_{0,x} = 8.4\,\text{mm}$ and $w_{0,y} = 8.6\,\text{mm}$ was obtained, respectively. Approximately 99% of the beam power flows through a circle of diameter $d = 3w_0$. Hence, the NIR beam can be transported with 2″ optics to the experimental setup.
Therefore, the compressed laser beam is guided with 2″ dielectric mirrors approximately 10 m to the experimental beamline. The beam size is sufficiently large to minimize nonlinear effects like self-phase-modulation or self-focusing on its propagation path to the experimental setup.

4.2 High-order harmonic radiation

Strong NIR pulses are focused into the HHG chamber whereby peak intensities on the order of $5 \times 10^{14}\,\text{W/cm}^2$ are reached and a superposition of odd harmonics is

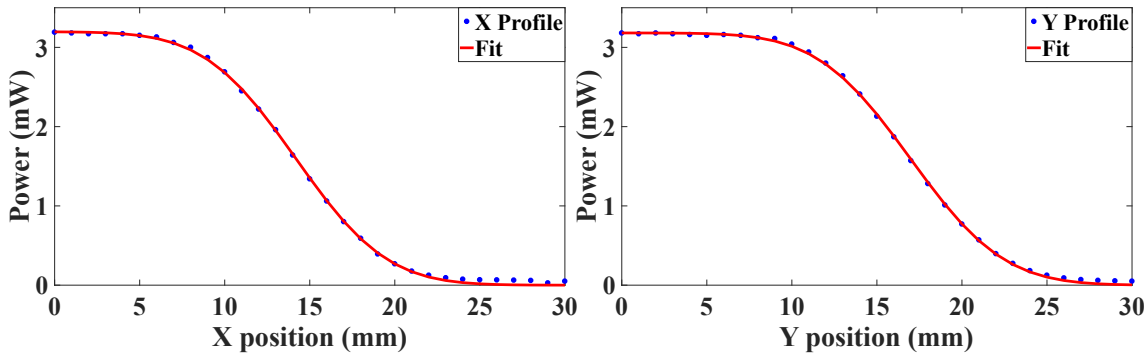

(a) X Profile: $w_{0,x} = 8.4\,\mathrm{mm}$ (b) Y Profile: $w_{0,y} = 8.6\,\mathrm{mm}$

Figure 4.3: Knife-Edge scans at compressor exit. Corresponding beam radii ($1/e^2$) are written below the graphs. (a) Horizontal scan (X Profile), (b) Vertical scan (Y Profile).

generated. A detailed description is given in section 2.3.1. The generated harmonics were spatially separated with an Au grating and observed using an MCP-detector. Usually, the HHG spectrum in the cut-off region was imaged (Fig. 4.4). The insertion of the Al filter in the beam path introduces a sharp absorption due to the atomic L-edge. This provides the opportunity to calibrate the energy spectrum. The first harmonic, that is above the L-edge, is identified as the order 47. The 51^{th} harmonic will be selected by the multilayer mirrors for the experiment. Harmonics up to the 57^{th} order were detected.

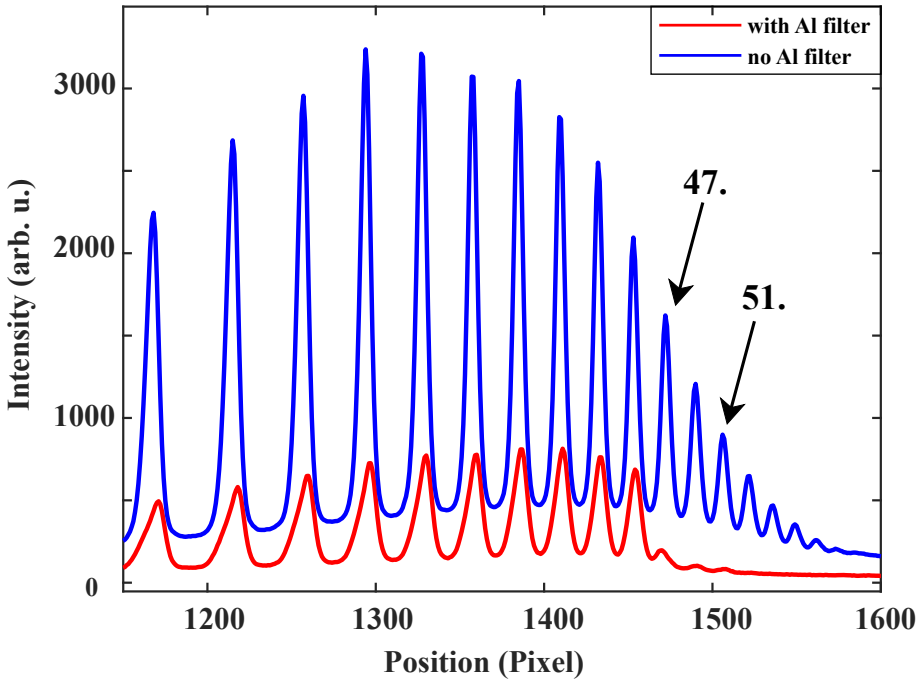

Figure 4.4: HHG spectrum obtained from the HHG source. The sharp L-edge of an Al-filter at 72.6 eV was used to calibrate the spectrum. The 47^{th} harmonic is the first that is blocked by the Al filter. In the experiment, the 51^{st} harmonic is used.

In order to achieve phase matching between the NIR and XUV electric field, the following experimental parameters can be varied:

- Position of the metallic gas tube
- Focusing of NIR beam (realized with aperture)
- Intensity of the driving NIR field
- Choice of noble gas/ applied target gas pressure

After the optimization process, the harmonic signal was measured by varying the pressure of the target gas Ne (Fig. 4.5). Depending on the selected harmonic, the signal rises up to a certain pressure and decreases afterwards for higher pressures.

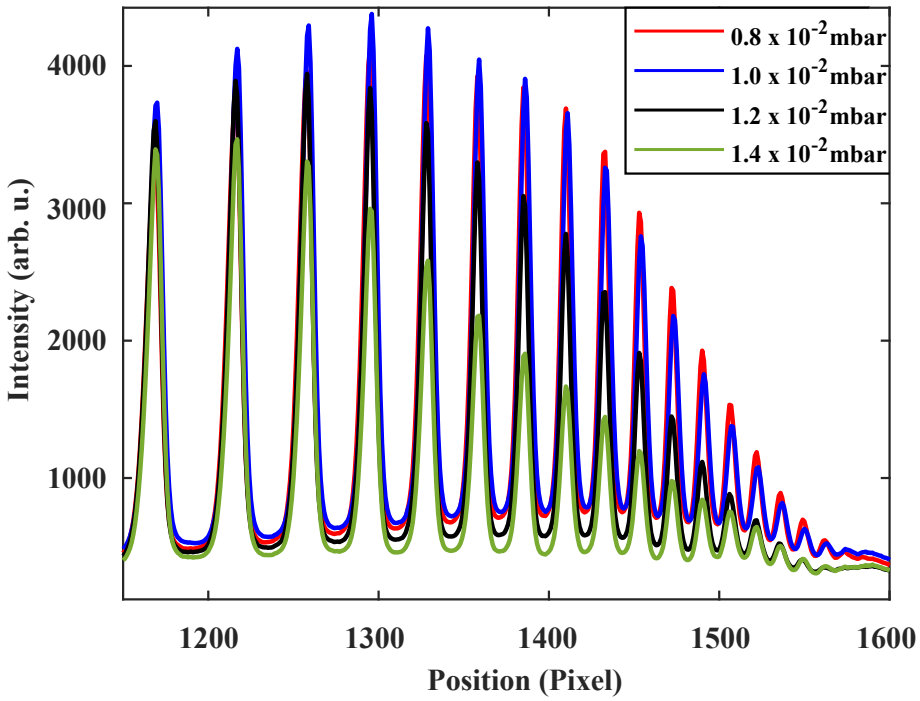

Figure 4.5: Comparison of HH spectra by changing the applied pressure of Ne.

Measurements with the previously described method only give a relative estimate of the efficiency of the HHG process. Since the energy of an individual harmonic is orders of magnitudes smaller than the initial NIR pulse energy, a calibrated XUV photodiode (SPD-1UVHCM, Technoxan Ltd.) was placed in the interaction region. A voltage modulation of $\Delta V = 8\,\mathrm{mV}$ was obtained, which results in a pulse energy of

$$E = \frac{\Delta V}{S_1 \times S_2} = \frac{8\,\mathrm{mV}}{0.25\,\mathrm{A}/W \times 1.1\,\mathrm{mV/(fC)}} = 29\,\mathrm{fJ}, \tag{4.1}$$

of the 51$^{\mathrm{st}}$ harmonic, where S_1 and S_2 denote the diode and preamplifier sensitivity, respectively. Since the generated harmonics are reflected from two multilayer surfaces (reflectivity of one multilayer mirror: $R_{\mathrm{ML}} = 0.65$ at 80 eV) and are transmitted through two Zr-filter (transmission of one Zr-filter: $T_{\mathrm{Zr}} = 0.41$ at 80 eV), the

conversion efficiency is calculated to be 0.39×10^{-9}. For the streaking experiment, only one Zr-filter is used thus the number of photons N in the interaction volume is estimated to

$$N = \frac{E}{T_{\mathrm{Zr}} \times \hbar\omega} = 5500. \tag{4.2}$$

Another measurement was performed to characterize the focus of the XUV beam in the streaking chamber. Since a normal camera is not sensitive to high energy photons, the CMOS chip of a Basler camera (daA1280-54um, $1280 \times 960\,\mathrm{pixel}^2$, Pixel size: $3.75\mu m \times 3.75\mu m$) was directly coated with phosphor. Therefore, the focus of the XUV beam can be directly measured (Fig. 4.6a) and a horizontal (X) and vertical (Y) beam radius of $58\,\mu$m and $25\,\mu$m, respectively, has been obtained (Figs. 4.6c and 4.6d). The residual signal was attributed to the NIR laser when Ne was switched off in the HHG chamber (Fig. 4.6b). The beam radius in the horizontal (X) and vertical (Y) direction was determined to $48\,\mu$m and $40\,\mu$m, respectively (Figs. 4.6e and 4.6f). Both beam profiles showed an astigmatism when scanning along the propagation direction. This behavior is expected because spherical focusing mirrors with focal lengths of 1215 mm and 500 mm when focusing into the HHG chamber and VMIS chamber, respectively, were used. In both cases, the angle of incidence was around 5°. However, the XUV beam profile reveals a stronger astigmatism.

4.3 Laser-based terahertz radiation

4.3.1 Conversion efficiency

During the optimization procedure the output THz energy behind the cLNB crystal was measured with a pyroelectric detector (LIE-329, Infratec GmbH). A cross-calibration with another pyroelectric detector (Microtech instruments inc.) yields a conversion factor of around $1.1\,\mu$J/V for the LIE-329 detector. The maximum voltage modulation of the LIE-329 detector was around 400 mV, which leads to a THz conversion efficiency of

$$\eta_{\mathrm{eff}} = \frac{0.4\,\mathrm{V} \times 1.1\,\mu\mathrm{J/V}}{800\mu\mathrm{J}} = 0.055\%, \tag{4.3}$$

where an NIR input energy of $800\,\mu$J was assumed. The conversion efficiency is lower than in other groups [122, 123].

4.3.2 Characterization of the terahertz focus

The THz focus size strongly depends on the THz beam collimation and the alignment of the OAPM. A good focusing is required since the momentum exchange between the photon and the photoelectron scales linearly with the amount of vector potential of the THz electric field. Without the VMIS inserted in the vacuum chamber, the THz focus was analyzed using a pyroelectric array camera (Pyrocam IV from *Spiricon*, pixel pitch: $80\,\mu$m), which was mounted on a linear translation stage to explore the focal region. At the THz focus, a nearly radial symmetric spot is observed (Fig. 4.7). The exposure time of the camera was set to 30 ms

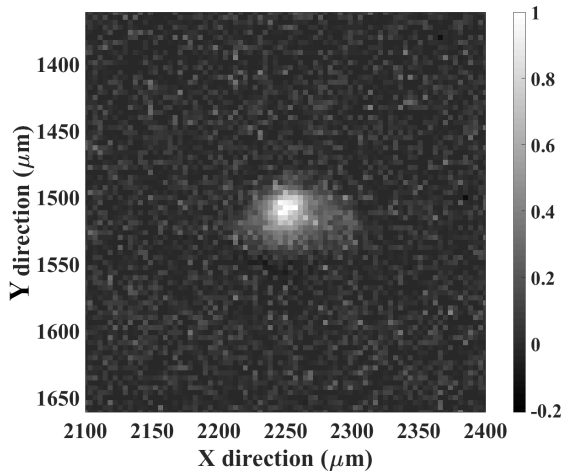

(a) Focus of XUV beam

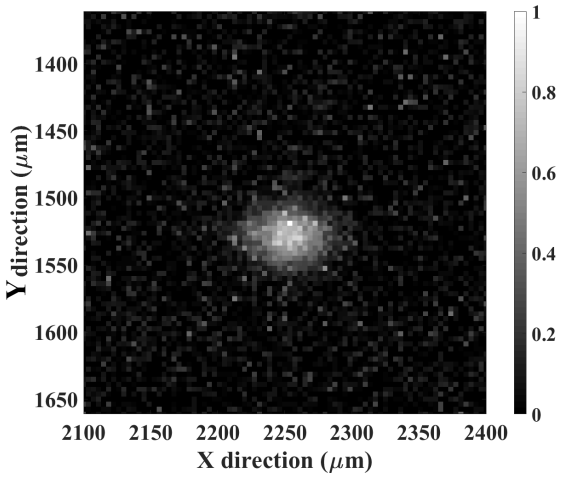

(b) Focus of NIR beam

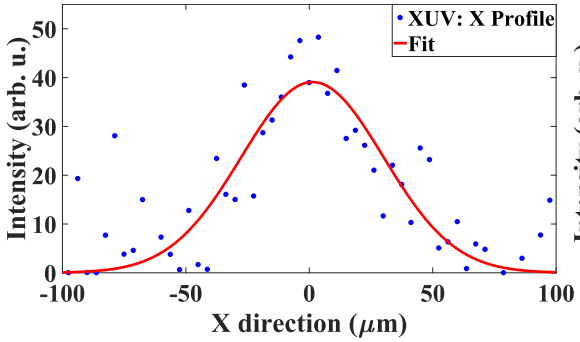

(c) XUV horizontal fit: $w_0 = (58 \pm 9)\,\mu$m

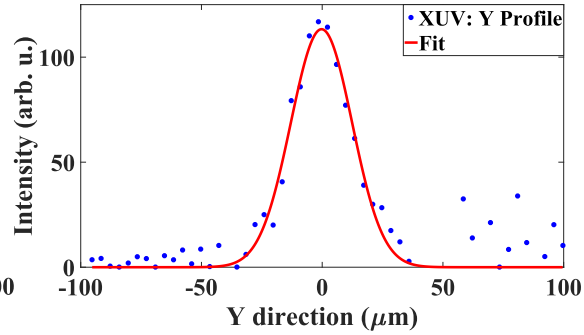

(d) XUV vertical fit: $w_0 = (25 \pm 2)\,\mu$m

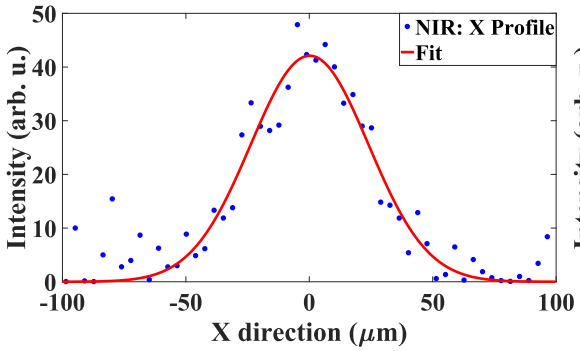

(e) NIR horizontal fit: $w_0 = (48 \pm 4)\,\mu$m

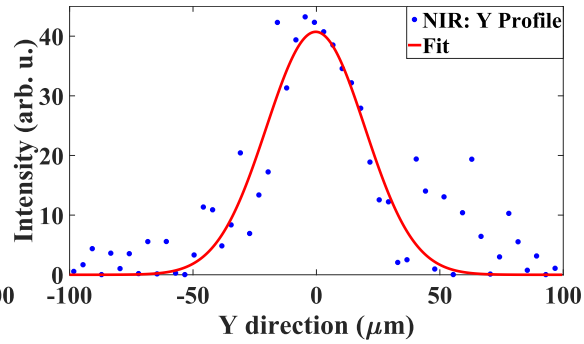

(f) NIR vertical fit: $w_0 = (40 \pm 5)\,\mu$m

Figure 4.6: Spatial profiles of the NIR and XUV laser beams using a phosphor coated daA1280-54um Basler camera.(a) XUV beam profile. (b) and (c) Corresponding horizontal and vertical line-outs are depicted together with a Gaussian fit. The beam radii ($1/e^2$) of both line-outs are extracted and written below each plot.

Assuming a TEM_{00} mode, the intensity can be modeled with a Gaussian profile and Eq. (A.10) in the Appendix A.2. The goal is to determine the beam waist w_0 ($(1/e^2)$ radius). The connection between the beam radius $w(z)$, the beam waist w_0 and the Rayleigh length z_r is given by Eq. (A.5), which can also be found in the appendix A.2.

For the focus measurement, the pyroelectric array camera was placed on a linear translation stage to scan the beam profile at various positions providing the oppor-

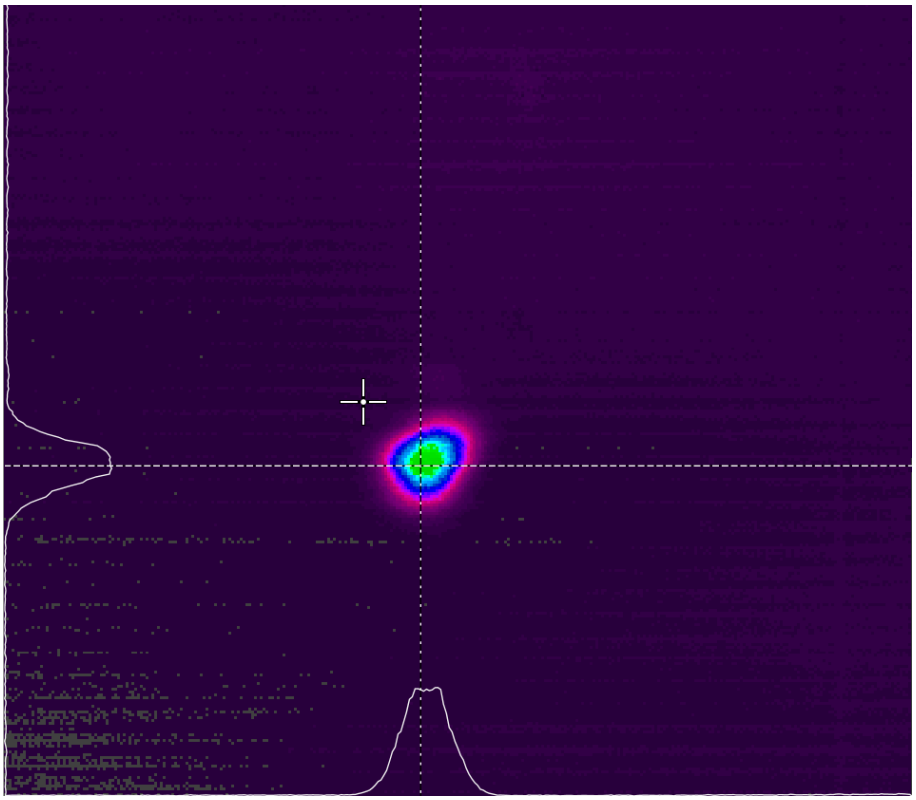

Figure 4.7: Average of the THz focus in the streaking chamber using a Pyrocam IV. The THz beam was focused with an OAPM and a focal length of $f = 101.6\,\mathrm{mm}$.

tunity to determine the horizontal and vertical beam waist (Fig. 4.8). The obtained horizontal and vertical beam radii are $(1.12 \pm 0.02)\,\mathrm{mm}$ and $(1.10 \pm 0.01)\,\mathrm{mm}$, respectively. The difference in the horizontal and vertical focus position of $\approx 16\,\mathbf{mm}$ is an indication for astigmatism. The reason for this effect could be a discrepancy of the various divergences in both directions of the generated THz beam after the cLNB crystal. This can be attributed to imaging errors in the tilted-pulse-front setup using only one achromatic imaging lens [124]. From both fits, the horizontal and vertical Rayleigh lengths are $(43 \pm 6)\,\mathrm{mm}$ and $(22 \pm 2)\,\mathrm{mm}$, respectively. The estimation of the M^2 value can be calculated using

$$M^2 = \frac{\theta_{\mathrm{exp}}}{\theta_{\mathrm{theo}}} = \frac{z_{r,\mathrm{theo}}}{z_{r,\mathrm{exp}}} = \frac{\pi w_0^2}{\lambda_{\mathrm{THz}} z_{r,\mathrm{exp}}} \tag{4.4}$$

where a monochromatic TEM_{00} mode with wavelength λ_{THz} as a reference is assumed. For the broadband THz radiation a center wavelength of about $0.375\,\mathrm{mm}$ was determined. The resulting M^2 values for the horizontal and vertical direction are 0.24 and 0.56, respectively. Of course, M^2 values below 1 are physically not correct. A possible reason for this could be the sensitivity of the THz camera. Away from the focus, when the beam size is large, the wings of the THz beam might not be detected leading to smaller THz images. Consequently, the beam size is underestimated and thus the measured Rayleigh length $z_{\mathrm{r,exp}}$ is larger than expected. According to Eq. (4.4), a smaller Rayleigh length $z_{\mathrm{r,exp}}$ means a larger M^2.

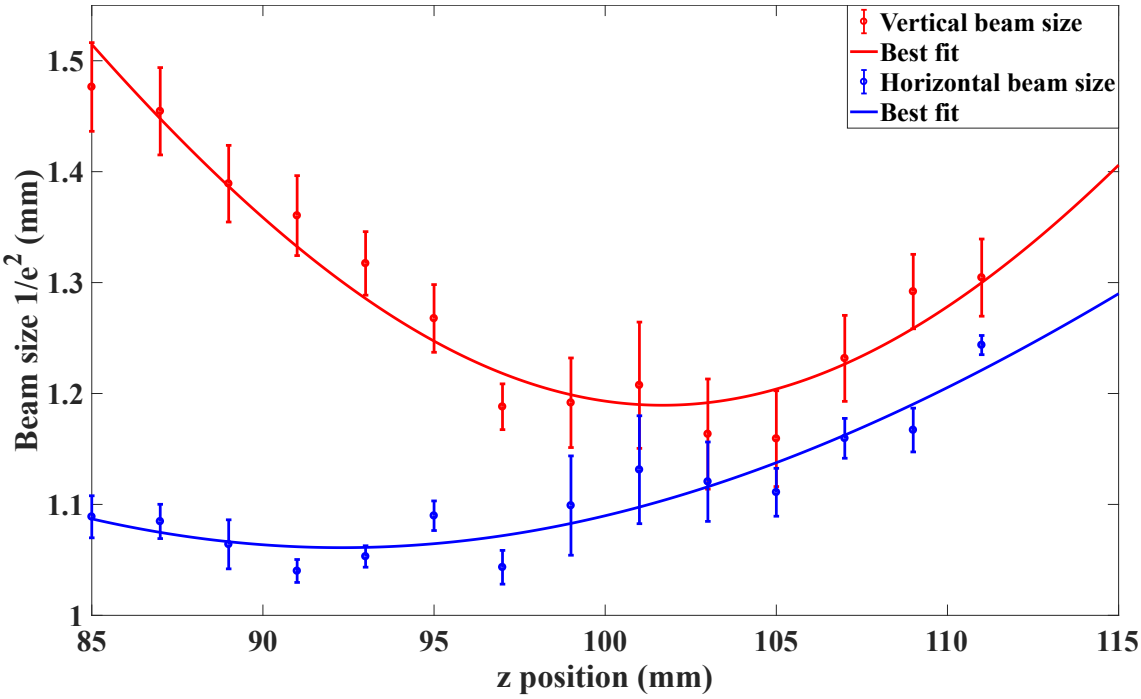

Figure 4.8: THz beam size in the focal region of the OAPM ($f = 101.6\,\mathrm{mm}$). At each position the THz beam profile was measured using a Pyrocam IV and fitted with a Gaussian profile described by Eq. (A.10).

4.3.3 Electro-optic sampling

The temporal profile of the THz pulse has been characterized with electro-optic (EO) sampling. The diagnostics of this measurement were placed behind the THz focus (Fig. 4.9).
The collimated THz beam (orange) is focused with an OAPM ($f = 101.6\,\mathrm{mm}$) into a ZnTe crystal (thickness $d = 220\,\mu\mathrm{m}$) and induces a transient birefringence. The modulated change of the refractive index is probed with an NIR laser, that is focused with a spherical mirror (not shown here) through a hole in the OAPM into the ZnTe crystal. After the collimation with a plano-convex lens (L, $f = 75\mathrm{mm}$), the probe beam passes through a quarter-waveplate before it hits a polarizing beamsplitter (PBS) that separates the horizontal and vertical components of the electromagnetic wave. Both components are indivdually detected with two distinct photodiodes ($\mathrm{PD}_{1/2}$). The angle of the THz beam polarization is defined as α while the angle of the NIR beam polarization is defined as φ with respect to the (001) axis of the ZnTe crystal. The relative angle $|\varphi - \alpha|$ can be varied with a half-waveplate before the OAPM. In case of $|\varphi - \alpha| = \pi/4$ no additional half-waveplate is needed and the optional half-waveplate (dashed box) can be removed. In any other case, $|\varphi - \alpha| \neq \pi/4$, an additional half-waveplate is necessary.
According to Eq. (2.54), the electric field strength of the THz radiation can be calculated at any point in time. The maximum electric field was measured to $E_{\mathrm{max}} = 1.56\,\mathrm{MV/m}$. The Fresnel reflection losses at the ZnTe surface are

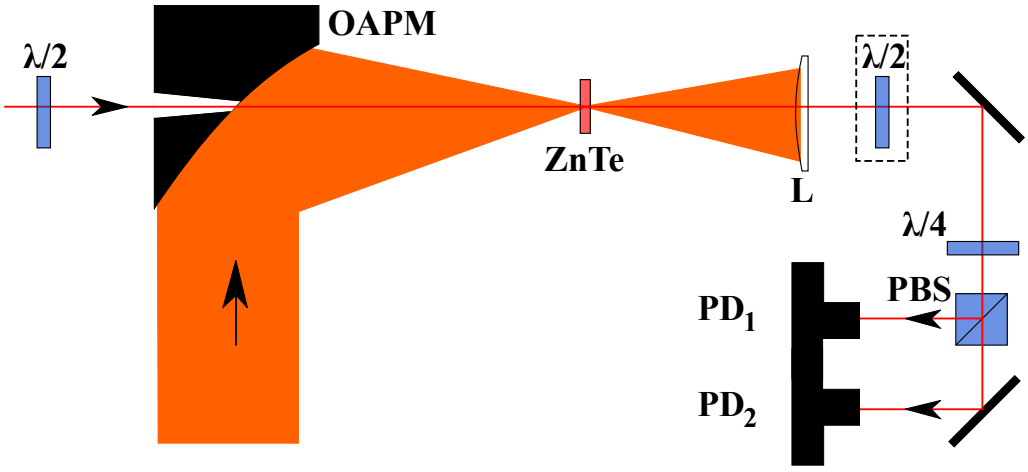

Figure 4.9: Sketch of the EO sampling experiment. The THz and NIR beam path is shown in orange and red, respectively. The abbreviations are off-axis parabolic mirror (OAPM), EO crystal (ZnTe), collimation lens (L), polarizing beamsplitter (PBS), photodiodes 1/2 ($PD_{1/2}$), half-waveplate ($\lambda/2$), quarter-Waveplate ($\lambda/4$). The second half-waveplate (dashed box) is optional.

$$t_{\mathrm{ZnTe}} = \frac{2}{n_{\mathrm{THz}} + 1} = 0.48, \tag{4.5}$$

where a refractive index of $n_{\mathrm{THz}} = 3.17$ in the THz range for ZnTe was assumed [125]. Therefore, the maximum electric field of $\tilde{E}_{\mathrm{max}} = 3.25\,\mathrm{MV/m}$ is obtained. The near single-cycle THz pulse is followed by an oscillatory tail over many picoseconds, which is attributed to the water absorption in ambient air (Fig. 4.10a). The positions of these absorption lines can be clearly seen when applying a fast Fourier transform (FFT) to the electric field. Due to the long EO sampling range, the resolution of the amplitude spectrum is improved (Fig. 4.10b). For the streaking experiment, this is also important since the THz pulse propagates from the $LiNbO_3$ crystal in air to the vacuum window. The peak frequency of the THz electric field is estimated to be 0.83 THz.

The EO sampling technique also provides the opportunity to determine the Gouy phase of the THz radiation in the focal region. This is important because the Gouy phase leads to a change of the THz electric field over the focus, which has to be taken into account. By mounting the ZnTe crystal on a translation stage, the electric field of the THz pulse was measured at 16 different positions along the focus. Assuming a Gaussian envelope and a periodic carrier wave function with an angular frequency ω_0, the electric field can be described as

$$E(t) = A_0 \exp\left(-\frac{(t-t_0)^2}{b^2}\right) \cos\left[\omega_0(t-t_0) + \Phi_{\mathrm{CE}}\right], \tag{4.6}$$

where the parameters A_0, b and t_0 denote the amplitude, the pulse width and the temporal offset of the electric field, respectively. In most light sources, the carrier envelope phase offset Φ_{CE} is randomly fluctuating from shot to shot. Fortunately, the offset Φ_{CE} is constant in our case because the THz pulse is produced by difference

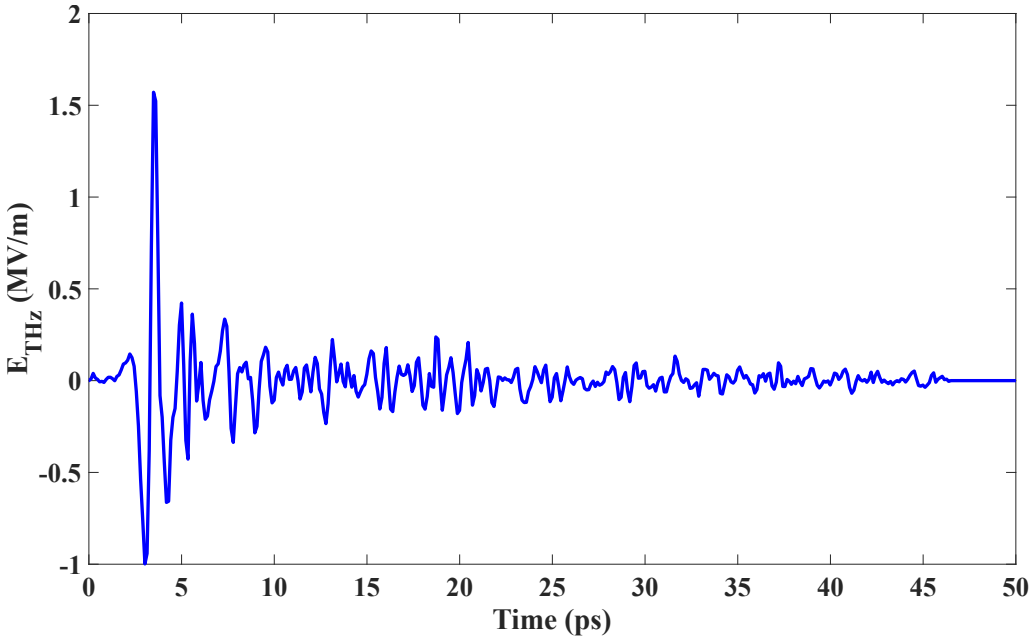

(a) THz electric field in the time domain

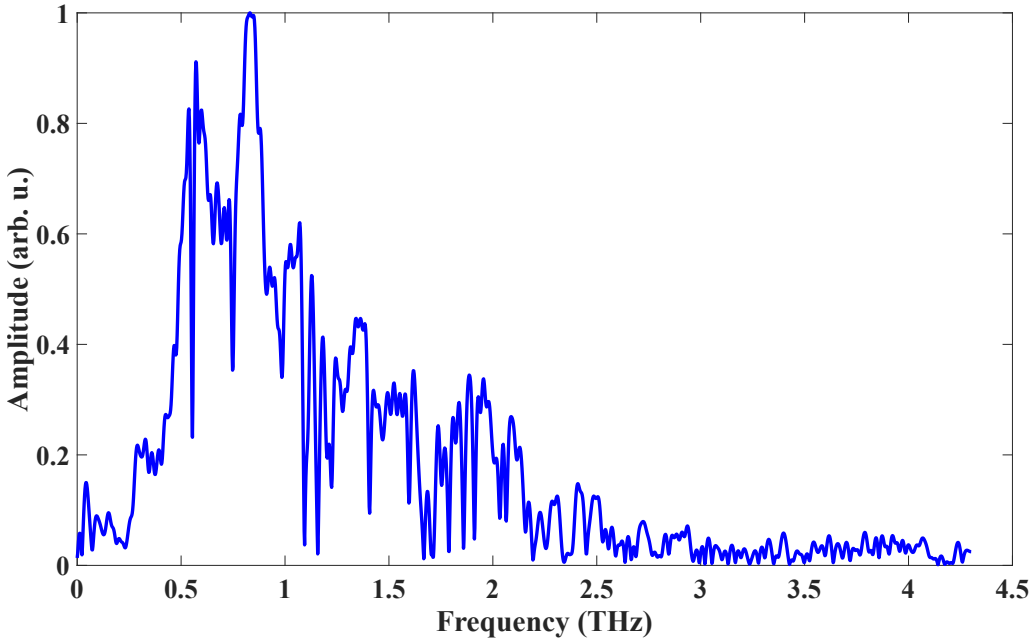

(b) THz electric field in the frequency domain

Figure 4.10: Evolution of the THz electric field measured with EO sampling. (a) Time domain. (b) Frequency domain. The amplitude spectrum is obtained by an FFT of the THz electric field. The visible dips in the spectrum are related to water absorption lines.

frequency generation within the broadband NIR pulse. Therefore, when propagating the THz beam through the focus, the change of the offset can be associated with the Gouy phase. To estimate the Gouy-phase change over the interaction region, the electric field distribution $E(t)$, obtained from EO sampling, is fitted with Eq. (4.6). Furthermore, the pulse trailing edge, which is a consequence of the water absorptions in air, was truncated. The amplitude of the electric field was calibrated using

Eq. (2.54). The temporal shape of the THz pulse changed along the longitudinal position (Fig. 4.11a). The maximum electric field (red curve) was measured at a longitudinal position $z = 13.11\,\text{mm}$. The other two electric fields (black and blue curve) were obtained at positions $z = 1.00\,\text{mm}$ and $z = 25.00\,\text{mm}$, respectively.

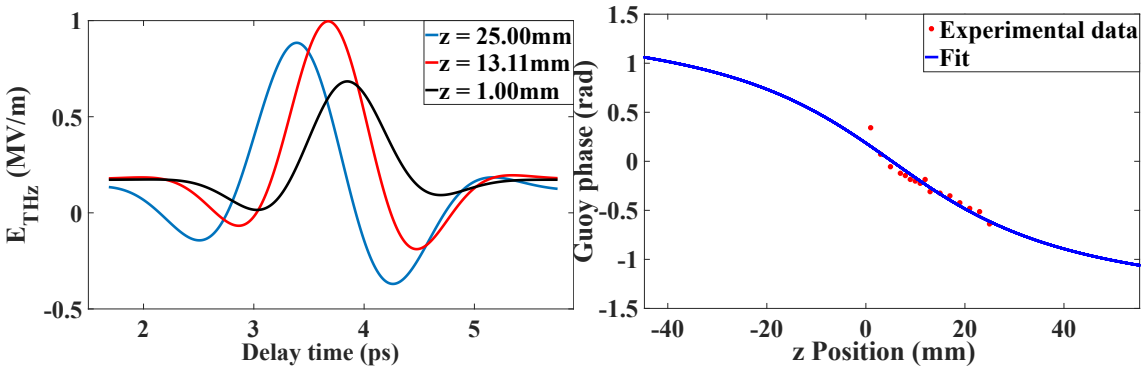

(a) THz electric field in the time domain (b) THz electric field in the frequency domain

Figure 4.11: Determination of the THz Gouy phase. (a) Fitted temporal evolution of the THz electric field at various positions along the focus. The positions are indicated with the longitudinal z-coordinate. Each individual trace was measured with EO sampling using Eq. (2.54) and fitted with a Gaussian envelope and a fast oscillating periodic function using Eq. (4.6). (b) THz Gouy phase dependence along the focus. All phase offsets Φ_{CE} were extracted by directly measuring the electric field via EO sampling using Eq. (2.54) and fitted with Eq. (4.6). The resulting phase offsets Φ_{CE} were fitted with Eq. (4.7).

For a Gaussian beam, the Gouy phase as a function of the longitudinal coordinate z is given by

$$\Phi_G = \arctan\left(\frac{z - z_0}{z_r}\right), \tag{4.7}$$

where z_0 and z_r represent the focus position and the Rayleigh length, respectively. The analytical fit for the Gouy phase Φ_G as a function of the propagation coordinate z reproduces quite well the experimental measurement (Fig. 4.11b). A value of $z_r = (28.0 \pm 5.0)\,\text{mm}$ was obtained for the Rayleigh length. The change of the Gouy phase Φ_G near the focus can be approximated with a linear function and a slope of $d\Phi_G/dz = (32 \pm 6)\,\text{mrad/mm}$.

Chapter 5

Velocity-map-imaging spectrometer

During this PhD work, a new VMIS was designed and used for a laser-based streaking experiment. This electron imaging detector has to fulfill the following requirements:

- large aperture between Repeller and Extractor for THz beam incoupling
- high target gas pressure in the interaction volume
- implementation of a novel capillary gas injector
- preserving energy resolution (due to gas capillary)
- compact detector design

Consequently, this chapter will be structured as followed. At the beginning, basic principles of a VMIS will be discussed. Based on the general detector layout, the specific geometry of the VMIS will be optimized by extensive numerical simulations. The experimental implementation of the electron imaging detector, including the novel capillary gas injector, will be discussed afterwards. To directly extract the energy and angular information of an experimental image, it is necessary to apply an Abel inversion. Several inversion methods will be described and compared.

5.1 Principles of velocity-map-imaging

A VMIS is a powerful tool that measures the velocity distribution of an expanding electron cloud that is projected onto a 2 dimensional (2d) position-sensitive detector (PSD). This concept was first introduced in 1997 by André Eppink and David Parker [27] and was later applied in different fields within the imaging community. The following descriptions are based on the book of Benjamin Whitaker [126]. Note that a VMIS can be either used for the detection of electrons or ions. For electron detection negative voltages have to be applied to the electrodes, whereas for positive ion detection positive voltages have to be applied. Within the scope of this work, only electron detection will be considered.
Let us consider a photoionization of an atom or molecule A:

$$A \xrightarrow{\hbar\omega} A^* \longrightarrow A^+ + e^-$$

In the center-of-mass frame, both ion fragments A^+ and e^- fly in opposite direction with the same momentum. By repeating this photoionization process several times the fragments themselves form spherical distributions, so-called Newton spheres in velocity space (Fig. 5.1). The size and shape of the Newton spheres will reveal information about the initial physical process.

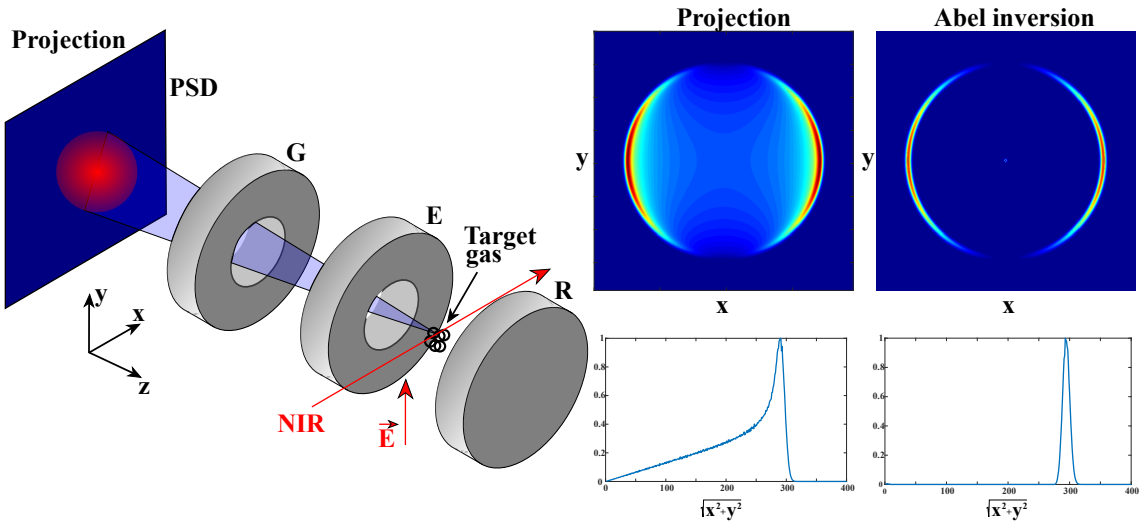

Figure 5.1: Principles of a VMIS spectrometer, which is formed by a Repeller (R), Extractor (E) and Ground (G) electrode. An electron cloud is generated by focusing an NIR laser into a gas target. The expanding Newton sphere is projected on a position-sensitive detector (PSD). The visualization of the VMIS was inspired by [127].

The general idea of the electron-imaging apparatus is now that all charged particles with the same initial velocity within a sufficiently small interaction region are mapped on the same point onto a 2d PSD. Thus, it is possible to map out the different reaction channels within the physical process. The image on the 2d PSD is essentially a projection of the Newton spheres along the TOF axis (z-axis) and can be inverted by a so-called Abel inversion to obtain the initial charged particle distribution provided that an axis of symmetry is parallel to the imaging plane. Here, the symmetry axis is defined by the polarization direction of the electric NIR field. This will be explained in more detail in Section 5.5. Experimentally, this projection is realized using an arrangement of three electrostatic electrodes. These electrodes are the Repeller (R), Extractor (E) and Ground (G). The VMIS has a rotational symmetry around its TOF axis (z-axis). In contrast to the Wiley-Mc Laren setup [128] that uses grid electrodes, grid electrodes were replaced by open aperture electrodes.
After the generation of photoelectrons between the Repeller and Extractor electrodes, they are accelerated and pass the Extractor and Ground electrodes towards a position-sensitive microchannel plate that is equipped with a phosphor screen (MCP + P). The electrodes form an electrostatic lens where the MCP + P detector is located in the focal plane. Photoelectrons with the same initial velocity but different positions will be mapped onto the same point on the detector. This principle is the so-called velocity-map imaging. The shape, the relative distances and the applied voltages of the electrostatic plates determine the spatial resolution of the electron-imaging apparatus. It is often useful to relate the kinetic energy E_{kin} of a photoelectron with its momentum p and the radial distance r_{det} where it is observed. The photoelectron momentum scales linearly with the radial distance for a VMIS, i.e. $p = c \cdot r_{\mathrm{det}}$ with a constant c provided that the initial photoelectron velocity

is parallel to the PSD. Therefore, the relation between the kinetic energy and the radial distance is given by

$$E_{\mathrm{kin}} = \frac{p^2}{2m} = \frac{(c \cdot r_{\mathrm{det}})^2}{2m}, \tag{5.1}$$

where m denotes the mass of the photoelectron. The kinetic energy of the photoelectron generated by multiphoton ionzation or direct photoionization can be obtained with Eqs. (2.1) and (2.29), respectively. Hence, Eq. (5.1) can be used for an experimental calibration. Another important remark is the energy resolution of a VMIS, defined by $\Delta E_{\mathrm{kin}}/E_{\mathrm{kin}}$, where ΔE_{kin} denotes the energy width (FWHM). The differentiation of Eq. (5.1) gives

$$\frac{dE_{\mathrm{kin}}}{E_{\mathrm{kin}}} = 2\frac{dp}{p} = 2\frac{dr_{\mathrm{det}}}{r_{\mathrm{det}}}. \tag{5.2}$$

Assuming a Gaussian shape of the radial distribution on the PSD

$$y\left(r_{\mathrm{det}}\right) = A \exp\left[-\frac{r-B}{C}\right]^2, \tag{5.3}$$

where A, B and C are fitting parameters, the energy resolution is obtained by

$$\frac{\Delta E_{\mathrm{kin}}}{E_{\mathrm{kin}}} = \frac{4C\sqrt{\ln 2}}{B}. \tag{5.4}$$

In the experiment the energy resolution is a superposition of the detector resolution ΔE_{VMIS} and the spectral width ΔE_2 of the observed physical process. Assuming two Gaussian distributions for both effects, the resulting energy resolution ΔE is given by

$$\Delta E = \sqrt{\Delta E_{\mathrm{VMIS}}^2 + \Delta E_2^2}. \tag{5.5}$$

In this context, it is worth to briefly define aberrations [27]. Charged particles, which are emitted in the same direction but different speeds, will be mapped on different points on the detector. This effect is referred to as chromatic aberration. On the other hand, charged particles, which are emitted with the same speed but different directions with respect to the TOF axis, will hit different spots on the detector. This phenomena is known as spherical aberration. However, in velocity-map-imaging these effects are intentional since particles with different initial conditions should be mapped on different points on the detector. Due to the fact that electrons will be created at different spots within a finite focus size of the interaction region, the image on the PSD will be deblurred [27]. In addition, space-charge effects can occur during the experiment. If the number of electrons within the interaction volume is too high their repulsive interaction will lead to a broadening of the ion cloud and consequently to an unclear image [129]. This effect can be compensated, for instance, by reducing the laser intensity or the gas density.

5.2 Optimization of the spectrometer design

For all numerical simulations the SIMION software [130, 131] was used. The assembly of the electrodes defines an inhomogeneous position-dependent electrostatic potential, which can be described by the Laplace equation. An electron trajectory can then be classically calculated by computing the electrostatic potential along its path.
The initial geometry of a conventional VMIS will be adapted to obtain the best suitable design (Fig. 5.2). Taken into account the cylindrical symmetry of the electron imaging detector with respect to the TOF axis (z-axis), the computational power needed to perform the numerical simulations is drastically reduced. Therefore, all computer simulations were only performed in the yz-plane. The following geometrical quantities were optimized:

1. Variation of the flight tube length (in z-direction)
2. Variation of Extractor electrode position (in z-direction)
3. Variation of Ground electrode position (in z-direction)
4. Variation of aperture opening of Extractor and Ground electrode (in y-direction)
5. Variation of electrode thickness (in z-direction)

An electron trajectory can be fully calculated for a given electrode geometry and corresponding applied potentials (V_R and V_E, respectively) as well as its initial spatial coordinates and velocity ($\vec{r}_0$ and $\vec{v}_0$, respectively). The electrons are exactly generated in the middle between Repeller and Extractor assuming an extension of 2 mm in y-direction along the laser focus. A good measure Q for the quality of a certain configuration is defined by the ratio of the standard deviation Δr and the average position r_mean of all electrons on the PSD:

$$Q = \frac{\Delta r}{r_\mathrm{mean}}. \tag{5.6}$$

The smaller Q the better the VMIS detector operates. The number of electrons per configuration was set to $N = 101$. For an arbitrary electrode arrangement and a given Repeller voltage V_R the quality parameter Q was calculated as a function of the Extractor voltage V_E and the corresponding geometry parameter $(1, \ldots, 5)$ for electrons with the same initial velocity but different initial positions. In an experiment often electrons with different energies are involved. Therefore, the optimum Extractor voltage $V_\mathrm{E}^{(\mathrm{opt})}$ also depends on the initial energy (1) and the direction with respect to the symmetry axis (2) of the emitted electrons. The less the optimum Extractor voltages differ from various initial conditions the better the VMIS operates. For clarity, significant differences between optimum Extractor voltages in case of (1) or (2) are called chromatic or spherical distortions, respectively. These two terms will be used throughout the following section and should not be mixed up with chromatic and spherical aberrations.

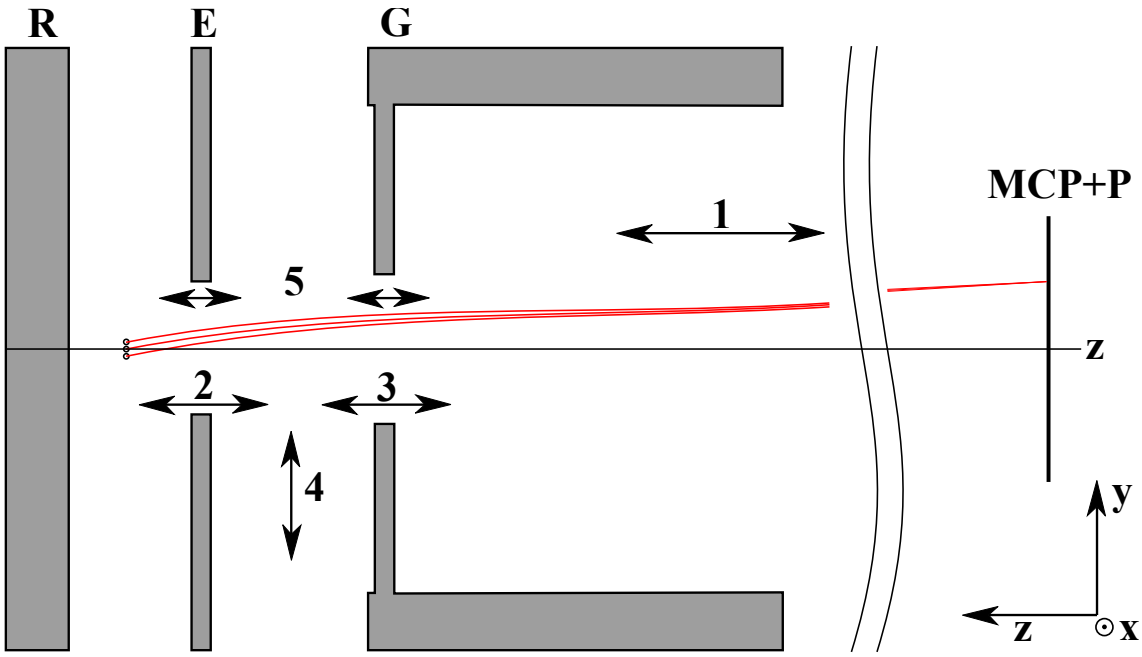

Figure 5.2: Sketch of a classical VMIS. The parallel static electrodes are abbreviated with **R** - Repeller, **E** - Extractor, **G** - Ground. Due to the cylinder symmetry around the TOF axis (z-axis), the numerical computations were only performed in the yz-plane. The arrows with the corresponding numbers indicate the geometrical quantity, which was adapted during the optimization process.

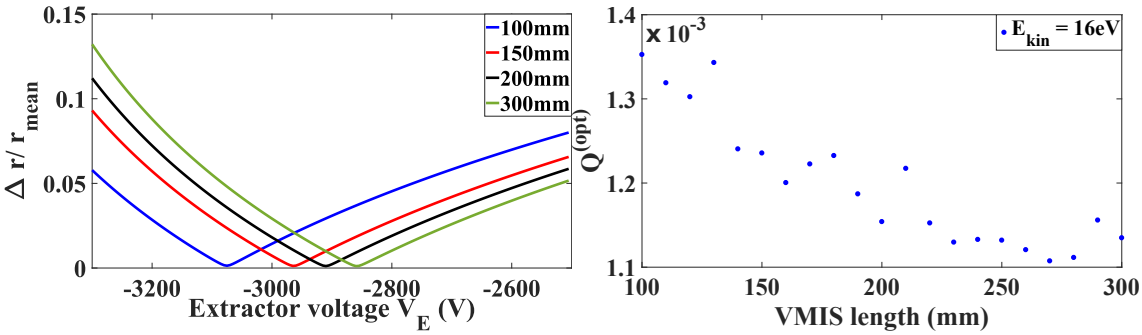

(a) Quality parameter

(b) Minimum quality parameter

Figure 5.3: Geometry optimization. For different drift tube lengths and different Extractor voltages V_E, the quality parameter from Eq. (5.6) was calculated. The initial electron energy was set to 16 eV and the initial velocity points along the y-direction. (a) Variation of V_E for several drift tube lengths, (b) Calculation of the minimum quality parameter ($Q^{(\mathrm{opt})}$) as a function of the drift tube length.

Variation of flight tube length

In a first iteration, the flight tube length was varied for electrons with an initial energy of 16 eV starting in the y-direction for a fixed Repeller voltage (Fig. 5.3).
It is clear that the quality parameter improves by increasing the drift tube length. However, the mean impact position r_mean of all electrons is also increasing. Hence, the drift tube length is restricted by the size of the PSD.

Variation of the Extractor electrode position

In a second iteration, the position of the Extractor plate along the TOF axis of the detector was varied for electrons with an initial energy of 16 eV starting in the y-direction (Figs. 5.4a and 5.4b).

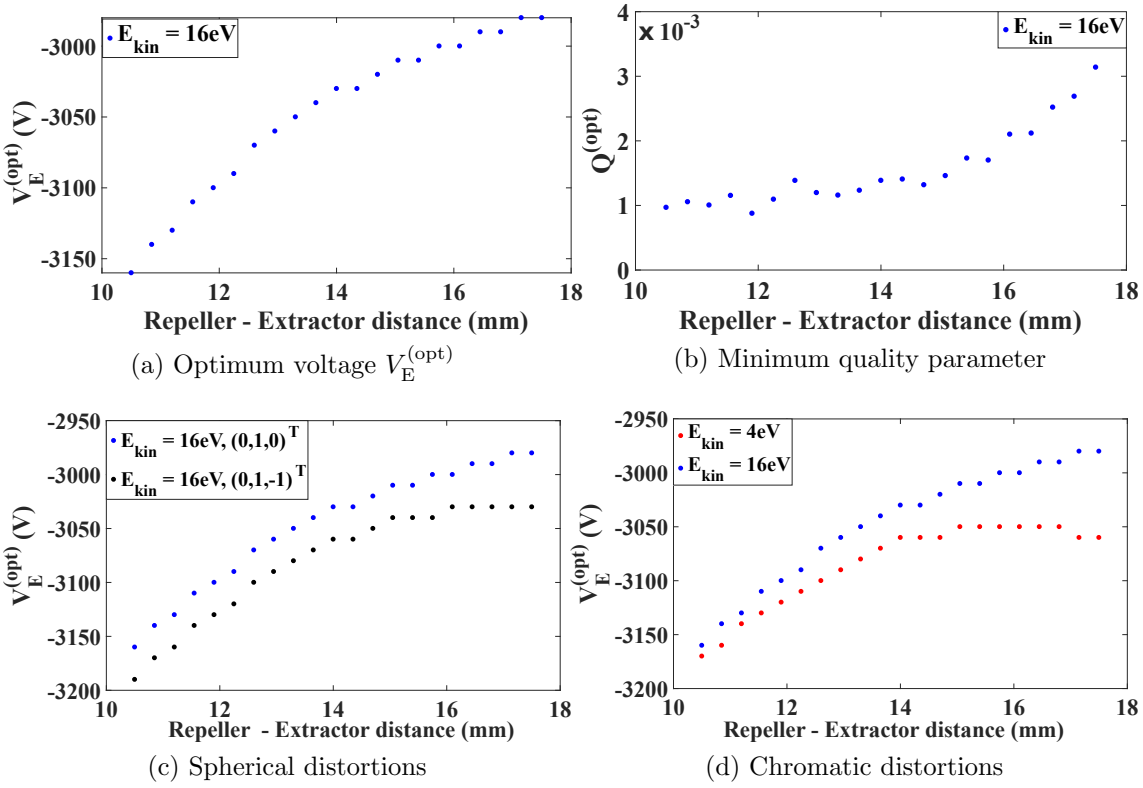

(a) Optimum voltage $V_{\mathrm{E}}^{(\mathrm{opt})}$

(b) Minimum quality parameter

(c) Spherical distortions

(d) Chromatic distortions

Figure 5.4: Geometry optimization. For different positions of the Extractor electrode and Extractor voltages V_{E} the quality parameter from Eq. (5.6) was calculated. (a) and (b) The initial electron energy was set to 16 eV and the initial velocity points along the y-direction. (c), (d) imaging errors.

By increasing the distance between the Repeller and Extractor electrodes the absolute optimum Extractor voltage V_{E}, that has to be applied to obtain the minimum quality parameter Q, is decreasing. At the same time, however, the optimum quality parameter Q is increasing, which means that charged particles, that originate from different initial positions, are focused worse on the PSD. This feature is a direct consequence of velocity-map-imaging. The curvature of the equipotential surfaces between the electrodes is the origin of the velocity mapping. By increasing the distance between Repeller and Extractor both electrodes merge into an ideal parallel plate-capacitor. The curvature of the equipotential surfaces is reduced and thus the performance of the VMIS is worse.

In addition, the distortions should be taken into account (Figs. 5.4c and 5.4d). An increase of the distance between the Repeller and Extractor electrodes leads to more chromatic and spherical distortions. The gap of the optimum Extractor voltages V_{E} for different initial angles or energies of the simulated electrons, associated with spherical and chromatic distortions, respectively, is getting larger.

As a consequence of these considerations, the distance between Repeller and Ex-

tractor electrodes should be as small as possible but big enough to couple in the THz. Taken into account the focusing of the THz radiation by an OAPM with a focal length of $f = 101.6\,\mathrm{mm}$ and a clear aperture of about $d = 50\,\mathrm{mm}$, the full angle Θ of the THz beam

$$\tan\frac{\Theta}{2} = \frac{d/2}{f} = \frac{d_{\mathrm{RE}}/2}{R}. \tag{5.7}$$

determines the ratio between the Repeller and Extractor distance d_{RE} and the radius R of the electrode.

Variation of the Ground electrode position

In a third iteration, the position of the Ground electrode along the TOF axis of the detector was varied for electrons with an initial energy of 16 eV starting in the y-direction (Fig. 5.5).

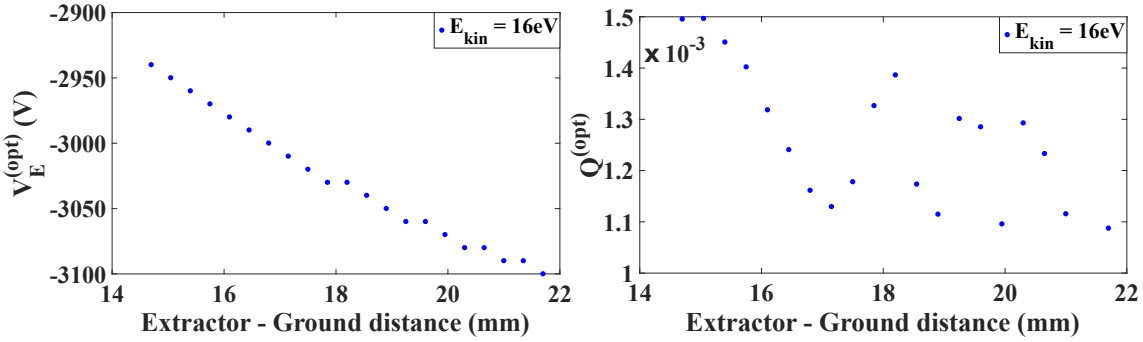

(a) Optimum voltage $V_{\mathrm{E}}^{(\mathrm{opt})}$ (b) Minimum quality parameter

Figure 5.5: Geometry optimization. For different positions of the Ground electrode the quality parameter from Eq. (5.6) was calculated. The corresponding Extractor voltages V_{E} were plotted as a function of distance between Extractor and Ground plate.

From the numerical simulations it is evident that the absolute value of the optimum Extractor voltage $V_{\mathrm{E}}^{(\mathrm{opt})}$ is raising for larger distances between Extractor and Ground electrodes. The corresponding optimum qualtity parameter $Q^{(\mathrm{opt})}$ does not significantly change. Therefore, the position of the Ground electrode on the TOF axis does not play a big role.

Variation of the aperture opening

In a forth iteration, the opening of the Extractor and Ground electrodes was varied for electrons with an initial energy of 36 eV starting in the y-direction (Figs. 5.6a and 5.6b).

By increasing the diameter of the aperture opening the curvature of the equipotential surface is enhanced thus giving a better velocity-map performance. As a result, the quality parameters is decreasing while the absolute values of the corresponding optimum Extractor voltages V_{E} are increasing. For a more complete analysis the arising distortions have to be considered (Figs. 5.6c and 5.6d). Similar to previous simulations, the optimum voltages V_{E} for electrons with different initial velocity angles but same energies and vice versa were obtained to visualize the spherical and

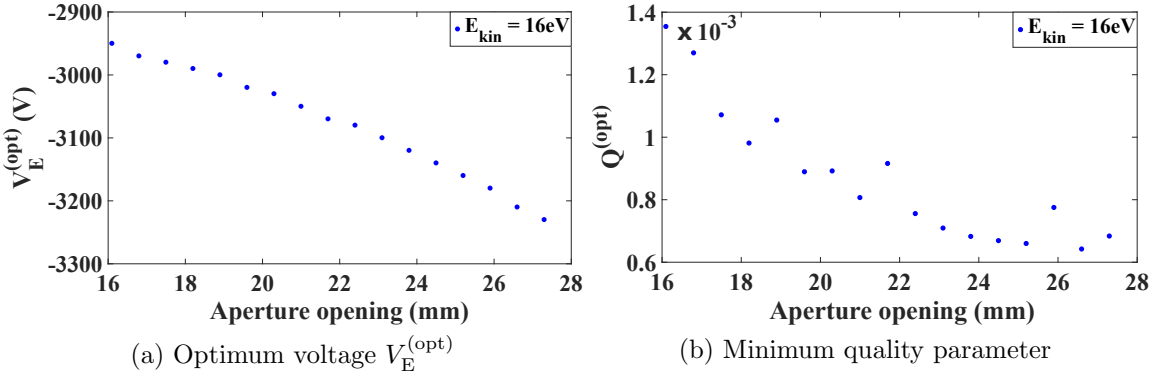

(a) Optimum voltage $V_{\mathrm{E}}^{(\mathrm{opt})}$ (b) Minimum quality parameter

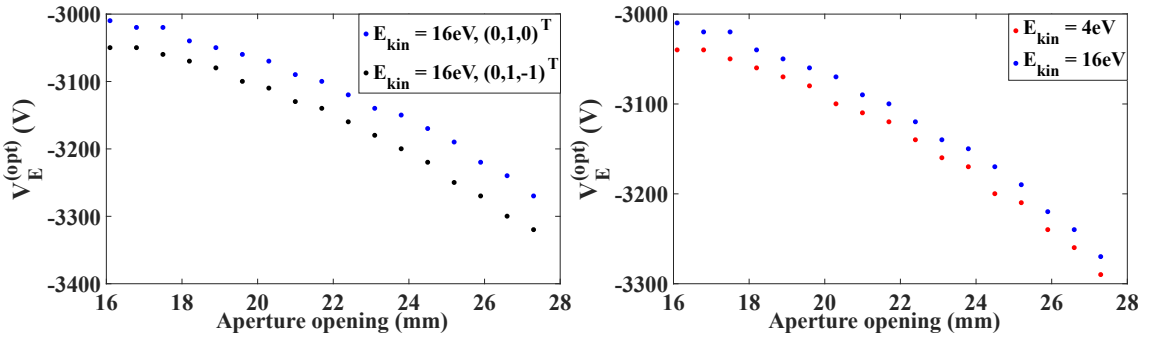

(c) Spherical distortions (d) Chromatic distortions

Figure 5.6: Geometry optimization. For different aperture openings of the Repeller and Extractor plates the quality parameter from Eq. (5.6) was calculated. (a), (b) The initial electron energy was set to 36 eV and the initial velocity points along the y-direction. (c), (d) imaging errors

chromatic distortions, respectively. It seems that the spherical distortions increase while the chromatic distortions improve while raising the opening diameter of the aperture. Another aspect, which should also be taken into account is the maximum detectable energy. A small opening diameter only leads to the detection of low energy particles since high energy particles cannot pass the Extractor opening. Therefore, the aperture opening should be defined by the maximum detectable energy, which is on the order of 60 eV (will be explained in the last part of section 5.3).

Variation of the electrode thickness

In a fifth iteration, the thickness of both the Extractor and Ground electrode was varied for electrons with an initial energy of 16 eV starting in the y-direction (Figs. 5.7a and 5.7b).

The minimum quality parameter for a certain configuration is monotonously increasing with the electrostatic electrode thickness. Thick electrodes distort the smooth curvature transition between between different areas resulting in a worse velocity-map performance. Another look at the chromatic and spherical distortions supports this observation (Figs. 5.7c and 5.7d). The difference of optimum Extractor voltages V_{E} of particles with initially different velocity angles but same energies and vice versa are getting bigger resulting in more distortions of the electron imaging apparatus.

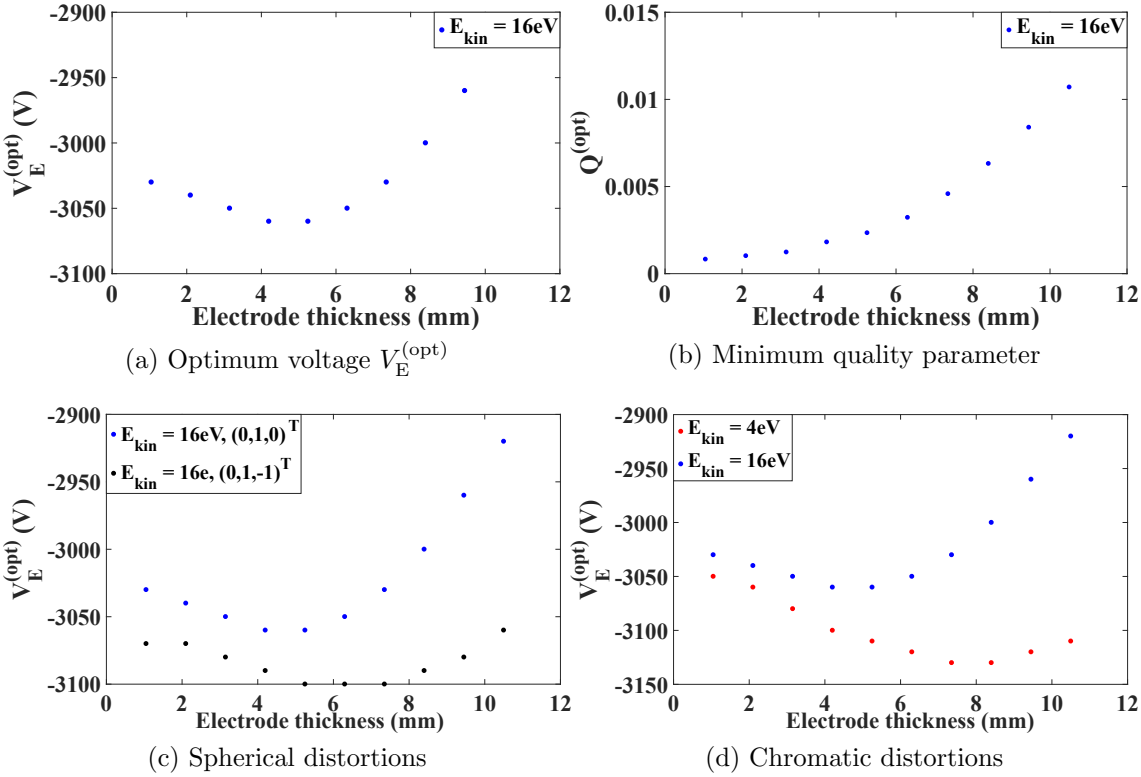

(a) Optimum voltage $V_{\mathrm{E}}^{(\mathrm{opt})}$

(b) Minimum quality parameter

(c) Spherical distortions

(d) Chromatic distortions

Figure 5.7: Geometry optimization. For different Extractor and Ground plate thicknesses the quality parameter from Eq. (5.6) was calculated. (a), (b) The initial electron energy was set to 16 eV and the initial velocity points along the y-direction. (c), (d) imaging errors

In practice, the electrodes cannot be machined infinitely thin. The thinner they are the more mechanical instabilities arise. It turns out that it is difficult to ensure flatness and parallelism for very thin electrodes. Therefore, the minimum achievable thickness by our on-site campus workshop was 2 mm.

5.3 Imaging spectrometer setup

After the optimization process the VMIS was constructed and implemented (Fig. 5.8). The design of the VMIS is very similar to the orginal VMIS (Fig. 5.2) and mainly the shape and the relative distance of the electrodes was adapted (see section 5.2). The edges of the Repeller and Extractor electrodes are conical to allow for efficient THz incoupling. A flight tube of length $L = 110$ mm is stacked on top of the electrostatic electrodes. At the end of the flight tube, the charged particles are amplified by a dual micro-channel-plate (MCP) with a diameter of $d = 40$ mm before they hit a $P47$-phosphor screen, which exhibits a broad emission spectrum with a maximum at approximately 430 nm [132]. The $P47$ phosphor was chosen since the emission decay time is on the order of 100 ns. Therefore, this detector can be used for singe-shot detection because the pulse-to-pulse distance is 1 ms for the 1 kHz laser. The insulating spacers between the electrodes were made out of the organic thermoplastic material **p**oly**e**ther **e**ther **k**etone (PEEK). The overall axial detector extension is 220 mm.

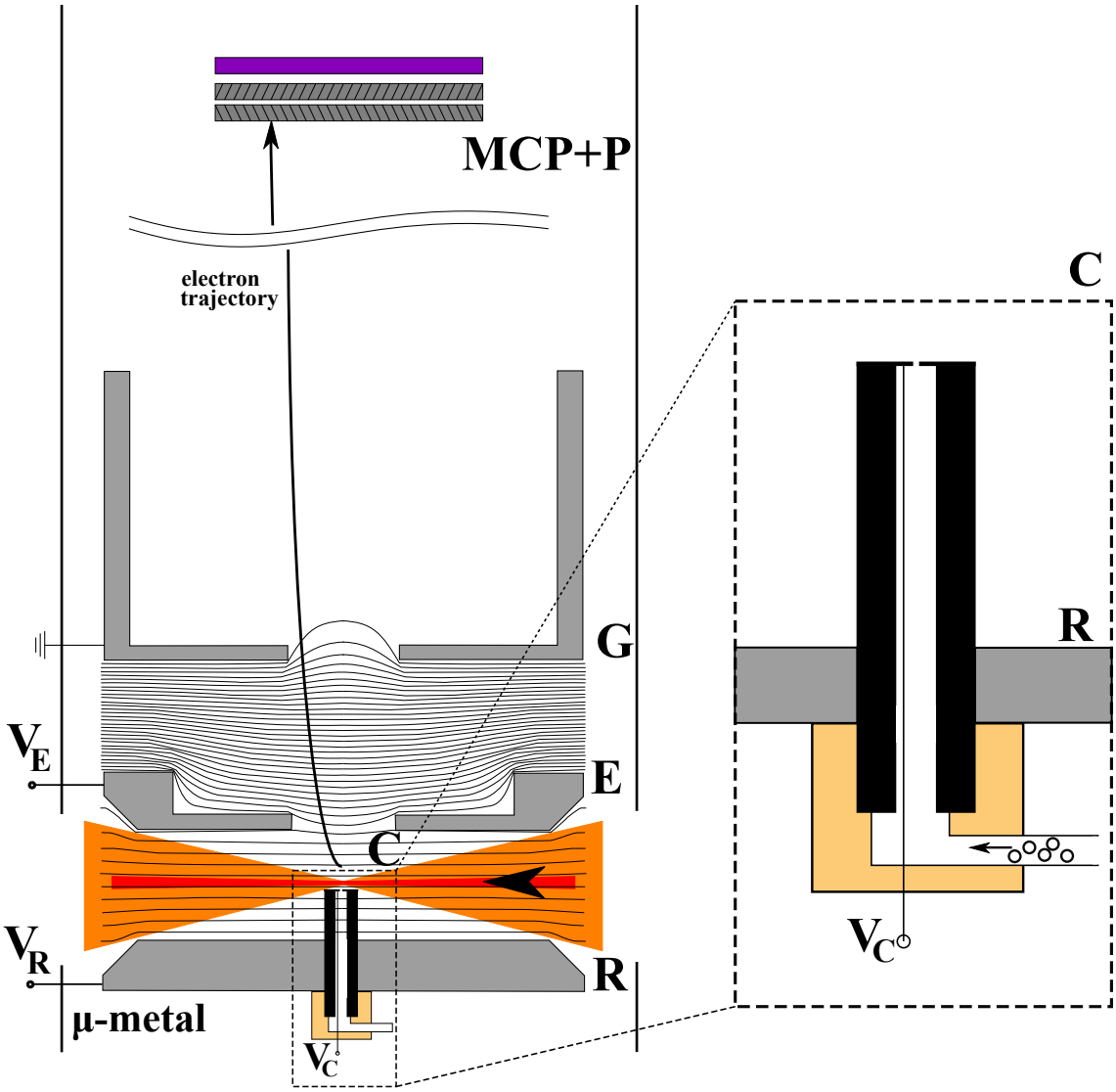

Figure 5.8: Sketch of the final electrode arrangement. The alignment of the static electrodes is quite similar to the initial case (Fig. 5.2) and mainly the shape and relative distances changed. The capillary gas injector **C** is integrated into the Repeller electrode and a voltage V_C is supplied to its exit. The intense NIR (red) is superimposed with the THz (orange) radiation. For visibility reasons, the equipotential surfaces are drawn with black lines. A zoom-in of the capillary gas injector is shown on the right. A PEEK holder (beige) is mounted at the bottom to connect the Repeller electrode and the capillary tube. A Pt aperture with a 50 μm hole is glued on top of the capillary tube. On the lower surface of the aperture, a thin Kapton insulated Cu wire is attached to supply the capillary voltage V_C.

A novel feature of the newly developed and constructed VMIS is a Repeller integrated capillary gas injector. The idea of this capillary is to directly supply a sufficient amount of target gas to the interaction volume without perturbing the electric potential surfaces. The gas capillary is integrated in the Repeller electrode, similar to the one from another research group in which the capillary tube is incorporated into the Repeller electrode [32]. The main difference is that we are using a

semiconductor lead glass tube (Photonis Inc.), which replicates the electric equipotential surfaces (Fig. 5.8, zoom-in on the right)[1]. The semiconductor tube has an inside and an outside diameter of 1 mm and 3 mm, respectively. Its resistance is assumed to be linear and a value of 11 MΩ was measured betweenV_C and V_R. In an ideal VMIS, i.e. without a capillary, the voltage as a function of the distance with respect to the Repeller surface on the TOF axis also shows a linear behavior (Fig. 5.9a). This is exactly the reason why a capillary inlet tube with a constant resistance R_C can be implemented to supply the target gas into the interaction volume without disturbing the potential surface. The thickness of the capillary inlet tube should be as small as possible because any off-axis distortions of the equipotential surface should be avoided. The actual thickness of 3 mm is a compromise to ensure good mounting of the tube with the Pt aperture and Cu wires. In order to match the correct capillary voltage V_C with the environment, a variable voltage divider is applied (Fig. 5.9b). By tuning the resistance R_{box}, the correct capillary voltage is applied in the presence of the Repeller V_R and Extractor electrodes.

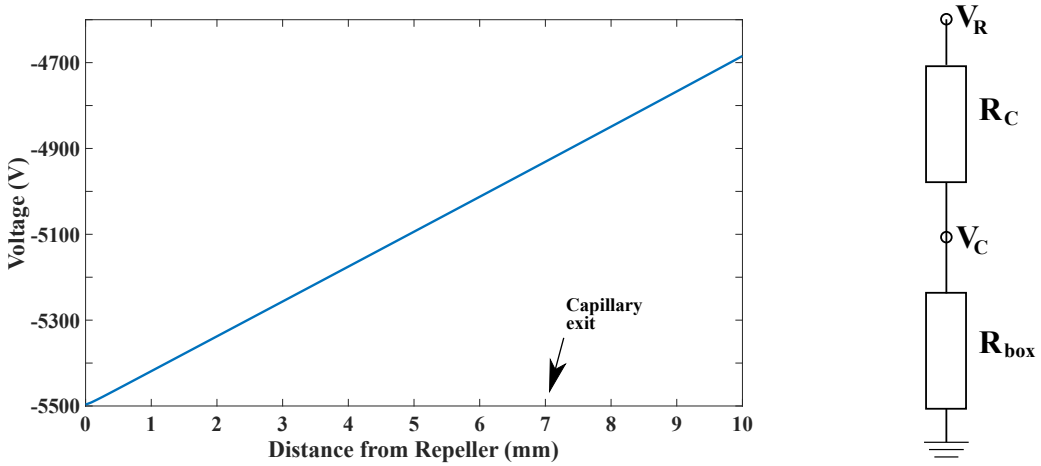

(a) Axial potential curve (b) Voltage divider

Figure 5.9: Characteristics of a the capillary tube assuming a constant resistance R_C. The distance between capillary exit and Repeller surface is 7 mm. (a) Axial potential curve (i.e. on TOF axis). (b) Depiction of a voltage divider to apply the correct potential V_C to the capillary exit. For this purpose, a variable resistance V_{box} was used.

On top of the capillary, a 100 μm thin Pt aperture with a diameter of 3 mm and a hole of 50 μm is glued to emit a well-defined effusive gas flow in the middle between the Repeller and Extractor electrodes. An appropriate potential V_C is supplied by two thin Kapton insulated Cu wires, which are glued on the inside of the capillary tube to preserve the electrostatic field generated by the electrodes. The capillary tube is supported by a PEEK mount at the bottom of the Repeller to combine target gas supply and electrical contacting. Note that during the assembly it was very crucial to contact the Pt aperture within a circle of diameter 1 mm but not exactly in the center since the target gas has to be released through the aperture hole. The

[1]inspired by Prof. M. Drescher

	Basler camera	Optronis camera
Specification	acA1920 − 40um	CL600 − 2
Sensor type	CMOS	CMOS
Resolution (pixel^2)	1920×1200	1280×1024
Pixel Size (μm^2)	5.86×5.86	14×14
Chip size (mm^2)	11.25×7.03	17.92×14.34
Color depth	8 bit grayscale	8 bit grayscale
Maximum frame rate (frames/s)	31	500*
Object distance (mm)	167	116**
Image distance (mm)	29	32**

Table 5.1: Summary of the imaging camera characteristics. The values were taken from the respective websites [133, 134]. The object and image distances were calculated for an objective with $f = 25\,\text{mm}$. *Maximum fram rate is 1000 for an image with $784 \times 784\,\text{pixel}^2$ **For a camera operation in the single-shot mode, i.e. a chip size of $784 \times 784\,\text{pixel}^2$.

high target gas pressure ensures adequate count rates since the number of photons generated with HHG is many orders lower than the number of NIR photons per laser shot. The maximum applied pressure is then only limited by the pressure sensitive MCP device, which operates well below $10^{-5}\,\text{mbar}$. Most of the experiments were carried out using the noble gas Xe. Since the target gas and the wires, that contact the aperture, are very close to each other in the capillary tube, a discharge at a breakdown voltage of approximately $-7.0\,\text{kV}$ is observed and thus limiting the voltage applied to the Repeller electrode. Consequently, the maximum energy of electrons that can be detected is on the order of 60 eV.
The whole imaging spectrometer is wrapped up in 0.25 mm thick μ-metal in order to shield the electron trajectories from external magnetic fields (e.g. earth magnetic field).

5.4 Electron imaging and data acquisition

A single electron, that hits the detector, is amplified by an MCP and visualized on a phosphor screen. The whole phosphor screen is imaged with a $f = 25\,\text{mm}$ Navitar objective on a chip of a Basler or Optronis camera (Tab. 5.1). Due to its MCP amplification process, an electron event extends over several pixels on the camera chip and forms a cluster.
The experimental images, that are acquired with the Basler camera, are processed with a home-built Labview routine (Fig. 5.10). With this camera it is not possible to capture single-shot images, since the maximum frame rate of the camera (31 frames/s) is almost two orders of magnitude lower than the laser repetition rate of $f_{\text{rep}} = 1\,\text{kHz}$. To obtain good statistics, image averaging was applied. The detection of weak signals requires a thresholding. In this operation mode, a threshold value is defined and all pixels below this value are set to 0 and thus noise is reduced.

If the exposure time of the Basler camera is considerably longer than $1/f_{\mathrm{rep}}$, then the camera can be used with an internal trigger.

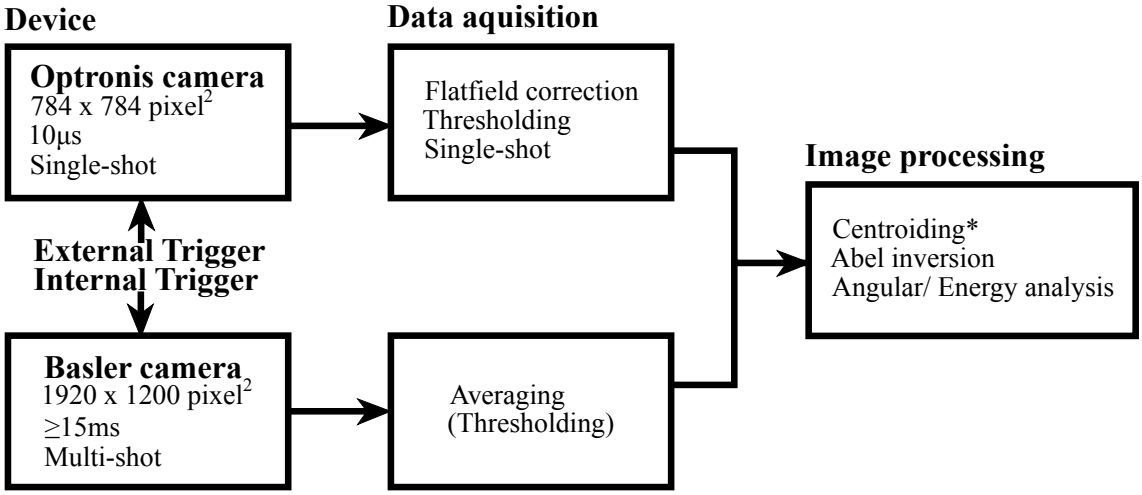

Figure 5.10: Flow Chart for the measurement of a photoelectron spectrum. *Centroiding was only applied to images obtained with the Optronis camera.

On the other hand, the Optronis camera can be used for continuous single-shot data acquisition with an external trigger. The camera development and implementation to measure the CEP-dependence of electrons emitted in the presence of an intense near single-cycle NIR laser from above-threshold-ionization in Xe was already performed by another group [135]. Note that the maximum frame rate is a function of the frame format. By reducing the number of pixels to 784×784 the Optronis camera can continuously acquire images with a maximum frame rate of 1 kHz. The camera can be operated with the commercial Marathon Pro software (GS Vitec). When using the single-shot acquisition mode, the camera is synchronized with the laser. During data acquisition a lot of hardware storage is required. Therefore, an efficient way to store experimental data is to use the camera operation in the threshold mode. For each individual shot the camera is then capable to store a fixed number of N pixels. This number can be chosen before the data acquisition and is limited to $N_{\mathrm{max}} = 1500$. Each pixel is represented by its x and y position as well as its intensity value $P_{x,y}$. All values are integer numbers and allocated with $S_1 = 2\mathrm{B}$ (B: Byte) thus leading to a maximum required storage of

$$S_{\mathrm{max}} = 3 \times S_1 \times N_{\mathrm{max}} = 9000\,\mathrm{B} \tag{5.8}$$

for each individual image. Considering a laser repetition rate of $f_{\mathrm{rep}} = 1\,\mathrm{kHz}$, a typical measurement of 10 min requires up to 5.4 GB and is stored as a binary file on an external hard drive. This results in an efficient way to store a huge amount of experimental data in a continuous mode. Additionally, a flat-field correction for each image is applied to remove artefacts from the image. This procedure should guarantee a homogeneous background signal on the CMOS chip. As an example an image is shown for a chip size of 6×6 (Fig. 5.11a). All sites can take a value

between 0 and 255. The value of the black sites is 0 while non-vanishing values of sites are labeld in blue. The application of a threshold value (in this case 60) sets all sites below this value to 0 (Fig. 5.11b). In a following step, a centroiding algorithm is applied to the acquired data with a home-built C++ code. The main idea of this procedure is to identify the electron events, i.e. connected sites (labeled in red with the same index), and calculate their sizes as well as their center-of-mass coordinates. The most time-consuming part is the identification of individual clusters, which was realized using a Hoshen-Kopelman (HK)-algorithm [136]. To improve the image quality, the center-of-mass coordinates for each individual clusters can be accumulated and plotted instead of the full acquired data from the Optronis camera. The performance of the C++ code was later enhanced by Malte Sumfleth. Experimentally, it turned out that even in thermal equilibrium the Optronis camera has a reasonable number of hot pixels. These are pixels that significantly exceed the average value of surrounding pixels. Consequently, these artifacts have to be removed before applying the HK-algorithm.
Further analysis and image visualization was performed with several sophisticated Matlab routines and a graphical user interface. Since the photoelectron images are a result of the Abel projection, an Abel inversion has to be applied to the acquired images before analyzing the angular and energy spectrum. The different Abel inversion algorithms will be discussed in the next section.

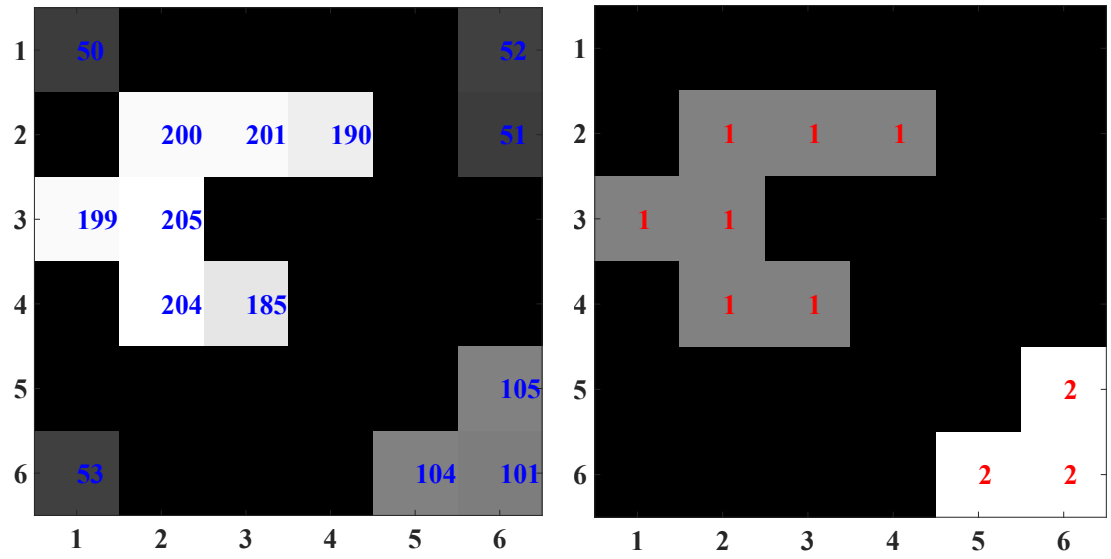

(a) Raw image (b) Cluster identification

Figure 5.11: Example image of size 6×6 pixel^2. Each pixel can take a value between between 0 and 255. (a) Raw image, each site is labeled according to its pixel value (blue), empty sites are black. (b) Cluster identification, sites with pixel values below a threshold of 60 are removed and connected clusters are labeled with the same index (red).

5.5 Reconstruction methods

5.5.1 Basic principles of reconstruction approaches

Generally speaking, in an electron-imaging experiment the 3 dimensional (3d) distribution of charged particles is projected onto a 2 dimensional (2d) image along the TOF axis. The goal is now to reconstruct the initial 3d ion distribution from the measured 2d projection. A general overview of reconstructions methods can be found in the book of Benjamin Whitaker [126]. The following descriptions are based on this book. Note that there is also an approach, which uses the maximum entropy for reconstruction rather than an Abel inversion [137].
In contrast to forward convolution methods, inversion methods assume that an axis of cylindrical symmetry exists, which is parallel to the projected 2d image plane. For linearly polarized light this axis is associated with the polarization axis of the incoming light (Fig. 5.1).
In Cartesian coordinates, the relation between the initial 3d ion distribution $g(x, y, z)$ and the 2d projection $f(x, y)$ is given by

$$f(x,y) = \int_{-\infty}^{\infty} g(x,y,z)dz. \tag{5.9}$$

For one line in the image plane at $y = y_0$, the projection reads

$$f(x,y_0) = \int_{-\infty}^{\infty} g(x,y_0,z)dz. \tag{5.10}$$

Assuming a cylindrical symmetry around the y-axis and performing a coordinate transform into polar coordinates ($r^2 = x^2 + z^2$), the projection and its inverse yield

$$f(x,y_0) = 2\int_{|x|}^{\infty} \frac{g(r,y_0)r}{\sqrt{r^2-x^2}}dr \qquad \text{(Abel projection)} \tag{5.11}$$

$$g(r,y_0) = \frac{1}{\pi}\int_{r}^{\infty} \frac{df/dx}{\sqrt{x^2-r^2}}dx \qquad \text{(Abel inversion).} \tag{5.12}$$

A direct integration of Eq. (5.12) is difficult since the denominator vanishes at $r^2 = x^2$ and noisy images will cause differentiation problems of the function $f(x, y_0)$. An elegant way to analytically solve this problem is to apply a Fourier transform [138]. In this case, the inversion is given by

$$g(r,y_0) = 2\pi \int_{0}^{\infty} qJ_0(2\pi rq) \int_{-\infty}^{\infty} f(x,y_0)\exp(-2\pi xqi)dxdq, \tag{5.13}$$

where the variable J_0 denotes the zero-order Bessel function. Using this approach, the overall Abel inversion will give less noise over the input image. However, the noise in the center cannot completely be suppressed since the Bessel function J_0 itself rapidly changes at the origin. Therefore, several other iterative approaches exist to perform the Abel inversion. A few of them will be discussed in the following section.

5.5.2 Abel inversion using a Legendre expansion

This Abel inversion uses the fact that the angular part of a 3d momentum distribution P_{3d} can be expressed as a superposition of Legendre polynomials $P_l(\cos\vartheta_{3d})$. The first terms are explicitely given in the appendix (see section A.1). The inversion procedure was implemented by M.J.J. Vrakking in an unpublished work [139] and is a further development of his powerful iterative method [140]. In the following description the notation of the Vrakking's unpublished work is used. The initial distribution P_{3d} can be expressed as a superposition of Legendre polynomials:

$$P_{3d}(v_{3d},\vartheta_{3d},\varphi_{3d}) = \sum_{l=0}^{l_{\max}} a_{v_{3d},l} P_l(\cos\vartheta_{3d}), \tag{5.14}$$

where the variables $\vartheta_{3d} \in [0,\pi)$ and $\varphi_{3d} \in [0,2\pi)$ denote the angular coordinates with respect to the symmetry axis and $l_{\max}$ being the finite number of Legendre polynomials, which are sufficient to describe the physical process. The speed v_{3d} is proportional to the radial expansion of the electron cloud. The momentum distribution from Eq. (5.14) can also be expressed as

$$P_{3d}(v_{3d},\cos\vartheta_{3d}) = 2\pi v_{3d}^2 \sum_{l=0}^{l_{\max}} a_{v_{3d},l} P_l(\cos\vartheta_{3d}), \tag{5.15}$$

which is a direct consequence of the cylindrical symmetry around the y-axis (i.e. no φ_{3d} dependency). Similarly, the projected 2d momentum distribution P_{2d} as a function of the radial v_{2d} and angular $\vartheta_{2d} \in [0,2\pi)$ coordinates yields

$$P_{2d}(v_{2d},\vartheta_{2d}) = \sum_{l=0}^{l_{\max}} b_{v_{2d},l} P_l(\cos\vartheta_{3d}). \tag{5.16}$$

The comparison of Eqs. (5.15) and (5.16) suggests that the coefficients $a_{v_{3d},l}$ and $b_{v_{2d},l}$ in the summation are entries of the vectors $\vec{a}$ and $\vec{b}$, respectively, and are linked with each other via a matrix $\hat{M}$

$$\vec{b} = \hat{M}\vec{a} \qquad \Rightarrow \qquad \vec{a} = \hat{M}^{-1}\vec{b}. \tag{5.17}$$

Note that the matrix $\hat{M}$ and its inverse are independent of the experimental images, hence the matrix can be separately calculated in advance and used for arbitrary Abel inversions (provided that the experimental detection does not change). The

dimension of matrix $\hat{M}$ is only a function of the detector dimensions and the number of Legendre polynomials. The most time-consuming computational part is the construction of $\hat{M}$. Since the matrix is independent of the initial momentum distribution, an arbitrary distribution can be projected to derive the entries of $\hat{M}$. Once the matrix is known, the angular distribution for each individual v_{2d} of the experimental projection can be fitted with a set of Legendre polynomials, and by multiplication with the inverse matrix, the initial 3d distribution can be obtained.

5.5.3 Abel inversion by using a polar basis function expansion

Another Abel inversion utilizes a polar basis function expansion (pBASEX). This method [141] mainly differs from a previously developed inversion procedure [142] by the choice of the coordinate system. By using polar instead of Cartesian coordinates, it is shown that the inversion quality is improved since the noise is accumulated at a central spot rather than at a central line. In this case, the experimental image is represented as a superposition of basis functions, which are well-behaved projections of Gaussian functions. The following mathematical descriptions is based on [141]. The relation between a projected distribution $P(R', \vartheta')$ and an initial distribution $F(R, \vartheta)$ can be described by Eq. (5.11) via

$$P(R', \vartheta') = 2 \int_{|x|}^{\infty} \frac{F(R, \vartheta) r}{\sqrt{r^2 - x^2}} dr, \tag{5.18}$$

where the angle ϑ is defined with respect to the symmetry axis and the coordinates x and r are calculated with $x = R' \sin \vartheta'$ and $r = R \sin \vartheta$, respectively. The original Newton sphere $F(R, \vartheta)$ can be expressed as a superposition of Gaussian functions $f_{kl}(R, \vartheta)$

$$\begin{aligned} F(R, \vartheta) &= \sum_{k=0}^{k_{\max}} \sum_{l=0}^{l_{\max}} c_{kl} f_{kl}(R, \vartheta) \\ f_{kl}(R, \vartheta) &= \exp\left[-\frac{(R - R_k)^2}{\sigma} \right] P_l(\cos \vartheta) \end{aligned} \tag{5.19}$$

For linear polarized light only even Legendre polynomials P_l have to be taken into account and the maximum number $l_{\max}$ is equal to twice the number of absorbed photons [143]. The variable $k_{\max}$ denotes the number of the Gaussian basis set functions. Combining Eqs. (5.18) and (5.19) yields

$$\begin{aligned} P(R', \vartheta') &= \sum_{k=0}^{k_{\max}} \sum_{l=0}^{l_{\max}} c_{kl} g_{kl}(R', \vartheta'), \\ g_{kl}(R', \vartheta') &= 2 \int_{|x|}^{\infty} \frac{r f_{kl}(R, \vartheta)}{\sqrt{r^2 - x^2}} dr. \end{aligned} \tag{5.20}$$

By comparing the experimental image with Eq. (5.20) the coefficients c_{kl} can be numerically extracted by using singular value decomposition to obtain the initial distribution $F(R, \vartheta)$ in Eq. (5.18).

5.5.4 Abel inversion by using polar onion-peeling

An additional approach to solve the Abel inversion is the so-called polar onion-peeling (POP). It is based on the onion-peeling method [144], which was first numerically implemented for velocity-map imaging experiments by Manzhos and Loock [145]. Since onion-peeling is described in Cartesian coordinates, it suffers from centerline noise, which can be drastically reduced when going to polar coordinates [146]. POP was later combined and coded with concepts from pBASEX to achieve high computational speed [147]. The general idea of onion-peeling [126, 144] will be explained in the following . Here, a photoelectron with a kinetic energy $W_0 = mv_0^2/2$, initial speed v_0, charge q and mass m in the presence of a homogeneous electric field F, which is parallel to the projection y-coordinate. The initial velocity coordinates are formulated by

$$\begin{aligned} v_{0x} &= v_0 \sin\Theta \cos\varphi, \\ v_{0y} &= v_0 \sin\Theta \sin\varphi, \\ v_{0z} &= v_0 \cos\Theta, \end{aligned} \tag{5.21}$$

where the colatitude Θ and the azimuthal angle φ are used. The axis of symmetry coincides with the z-axis and the image plane is perpendicular to the y-axis and of distance L away from origin of the released electrons. Utilizing Newton's laws of motion and Eq. (5.21), the respective coordinates on the detector can be derived as

$$\begin{aligned} X &= \frac{2L\cos\varphi\sin\Theta}{\rho} \times \left(\sqrt{\sin^2\varphi\sin^2\Theta + \rho} - \sin\varphi\sin\Theta\right), \\ Z &= \frac{2L\cos\Theta}{\rho} \times \left(\sqrt{\sin^2\varphi\sin^2\Theta + \rho} - \sin\varphi\sin\Theta\right), \\ \rho &= \frac{qFL}{W_0}. \end{aligned} \tag{5.22}$$

In an electron imaging experiment the acceleration field is usually many orders of magnitude higher than the initial charged particle energy W_0 and consequently $\rho \to \infty$ and Eq. (5.22) can be reduced to

$$\begin{aligned} X &= \frac{2L\cos\varphi\sin\Theta}{\sqrt{\rho}} \\ Z &= \frac{2L\cos\Theta}{\sqrt{\rho}}. \end{aligned} \tag{5.23}$$

It is obvious that by inverting Eq. (5.23) the colatitude Θ only depends on the coordinate Z and for a given pair of Z and ρ, the azimuthal angle φ is uniquely determined by X. Assuming now a physical process with many electron channels the projection on the detector will also have several electron contributions. Therefore, in this method the electron contribution with the highest energy is removed from the experimental image and it is proceeded with the next highest energy part until the center of the image is reached. This is why this method is called onion-peeling.

5.5.5 Comparison of Abel inversion approaches

In this section the Abel inversion approaches based on pBASEX, POP and the Vrakking procedure will be compared with each other. All Abel inversion methods

are integrated into a Matlab graphical user interface, which can also analyze the radial and angular inversion results. The Matlab implementations of POP [148] and pBASEX [149] are open source solutions. However, the source code for the Vrakking inversion procedure is unpublished [139]. All numerical approaches operate on a 8 GB computer memory desktop and are limited by its maximum number of Legendre polynomials $l_{\max}$ that are used for the Abel inversion. For pBASEX and the Vrakking approach the value $l_{\max}$ is relatively small (8 and 16, respectively), while for the POP algorithm even more than 42 Legendre polynomials are considered. Note that in the following evaluations no attention will be paid to THz-induced streaking images. A detailed analysis of this can be found elsewhere [150].
Initially, a test function $g(x, y, z)$ is generated, which is a superposition of a one, two and three-photon ionization. Each individual photoionization can be described by an angular and a radial contribution. The angular part of N-photoionization can be calculated by a superposition of Legendre polynomials (see Eq. (2.31)). For the radial part a Gaussian function is assumed. The test function yields

$$g(x,y,z) = \sum_{i=1}^{3} \exp\left(-2\frac{(R-R_{0i})^2}{\Delta R_i^2}\right) \sum_{j=0}^{2N_i} \beta_{i,2j} P_{2j}(\cos\Theta), \tag{5.24}$$

where the angle Θ and the radius R are defined as

$$\cos\Theta = \sqrt{\frac{y^2}{x^2+y^2+z^2}} \qquad R = \sqrt{x^2+y^2+z^2}.$$

The angle Θ is defined with respect to the y-axis, i.e. the symmetry axis due to the linear polarization of the electric field. The coefficients of Eq. (5.24) are summarized in Tab. 5.2.

Ring	ΔR (pixel)	R_0 (pixel)	β_0	β_2	β_4	β_6
1	5.54	97.88	1	2	0	0
2	4.15	195.75	1	1	−0.5	0
3	2.77	293.63	1	2	−1	1

Table 5.2: Summary of the coefficients of a test function $g(x, y, z)$, which is described by Eq. (5.24).

First, the test function will be Abel projected according to Eq. (5.11) along the y-axis using the Riemann sum (Fig. 5.12). The test function is discretized on a grid of 784 pixels in each dimension to be as close as possible to the experimental results.
Second, the different Abel inversion algorithms are applied to the projected test function and an angular and radial analysis of the images was applied to retrieve the values $\tilde{R}_0$, $\Delta\tilde{R}$ and $\tilde{\beta}_2/\tilde{\beta}_0$, $\tilde{\beta}_4/\tilde{\beta}_0$, $\tilde{\beta}_6/\tilde{\beta}_0$. For the radial analysis an angular integration of 2π was carried out. Complementary to the angular analysis, an inversed photoionized cloud with a certain radius was selected and fitted with a set of even Legendre polynomials up to $P_6(\cos\Theta)$. The retrieved β-parameters are normalized to β_0. All calculated values are summarized in Tab. 5.3 and are subsequently

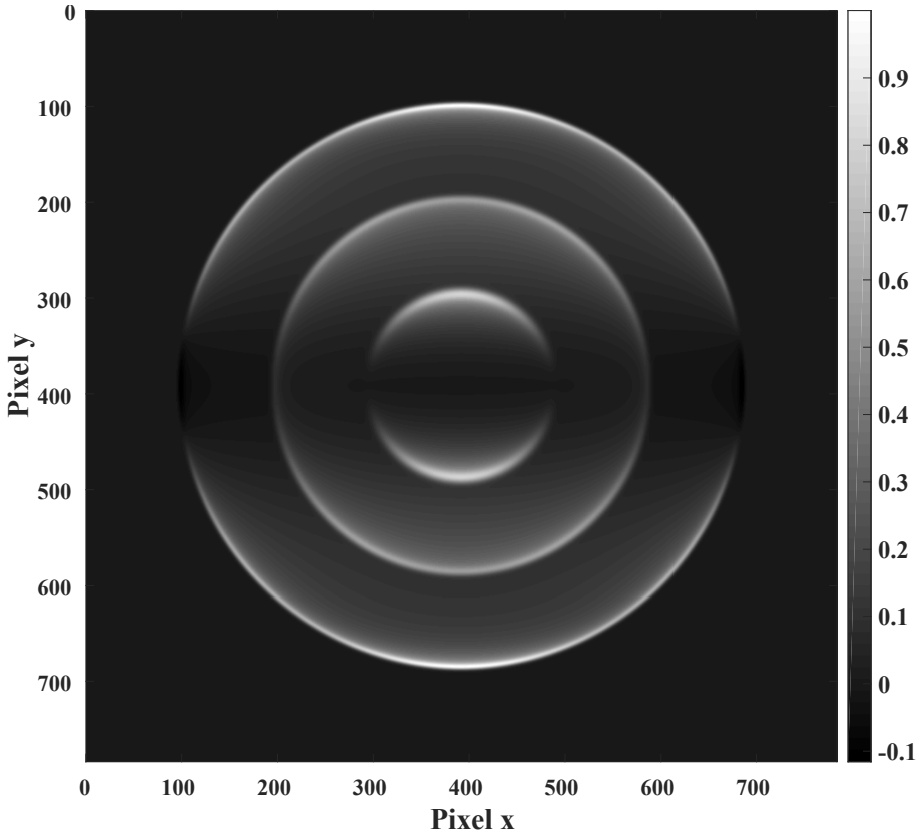

Figure 5.12: Abel projection of a test function $g(x, y, z)$, which is calculated by Eq. (5.24). The corresponding coefficients are summarized in Tab. 5.2. Each ring corresponds to a projection of a Newton sphere.

compared with the initial coefficients (Tab. 5.2). The error bars indicate the 95% confidence bounds. As will be shown elsewhere [150] THz-streaked images should be analyzed with a modified POP inversion algorithm.
All inversion algorithms estimate similar radial coefficients with only minor differences with respect to the initial values. The POP method gives the best results. The difference between the confidence bound and the simulated results is only very small. The pBASEX method gives slightly higher amplitudes and small modulations at the wings of the second and third peak (Fig. 5.13a).
In the case of the angular distribution, the pBASEX approach gives the best results. The initial simulation values are reproduced quite well. The β values of the Vrakking inversion and POP approaches of the three-photon absorption show some significant differences from the simulated values. However, small artefacts for the first and second ring appear for all inversion codes at 0° and 180° (Fig. 5.13b).

5.5.6 Performance of novel imaging detector

Previously, the VMIS with the integrated capillary gas injector as well as several Abel inversion algorithms have been introduced. Nevertheless, a rigorous comparison between the newly developed and a conventional VMIS is still missing. This important issue will be analyzed in detail in the following.
Using SIMION the geometry of the electron imaging detector can be modeled with-

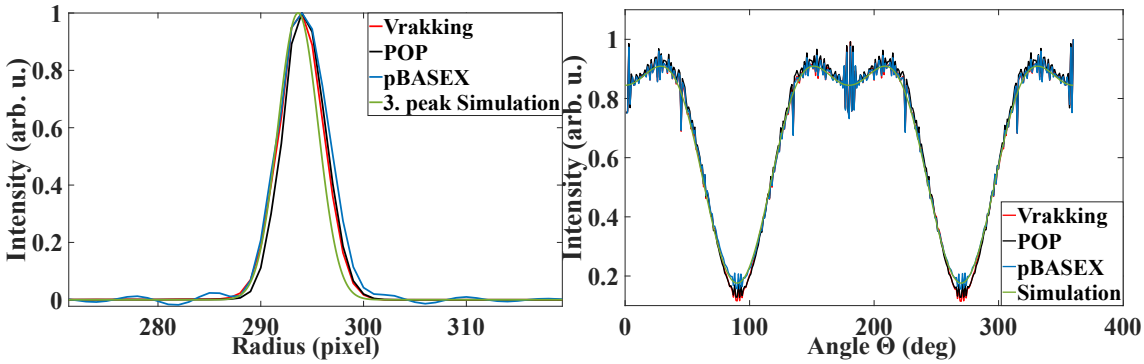

(a) Radial distribution (b) Angular distribution

Figure 5.13: A comparison of the different inversion methods (Vrakking, POP, pBASEX) with the simulated results. (a) Radial distribution of the reconstructed third ring. (b) Angular distribution of the reconstructed second ring.

POP:

Ring	$\Delta\tilde{R}$ (pixel)	$\tilde{R}_0$ (pixel)	$\tilde{\beta}_2/\tilde{\beta}_0$	$\tilde{\beta}_4/\tilde{\beta}_0$	$\tilde{\beta}_6/\tilde{\beta}_0$
1	5.45 ± 0.05	98.68 ± 0.03	2.04 ± 0.06	0.01 ± 0.00	-0.02 ± 0.00
2	4.09 ± 0.03	196.38 ± 0.01	1.06 ± 0.02	-0.57 ± 0.02	0.03 ± 0.01
3	2.88 ± 0.01	294.20 ± 0.01	1.69 ± 0.03	-0.73 ± 0.03	0.77 ± 0.03

pBASEX:

Ring	$\Delta\tilde{R}$ (pixel)	$\tilde{R}_0$ (pixel)	$\tilde{\beta}_2/\tilde{\beta}_0$	$\tilde{\beta}_4/\tilde{\beta}_0$	$\tilde{\beta}_6/\tilde{\beta}_0$
1	5.86 ± 0.09	98.59 ± 0.06	1.99 ± 0.06	-0.01 ± 0.00	0.00 ± 0.00
2	4.61 ± 0.05	196.30 ± 0.01	1.00 ± 0.02	-0.50 ± 0.02	0.00 ± 0.00
3	3.33 ± 0.02	294.10 ± 0.01	2.00 ± 0.03	-0.99 ± 0.03	0.99 ± 0.03

Vrakking:

Ring	$\Delta\tilde{R}$ (pixel)	$\tilde{R}_0$ (pixel)	$\tilde{\beta}_2/\tilde{\beta}_0$	$\tilde{\beta}_4/\tilde{\beta}_0$	$\tilde{\beta}_6/\tilde{\beta}_0$
1	5.64 ± 0.05	98.36 ± 0.03	2.01 ± 0.06	0.01 ± 0.00	0.00 ± 0.00
2	4.29 ± 0.03	196.10 ± 0.01	1.04 ± 0.02	-0.54 ± 0.02	0.02 ± 0.00
3	3.00 ± 0.01	293.90 ± 0.01	1.77 ± 0.03	-0.79 ± 0.03	0.85 ± 0.04

Table 5.3: Summary of the retrieved coefficients obtained from different Abel inversion approaches (POP, pBASEX, Vrakking). After each Abel inversion, the radial distribution of each ring was fitted with a Gaussian function and the angular distribution of each ring was fitted with a superposition of Legendre polynomials (see Eq. (5.24). The results were compared to the simulated input parameters.

out or with the capillary gas injection. The first case corresponds to the standard VMIS [27] whereas the latter one corresponds to the newly developed VMIS. Similarly to previous simulations, electrons were generated in the middle between Repeller and Extractor electrode within a line source, which has a spatial extension of 2 mm. For a realistic simulation several groups of electron trajectories were acquired

in the detector plane. Each group consists of 2×10^5 monochromatic electrons with energy E and isotropic angular distribution. After electron binning, the POP Abel inversion is applied to the simulated image to obtain a slice of the initial electron distribution of the corresponding VMIS geometry. Afterwards, a full 2π angular integration is carried out and the resulting energy spectra were fitted with a superposition of N Gaussian functions

$$y(r) = \sum_{j=1}^{N} A_j \exp\left[-\frac{r - B_j}{C_j}\right]^2, \tag{5.25}$$

with parameters A_j, B_j, C_j, whereas the energy resolution of each peak can be calculated using Eq. (5.4)

$$\frac{\Delta E}{E} = \sum_{j=1}^{N} \frac{4C_j\sqrt{\ln 2}}{B_j}. \tag{5.26}$$

Assuming the geometry of a standard VMIS, groups of electrons with initial energies $[5, 10, \ldots 40]$ eV for a fixed Repeller voltage of $V_\mathrm{R} = -5500V$ were simulated (Fig. 5.14).
To find the optimum energy resolution the Extractor voltage V_E is varied. For each run an Abel projection was measured. By applying an Abel inversion, the radial distribution of the electrons can be obtained (Figs. 5.14a and 5.14a), respectively. It can be seen that the best resolution for any initial energy is below 0.02, which is in good agreement with the literature [32]. Only for 5 eV and 10 eV the energy resolutions were around 0.03 and 0.024, respectively. The higher the initial kinetic energy the smaller is the corresponding absolute value of the Extractor voltage. This effect is known as chromatic distortion and it leads to a compromise of the chosen Extractor voltage (Fig. 5.14c).

In contrast to a standard VMIS, the capillary voltage V_C of the novel imaging detector is another degree of freedom. For a realistic simulation the capillary tube was discretized with 19 pieces. Since the voltage between the capillary exit and the Repeller electrode drops linearly, the corresponding voltage for each discretized piece can be calculated according to its position. Similar to the previous simulations, the Repeller voltage was fixed at $V_\mathrm{R} = -5500V$ and electrons with an initial energy of $[5, 15, 25]$ eV and an isotropic angular distribution were defined. The electrons were spatially defined within a line source of 2 mm length. The Extractor voltage V_E was varied in the range of $[-4250, -4200, -4150, -4100]V$ and the capillary voltage V_C was changed in the range of $[-4970, -4968, \ldots, -4850]V$. Each run was simulated with 2×10^5 monochromatic electrons and Abel inverted before the energy spectrum was obtained (Fig. 5.15). Due to the simulations, energy resolutions slightly above 0.02 for the different initial energies can be achieved. Only the energy resolution for an initial energy of 5 eV is on the order of 0.04. Therefore, the energy resolution is a bit worse than in the case without capillary tube. Interestingly, the VMIS can compensate for a detuned Extractor voltage. For example, from the case without capillary tube it is expected the the optimum Extractor voltage is at $V_\mathrm{E}^{(\mathrm{opt})} = -4180$ V for an initial energy of $5eV$ (Fig. 5.14c). The simulations with capillary tube show that the optimum Extractor voltages can be achieved with any voltage between -4250 V and -4100 V by adjusting the capillary voltage (Fig. 5.15).

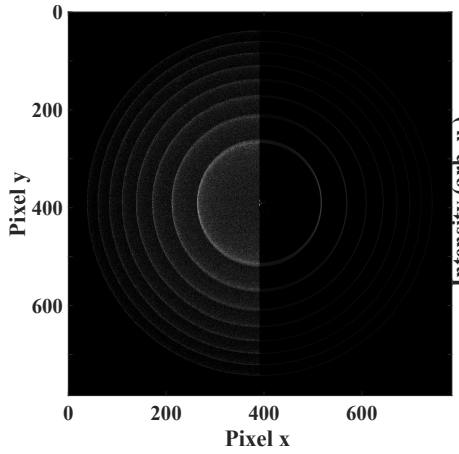

(a) $V_{\mathrm{E}} = -4120V$

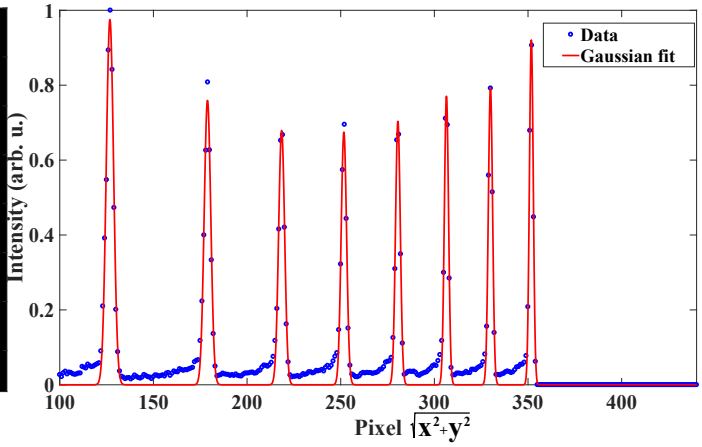

(b) $V_{\mathrm{E}} = -4120V$

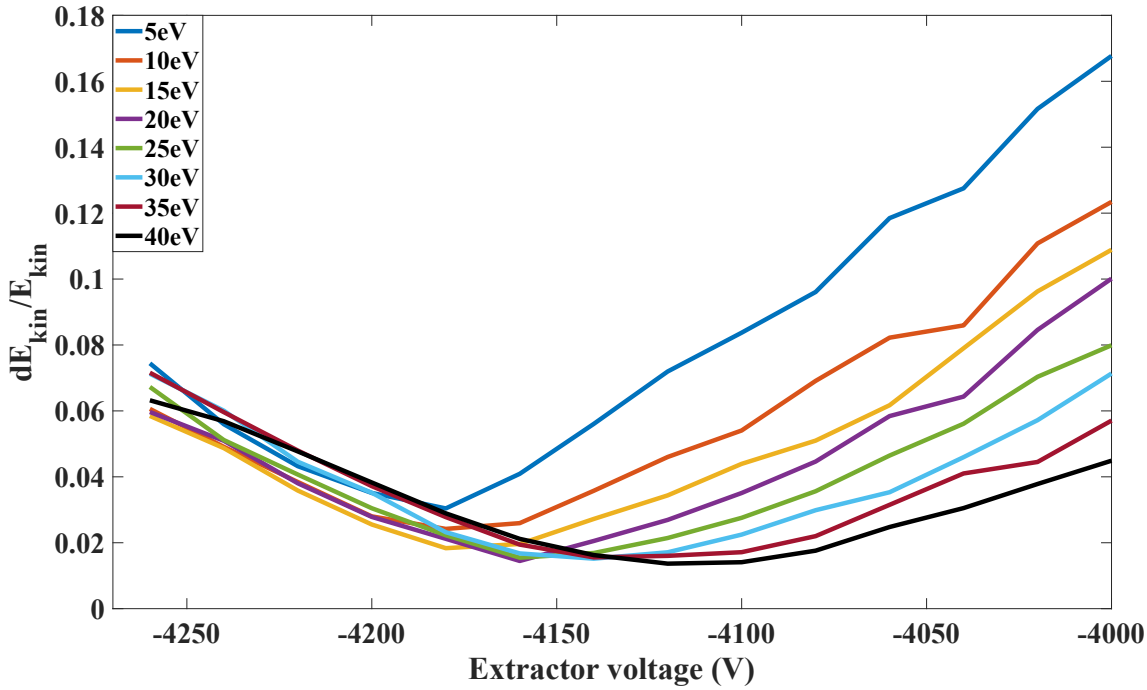

(c) Chromatic distortions

Figure 5.14: Simulations for a standard VMIS. For a fixed Repeller voltage of $V_{\mathrm{R}} = -5500V$ the Extractor voltage V_{E} was varied to obtain the best energy resolution of the imaging device. (a) Abel projection (left), Abel inversion (right), (b) Radial spectrum, (c) Energy resolution

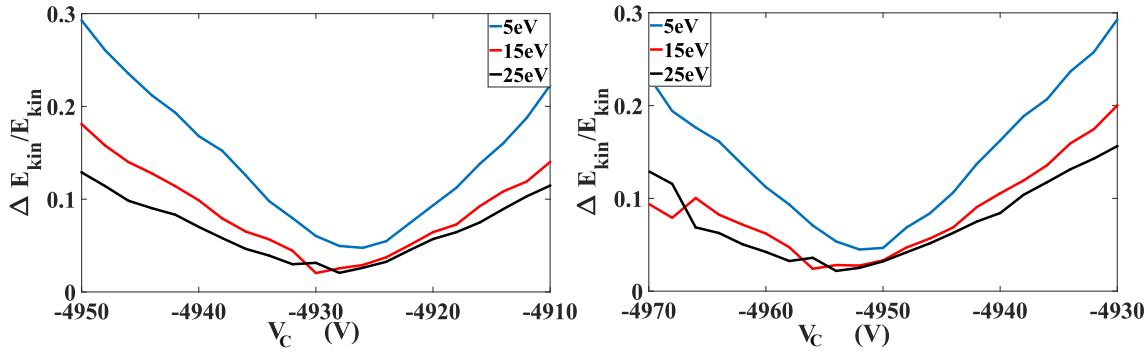

(a) $V_{\mathrm{E}} = -4250\,\mathrm{V}$

(b) $V_{\mathrm{E}} = -4200\,\mathrm{V}$

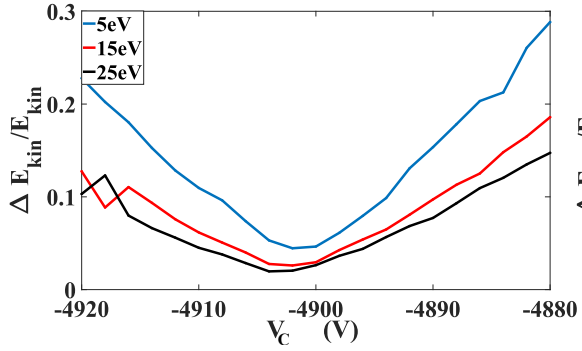

(c) $V_{\mathrm{E}} = -4150\,\mathrm{V}$

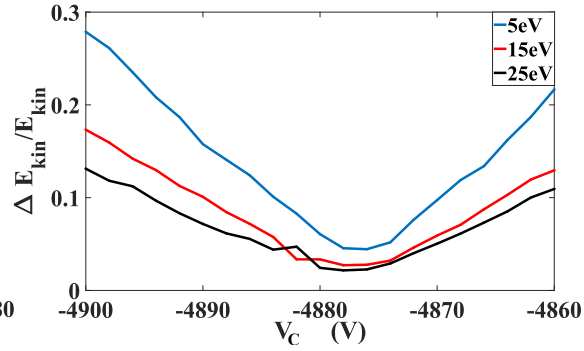

(d) $V_{\mathrm{E}} = -4100\,\mathrm{V}$

Figure 5.15: Energy resolution as a function of the applied capillary voltage V_{C}. Each curve was obtained was obtained for a fixed initial energy (see legend) and fixed Extractor voltage V_{E} (see below graph). In all measurements the Repeller voltage fixed to $V_{\mathrm{R}} = -5500V$.

Chapter 6

Characterization of the velocity-map-imaging spectrometer

In the previous chapter the design and experimental implementation of a VMIS with a novel capillary gas inlet were extensively discussed and supported by computer simulations. Therefore, the focus of this chapter will be the performance of the VMIS under experimental conditions. The required photoelectrons, which are necessary for a spectrometer characterization, are either generated by multiple- or single-photon absorption. In both cases the noble gas Xe was used since it has a relatively low ionization potential and a high absorption cross section for photons with an energy of 80 eV. In the first case, the intense NIR laser was focused into a gas target and the simultaneous absorption of multiple photons leads to the ejection of ATI electrons. In the second case, high-energy photons were produced by focusing the intense NIR laser into a Ne target via HHG and used to directly ionize the target atoms provided that the photon energy exceeds the atomic binding energy.

6.1 General experimental conditions

The characterization of the photoelectrons with the VMIS was performed with the same experimental setup (Fig. 3.1) in the absence of THz radiation. A single-photon absorption in Xe was realized with HHG and then transported with two multilayer mirrors into the interaction volume (Fig. 6.1a). Residual copropagating NIR radiation was separated from the harmonic radiation with a hole mirror and a thin Zr-filter. The photon energy of $n\hbar\omega_L = 79.6\,\mathrm{eV}$ (corresponding to the 51. harmonic of the fundamental) exceeds the binding energies of the $4d$ orbitals, $E_{\mathrm{b},1} = 69.5\,\mathrm{eV}$ ($4\mathrm{d}_{3/2}$) and $E_{\mathrm{b},2} = 67.5\,\mathrm{eV}$ ($4\mathrm{d}_{5/2}$). The splitting of the $4d$ orbital comes from spin-orbit coupling (relativistic effect). The kinetic energy of the photoelectron can be calculated using Eq. (2.1) to give

$$\begin{aligned} E_{\mathrm{kin},1} &= n\hbar\omega_L - E_{\mathrm{b},1} = 10.1\,\mathrm{eV}, \\ E_{\mathrm{kin},2} &= n\hbar\omega_L - E_{\mathrm{b},2} = 12.1\,\mathrm{eV}. \end{aligned} \tag{6.1}$$

The photon energy $n\hbar\omega_L$ at around 80 eV was chosen because Xe exhibits a high photoionization cross section for the $4d$ orbital (Fig. 6.2a). The release of a $4d$ photoelectron leads to the emission of an $\mathrm{N}_{4,5}\mathrm{OO}$ Auger electron, which covers the range from 8 eV to 36 eV (Fig. 6.2b). Note that also $5p$ and $5s$ photoelectrons are generated and contribute to the energy spectrum. Due to their low photoionization cross sections, they only give a small signal.

For multiphoton absorption, the NIR radiation passes through the HHG chamber without any gas and the Zr-filter was removed from the beam path. The fundamental laser has a photon energy of $\hbar\omega_L = 1.56\,\mathrm{eV}$ and hence at least 8 photons have to be simultaneously absorbed (Fig. 6.1b) to exceed the ionization potential $E'_{\mathrm{b},2} =$

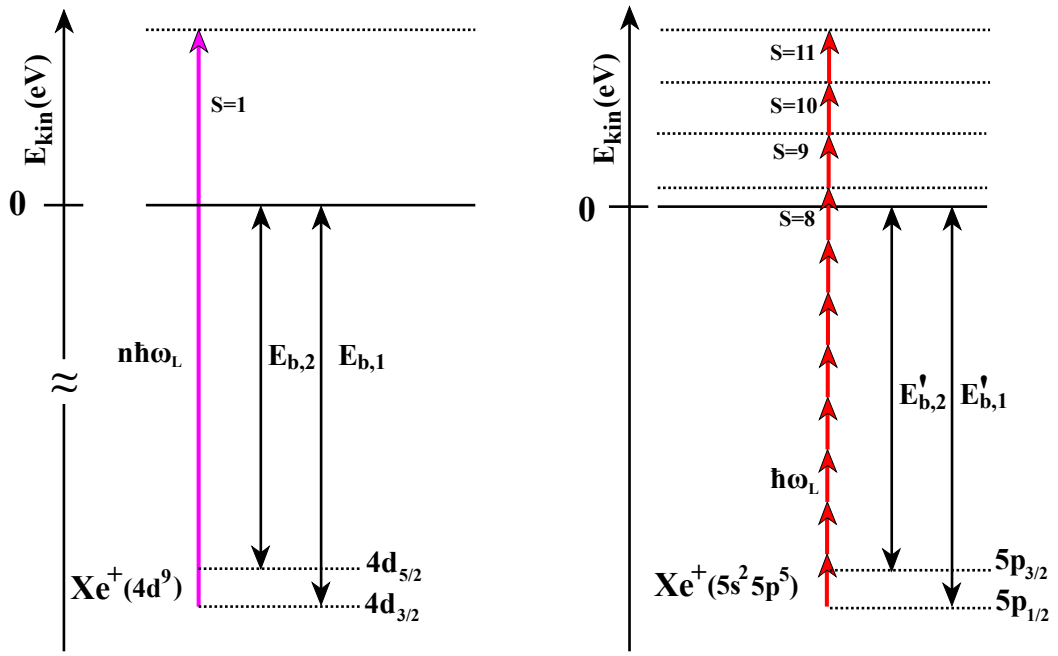

(a) Single-photon absorption

(b) Multiphoton absorption

Figure 6.1: Excitation schemes. The number of simultaneously absorbed photons is S. (a) Single-photon absorption. The photon energy is $n\hbar\omega_L = 79.6\,\mathrm{eV}$ ($n = 51$). $E_{\mathrm{b},1} = 69.5\,\mathrm{eV}$ ($4\mathrm{d}_{3/2}$), $E_{\mathrm{b},2} = 67.5\,\mathrm{eV}$ ($4\mathrm{d}_{5/2}$), (b) Multiphoton absorption. The photon energy is $\hbar\omega_L = 1.56\,\mathrm{eV}$. $E'_{\mathrm{b},1} = 13.4\,\mathrm{eV}$ ($5\mathrm{p}_{1/2}$), $E'_{\mathrm{b},2} = 12.1\,\mathrm{eV}$ ($5\mathrm{p}_{3/2}$).

12.1 eV ($5\mathrm{p}_{3/2}$). The additional absorption of a further photon is necessary to exceed the second ionization potential $E'_{\mathrm{b},1} = 13.4\,\mathrm{eV}$ ($5\mathrm{p}_{1/2}$). The intensity of the NIR radiation at the focus in the interaction volume was on the order of $(0.5 - 1.0) \times 10^{13}\,\mathrm{W/cm^2}$, which results in a ponderomotive potential in the range of $U_p = (0.295 - 0.590)\,\mathrm{eV}$, using Eq. (2.7). The corresponding Keldysh parameters were calculated with Eq. (2.8) for both ionization potentials and are in the range of $(3.2 - 4.5)$ and $(3.4 - 4.8)$, respectively. The Keldysh parameters suggest that we were in the MPI regime. Note that due to Eq. (2.29) the kinetic energy of the photoelectrons is shifted by U_p.

A general introduction of the data acquisition and image processing was given erlier (see section 5.4). Here, further details will be discussed. First images were acquired with the Basler camera because the image quality is not too sensitive on the camera alignment. A small tilt angle between the phosphor screen and the CMOS chip of the Basler camera did not lead to substantial asymmetries in the brightness of the acquired images. In contrast, the Optronis camera can be used to acquire single-shot images. In this mode a definition of a threshold value is necessary and leads to an increased sensitivity of the camera alignment, which affects the image quality. An electron event on the phosphor screen is extended over several pixels. A tilt of the camera chip with respect to the phosphor screen leads to the illumination of more pixels. Since the total intensity is constant, the average intensity per pixel is reduced and some pixels might not be stored because they do not exceed the threshold value anymore. As a consequence, brightness asymmetries in the image are visible and become even more pronounced when the threshold value is close

to the weakest illuminated pixel. Another problem occurs for an objective with a small focal length. Although the overall brightness of an image is increased, spherical aberrations lead to more extended off-axis electron events. The average intensity of these illuminated pixels is reduced and also does not exceed the threshold value. A compensation of these effects is realized by centroiding. Instead of all pixels, only the center-of-mass coordinates will be taken into account resulting in a more homogeneous image. Hot pixels can also be drastically reduced when using this post-processing algorithm. As a consequence, for the experiments the Optronis camera was used to detect the electrons from the NIR laser or the HHG beam. The average number of photoelectrons per pulse for both photon ionization processes was $0.5 - 1.0$. Hence, space-charge effects can be neglected.

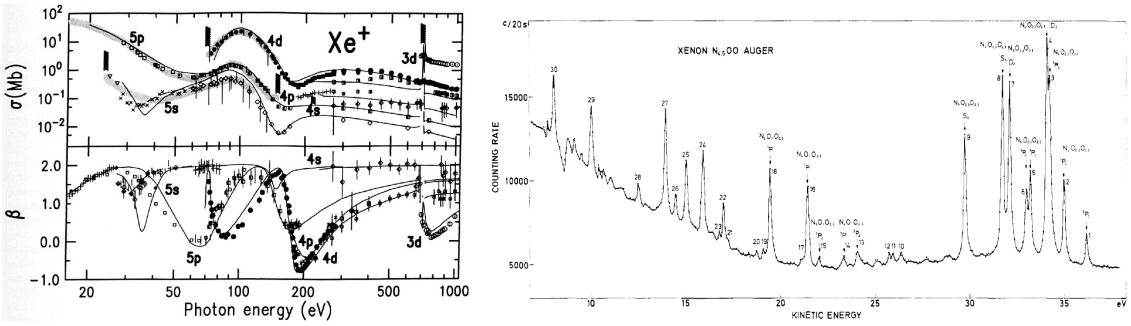

(a) Photoelectrons (b) $N_{4,5}OO$ Auger electrons

Figure 6.2: Photionization properties of Xe. (a) Photoionization cross sections and anisotropy parameters as a function of the photon energy (Fig. 20 of chapter 5 reprinted from [55] with permission from SpringerNature), (b) $N_{4,5}OO$ Auger decay channels in Xe as a function of the kinetic energy (Fig. 7 reprinted from [151] with permission from IOP Publishing).

6.2 Multiphoton ionization

6.2.1 Energy resolution

In a first experiment the energy resolution of the VMIS is investigated by carefully tuning the Extractor voltage V_{E}. The ejected photoelectrons have expected energies on the order of a few eV an therefore the Repeller voltage V_{R} was fixed at around $-1\,\mathrm{keV}$. For fine-adjustment of the high voltage V_{C} at the capillary exit, the resistance R_{box} (Fig. 5.9) is variable in the range of a few MΩ. The data was acquired for 600 s with the Optronis camera in the single-shot mode and approximately 0.6 photoelectrons per shot were detected. The sharpest peaks were obtained with a Extractor voltage of $V_{\mathrm{E}} = -0.80\,\mathrm{kV}$ (Fig. 6.3a). The NIR laser is linearly polarized along the p_y axis. The intense signal in the center was reduced in order to put the focus on the ring structure. The difference in the photoelectron energies between an S and $(S+1)$ photon-absorption is given by the photon energy $\hbar\omega_L = 1.56\,\mathrm{eV}$ ($S \geq 8$). Using this, the peak positions of the photoelectron spectra can be used for calibration (Eq. (5.1)) because the intensity to determine the ponderomotive shift can only be estimated. The Abel inversion was performed utilizing the POP algorithm (Fig. 6.3b). As known from the literature, the energy resolution is improved

by centroiding [135]. The photoelectron spectra are obtained by a 360° angle integration of the raw and Abel inversion images (Figs. 6.3c and 6.3d). Obviously, the application of the Abel inversion diminishes the lower energy part of each ATI peak resulting in a more symmetric peak shape. The low energy contribution centered around 0.1 eV is quite broad and neglected for the moment. However, the involved photoelectrons will play an important role once they are superimposed with intense THz radiation. The dynamics of this process will be comprehensively discussed in chapter 7.

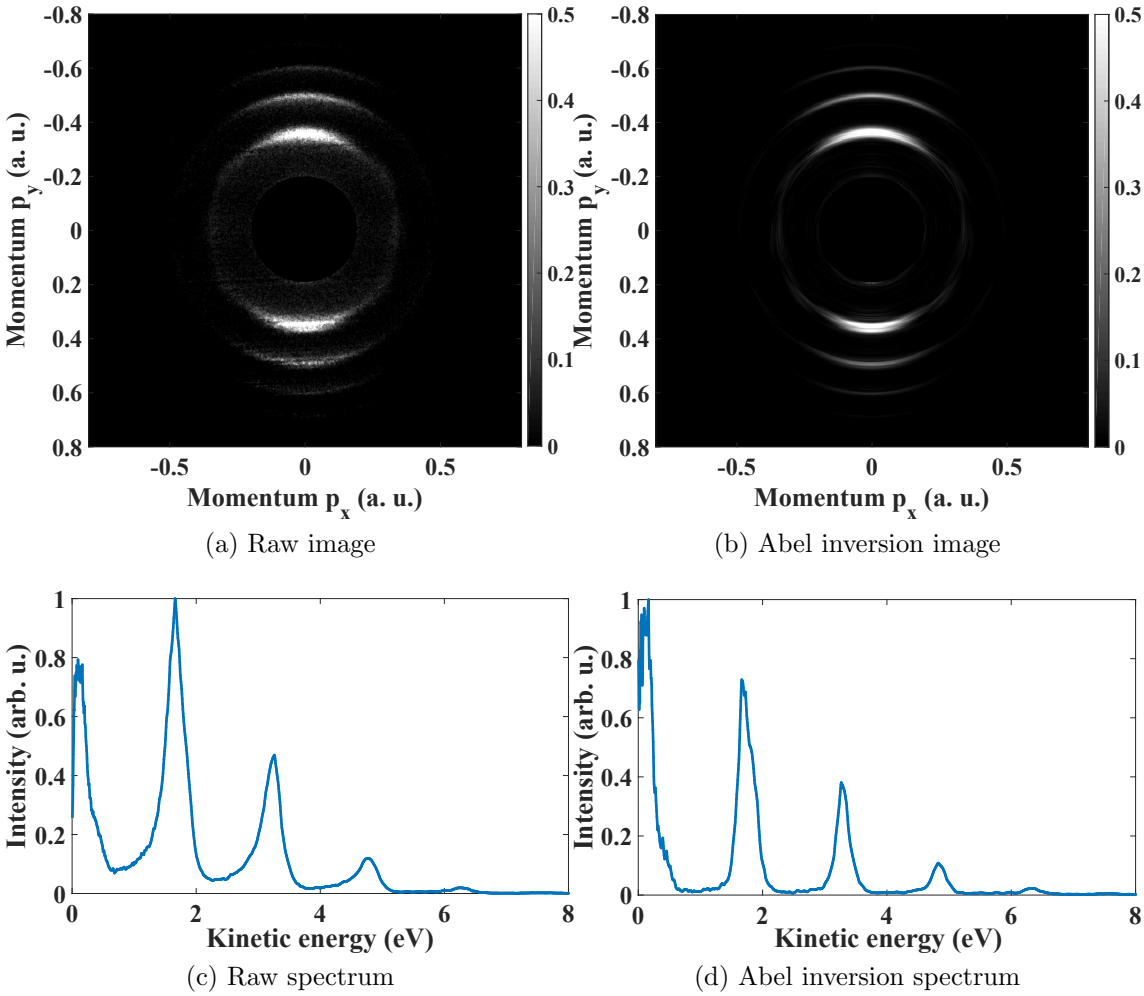

(a) Raw image (b) Abel inversion image

(c) Raw spectrum (d) Abel inversion spectrum

Figure 6.3: Repeller voltage: $V_{\mathrm{R}} = -1.12\,\mathrm{kV}$, Extractor voltage: $V_{\mathrm{E}} = -0.80\,\mathrm{kV}$, linear polarization of the NIR laser along p_y-axis (a) Experimental Image of a photoelectron distribution, (b) Abel inversion using POP, (c) Radial spectrum of the raw image, (d) Radial spectrum of the Abel inversion image. For clarity, the photoelectron signal in the center of the image was removed in (a) and (b).

The spin-orbit coupling in Xe leads to a splitting of the outermost electron orbital ($P_{1/2}$, $P_{3/2}$) and therefore to two ionization potentials $E'_{\mathrm{b},1/2}$. Although the energy splitting in Kr can be neglected Xe was chosen since it has a higher cross section and consequently more events are expected. The energy difference of both ionization potentials in Xe is 1.3 eV, which is close to the photon energy $\hbar\omega_{\mathrm{L}} = 1.56\,\mathrm{eV}$. This implies that the energy difference ΔE_{kin} between neighboring photoelectron peaks is

$$\Delta E_{\mathrm{kin}} = E_{\mathrm{kin}}(S+1, E'_{\mathrm{b},1}) - E_{\mathrm{kin}}(S, E'_{\mathrm{b},2}) \overset{Eq.\,(2.29)}{=} \hbar\omega_{\mathrm{L}} - E'_{\mathrm{b},1} + E'_{\mathrm{b},2} = 0.26\,\mathrm{eV}. \tag{6.2}$$

By fitting the photoelectron peaks with a superposition of N Gaussian functions (see Eq. (5.25)), the energy resolution of a photoelectron spectrum is calculated by Eq. (5.26). Instead of a 360° angle integration, the photoelectron spectrum was also investigated for a small slice with an angle ϕ with respect to the p_y polarization axis. The analysis showed that the energy resolution is getting better when the angle ϕ is reduced. The primary cause of this difference lies in the imperfect geometry of the electron imaging spectrometer [32]. Geometrical deviations from the cylinder symmetry potentially lead to distortions in the electron imaging. Especially imperfections of the capillary inlet tube might be the reason for an imperfect electron imaging.
As an example, the energy spectrum for $\phi = 10°$ with a Repeller voltage of $V_{\mathrm{R}} = -1.12\,\mathrm{kV}$ and an Extractor voltage of $V_{\mathrm{E}} = -0.80\,\mathrm{kV}$ was integrated (Fig. 6.4a). The full curve was fitted by a superposition of 4 Gaussian functions. For clarity, the LE structure was again removed. The double peak structure centered at 1.8 eV probably indicates the overlap of the $P_{1/2}$ and $P_{3/2}$ photoelectrons. A scan of the Extractor voltage V_{E} confirms that the best resolution of the third peak was obtained at $-0.80\,\mathrm{kV}$ (Fig. 6.4b) at a fixed Repeller voltage $V_{\mathrm{R}} = -1.12\,\mathrm{kV}$. As already mentioned the best photoelectron spectra are obtained for an angular integration with a small angle ϕ. The best resolution for the third peak is $\Delta E_{\mathrm{kin}}/E_{\mathrm{kin}} = 4.0\%$. This value, of course, is an upper limit since the excitation with a broadband NIR laser results in an intrinsic bandwidth of this ATI peak. If the bandwidth of the ATI peak would have been known, the energy resolution of the VMIS ΔE_{VMIS} could be calculated utilizing Eq. (5.5). In practice, however, it is difficult to estimate the bandwidth of such a highly nonlinear process.

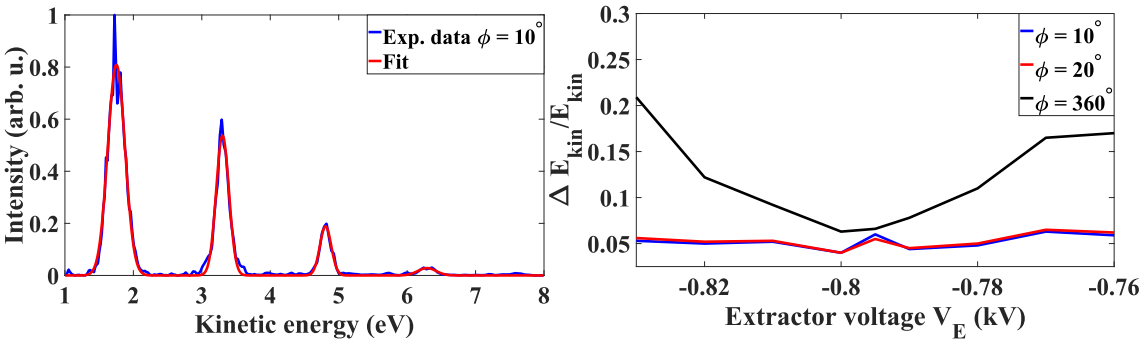

(a) Photoelectron spectrum (b) Resolution scan

Figure 6.4: Repeller voltage $V_{\mathrm{R}} = -1.12\,\mathrm{kV}$ (a) $\phi = 10°$, $V_{\mathrm{E}} = -0.80\,\mathrm{kV}$, (b) Energy resolution $\Delta E_{\mathrm{kin}}/E_{\mathrm{kin}}$ of the third peak for several angles ϕ.

6.2.2 Angular distribution

The angular distribution for a given photoelectron structure is characterized by the angle-dependent photoionization cross section (see Eq. (2.31)). According to section 5.5.5, the best anisotropy parameters were retrieved by applying the pBASEX

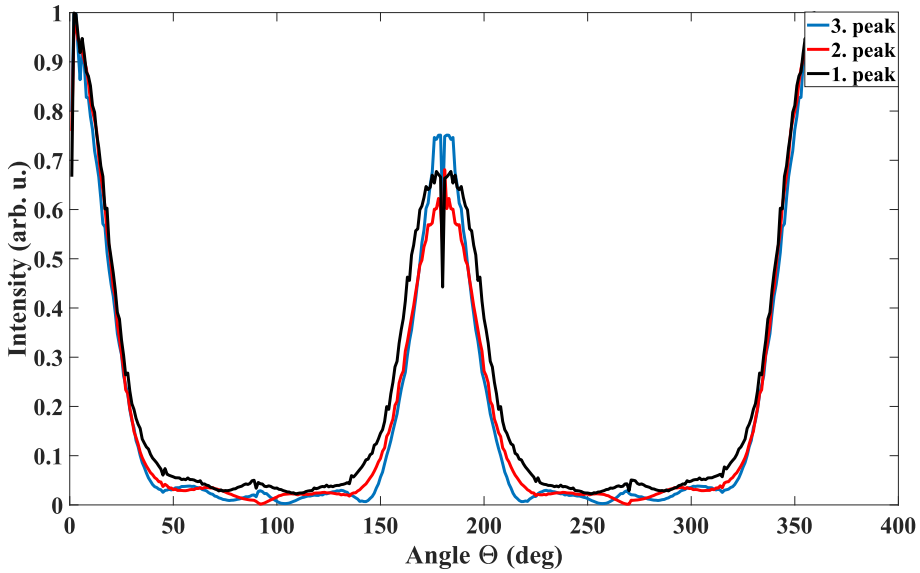

Figure 6.5: Angular distribution of the three ATI peaks at the positions 1.6 eV, 3.2 eV and 4.8 eV.

method to the experimental data. The radial integration was chosen such that the main contribution of the signal lies within the region of interest. The angular distributions of the three consecutive ATI peaks centered at 1.6 eV, 3.2 eV and 4.8 eV were obtained (Fig. 6.5). All angular distributions are very similar and show intense contributions along the NIR laser polarization axis, i.e. at $\Theta = 0°, 180°$. The small wiggles, which occur along the polarization axis, are artefacts from the Abel inversion procedure. In all cases the signal is bigger for $\Theta = 0°$ in comparison to 180° giving rise to a small asymmetry. The angular width of the first ATI peak is broader than the width of the second or third ATI peak, respectively. The modulation of the signal between $\Theta = 0°$ and $\Theta = 180°$ is very weak and in case of the first ATI peak almost flat. The similarity of all angular distributions suggests that low-order anisotropy parameters dominate and higher terms can be disregarded. However, a comparison with the anisotropy values from the literature ([152, 153]) is challenging because the photoelectron spectrum is very sensitive to the bandwidth and intensity of the excitation pulse. Especially the latter parameter could not be accurately measured.

6.2.3 Spatial-map imaging

In many cases a VMIS is used in the velocity-map imaging mode, which means that photoelectrons within the interaction volume with the same initial velocity will be mapped onto the same point onto the PSD. Another imaging mode is called the spatial-map imaging (SMI) and was already proposed in [27] and presented in detail elsewhere [154]. In this mode the interaction region, i.e. the superposition of the NIR laser and the gas distribution, is directly mapped on the detector and its spatial extensions can be estimated. The applied voltages for the Repeller and Extractor electrodes are −1.12 kV and −0.90 kV, respectively. The images were acquired with the Optronis camera in the single-shot mode. A horizontal stripe is observed on the phosphor screen (Fig. 6.6a). In analogy with ray optics, this corresponds to a

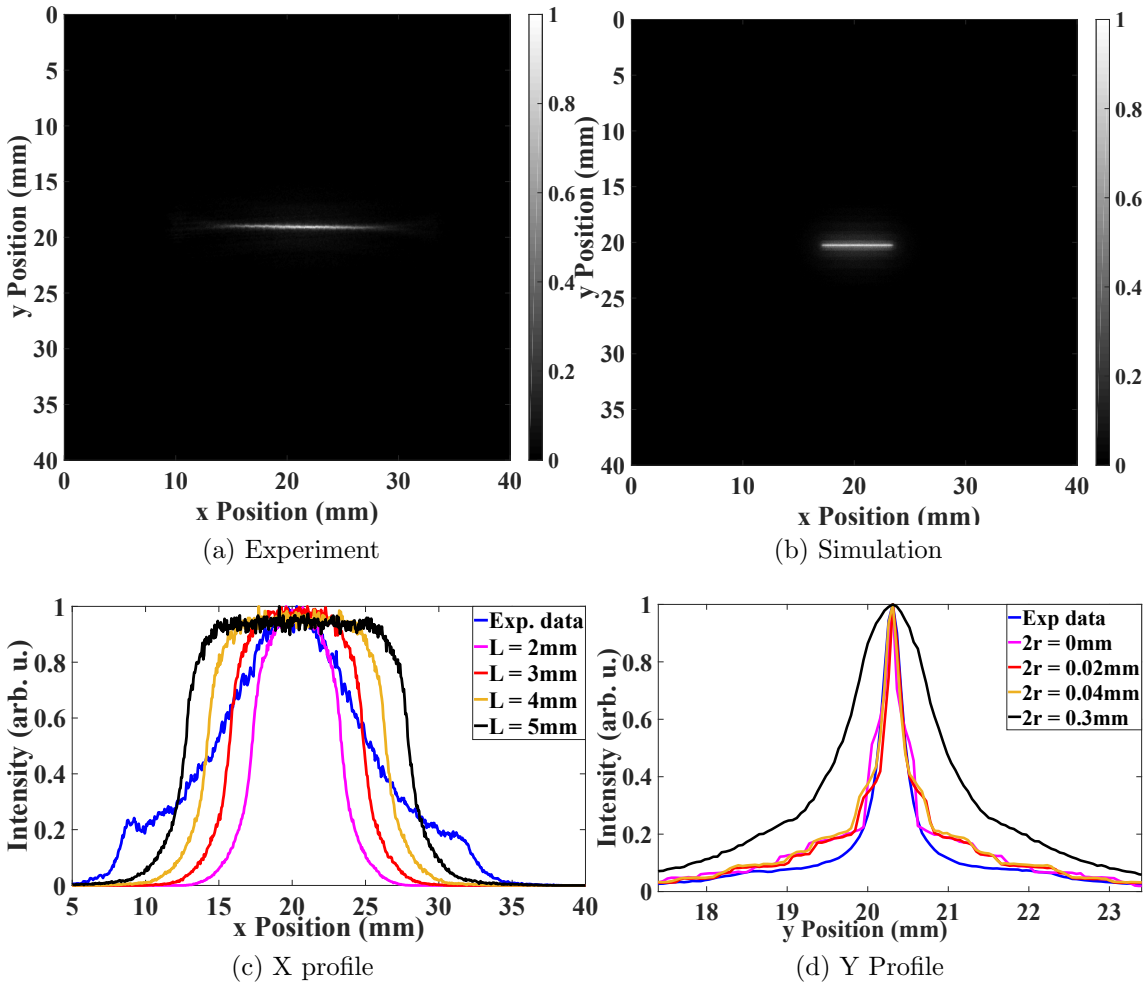

(a) Experiment (b) Simulation

(c) X profile (d) Y Profile

Figure 6.6: SMI mode, where the measured (a) and simulated (b) image on the phosphor screen is shown. (a) Experiment, $V_{\mathrm{R}} = -1.12\,\mathrm{kV}$, $V_{\mathrm{E}} = -0.90\,\mathrm{kV}$, (a) Simulation, $V_{\mathrm{R}} = -1.12\,\mathrm{kV}$, $V_{\mathrm{E}} = -1.06\,\mathrm{kV}$, $L = 2\,\mathrm{mm}$, $2r = 0.2\,\mathrm{mm}$ (c) X profile obtained by integration along y axis for experimental data and simulations with different lengths L of the interaction volume (d) Y profile obtained by integration along x axis for experimental data and simulations with different widths $2r$.

magnified imaging of a real object.

In a first step, the extensions of the interaction zone should be estimated by the dimensions of the NIR laser. According to section 4.2, the beam diameter of the NIR laser was measured to approximately $2w_0 = 90\,\mu\mathrm{m}$, which corresponds to an expected focus depth of $2z_R = 2\pi w_0^2/\lambda M^2 = 16\,\mathrm{mm}/M^2$, where $M^2 > 1$ is the beam quality factor. Both values give an upper limit for the width $2r$ and the length L of the interaction volume because the extension of the gas volume was not taken into account. For a quantitative comparison, the SMI mode was implemented in SIMION for the present VMIS geometry by varying the length L and the width $2r$ of a cylinder-like interaction volume. It is assumed that the electrons are homogeneously distributed inside the interaction volume. For simplicity, the capillary inlet tube was ignored in the simulation. Monochromatic photoelectrons with initial kinetic energies $0.5\,\mathrm{eV}, 2.0\,\mathrm{eV}, \ldots, 6.5\,\mathrm{eV}$ and arbitrary direction were assumed. The best images were obtained for a Repeller voltage of $V_{\mathrm{R}} = -1.12\,\mathrm{kV}$ and an

Extractor voltage of $V_E = -1.06\,\mathrm{kV}$ (Fig. 6.6b). The difference of the applied Extractor voltage between experiment and simulation is attributed to the capillary gas injector (see section 5.5.6). The extensions of the interaction volume were estimated by a projection of the images along the y direction (X profile: Fig. 6.6c) and the x direction (Y profile: Fig. 6.6d). The width $2r$ and the length L of the interaction volume are mapped onto the phosphor screen with the functions f_1 and f_2

$$\begin{aligned} 2r &\xrightarrow{f_1} 2r', \\ L &\xrightarrow{f_2} L'. \end{aligned} \tag{6.3}$$

Thus, $2r'$ and L' are measured on the phosphor screen. Assuming a bijective function, a comparison of the experiment with the simulation will reveal information about L and $2r$.
The experimental X profile shows a relatively smooth decay away from the peak position. In contrast, the peaks in the simulations show a sharp cut-off due to the definition of the length of the cylinder axis. The signal in the experimental X profile drops to 50% and intersects a simulation with a $L = 3.5\,\mathrm{mm}$ long cylinder axis (not shown in the graph). The width of the measured Y profile is always smaller than the width of the simulated profiles. A good agreement of the Y profile between the measurement and simulation is good for $2r \leq 0.04\,\mathrm{mm}$. The measured shape of the X profile deviates from the shape of all simulated X profiles (Fig. 6.6c). This might be a consequence of the definition of the interaction volume in the simulation. In this case a homogeneous distribution of electrons within the interaction volume is assumed while in the experiment more events are expected in the center because at this point the NIR laser intensity as well as the target gas density have the highest values. The simulation also showed that the optimum Extractor voltages are different for each photoelectron group, which might explain the intensity differences in the wings with the experiment (Fig. 6.6d). Generally, the simulations confirmed that the interaction volume is considerably more extended along than perpendicular the NIR laser propagation axis. The actual dimensions depend on the ionization process and will be smaller the higher the nonlinearity is.

6.2.4 Profiling the gas density distribution

In the experiment the target gas was supplied to the interaction zone by a capillary, which was integrated into the Repeller electrode. The details of the electrode geometry was already explained in section 5.3. The pressure at the capillary exit was on the order of $p_{\mathrm{exit}} = 10^{-4}\,\mathrm{mbar}$. Using the kinetic gas theory, the corresponding mean free path is calculated to $\bar{I} = 0.40\,\mathrm{m}$ at room temperature [155]. The inner diameter of the capillary is $d_1 = 1\,\mathrm{mm}$ and therefore the Knudsen number is obtained by

$$K_n = \frac{\bar{I}}{d_1} = 400 \gg 0.5 \tag{6.4}$$

and indicates that there is a molecular flow. Consequently, the collision between Xe atoms can be disregarded and an effusive beam with the particle number density $n(R, \vartheta)$ is given by [156]

$$n(r,\vartheta) = A\frac{\cos\vartheta}{r^2} = \frac{A}{z_0^2}\frac{1}{(1+y^2/z_0^2)^{1.5}}, \tag{6.5}$$

where A is a constant. The capillary points along the TOF axis, i.e. z-axis (Fig. 6.7). From this equation the width of the gas distribution Δy (FWHM) is calculated to

$$\Delta y = 2z_0\sqrt{2^{2/3}-1}. \tag{6.6}$$

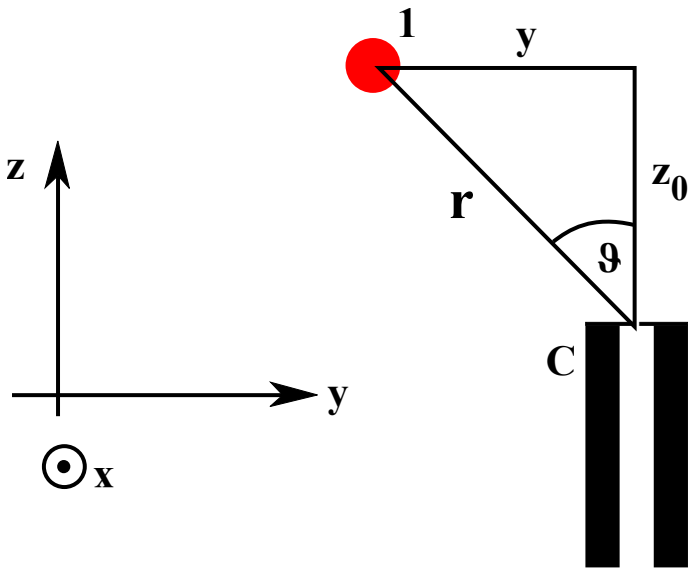

Figure 6.7: Sketch of the experimental geometry. C: capillary, 1: interaction point at the NIR laser focus, r distance to interaction point, $r^2 = y^2 + z_0^2$. The NIR laser propagates along the x-direction and the linear polarization points in the y-direction. The capillary points along the TOF axis (z-axis).

The density distribution of Xe atoms was measured as a function of the y and z position and by counting the number of photoelectrons that are detected with the Optronis camera while scanning the VMIS position with respect to the NIR focus (Fig. 6.7). During the measurement the beam was kept constant and only the VMIS was translated along the y and z position. The Repeller and Extractor voltages $V_\mathrm{E} = -2.00\,\mathrm{kV}$ and $V_\mathrm{E} = -1.46\,\mathrm{kV}$, respectively, were higher than in the previous measurement to capture all photoelectrons. A horizontal, i.e. along the y position, gas density distribution (Fig. 6.8a) was fitted with Eq. (6.5). A resulting beam width $\Delta y = 2.50\,\mathrm{mm}$ (FWHM) was obtained. In addition, the distance $z_0 = 1.63\,\mathrm{mm}$ can be extracted from the fit. This value is significantly bigger than the beam waist w_0 of the THz focus (see section 4.3.2). Hence, this measurement confirms that the THz beam does not clip at the capillary exit, which is important for the THz induced dynamics in the next chapter. Another gas density distribution was measured by shifting the VMIS in the vertical direction (Fig. 6.8b). As expected, according to Eq. (6.5), the photoelectron signal drops quadradically with the distance. Due to the radial symmetry of the capillary, it is assumed that gas density distribution in x-direction is the same as in the y-direction.

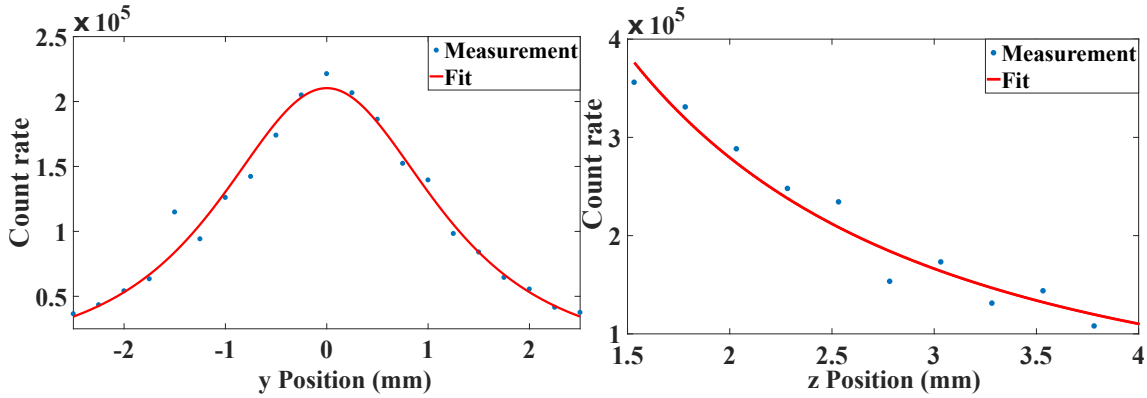

(a) Y profile (b) Z profile

Figure 6.8: Gas density distribution measurement. (a) Y Profile (along polarization direction), $z_0 = 1.63\,\text{mm}$, $\Delta y = 2.50\,\text{mm}$ (FWHM), (b) Z Profile (along TOF axis).

6.3 Single-photon ionization

6.3.1 Energy resolution

In a second experiment, HHG was used to directly ionize photoelectrons of the Xe 4d orbital (Fig. 6.9a). The linear polarization of the HHG beam points along the p_y axis. According to Eq. (6.1), the kinetic energies of the photoelectrons are on the order of 10 eV and therefore higher static voltages were applied to the electrodes. The best images were obtained with a Repeller and Extractor voltage of $V_\text{R} = -3.20\,\text{kV}$ and $V_\text{E} = -2.37\,\text{kV}$, respectively. The data was acquired for 2000 s and approximately 1 photoelectron per shot was detected. Afterwards, an Abel inversion using the POP algorithm was performed and clearly revealed both 4d photoelectron rings (Fig. 6.9b). The photoelectron spectra were again obtained by a 2π integration of the signal of the raw and inverted images (Figs. 6.9c and 6.9d). A variation of the Extractor voltage V_E at a fixed Repeller voltage $V_\text{R} = -3.20\,\text{kV}$ confirmed that the best images were obtained for $V_\text{E} = -2.37\,\text{kV}$ (Fig. 6.10b). Both peaks in the photoelectron spectrum, which correspond to the $4d_{3/2}$ and $4d_{5/2}$ Xe orbitals, were fitted with a superposition of two Gaussian functions (Fig. 6.10a) to extract the energy resolution $\Delta E_\text{kin}/E_\text{kin}$. The modulation of the photoelectron spectrum further away from the optimum was very small, hence, a fitting with two separated Gaussian functions was necessary. For an integration of 360° an energy resolution of 10.8% and 8.5% for the $4d_{3/2}$ and $4d_{5/2}$ photoelectrons were determined. It also turned out that the width of the photoelectron peak was reduced by decreasing the integration angle ϕ. Possible reasons for that were already discussed in section 6.2. For small angles ϕ energy resolutions below 7% can be achieved. This relatively large value can be explained by two observations. On the one hand, direct photoionization is a linear process, thus the interaction volume is expected to be bigger than in the multiphoton scenario. In case of an absorption of a single high-energy photon, the number of events scales linearly with the HHG intensity. On the other hand, the finite excitation bandwidth of the HHG beam has to be considered to determine the energy resolution ΔE_VMIS of the VMIS (see Eq. (5.5)).
A better way to determine the characteristics of the VMIS is to use Auger elec-

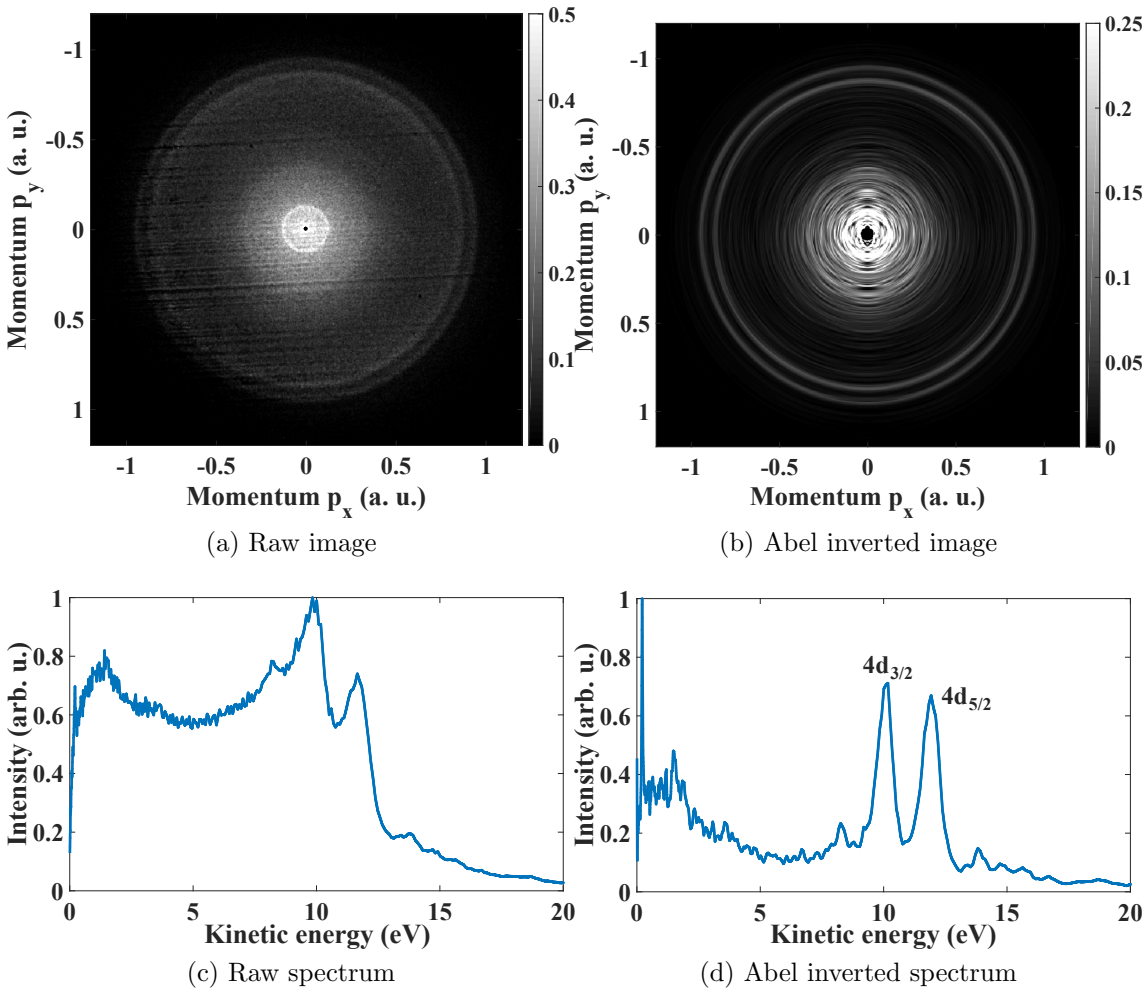

(a) Raw image (b) Abel inverted image

(c) Raw spectrum (d) Abel inverted spectrum

Figure 6.9: Repeller voltage: $V_{\mathrm{R}} = -3.20\,\mathrm{kV}$, Extractor voltage: $V_{\mathrm{E}} = -2.37\,\mathrm{kV}$, linear polariztion along p_y-axis (a) Experimental Image of a photoelectron distribution, (b) Abel inversion using POP, (c) Radial spectrum of the raw image, (d) Radial spectrum of the Abel inversion image. For clarity, the photoelectron signal in the center of the image was removed in (a) and (b).

trons because their kinetic energy does not depend on the photon excitation energy. As already mentioned earlier, the $N_{4,5}OO$ Auger electrons have kinetic energies in the range of 8 eV and 36 eV (Fig. 6.2b). Neglecting post-collision interaction, the spectral width of Auger electrons is defined by the natural linewidth. For example, the natural linewidths of Xe are 104 meV and 111 meV [56] for the $4d_{3/2}$ and $4d_{5/2}$ orbitals, respectively. The detection of electrons above 30 eV requires also higher voltages of the static electrodes. An observation of Auger electrons around 30 eV was obtained with a Repeller voltage of $V_{\mathrm{R}} = -5.50\,\mathrm{kV}$ and an Extractor voltage of $V_{\mathrm{E}} = -4.16\,\mathrm{kV}$ (Fig. 6.11a). Two photoelectron peaks are clearly visible. In addition, a faint modulation at momenta around $p = 1.5$ a.u. indicates further Auger electrons. The structure is more apparent after applying an Abel inversion (Fig. 6.11b) utilizing the POP approach. The experimental data and its inversion is presented on a logarithmic scale for a better visibility of weak contributions. Both strong photoelectron peaks at 10.1 eV and 12.1 eV were again used for the calibration of the energy axis. The spectrum consists of a superposition of Auger and

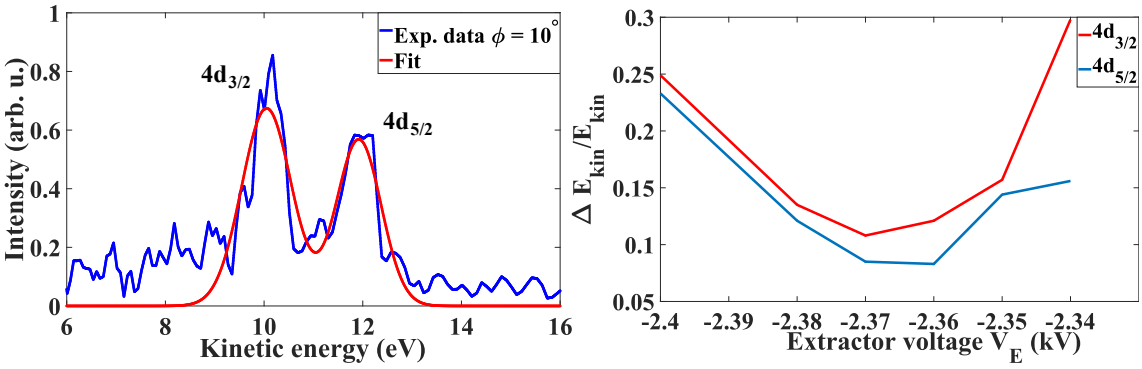

(a) Fit (b) Resolution scan

Figure 6.10: Repeller voltage $V_R = -3.20\,\text{kV}$ (a) $\phi = 10°$, $V_E = -2.37\,\text{kV}$, (b) Energy resolution $\Delta E_{kin}/E_{kin}$ of the $4d_{3/2}$ and $4d_{5/2}$ photoelectrons, for an angular integration of $\phi = 360°$.

photoelectrons. Since the natural linewidth of the Auger electrons is known, their spectrum can be convolved with the detector resolution ΔE_{VMIS}. Assuming a constant ΔE_{VMIS} in the respective energy range and an average natural linewidth of 0.1 eV, the expected Auger spectrum was obtained (Fig. 6.11c). The relative intensities of each Auger peak were taken from the literature [151]. The smaller ΔE_{VMIS} the better the individual Auger peak structure is evident. The different Auger spectra were afterwards superimposed with the electron spectrum and scaled according to the height of the experimental acquired and inverted data (Fig. 6.11d). A good agreement between the Auger spectrum and the energy spectrum is obtained for a VMIS energy resolution of $\Delta E_{VMIS} = 1.0\,\text{eV}$ This implies a relative energy resolution $\Delta E_{VMIS}/E_{kin}$ of approximately 3.3%.
For a complete characterization of the Xe photoelectron spectrum it would be beneficial to measure also photoelectrons from the 5 s and 5 p orbital. However, such a measurement was not possible due to the following two reasons: (i) low photoelectron count rate and (ii) limitation of applied voltage to static electrodes of the VMIS. On the one hand, the photoionization cross sections for the 5p and 5s orbitals are 0.75 Mb and 0.27 Mb, respectively and more than one order of magnitude lower than for the 4d shell, which is 8.5 Mb [157]. The low photon flux of the HHG source made it difficult to obtain a good signal-to-noise ratio within decent acquisition time. On the other hand, the detection of fast 5p and 5s photoelectrons requires an application of the Repeller electrode voltages above $-7.0\,\text{kV}$. As already mentioned in section 5.3, an electrical discharge within the capillary inlet tube takes place at such high voltages an impedes a measurement.
Another signature of the 4d photoelectron peaks is the branching ratio (BR), which determines the fraction of $4d_{5/2}$ and $4d_{3/2}$ photoelectrons. An important feature of a VMIS is to collect all electrons that are generated within the interaction volume. Consequently, the ratio of the integrals of the photoelectron is determined to

$$\text{BR} = \frac{I(4d_{5/2})}{I(4d_{3/2})} = 0.89 \tag{6.7}$$

for an angular integration of 360°. This value is close to the literature value of 1.0

for a photon energy of approximately 80 eV [158] and significantly deviates from the statistical BR of 1.5.

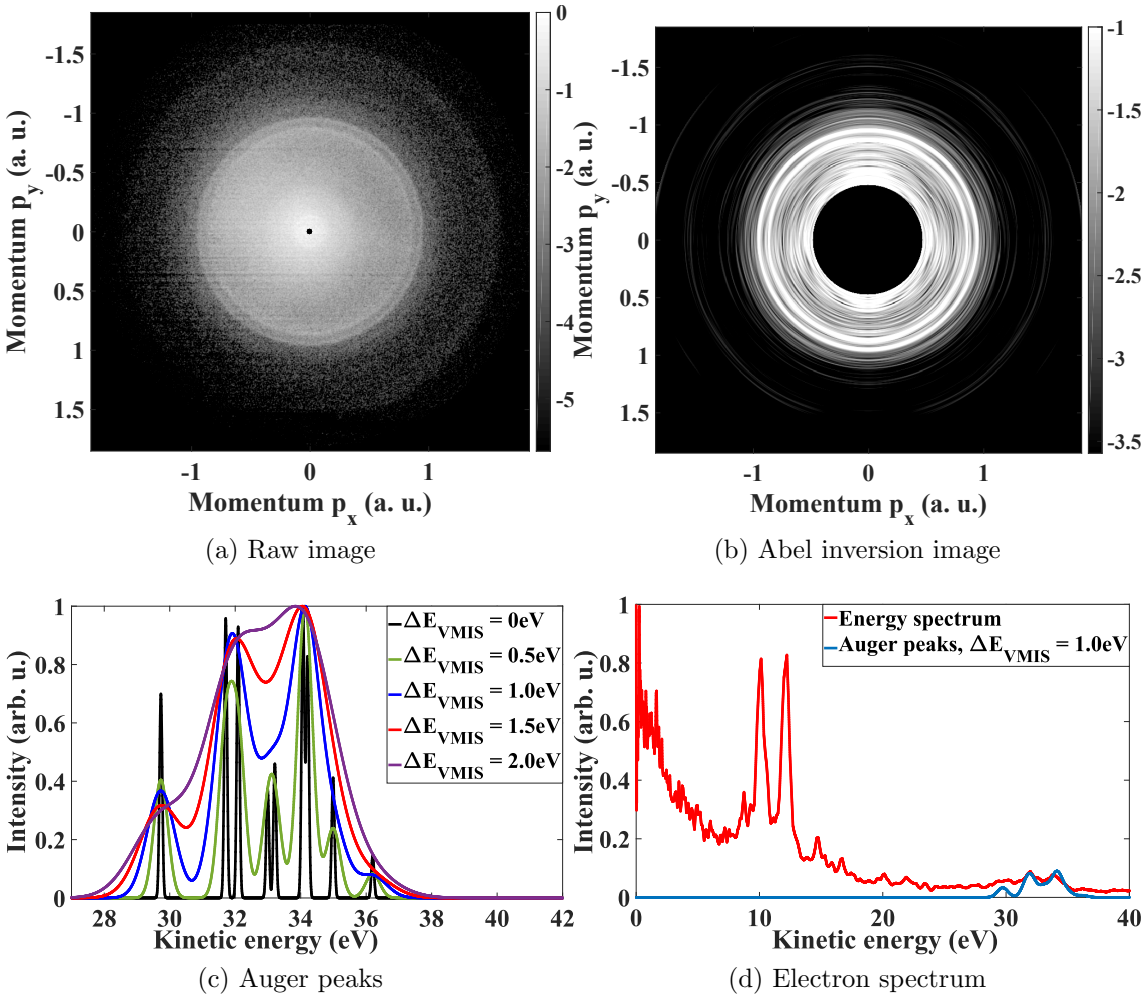

(a) Raw image (b) Abel inversion image

(c) Auger peaks (d) Electron spectrum

Figure 6.11: Repeller voltage $V_{\mathrm{R}} = -5.50\,\mathrm{kV}$, Extractor voltage $V_{\mathrm{E}} = -4.16\,\mathrm{kV}$. (a) Raw image, (b) Abel inversion image, (c) $N_{4,5}OO$ Auger electrons between 30 eV and 36 eV, the Auger spectrum is obtained by a convolution of the natural linewidth and the intrinsic energy resolution ΔE_{VMIS} utilizing Eq. (5.5) (d) Energy spectrum obtained by an integration of the right half of the image together with the Auger spectrum. For clarity, the photoelectron signal in the center of the image was removed in (a) and (b) and presented on a logarithmic scale.

6.3.2 Angular distribution

Generally, the partial photoionization cross section determines the angular distribution of a photon-absorption process (see Eq. (2.31)). In case of a single-photon absorption, the number of required Legendre polynomials is reduced to the zeroth and second order

$$\frac{d\sigma^{(1)}}{d\Omega}(\Theta) = A\left[1 + \frac{\beta_2}{\beta_0}\frac{1}{2}\left(3\cos^2\Theta + 1\right)\right]. \tag{6.8}$$

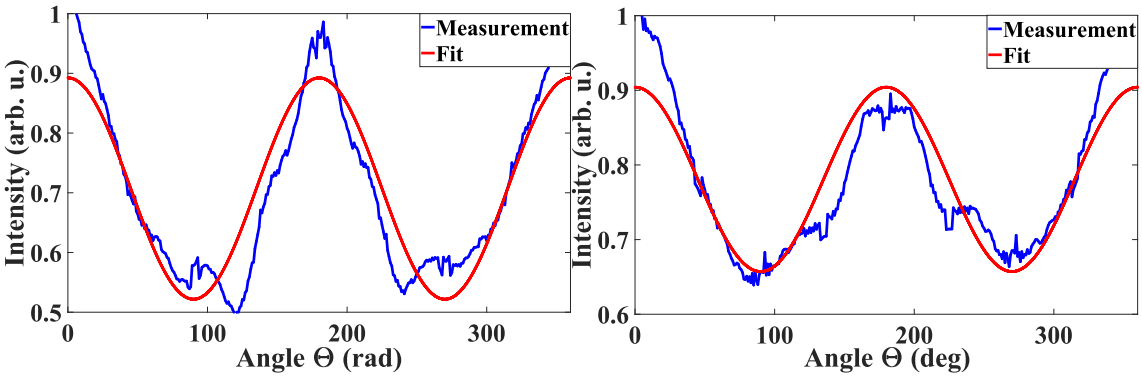

(a) $4d_{3/2}$ (b) $4d_{5/2}$

Figure 6.12: Angular distribution of the photoelectron peaks for a Repeller voltage of $V_R = -5.50\,\text{kV}$ and an Extractor voltage of $V_E = -4.16\,\text{kV}$. (a) $4d_{3/2}$, (b) $4d_{5/2}$

The angular distribution of both photoelectron peaks $4d_{3/2}$ and $4d_{5/2}$ was obtained for a Repeller voltage of $V_R = -5.50\,\text{kV}$ and an Extractor voltage of $V_E = -4.16\,\text{kV}$ after applying an Abel inversion utilizing the POP algorithm. The intensity as a function of the angle Θ, which is defined with respect to the polarization axis, is modulated (Figs. 6.12a and 6.12b). A local maximum at $\Theta = 0°$ and $\Theta = 180°$ for both photoelectron peaks is clearly visible. The resulting anisotropy parameter β_2/β_0 from the fitting is 0.38 ± 0.02 and 0.22 ± 0.01 for the $4d_{3/2}$ and $4d_{5/2}$ photoelectron peak, respectively. As can be already seen from the plots, there is an apparent discrepancy between the experiment and the fit in the range between $\Theta = 90°$ and $\Theta = 270°$. Nevertheless, the retrieved anisotropy parameters are close to the value of 0.25 from the literature ([55]).

6.4 Towards Photo- and Auger electron coincidence detection

A possible application of the experimental setup is a single-shot coincidence detection in Xe of the $4d$ photoelectron with an energy around 10 eV and the corresponding fast $N_{4,5}OO$ Auger electron with an energy on the order of 30 eV, such as in [159, 160]. In the latter experiment, the photoelectron/ Auger electron correlation was measured with four rotatable TOF spectrometers. On the one hand, a TOF spectrometer provides high spectral resolution but on the other hand, due to its small acceptance angle, a simultaneous measurement of all ejected electrons is not possible. However, the simultaneous measurement can be realized with the current VMIS, which has a slightly worse energy resolution. In another experiment [26] it was already shown that the fast Auger electron, which is ejected later, will overtake the slow photoelectron and exchange energy due to the long-range post-collision interaction leading to a modulation of the kinetic energy of the Auger electron as a function of time, i.e. of asymmetric line widths of consecutive slopes in a streaking curve. Since the acquired signal in this experiment was averaged over several electron pairs, the goal for a future experiment would be to detect this so-called energetic chirp for individual photoelectron/ Auger electron pairs and analyze their angular correlation. The prerequisites of this experiment will be shortly discussed

in the following.
A correlation of the photoelectron and the respective Auger electron requires that both electrons originate from the same atom. The ejection of $4d$ photoelectrons in Xe using photons of energy $\hbar\omega = 79.6\,\mathrm{eV}$ is the strongest contribution because the photoionizing cross sections σ_{4d} is the highest. Additional signal potentially comes from the ejection of $5s$ and $5p$ with the corresponding cross section σ_{5s} and σ_{5p}, respectively, which are also superimposed with double Auger decays [161] and background electrons. Assuming a probability of p_{4d} to ionize a $4d$ photoelectron with a subsequent Auger electron per laser shot, a Monte Carlo simulation has been made to obtain the detected electron distribution. The probabilities p_{5s}, p_{5p} and p_{bg} to ionize a $5s$, $5p$ photoelectron or a background electron, respectively, can be defined as

$$\begin{aligned} p_{5s} &= p_{4d}\frac{\sigma_{5s}}{\sigma_{4d}} \\ p_{5p} &= p_{4d}\frac{\sigma_{5p}}{\sigma_{4d}}, \\ p_{bg} &= 0.1 p_{4d}. \end{aligned} \tag{6.9}$$

The occurrence of double Auger decays were neglected in this simulation. The values for the partial photoionization cross sections were taken from literature [157]. Whether a photoelectron is detected or not depends on the detection efficiency η of the imaging setup. The detection efficiency η is a function of the following parameters:

- MCP geometry, i.e. open area ratio and wall material
- applied MCP voltages
- applied voltage of the phosphor screen
- camera chip and objective, i.e. whether the pixel values exceed the camera threshold value in the single-shot detection mode
- angle of incidence and energy of photoelectron that hits the MCP surface

Using SIMION, typical values for the Repeller and Extractor voltages are $V_{\mathrm{R}} = -5.5\,\mathrm{kV}$ and $V_{\mathrm{E}} = -4.16\,\mathrm{kV}$, respectively, to detect a $4d$ photoelectron and a corresponding Auger electron. These electrons will hit the MCP surface with energies around 4.8 keV and angles up to 6° with respect to the normal. According to [132], this results in a detection efficiency on the order of 50%, i.e. $\eta = 0.5$. For an ideal detection efficiency of $\eta = 1$, the photoelectron distribution is characterized by peaks of even numbers of electron events (Fig. 6.13a, red curve) due to the highest probability p_{4d} to create a photoelectron and an Auger electron at the same time. For example, the second peak at $N = 4$ could come from (i) two photoelectron/Auger electron events, (ii) one photoelectron/ Auger electron event and two single photoelectron events or (iii) four single photoelectron events. The detection efficiency $\eta < 1$ leads to a reduction of the measured electrons and consequently to a modified electron distribution (Fig. 6.13a, blue curve). The electron distribution is then characterized by an exponential decay. During a measurement it is important to know whether a detection of two electrons is attributed to the photoelectron/ Auger

electron case. Therefore, the true detection efficiency η_c is defined as the number of frames with exactly one photoelectron/Auger electron pair divided by the total number of frames where two electrons are detected. The value of η_c is a function of p_{4d} and η (Fig. 6.13b). For example, a true detection efficieny of $\eta_c = 0.99$ means that 99% of the frames containing two electrons originate from the photoelectron/ Auger electron case. From the Monte Carlo simulation it is obvious, that the values of η_c increases when the probability p_{4d} as well as the the detection efficiency η is decreased. On the one hand, a variation of the detection efficiency η gives small differences in η_c for a given small value of p_{4d}. On the other hand, a reduction of p_{4d} can experimentally achieved by reducing the Xe target gas density or the gas density in the HHG chamber. Of course, a reduction of p_{4d} also leads to a higher acquisition time. Generally, a high laser repetition rate is beneficial for a coincidence experiment, which is in our case limited to the NIR laser repetition rate of 1 kHz. Note that the repetition rate is also limited by the data acquisition device.

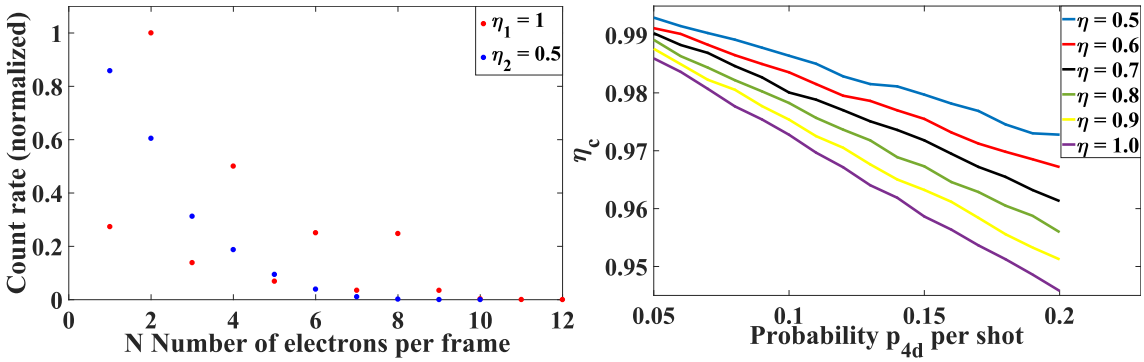

(a) Electron distribution

(b) η_c True detection efficiency

Figure 6.13: Monte Carlo simulation for coincidence detection. (a) Histogram of the number N of detected photoelectrons per frame. It is assumed that in average a $4d$ photoelectron is generated every second laser shot (i.e. $p_{4d} = 0.5$). The electron distribution is compared for two detection efficiencies $\eta_1 = 1$ and $\eta_2 = 0.5$. The count rate is normalized to the case were $N = 2$ and $\eta_1 = 1$. (b) The true detection efficiency η_c is better the smaller p_{4d} and the smaller η is.

An additional challenge emerges by applying the Abel projection, which will be applied to the VMIS images. Due to the Abel projection, only images with two well separated electrons can be taken into account. In this case, the fast electron can be identified as the Auger electron and hence the other electron is associated with the photoelectron. In the other case, i.e. where both events lie near the center of the image, the data cannot be used. The consequences of this effect on the reconstructed relative angle between the photoelectron and Auger electron are discussed in detail elsewhere [150]. A possible way to circumvent this restriction is to use a reaction microscope [162]. The advantage of this device is the simultaneous detection of electrons and ions and therefore the true detection rate η_c is 100%.

Chapter 7

Time-resolved terahertz streaking

The generation of photoelectrons by absorption of either a single or multiple photons was used in the previous chapter to characterize the VMIS for a photon excitation energy of 76.6 eV and 1.56 eV, respectively. Numerous experimental and theoretical studies investigated these light-induced effects over a wide range of excitation energies, intensities and different target gases and provided characteristic spectra. The superposition of an additional synchronized long-wavelength light field in the THz range gives the opportunity to transfer energy to the ejected photoelectron and thus manipulate its corresponding trajectory in space and time. The induced dynamics can be controlled by the time-delay between the ionization of the target gas and the arrival time of the THz pulse. Similar to the last chapter the photon excitation energies are again 1.56 eV (multiphoton ionization) or 79.6 eV (single-photon ionization).

7.1 Dynamics of multiphoton ionized electrons

7.1.1 Estimation of the terahertz field strength using multiphoton ionization

In the first part of this chapter the multiphoton absorption of Xe atoms is investigated. The measurement of the ultrafast dynamics was carried out with the full experimental setup in the presence of the THz radiation (Fig. 3.1). The used NIR laser intensities for the multiphoton ionization are on the order of $(0.5-1.0)\times10^{13}\,\mathrm{W/cm^2}$. The reconstruction of the THz electric field is performed with the streaking method (details see section 2.5). This method relies on the measurement of the photoelectron spectrum in the presence of the THz field (Fig. 7.1). Here, only the dynamics of the ATI photoelectron rings are investigated. Therefore, the center of the image is blackened. A detailed analysis of LE photoelectron will be given in section 7.1.3. By varying the time delay between the NIR pulse and the THz electric field, the momentum transfer and thus the THz vector potential can be calculated using Eq. (2.57). Repeller and Extractor voltages of $V_\mathrm{R} = -1.12\,\mathrm{kV}$ and $V_\mathrm{E} = -0.79\,\mathrm{kV}$, respectively, were applied to the VMIS. Measurements were carried out with the Basler camera because it can be synchronized with the translation stage. The exposure time was set to 15 ms and a gain of 25 was used. After averaging 2500 images for each time delay a slice along the polarization direction of the projected 2d photoelectron distribution provides a photoelectron spectrum. The position of the peaks were changing as a function of the temporal overlap of both pulses. Initially, the shift of the first photoelectron peak at around 1.6 eV was investigated (Fig. 7.2a). The time delay was varied in steps of 29 fs. An Abel inversion was not used. The positions of the photoelectron peaks were again used for a VMIS calibration assuming an energy separation of 1.56 eV and a linear mapping between the initial photoelectron mo-

mentum and the measured position on the phosphor detector (see Eq. (5.1)). The THz vector potential was subsequently differentiated with respect to the time delay to get the THz electric field (Fig. 7.2b). A smoothing of the THz electric field was applied to diminish a few ripples from the curve. The analysis showed that the THz induced momentum shifts of the other ATI photoelectron peaks at around 3.2 eV and 4.8 eV are the same. Surprisingly, the amplitude of the electric field is around 8 MV/m and more than a factor of two bigger than measured with EO sampling (see section 4.3.3). The significant difference could come from the following two reasons: (i) surface quality of the ZnTe crystal and (ii) underestimation of THz electric field in EO sampling. On the one hand, the EO sampling measurement indicated that the signal strongly depends on the ZnTe crystal position, where both beams spatially overlap. This implied a crystal surface inhomogeneity and effected the calculated THz electric field strength. On the other hand, the induced birefringence of the ZnTe crystal is proportional to small THz electric fields. However, when increasing the THz electric field, the EO signal reaches a maximum and is afterwards decreased [163]. In this case, it would be beneficial to attenuate the THz field strength with e.g. a Si-plate to be in the linear regime. Unfortunately, this was not measured. Note that the constant electric field strength 17 kV/m of the VMIS in the interaction volume can be neglected in comparison to the transient THz pulse electric field strength.

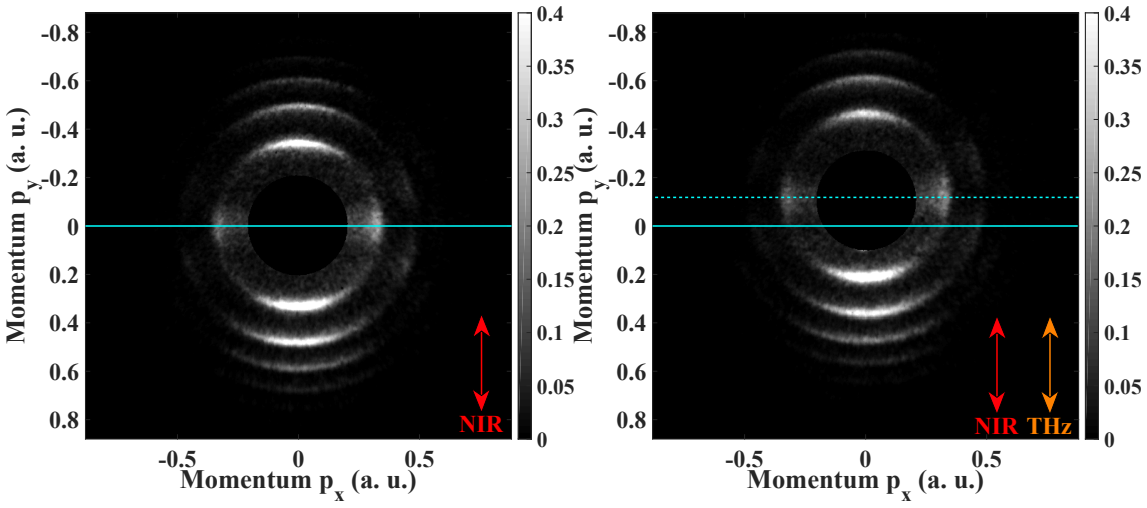

(a) Without THz (b) With THz

Figure 7.1: Measured ATI photoelectron momentum distribution without Abel inversion, i.e. raw image. The linear polarizations of the NIR pulse (red) and the THz pulse (orange) are aligned vertically. In the presence of the THz field, the photoelectron distribution is shifted (dotted cyan line) with respect to the case with no THz (solid cyan line). Repeller and Extractor voltage are $V_{\mathrm{R}} = -1.12\,\mathrm{kV}$ and $V_{\mathrm{E}} = -0.79\,\mathrm{kV}$, respectively. For clarity, the center of the image is blackened. (a) Field-free (without THz), (b) Streaked (with THz) with the maximum photoelectron momentum shift of $\Delta p_y = 0.114$ a.u.

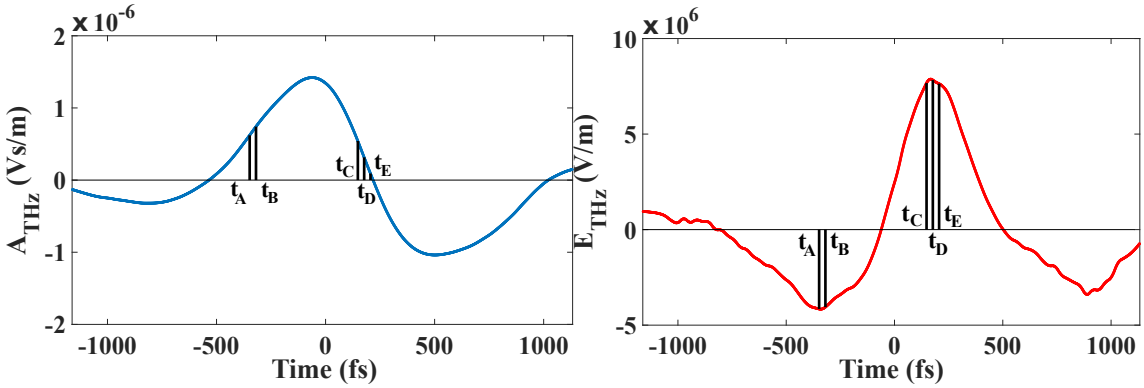

(a) THz vector potential (b) THz electric field

Figure 7.2: Reconstruction of the THz streaking field for the first ATI photoelectron peak at around 1.62 eV. Repeller and Extractor voltage are $V_{\mathrm{R}} = -1.12\,\mathrm{kV}$ and $V_{\mathrm{E}} = -0.79\,\mathrm{kV}$, respectively. The positions in time $t_{\mathrm{A}} = -348\,\mathrm{fs}$, $t_{\mathrm{B}} = -319\,\mathrm{fs}$, $t_{\mathrm{C}} = 148\,\mathrm{fs}$, $t_{\mathrm{D}} = 177\,\mathrm{fs}$, $t_{\mathrm{E}} = 206\,\mathrm{fs}$ were labeled for a determination of the NIR pulse duration. (a) THz vector potential $A_{\mathrm{THz}}(t) = \Delta p/e$, (b) THz electric field $E_{\mathrm{THz}} = -\partial A_{\mathrm{THz}}/\partial t$.

7.1.2 Determination of the near-infrared pulse duration

The THz streak camera is capable to determine the duration of the ionizing laser pulse. A detailed description of this process was given earlier (see section 2.5). In this case, the duration of the NIR laser pulse will be calculated. The ionizing NIR laser is coupled into the vacuum through a 1 mm thick SiO_2 window and reflected with two multilayer mirrors into the interaction volume. The NIR pulse duration τ is given by Eq. (2.69)

$$\tau = \frac{\sqrt{\sigma_s^2 - \sigma_{us}^2}}{s}, \tag{7.1}$$

assuming that the linear chirp can be neglected. According to Eq. (2.70), the streaking speed s is a function of THz electric field E_{THz}, the THz vector potential A_{THz} and the initial momentum p_0. For three ATI photoelectron peaks, the streaking speed was calculated using the previous results from section 7.1.1. The value φ is defined as the angle between the streaking direction and the measured photoelectron. For the angles $\varphi = 0°$ (Fig. 7.3a) and $\varphi = 180°$ (Fig. 7.3b) the local extrema at $-347\,\mathrm{fs}$ and $220\,\mathrm{fs}$ coincide approximately with the ones of the THz electric field. Therefore, the widths of the photoelectron peaks was estimated at positions $-348\,\mathrm{fs}$, $-319\,\mathrm{fs}$, $148\,\mathrm{fs}$, $177\,\mathrm{fs}$ and $206\,\mathrm{fs}$. The experimental data was Abel inversed using the POP approach, which was adapted for the streaked case. More details about the modification can be found elsewhere [150]. Afterwards, the radial distributions of the inversed images were calculated by integration over a full angle of 20°. The calculated NIR pulse durations show a huge spread and are varying for the different ATI peaks and different directions $\varphi = 0°$ and $\varphi = 180°$ (Fig. 7.4). The errorbars were determined by uncertainty propagation of Eqs. (2.69) and (7.1). The errors for A_{THz} and E_{THz} were estimated to 5% and the errors for the peak widths were directly taken from the fit (95% confidence interval). Obviously, all except one obtained NIR

pulse durations are on the order of 60 fs and significantly bigger than the expected value around 25 fs, which was measured with the SPIDER tool (Fig. 4.2). The slight increase of the NIR pulse duration of 0.5 fs is a result of the transmission through the 1 mm thick vacuum window assuming a transform-limited Gaussian pulse.
The actual value of the pulse duration $\tilde{\tau}$ is obtained by the measured pulse duration τ and has to be deconvolved with the contribution τ_G, which comes from the Gouy phase change over the focus. Assuming a length of $\Delta G = 3.5\,\mathrm{mm}$ (section 6.2.4), a Gouy phase change of $d\Phi/dz = 0.032/\,\mathrm{mm}$ (section 4.3.3) and a central frequency of $f_{\mathrm{THz}} = 0.83\,\mathrm{THz}$ leading to

$$\tau_G = \frac{\Delta G d\Phi/dz}{2\pi f_{\mathrm{THz}}} = \frac{3.5\,\mathrm{mm} \times (0.032 \pm 0.006)/\,\mathrm{mm}}{2\pi \times 0.83\,\mathrm{THz}} = (21.5 \pm 3.8)\,\mathrm{fs}. \tag{7.2}$$

Even in this case the measured pulse duration $\tau = 33\,\mathrm{fs}$ is expected to obtain a pulse duration of $\tilde{\tau} = 25\,\mathrm{fs}$ of the NIR field.
A possible reason for this big deviation could come from the pulse-to-pulse fluctuations of the THz electric field. At the time delays $t_A, \ldots, t_E$ the THz electric field strength is fluctuating, which was observed during EO-sampling. However, only a fluctuation on the order of a few percent was seen, which does not explain the discrepancy between the measured and expected NIR pulse durations of 25 fs.
Another error source might come from temporal jitter between the THz and NIR pulse after the beamsplitter. However, this effect might be small, because the vacuum chambers and optics were placed on a single experimental table. A further error source might originate from an inadequate spatial overlap in the focus between the THz and NIR beam.

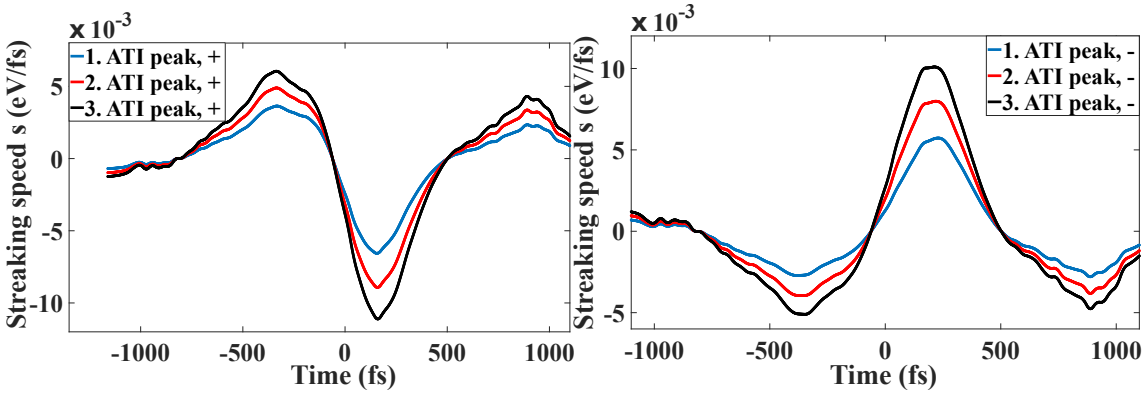

(a) $\varphi = 0°$ (b) $\varphi = 180°$

Figure 7.3: Calculated streaking speed using Eq. (2.70). (a) parallel (+) to the streaking direction, i.e. $\varphi = 0°$, (b) antiparallel (−) to the streaking direction, i.e. $\varphi = 180°$.

7.1.3 Low-energy photoelectron rescattering from ionic core

Until this point the focus of the analysis was always on the outer ATI rings. We have already seen that the shift of these ATI rings directly represents the vector potential A_{THz} of the THz streaking field. Little attention so far was paid to the

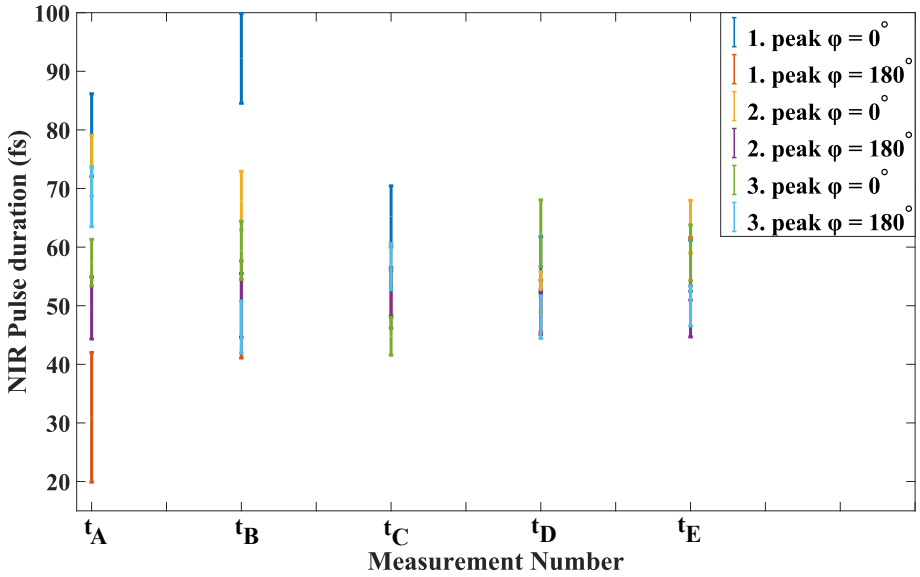

Figure 7.4: The measurement numbers correspond to the following time delays: $t_A = -348\,\text{fs}$, $t_B = -319\,\text{fs}$, $t_C = 148\,\text{fs}$, $t_D = 177\,\text{fs}$, $t_E = 206\,\text{fs}$ (see Fig. 7.2).

slow photoelectrons with energies around 70 meV. Momentum is also transferred to them from the THz electric field and depending on the relative time delay Δt between both laser pulses the shape of the measured pattern rapidly changes. The measured pattern for very low energies has a butterfly-like shape (Fig. 7.5a). The polarization axis of both lasers points again along the p_y axis and the voltages for the Repeller and Extractor are $V_R = -1.12\,\text{kV}$ and $V_E = -0.80\,\text{kV}$, respectively. An Abel inversion of these low photoelectron energies was not applied because artefactacts with the previously used algorithms (see section 5.5) would be produced. However, another inversion method, which is based on [144, 164] and implemented in a Python open-source code [165], only produces artefacts along the polarization axis but reconstructs the initial photoelectron distribution without further distortions (Fig. 7.5b). In the presence of THz radiation these LE photoelectrons are streaked. In the following a qualitative model will be described to explain some features of the induced dynamics before comparing them to the measured photoelectron distribution.

Qualitative description

As already discussed in section 2.3.2, the Coulomb interaction between the LE photoelectron and the remaining ion has to be taken into account. Within a purely classical approach, the photoelectron trajectory is described by the following two steps:

1. The photoelectron is liberated by muliphoton ionization with the NIR laser. In this step the influence of the THz electric field E_{THz} can be neglected.

2. The motion of the photoelectron is driven by the electric THz force $\vec{F}_E$ and the Coulomb force $\vec{F}_C$. In this step the influence of the electric NIR field can be neglected.

The photoelectron trajectory in the second step is described classically by Newton's equations. Due to the divergence of the long-range Coulomb potential at zero, a

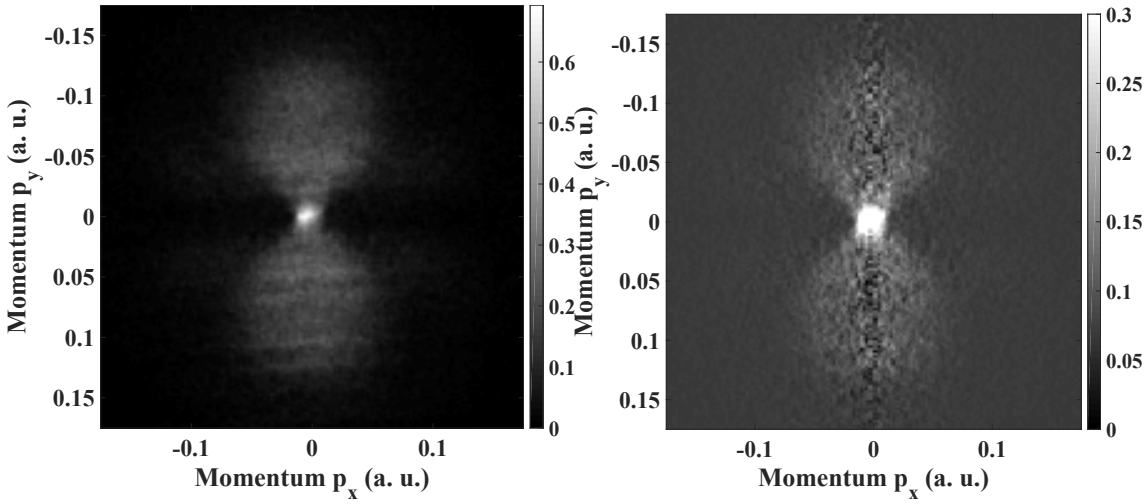

(a) Raw image (b) Abel inversion image

Figure 7.5: LE photoelectron structure. Repeller voltage: $V_{\mathrm{R}} = -1.12\,\mathrm{kV}$, Extractor voltage: $V_{\mathrm{E}} = -0.80\,\mathrm{kV}$, linear polariztion along p_y-axis (a) Experimental Image of a photoelectron distribution, (b) Abel inversion using an adapted onion-peeling approach

potential similar to the soft-core potential [166] is used to avoid numerical problems. It can be written as

$$V_{\mathrm{C}}(r) = \frac{Q_1 Q_2}{4\pi\epsilon_0\sqrt{a^2 + r^2}}, \tag{7.3}$$

where Q_1 and Q_2 denote the charges of both particles, ϵ_0 is the vacuum permittivity and a is a constant, which can be chosen such that at $r = 0$ the ionization potential I_p of the target gas is reproduced. For example, in Xe, where $I_p = 12.1\,\mathrm{eV}$, the constant is $a = 1.19\,\text{Å}$. The ionization of a photoelectron leads to a positively charged ion, i.e. Xe^+ with $Q_1 = -e$ and $Q_2 = +e$. The Coulomb force $\vec{F}_{\mathrm{C}} = -\nabla_r V_{\mathrm{C}}$ is the negative derivative of the Coulomb potential with respect to r. Due to the spherical symmetry of the Coulomb potential and the fact that the THz electric field is linearly polarized, the computational problem can be reduced to two dimensions. Consequently, the equation of motion of a photoelectron in the presence of driving laser $\vec{F}_{\mathrm{THz}} = -e\vec{E}_{\mathrm{THz}}$ and the Coulomb potential $\vec{F}_{\mathrm{C}}$ can be calculated by

$$\begin{aligned} m\ddot{\vec{r}} &= \vec{F}_{\mathrm{THz}} + \vec{F}_{\mathrm{C}}, \\ m\begin{pmatrix} \ddot{x} \\ \ddot{y} \end{pmatrix} &= -e\begin{pmatrix} E_x \\ E_y \end{pmatrix} + \frac{Q_1 Q_2}{4\pi\epsilon_0\left(x^2 + a^2 + y^2\right)^{3/2}}\begin{pmatrix} x \\ y \end{pmatrix}. \end{aligned} \tag{7.4}$$

The coupled two dimensional equation of motion given by Eq. (7.4) was numerically implemented using a Runge-Kutta ODE-solver with a variable time step in Matlab. The boundary conditions, i.e. the initial position and initial velocity of the photoelectron are necessary to calculate its trajectory. However, the boundary conditions are determined by the multiphoton ionization, which cannot be described classically. Even semiclassical approaches cannot easily be applied due to the large Keldysh parameter and numerical methods solving the TDSE directly should be used [167, 168].

This is beyond the scope of these thesis. The goal of this approach is to calculate possible classical photoelectron trajectories to give an intuitive explanation of the resulting photoelectron momentum distributions.
The linear electric field of the THz pulse for the numerical implementation is modeled by fitting the experimentally retrieved THz field (Fig. 7.2b) with a Gaussian envelope and a periodic carrier wave function. According to Eq. (4.6), the THz electric field is given by

$$\begin{aligned} E_{\mathrm{THz}} &= A_0 \exp\left(-\frac{(t-t_0)^2}{b^2}\right) \cos\left[\omega_0(t-t_0) + \Phi_{\mathrm{CE}}\right], \\ A_0 &= 8.0\,\mathrm{MV/m}, \qquad b = 882.0\,\mathrm{fs}, \qquad t_0 = 131.7\,\mathrm{fs} \\ \omega &= 4.9\,\mathrm{THz}, \qquad \Phi_{\mathrm{CE}} = 1.132. \end{aligned} \tag{7.5}$$

The linear polarization of the THz field points along the y direction. Small deviations between the modeled and experimental THz field occur at the trailing edge and might be a consequence of missing spectral components to describe the experimental THz field. However, this effect as well as additional oscillations, that are attributed to water absorptions in air, are disregarded. The resulting THz pulse is a near single-cycle pulse (Fig. 7.6a). The time between the ionization of the photoelectrons and the arrival of the THz pulse defines the temporal delay Δt. In the numerical simulation the THz electric field is shifted according to Δt. Electric field components before the temporal overlap were set to zero.
The free parameter $a = 1.19\,\text{Å}$ of the potential is chosen such that the ionization potential $I_p = 12.1\,\mathrm{eV}$ of Xe is reproduced (Fig. 7.6b). Note that the force $|\vec{F}_x|$ has a global maximum at $a/\sqrt{2}$ and converges asymptotically to zero for larger distances. At the origin the force $|\vec{F}_x|$ drops to zero, unlike the classical Coulomb potential, which diverges at this point.

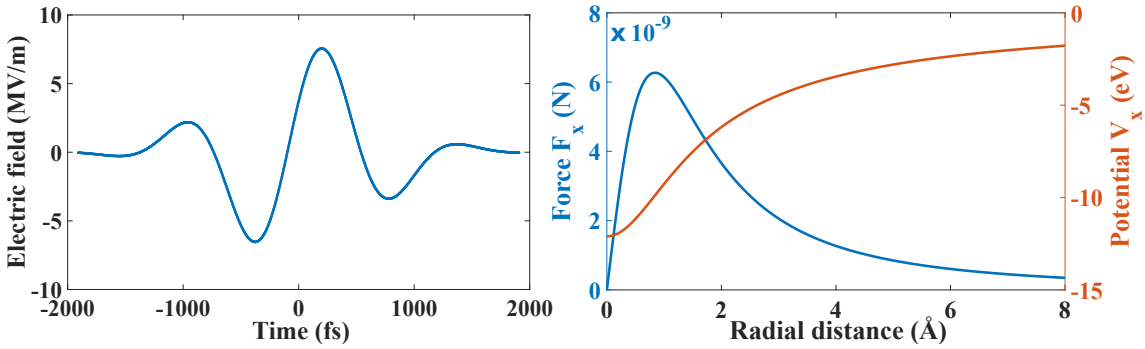

(a) THz electric field (b) Potential

Figure 7.6: Classical model for a qualitative description of the rescattering (a) Evolution of the THz electric field E_{THz}, (b) Potential V_x (red) and corresponding force F_x (blue) along the x direction (see Eqs. (7.3) and (7.4)).

The generated photoelectrons were initially defined on a sphere around the ionic core at a distance of $r_0 = 1.08\,\text{Å}$ and a uniform angular distribution $\varphi \in [0, \pi)$

$$\begin{aligned} x_0 &= r_0 \cdot \cos\varphi, \\ y_0 &= r_0 \cdot \sin\varphi. \end{aligned} \tag{7.6}$$

The angle $\varphi = 0°$ points along the linear polarization axis of the THz electric field. The distance r_0 was set to the atomic radius $r_0^{\mathrm{a}} = 1.08\,\text{Å}$ of Xe [169]. Due to symmetry reasons, the trajectories for $\varphi \in [\pi, 2\pi)$ were afterwards mirrored along the $-y$ symmetry axis. The initial velocity was also assumed to be on a sphere with the same uniform angular distribution

$$\begin{aligned} v_{x,0} &= v_0 \cdot \cos\varphi, \\ v_{y,0} &= v_0 \cdot \sin\varphi. \end{aligned} \tag{7.7}$$

The initial energy $E_0 = mv_0^2/2$ was chosen such that in absence of the THz pulse ($E_{\mathrm{THz}} = 0$), the photoelectron energy in the continuum was around 70 meV, which is close to the maximum of the measured photoelectron spectrum. As already mentioned before, these initial conditions are not calculated from a semiclassical or fully quantum-mechanical model. This is only an assumption.
The role of the Coulomb force $\vec{F}_C$ can be better understood by setting the force to zero. In this case only the THz electric field acts on the photoelectron and leads to a different trajectory. For a linearly polarized THz electric field E_{THz} along the y direction, the energy of the photoelectron in the continuum E_1 can be directly calculated using Eq. (2.57). As in the case where $F_C \neq 0$, a uniform angular distribution (see Eq. (7.7)) is assumed resulting to

$$\begin{aligned} E_1 &= \frac{1}{2m}\left(p_{x,0}^2 + (p_{y,0} + eA_{\mathrm{THz}})^2\right) \\ &= \frac{p_0^2}{2m}\left(\cos^2\varphi + (\sin\varphi + eA_{\mathrm{THz}}/p_0)^2\right). \end{aligned} \tag{7.8}$$

Note that the initial velocity $v_0 = \sqrt{2E_0/m}$ with $E_0 = 70\,\text{meV}$ can be directly calculated due to the fact that the Coulomb force is neglected.

Comparison of measurement with qualitative model
After the introduction of the classical model the simulations are now compared to the dynamics of the LE photoelectron distributions for the selected time delays $\Delta t_i, i \in \{1, \ldots, 5\}$ (Fig. 7.7). Due to the temporal derivative, the THz electric field E_{THz} has a phase difference with respect to the THz vector potential A_{THz}. The shape of the LE photoelectron structure looks very interesting for the selected time delays (Figs. 7.8 and 7.9). The experimental images (left column) were taken again with the Basler camera. The synchronization of the imaging camera with the delay stage came with a reduced energy resolution due to the lack of single-shot detection. The corresponding results of the simulations (right column) were obtained by calculating the trajectories of $N = 1003$ photoelectrons with the initial conditions for the position and velocity given in Eqs. (7.6) and (7.7). The depicted plots show the photoelectron momenta in the continuum. Afterwards, the results were mirrored along the p_y symmetry axis. Note that the experimental images are not Abel inverted due to the occurance of noise. This noise is either concentric around the image origin or along the polarization axis. A further comparison was obtained by setting the Coulomb attractive force F_C to zero (Fig. 7.10). The results for particular time delays are summarized in Tab. 7.1.

Time delay	Initial ejection angle (°)	Minimum distance to core (nm)	Returning point (nm)
$\Delta t_1 = -406\,\mathrm{fs}$	$0.3 - 16.0$	≤ 3.2	≈ 24
$\Delta t_2 = -58\,\mathrm{fs}$	no rescattering		
$\Delta t_3 = 145\,\mathrm{fs}$	$157 - 180$	≤ 13.9	≈ 20
$\Delta t_4 = 261\,\mathrm{fs}$	$155 - 177$	≤ 5.3	≈ 21
$\Delta t_5 = 493\,\mathrm{fs}$	no rescattering		

Table 7.1: Summary of results obtained with the simulation of classical trajectories.

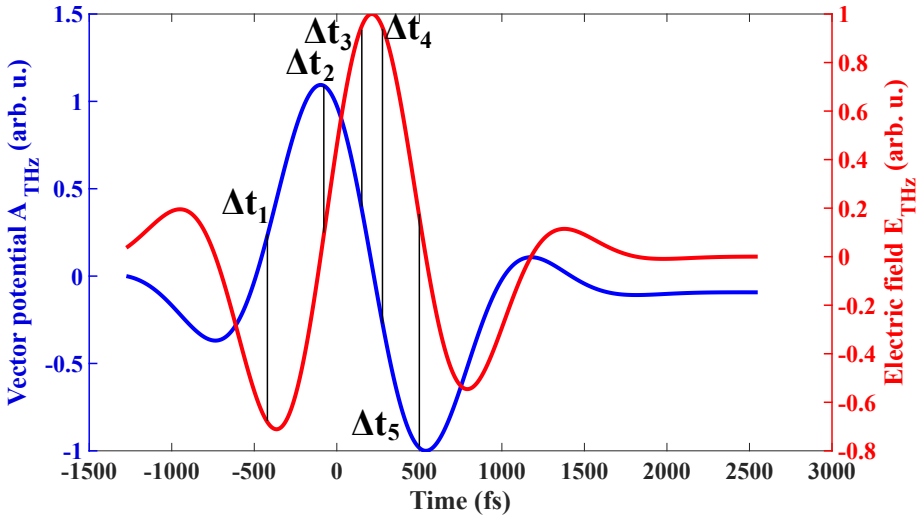

Figure 7.7: Behavior of the fitted THz electric field E_{THz} (red) and the corresponding vector potential A_{THz} (blue). The labeled positions indicate the selected delay times for the comparison between the experiment and the qualitative model. $\Delta t_1 = -406\,\mathrm{fs}$, $\Delta t_2 = -58\,\mathrm{fs}$, $\Delta t_3 = 145\,\mathrm{fs}$, $\Delta t_4 = 261\,\mathrm{fs}$, $\Delta t_5 = 493\,\mathrm{fs}$.

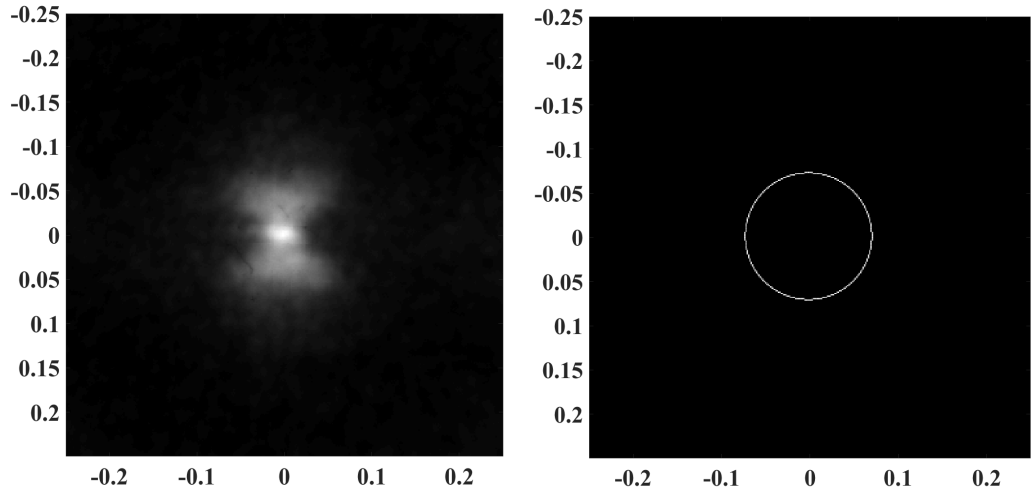

(a) no THz

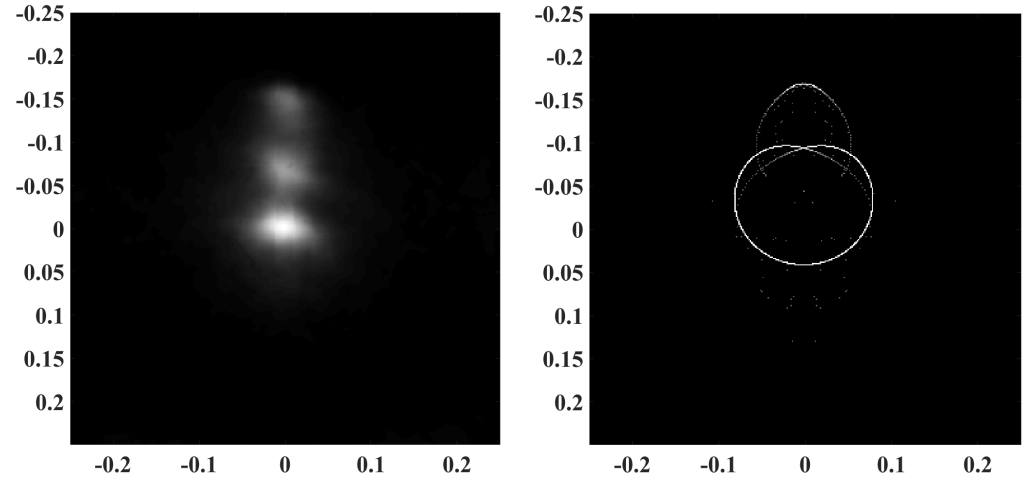

(b) $\Delta t_1 = -406\,\mathrm{fs}$

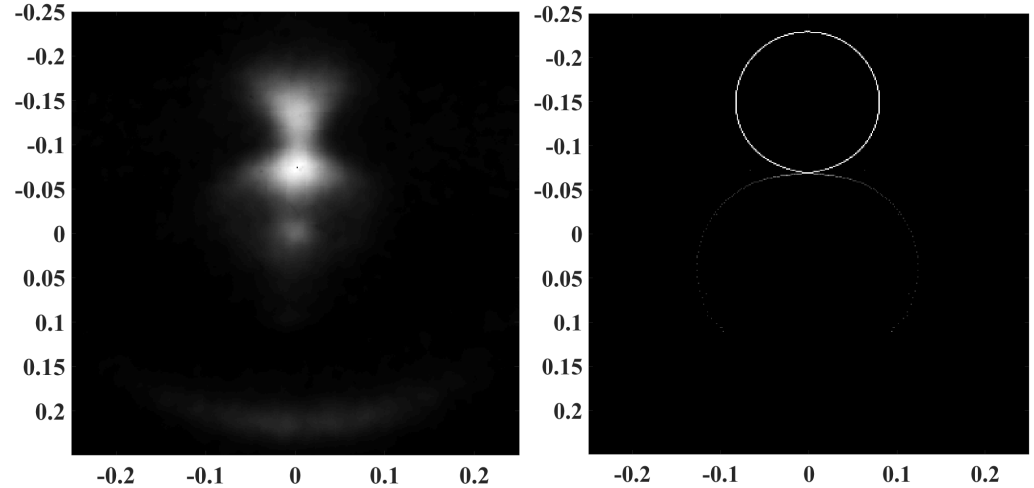

(c) $\Delta t_2 = -58\,\mathrm{fs}$

Figure 7.8: LE photoelectron structure. left column: experimental data, right column: qualitative description. The linear polariztion is along the vertical axis. The axes represent the momenta (a.u.). The corresponding time delays are written below each image (see Fig. 7.7 for corresponding THz electric field/ vector potential).

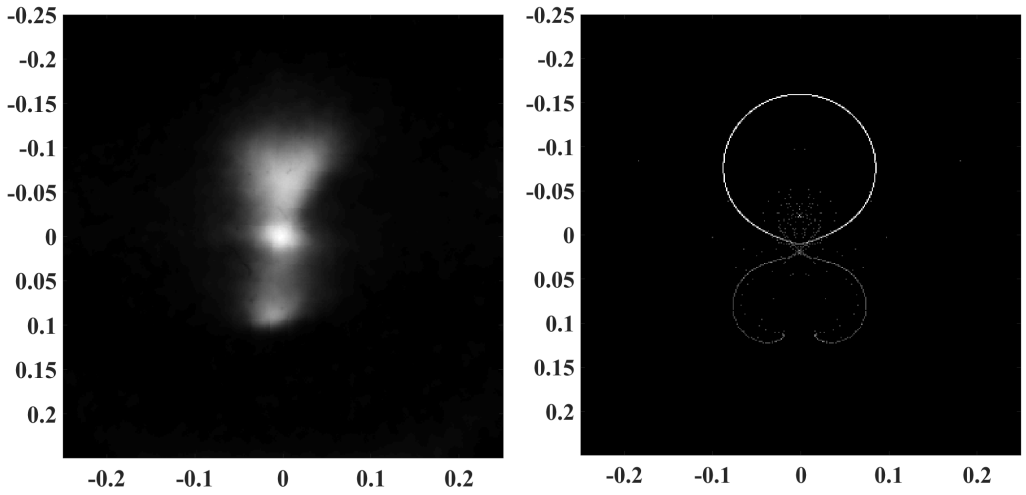

(a) $\Delta t_3 = 145\,\mathrm{fs}$

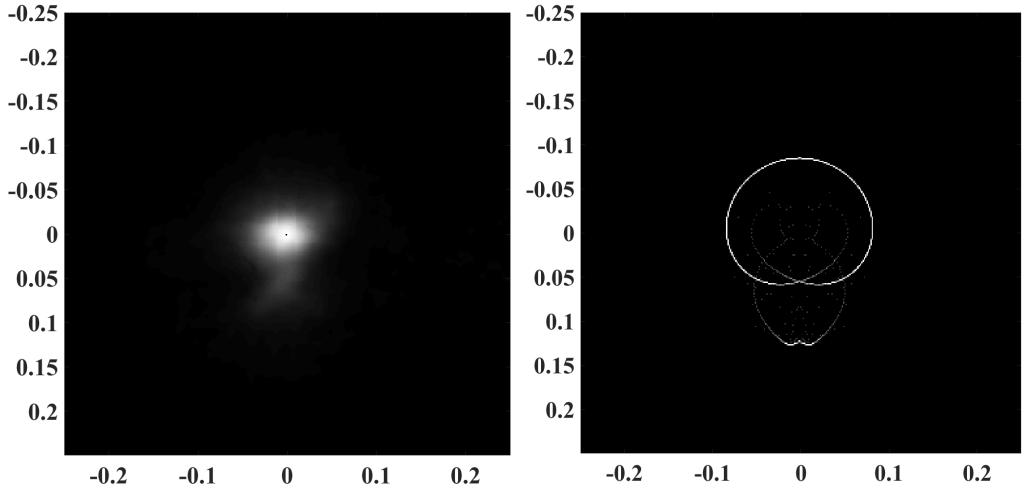

(b) $\Delta t_4 = 261\,\mathrm{fs}$

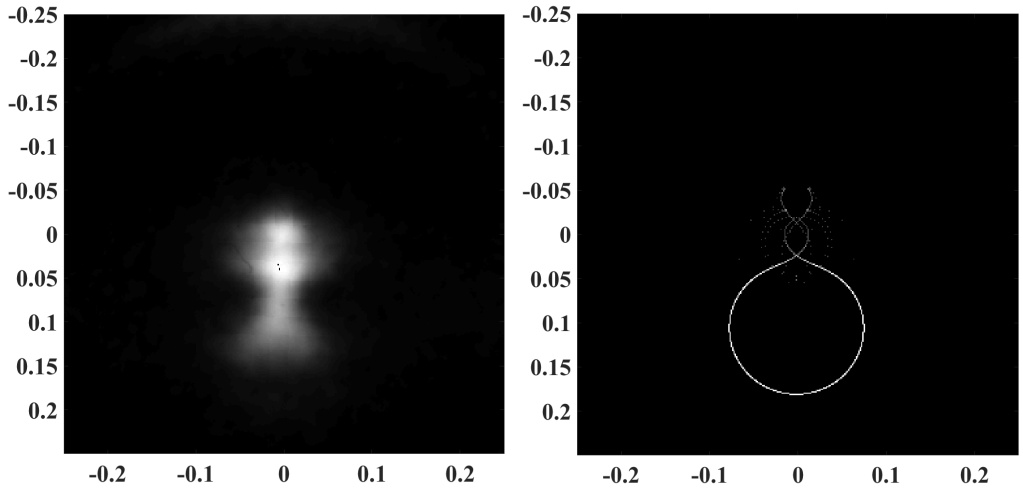

(c) $\Delta t_5 = 493\,\mathrm{fs}$

Figure 7.9: LE photoelectron structure. left column: experimental data, right column: qualitative description. The linear polariztion is along the vertical axis. The axes represent the momenta (a.u.). The corresponding time delays are written below each image (see Fig. 7.7 for corresponding THz electric field/ vector potential).

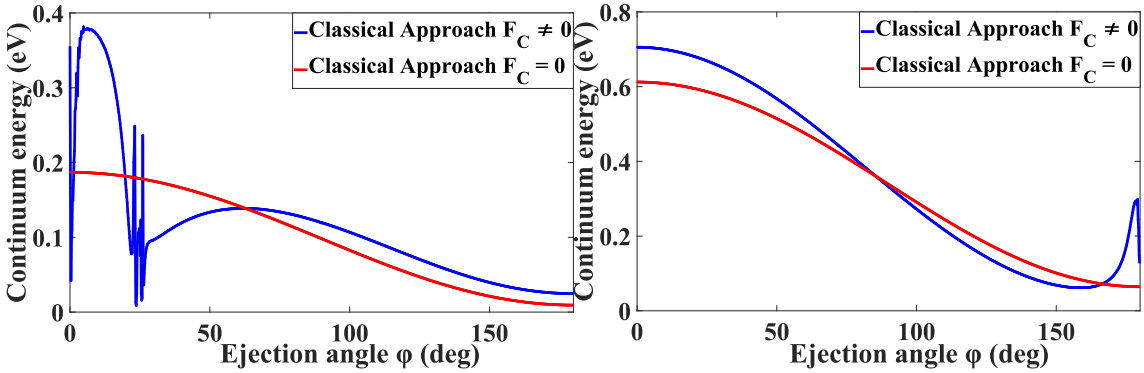

(a) $\Delta t_1 = -406\,\text{fs}$, forward rescattering

(b) $\Delta t_2 = -58\,\text{fs}$, no rescattering

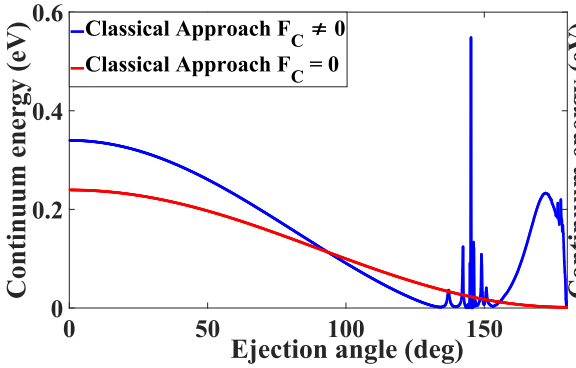

(c) $\Delta t_3 = 145\,\text{fs}$, backward rescattering

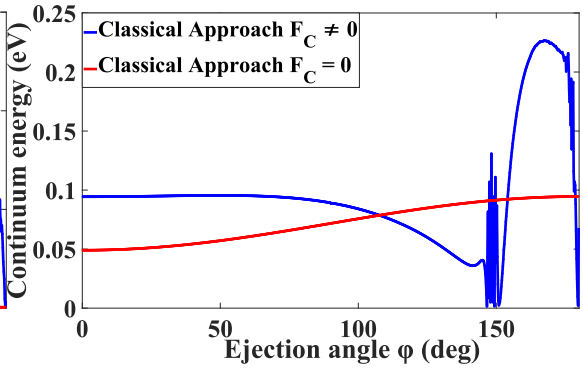

(d) $\Delta t_4 = 261\,\text{fs}$, backward rescattering

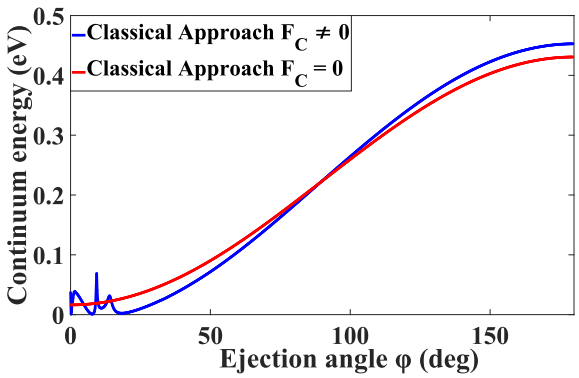

(e) $\Delta t_5 = 493\,\text{fs}$, no rescattering

Figure 7.10: Continuum energy of the LE photoelectron structure as a function of the ejection angle φ. The respective time delays between the ionization and arrival of the THz pulse are written below each graph. For a qualitative comparison the classical trajectories were also calculated for $F_C = 0$.

Absence of THz
In addition to the butterfly shape of the LE photoelectron structure (Fig. 7.8a) in the absence of THz radiation, an intense part in the center is apparent. A fraction of this intense part might be attributed to photons, which are a result of the recombination of photoelectrons with the positive Xe^+ ions. Only photons, that fly on the TOF axis towards the MCP detector, would contribute to this signal.

Time delay $\Delta t_1 = -406$ fs
Beside the intense part in the center, two separated contributions appear for $\Delta t_1 = -406$ fs in the upper half of the image, which is close to the minimum of the THz electric field (Fig. 7.8b). The corresponding value of the vector potential is less than the half of the maximum value. However, the upper intense part contains photoelectron signals with higher values. A look at the calculated classical trajectories as a function of the ejection angle φ indicates that there are some photoelectrons, which accumulate more energy (Fig. 7.10a). Photoelectrons, which are initially ejected in the range of $0.3° - 16.0°$ (forward scattering) reach a distance on the order of 24 nm (i.e. returning point) before they are decelerated back to the ionic core. The calculation showed that the photoelectrons have a minimum distance below 3.2 nm to the core. Photoelectrons with a bigger ejection angle φ have a similar continuum energy compared to the case where the Coulomb attraction F_C is neglected.

Time delay $\Delta t_2 = -58$ fs
For a time delay $\Delta t_2 = -58$ fs, the LE photoelectron structure has a maximum displacement in the upper direction, which means that the maximum momentum is transferred to the photoelectrons (Fig. 7.8c). This is in good agreement with the fact that the THz vector potential has a maximum, or equivalently, the electric field is zero. The shape of the LE photoelectron structure for this time delay is mainly preserved. The energy differences in the continuum for all ejection angles φ are very small compared to the case of $F_C = 0$ (Fig. 7.10b).

Time delay $\Delta t_3 = 145$ fs
The LE photoelectron structure for $\Delta t_3 = 145$ fs is characterized by an asymmetric shape with respect to the origin. The upper part is more intense than the lower part, which is also reflected in the classical description (Fig. 7.9a), where the lower half of the image is less intense with a different pattern. The biggest differences of the continuum energy for individual photoelectron trajectories occurs for ejection angles in the range of $157° - 180°$ (Fig. 7.10c), i.e. backward-scattering. In this range the photoelectrons are retracted at a distance of approximately 20 nm to the ionic core (i.e. returning point) and swing by at a minimum distance below 13.9 nm to the core into the continuum. During this process the photoelectrons gain kinetic energy.

Time delay $\Delta t_4 = 261$ fs
The measured LE photoelectron structure for a time delay of $\Delta t_4 = 261$ fs almost collapses to a single spot in the origin with a small further contribution on the lower image half (Fig. 7.9b). The direct comparison with the classical description also shows a nearly circular pattern centered around the origin with a substructure inside. An additional contribution is also visible at the lower half. Further analy-

sis showed that backward scattering takes place for ejection angles in the range of $155° - 177°$. In this regime, the photoelectrons reach a maximum distance of about 21 nm before they return to the ionic core with a minimum distance below 5.3 nm. The closest approach also leads to a higher kinetic energy in the continuum.

Time delay $\Delta t_5 = 493$ fs
Similar to the time delay t_2, the LE photoelectron structre has a maximum displacement in the lower direction for $\Delta t_5 = 493$ fs (Fig. 7.9c) due to the maximum THz vector potential $A_{\mathrm{THz}}(\Delta t_5)$. This is also in good agreement with the calculated classical trajectories. Small deviations only occur for small ejection angles φ. For all other values of φ the obtained continuum energies are very close to the values where the Coulomb attraction was neglected (Fig. 7.10e).

Discussions
The application of the classical model attributes some features of the measured dynamics to recattering of photoelectrons at the ionic core. Photoelectrons, which are initially ejected in a certain direction, are decelerated and return to the parent ion. A closest approach of these particles at the ionic core with a minimum distance on the order of a few nanometers or less leads to an accumulation of kinetic energy in the continuum. This effect strongly depends on the ejection angle φ and the relative phase Δt of the THz pulse, which is described well by the classical model. According to the calculated trajectories, the photoelectrons are only scattered once from the ionic core, which might be a direct consequence of the near single-cycle shape of the THz pulse. Although the maximum THz electric field is around $E_0 = 8\,\mathrm{MV/m}$, the small center frequency of $f_c = 0.78\,\mathrm{THz}$ leads to a ponderomotive potential of $U_p = 0.12\,\mathrm{eV}$, where Eqs. (2.7) and (A.13) have been used. The photoelectrons in the presence of the THz pulse propagate around 20 nm away from the ionic core before they come back and rescatter. Quantum mechanically, the photoelectrons are described by a wave packet and the transversal spread scales with $\lambda_{\mathrm{THz}}^{-2}$ of the rescattered electrons. The number of returning photoelectrons also scales with $\lambda_{\mathrm{THz}}^{-2}$ and therefore the total number of scattered photoelectrons scales with $\lambda_{\mathrm{THz}}^{-4}$ assuming that the influence of the Coulomb potential can be neglected [170]. Consequently, the number of rescattered photoelectrons should be drastically reduced in the long-wavelength range. However, in the current experiment the Coulomb potential cannot be neglected and the actual portion of rescattered photoelectrons should be calculated by solving the TDSE. An estimation of the mean free path of the Xe atoms in the interaction volume is $\bar{I} = 0.40\,\mathrm{m}$ at room temperature assuming a target gas pressure on the order of $10^{-4}\,\mathrm{mbar}$ [155]. This value is many orders of magnitude larger than the maximum distance that a photoelectron reaches before it is reversed and scattered from the ionic core. Therefore, collisions between photoelectrons and neighboring Xe atoms or ions can be neglected.
As already mentioned earlier, the conditions for the initial velocity (Eq. (7.7)) are assumed to be spherically symmetric around the position of the origin. However, the actual velocity distribution of the photoelectrons is a result of the multiphoton ionization process, which has to be calculated by solving the TDSE or using semi-classical approaches. On the one hand, the variation of the initial position r_0 in the classical model requires to adapt the initial energy E_0, such that without the THz electric field ($F_E = 0$) the energy of the photoelectron in the continuum remains

70 meV. The resulting trajectories are reproduced as long as the initial position of the photoelectron is not too close to the ionic core. For values close to the core the attractive force of the potential decreases with decreasing distance and may lead to different trajectories. On the other hand, a variation of the angle of the initial velocity leads to a dramatic change of the calculated trajectory, which indicates one limitation of this classical model. As soon as the initial velocity does not point away from the core the model breaks down. Another limitation is the choice of the Coulomb potential. The potential was chosen because it does not diverge at the origin and therefore does not lead to computational problems. Another possibility could be to use a modified Yukawa potential where the singularity at zero vanishes [171]. The application of such a potential requires at least the use of a semiclassical model.

7.2 Dynamics of single-photon ionized electrons

7.2.1 Double Auger decay in Xenon

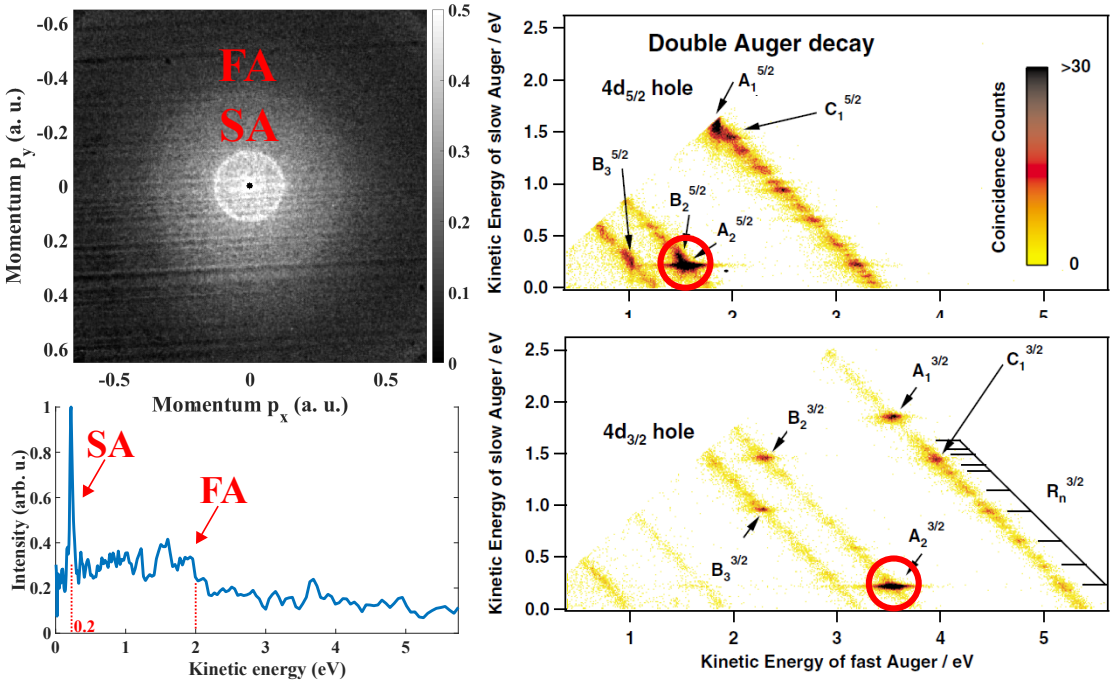

(a) Measurement

(b) Double Auger decays

Figure 7.11: Double Auger decay in Xe. (a) Measurement with $V_R = -3.20\,\text{kV}$ and $V_E = -2.37\,\text{kV}$. The slow Auger (SA) electrons have kinetic energies of 0.2 eV and the fast Auger (FA) electrons have kinetic energies up to 2 eV. Upper image: Abel projection, lower image: energy spectrum after Abel inversion and an integration angle of $\varphi = 120°$. (b) Coincidence maps of the FA electron (x-axis) and the SA electron (y-axis). The relevant regions of interest are marked in red (both reprinted from [161] with permission from American Physical Society).

In the previous section, attention was paid to the induced dynamics of Xe using an NIR laser to ionize electrons by the simultaneous absorption of multiple photons. Here, the 51. harmonic from a 800 nm laser will be used to trigger Auger decays in Xe. The illumination of Xe with XUV light with a photon energy of 79.6 eV will lead to $4d_{3/2}$ and $4d_{5/2}$ photoelectrons with energies of 10.1 eV and 12.1 eV, respectively. The inner-shell vacancy may lead to Auger decays. Only little attention so far was paid to the electron structure with smaller energies (Fig. 7.11a). The intense ring in the center with an energy of 0.2 eV is not apparent in the high resolution $N_{4,5}OO$ Auger spectrum of Xe [151].
After the emission of a $4d$ photoelectron, instead of a single Auger decay, a cascaded double Auger decay is observed, where a fast Auger (FA) electron is emitted first and a slow Auger (SA) electron second [161]. Therefore, the strong peak around 0.2 eV is attributed to a SA electron (Fig. 7.11b). The other FA electron is continuously distributed above the SA electron and well below both $4d_{3/2}$ and $4d_{5/2}$ photoelectron rings. In [161] both Auger electrons were measured in coincidence with a magnetic

bottle spectrometer. The ejection of a $4d_{3/2}$ or $4d_{5/2}$ photoelectron triggers several double Auger decay channels. For a certain channel both Auger electron kinetic energies are distributed along a line because they share their kinetic energy sum. In case of a $4d_{5/2}$ hole and a kinetic energy of around 0.2 eV of the SA electron, the FA electron is associated with different Auger decay channels with kinetic energies in the range of 1 eV to 2 eV. Another double Auger decay channel leads to a FA electron with a kinetic energy around 3.2 eV. The spectrum gets even more complicated because the different double Auger decay channels for the $4d_{3/2}$ hole have to be considered as well. A look at the current measurement shows a contribution of electrons up to 1.8 eV, which might be attributed to the FA electrons of the $4d_{5/2}$ hole. Unfortunately, a direct identification of the double Auger decay channels is not possible because, in contrast to the literature, the measurement here was not performed in the coincidence mode. The lifetimes of the FA and SA electrons in the literature were estimated to 6 fs and > 23 fs, respectively, by fitting Lorentzian functions to the measured peaks [161].
At these low energies time delays in photoemission will play an important role. The intrinsic Auger lifetime will lead to a time delay in the emission of an Auger electron. In addition, an energy-dependent time delay between the SA electron and the photoelectron is expected and experimentally investigated in section 7.2.4 using a THz sreak camera. A similar experiment was performed at FLASH to measure the time delays between shake-up electrons and photoelectrons in Ne with a reaction microscope [53].

7.2.2 Estimation of the terahertz field strength using single-photon ionization

In the presence of THz radiation, electron images were obtained in time steps of 29 fs (Fig. 7.12). The measurements were acquired with a Basler camera, where individual images were taken with an exposure time of 30 ms and a gain of 25. For each time delay 25 k images were averaged. For all measurements the voltages -5.50 kV and -4.16 kV were applied to the Repeller and Extractor electrodes. The maximum transferred momentum to the photoelectrons is about $\Delta p_y = 0.114$ a.u. (Fig. 7.12b). Obviously, the intense ring of the SA electrons is smeared out over the background electrons while the $4d$ photoelectrons are shifted upwards.
The vector potential A_{THz} can be obtained from the shift of the $4d_{3/2}$ and $4d_{5/2}$ photoelectron rings (Fig. 7.13a). Unfortunately, a complete temporal profile of the THz pulse cannot be reconstructed because streaking data was not acquired for all relevant time delays. The maximum vector potential A_{THz} is close to the value obtained from the ATI measurements (Fig. 7.2a). A temporal derivative of the vector potential leads to the electric field (Fig. 7.13b), which is also similar to the values extracted from the multiphoton THz streaking experiment (Fig. 7.2b). Note that the acquisition time was not long enough to obtain a sufficient signal-to-noise ratio for a determination of the XUV pulse duration.

7.2.3 Low-energy Auger electron rescattering from ionic core

As shown in the experimental measurement in the presence of THz radiation, the structure of the SA electrons is smeared out (Fig. 7.12b). A possible explanation

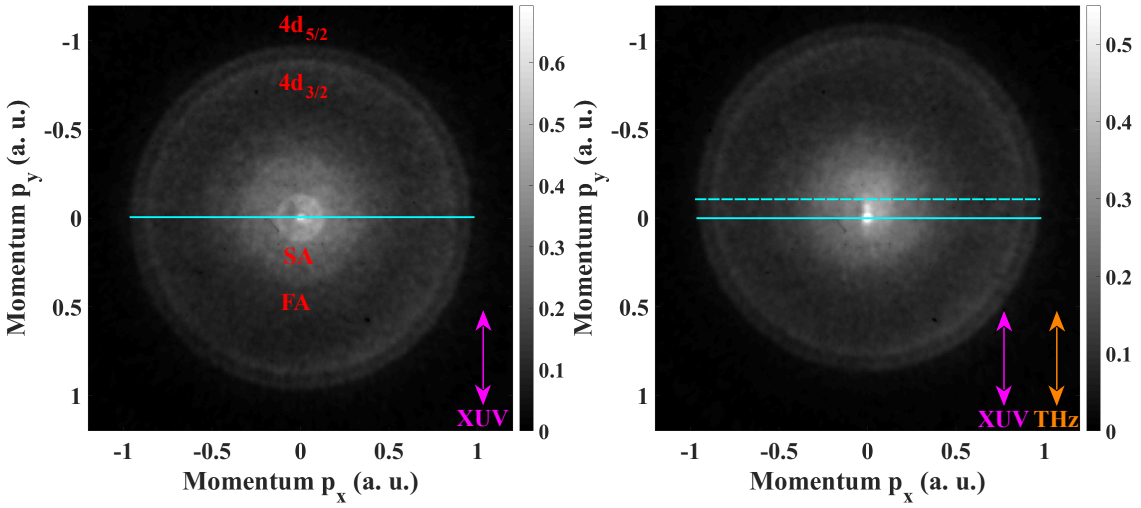

(a) Without THz (b) With THz

Figure 7.12: Measured HHG photoelectron momentum distribution without Abel inversion, i.e. raw image. The linear polarizations of the XUV pulse (purple) and the THz pulse (orange) are aligned vertically. In the presence of the THz field, the photoelectron distribution is shifted (dashed cyan line) with respect to the case with no THz (solid cyan line). Repeller and Extractor voltage are $V_{\mathrm{R}} = -5.50\,\mathrm{kV}$ and $V_{\mathrm{E}} = -4.16\,\mathrm{kV}$, respectively. (a) Without THz, the outer rings correspond to the $4d_{3/2}$ and $4d_{5/2}$ orbitals while FA and SA denote the fast Auger and slow Auger electrons, respectively. (b) Streaked (with THz) with the maximum photoelectron momentum shift around $\Delta p_y = 0.114\,\mathrm{a.u.}$

of this effect could be rescattering of the SA electrons at the ionic core. Consequently, the classical model, which was introduced in section 7.1.3, will be used to qualitatively describe the rescattering process. Due to the double Auger process, the SA electron will move in the vicinity of a Xe^{3+} ion and thus the product Q_1Q_2 in Eq. (7.4) is set to $-3e^2$. Similar as described in that section, the initial conditions for the position and velocity were defined according to Eqs. (7.6) and (7.7), where the initial radius $r_0 = 1.08\text{Å}$ is chosen for simplicity and the initial velocity v_0 is defined such that the energy of the SA electron in the continuum in the absence of THz radiation is 0.2 eV. The time delay between the XUV and THz pulse was set to the case of maximum streaking, i.e. maximum THz vector potential, $\Delta t_2 = -58\,\mathrm{fs}$ (Fig. 7.7). For a qualitative description, the THz electric field (Eq. (7.5)) was scaled to $E_{\mathrm{THz}} \rightarrow qE_{\mathrm{THz}}$ with $q = 0.40; 0.50; 0.60; 0.75; 1.00$ (Fig. 7.14). The bigger the scaling parameter q the larger is the shift of the circular pattern in the vertical direction. Furthermore, at $q = 0.60$ another pattern occurs below the main pattern and is attributed to rescattering in the backward direction. The contribution of this additional part is more pronounced for higher q parameters. To avoid rescattering effects, $q = 0.60$ will be chosen for the experimental investigation.

7.2.4 Time delays in photoemission of Xenon

As already mentioned in section 7.2.1 the time delay between the SA electrons and the $4d_{5/2}$ photoelectrons will be analyzed. Generally, the emission of an inner-shell

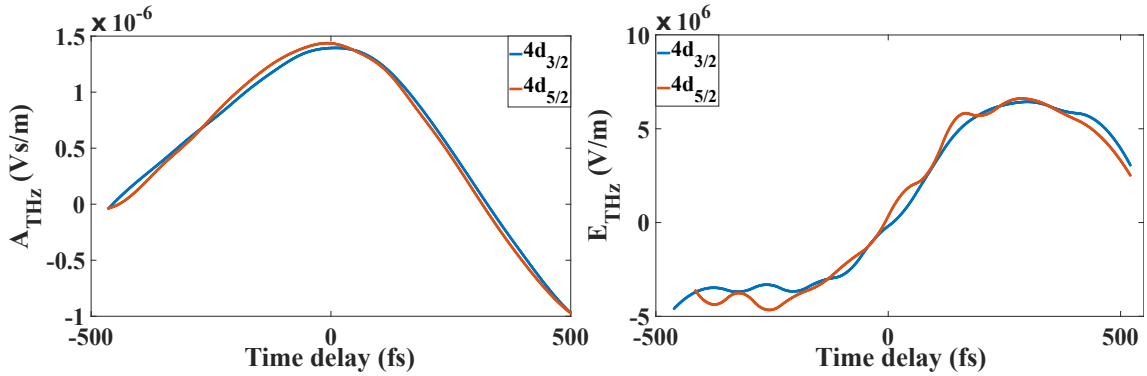

(a) THz vector potential (b) THz electric field

Figure 7.13: Reconstruction of the THz streaking field for the $4d_{3/2}$ and $4d_{5/2}$ photoelectron peaks. Repeller and Extractor voltage are $V_{\mathrm{R}} = -5.50\,\mathrm{kV}$ and $V_{\mathrm{E}} = -4.16\,\mathrm{kV}$, respectively. (a) THz vector potential $A_{\mathrm{THz}}(t) = \Delta p/e$, (b) THz electric field $E_{\mathrm{THz}} = -\partial A_{\mathrm{THz}}/\partial t$.

photoelectron can be followed by an Auger electron, which is ejected at a later time. The release of the Auger electron is mainly determined by the Auger lifetime τ_{AE}. For example, the lifetime of an $\mathrm{N_{4,5}OO}$ Auger electron in Xe after the ionization of a $4d_{3/2}$ photoelectron is $\tau_{\mathrm{AE}} = 6.3\,\mathrm{fs}$. In addition, the ejection of any electron lead to a time delay τ_d, which is strongly pronounced for low kinetic energies and plays an important role in the current experiment. After a short introduction of time delays in photoemission and Auger decays, the experimental results will be presented.

Time delays in photoemission

The time delay acquired by an electron during the emission process is given by

$$\tau_d = \tau_{\mathrm{EWS}} + \tau_{\mathrm{CLC}}, \tag{7.9}$$

where τ_{EWS} is the Eisenbud-Wigner-Smith (EWS) shift and τ_{CLC} the shift induced by Coulomb-laser coupling (CLC). According to the literature [172], the EWS shift is a function of the electron kinetic energy E_{kin}, the ionization state Z (e.g. $\mathrm{Xe}^{3+} \rightarrow Z = 3$) and the quantum number l and in atomic units given by

$$\tau_{\mathrm{EWS}} = \frac{Z}{(2E_{\mathrm{kin}})^{1.5}} \ln \sqrt{\eta^2 + L^2}, \tag{7.10}$$

where $L = l{+}1/2$ is the angular momentum of the bound electron and $\eta = Z/\sqrt{2E_{\mathrm{kin}}}$ the Coulomb-Sommerfeld parameter. For small energies the η-parameter becomes dominant and converges to

$$\tau_{\mathrm{EWS}}(\eta \gg L) = \frac{Z}{(2E_{\mathrm{kin}})^{1.5}} \ln \eta. \tag{7.11}$$

This formulation is in agreement with another theory paper [173]. In case of an electron with a kinetic energy $E_{\mathrm{kin}} = 0.2\,\mathrm{eV}$ and $Z = 3$, the EWS time shift is 130 fs (Fig. 7.15a).

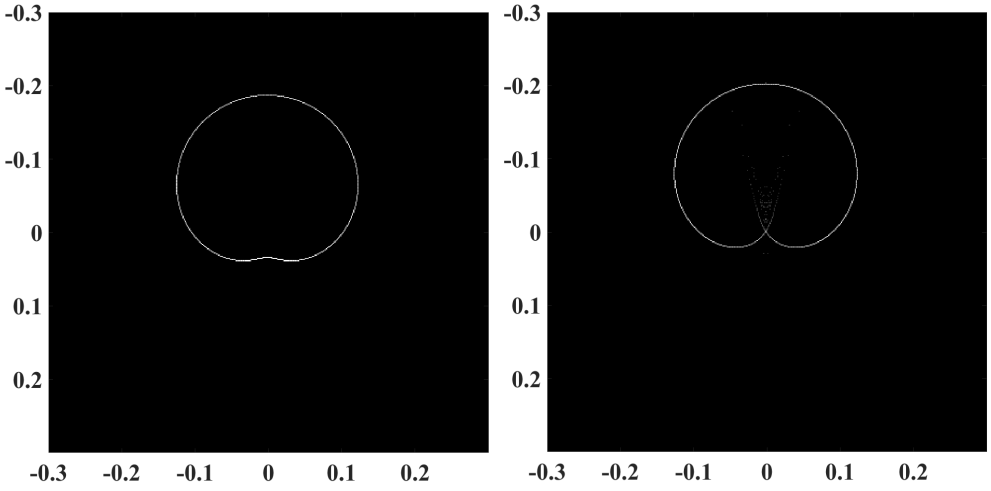

(a) $q = 0.40$ (b) $q = 0.50$

(c) $q = 0.60$ (d) $q = 0.75$

(e) $q = 1.00$

Figure 7.14: SA electron in the presence of the THz field for a time delay of $\Delta t_2 = -58\,\mathrm{fs}$ (see Fig. 7.7). Both axes represent the momentum the SA electron (in atomic units). The THz electric field is linearly polarized along the vertical axis, modeled according to Eq. (7.5) and scaled with q, i.e. $E_{\mathrm{THz}} \to qE_{\mathrm{THz}}$. The corresponding q-parameters are listed below each graph.

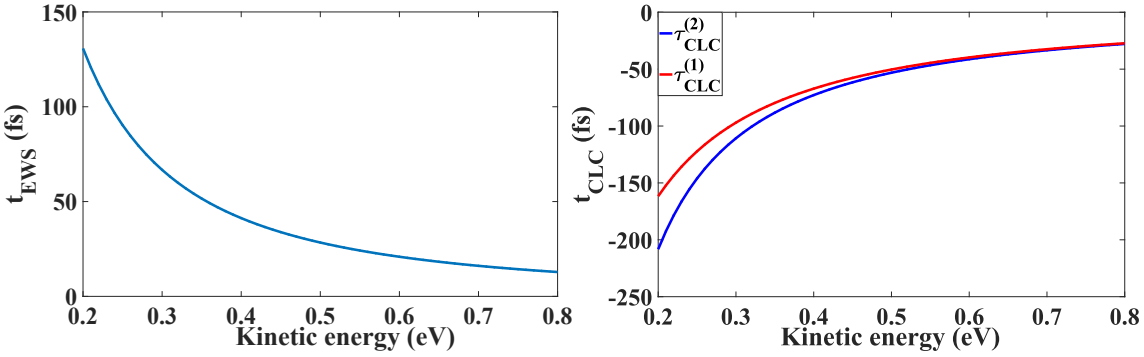

(a) EWS time shift (b) CLC time shift

Figure 7.15: Time shifts as a function of the kinetic energy and $Z = 3$. (a) EWS time shift t_{EWS} using Eq. (7.11), (b) CLC time shift $t^{(1,2)}_{\mathrm{CLC}}$ using Eqs. (7.12) and (7.13). The energy of the streaking field is $\hbar\omega = 3.23\,\mathrm{meV}$ (0.78 THz).

The second time shift, t_{CLC}, is induced by the streak field in combination with the $-Z/r$ long-range character of the Coulomb potential and is a universal feature, thus does not depend on the target gas [174]. According to [172], the CLC time shift in atomic units is given by

$$\tau^{(1)}_{\mathrm{CLC}} = \frac{Z}{(2E_{\mathrm{kin}})^{1.5}}\left[1 - \ln\left(0.37E_{\mathrm{kin}}\frac{2\pi}{\omega}\right)\right], \tag{7.12}$$

where ω is the streaking frequency. Another formulation of the CLC time shift in atomic units is given by [175]

$$\tau^{(2)}_{\mathrm{CLC}} = -\alpha(a)t_{\mathrm{EWS}} - \frac{1}{1+\alpha(a)(2E_{\mathrm{kin}})^{1.5}}\frac{Z}{(2E_{\mathrm{kin}})^{1.5}}\left[\ln\frac{4E_{\mathrm{kin}}}{\omega} - 1 - \gamma + \frac{0.75\pi\omega Z}{(2E_{\mathrm{kin}})^{1.5}}\right], \tag{7.13}$$

where $a = Z\omega/(2E_{\mathrm{kin}})^{1.5}$, $\alpha = \frac{\pi}{2}a - \frac{3}{2}a^2\left(\ln\frac{2}{a} - \frac{1}{6} - \gamma\right)$ and $\gamma \approx 0.5772$. Obviously, both time shifts $\tau^{(1,2)}_{\mathrm{CLC}}$ are more pronounced for small energies E_{kin} and small streaking frequencies ω. Note that bigger differences between both curves appear at low electron energies E_{kin} (Fig. 7.15b). For the double Auger decay, $Z = 3$ was assumed and the energy of the streaking field was $\hbar\omega = 3.23\,\mathrm{meV}$, which corresponds to a frequency of 0.78 THz.

Auger decay

The following theoretical description is based on [176]. The absorption of a high-energy photon may lead to the ejection of an inner-shell photoelectron and one Auger electron in the case of a single Auger decay. Note that the theoretical approach is also valid for a double Auger decay process. In this case the photoelectron is associated with the Xe $4d_{5/2}$ orbital and the Auger electron is associated with the SA electron from the double Auger decay. For simplicity, the FA electron of the double Auger decay process is neglected.

On a femtosecond timescale the photoelectron follows instantaneously the envelope

of the ionizing ultrashort light pulse, i.e. $I_{\mathrm{PE}}(t) \propto I_{\mathrm{XUV}}(t)$. Assuming a Gaussian profile, the intensity of the XUV light pulse is given by

$$I_{\mathrm{XUV}}(t) = I_0 \exp\left(-\frac{t^2}{2\sigma^2}\right), \tag{7.14}$$

where σ denotes the root mean square of the Gaussian envelope and is related by $\tau = 2\sigma\sqrt{2\ln 2}$ to the FWHM. The subsequent Auger electron decays exponentially

$$\mathrm{AE}(t) = \begin{cases} A_1 \exp\left(-\frac{t-t_0}{\tau_{\mathrm{AE}}}\right), & \text{if } t \geq t_0 \\ 0, & \text{otherwise,} \end{cases} \tag{7.15}$$

where τ_{AE} is the Auger lifetime, t_0 the beginning of the Auger decay and A_1 the initial number of core vacancies. The resulting Auger emission rate is then calculated by a convolution of the intensity of the XUV light pulse and the Auger electron decay.

$$\begin{aligned} I_{\mathrm{Auger}}(t) &= I_{\mathrm{XUV}}(t) \circledast \mathrm{AE}(t) \\ &= A_1 \frac{\sigma\sqrt{2\pi}}{2} \exp\left[\frac{1}{\tau_{\mathrm{AE}}}\left(t_0 - t + \frac{\sigma^2}{2\tau_{\mathrm{AE}}}\right)\right] \cdot \left[1 - \mathrm{erf}\left(\frac{1}{\sigma\sqrt{2}}\left(t_0 - t + \frac{\sigma^2}{\tau_{\mathrm{AE}}}\right)\right)\right] \end{aligned} \tag{7.16}$$

A detailed derivation of this formula can be found in the appendix (see section A.3). According to the convolution, the shape of the Auger emission rate strongly depends on the ratio of the XUV pulse duration σ and the Auger lifetime t_{AE}. If the pulse duration σ is larger than the Auger lifetime τ_{AE}, the shape of the Auger emission rate follows the shape of the XUV intensity. The occurring time shift Δt between both profiles is a function of σ, τ_{AE} and t_0. For example, the ionization of a $4\mathrm{d}_{3/2}$ photoelectron in Xe with an ultrashort pulse $\sigma = 8.59\,\mathrm{fs}$ (corresponds to 20 fs FWHM) may lead to the emission of an Auger electron that decays with $\tau_{\mathrm{AE}} = 5.90\,\mathrm{fs}$. Even in case of no additional delay ($t_0 = 0$), the resulting time delay between both Auger electron and photoelectron is around 4.6 fs (Fig. 7.16a). The analysis shows that for a given Auger lifetime τ_{AE} the corresponding time shift Δt changes rapidly the smaller the pulse duration σ is. On the other side, the differences in Δt decrease the larger the pulse duration σ is (Fig. 7.16b). Note that the time delay was defined as the difference between the maxima of the photoelectron and Auger electron signal.

Experimental results

After the introduction of time delays in photoemission and a quantitative description of an Auger decay, details of the experimental measurement will be provided. As already mentioned, a double Auger decay at low energies after ionizing the $4d$ shell is observed. The strong peak at 0.2 eV is associated with SA electrons while the FA electrons are distributed continuously up to 2 eV. As shown in the previous section for maximum electric field ($q = 1.0$), rescattering of the SA electrons at the ionic core occurs and the corresponding ring cannot be distinguished from the background. Therefore, the THz electric field was reduced to 60% ($q = 0.60$). The maximum momentum transferred to the SA electrons is around $\Delta p_y^{\mathrm{max}} = 0.068$ a.u.

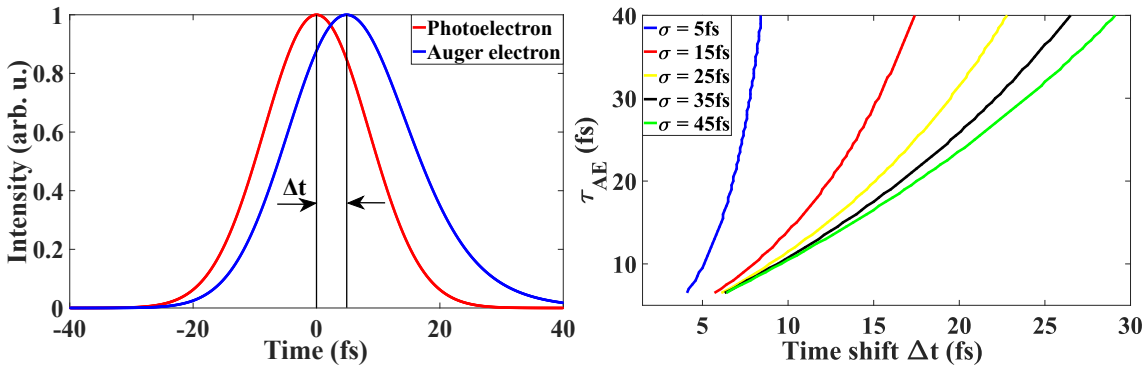

(a) $\sigma = 8.59\,\text{fs}$, $\tau_{\text{AE}} = 5.90\,\text{fs}$ (b) $\sigma = 8.59\,\text{fs}$, varying τ_{AE}

Figure 7.16: Calculation of the Auger decay emission rate using Eq. (7.16) assuming $t_0 = 0$ (a) Time delay $\Delta t = 4.9\,\text{fs}$ between the emission of a $4\text{d}_{3/2}$ photoelectron (red curve) in Xe and an Auger electron (blue curve) with a lifetime of 5.90 fs. The red curve was calculated from Eq (7.14). (b) Relation between Δt and the Auger lifetime. The respective pulse durations (rms) are given in the legend.

(Fig. 7.17). Experimentally, the reduction of the THz field strength was realized by turning the half-waveplate before the cLNB crystal in the THz setup. For a better quality single-shot images were acquired with the Optronis camera together with centroiding at variable time delays between the XUV and THz electric field. Both electric fields were again linearly polarized along the vertical axis. The time delay between both fields was also varied in steps of 29 fs and a clear shift between the $4d_{5/2}$ photoelectrons and the SA electrons is visible (Fig. 7.18). The idea is now to study the dynamics of the SA electrons and the $4d_{5/2}$ photoelectrons.
The momentum of the streaked electrons along the linear polarization of the THz field can be modeled with a periodic function and a fixed THz frequency of $f_{\text{THz}} = 0.78\,\text{THz}$, which was obtained from fitting the experimental streak curve. This approach is similar the the one that was applied to another experiment [53]. Therefore, the electron momentum along the streak direction is given by

$$p_i(t) = p_{i,0} + \hat{p}_e \cos\left[2\pi f_{\text{THz}}\left(t + \Delta t_i\right)\right], \tag{7.17}$$

where $i \in \{P, A\}$ (P: photoelectron, A: Auger electron). The offset $p_{i,0}$ was fixed to $-0.017\,\text{a.u.}$ in both cases. A fit of both curves provides a measured time shift $\Delta t^{(\text{exp})}$ of

$$\begin{aligned} \Delta t_A &= (51.4 \pm 34.8)\,\text{fs} \\ \Delta t_P &= (94.0 \pm 20.8)\,\text{fs} \\ \Rightarrow \Delta t^{(\text{exp})} &= \Delta t_P - \Delta t_A = (45.6 \pm 55.6)\,\text{fs} \end{aligned} \tag{7.18}$$

This value should be now compared to the expected theoretical value. On the one hand, the induced time delay for the $4d_{5/2}$ photoelectron can be neglected because at these high kinetic energies t_{CLC} and t_{EWS} are in the sub femtosecond regime. On the other hand, the SA electron with a kinetic energy of $E_{\text{kin}} = 0.2\,\text{eV}$ and a streaking energy of $\hbar\omega = 3.23\,\text{meV}$ (corresponding to 0.78 THz) leaves behind a Xe^{3+} ion (i.e. $Z = 3$) and a total time delay of

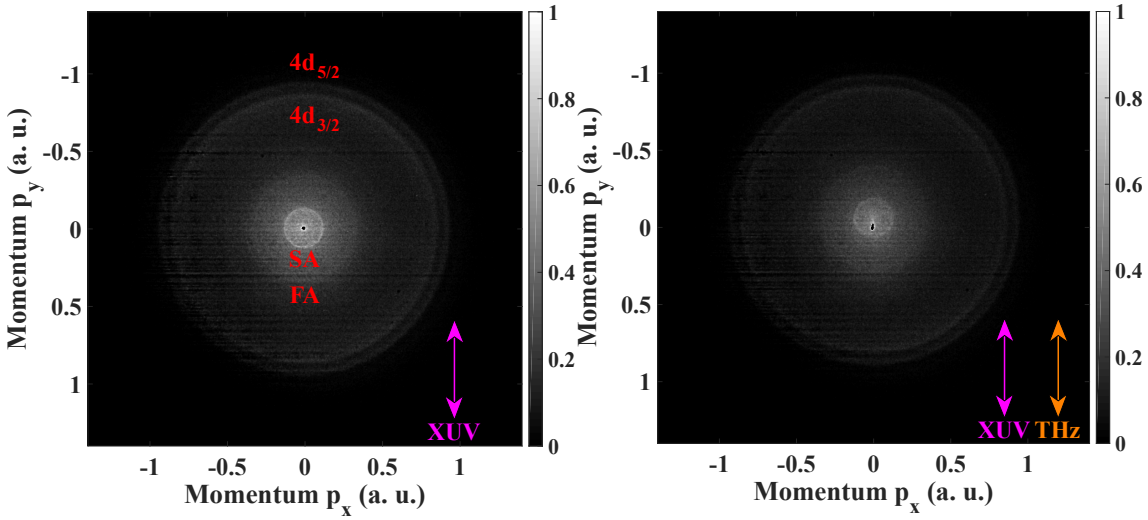

(a) Without THz (b) With THz

Figure 7.17: Momentum distribution with an excitation energy of 79.6 eV. The polarization of the XUV and THz beam point along the p_y direction. Repeller and Extractor voltage are $V_{\mathrm{R}} = -3.20\,\mathrm{kV}$ and $V_{\mathrm{E}} = -2.36\,\mathrm{kV}$, respectively. (a) no THz, the outer rings correspond to the $4d_{3/2}$ and $4d_{5/2}$ orbitals while FA and SA denote the fast Auger and slow Auger electron, respectively. (b) reduced THz with the maximum positive shift.

$$\begin{aligned} \tau_d^{(1,2)} &= \tau_{\mathrm{EWS}} + \tau_{\mathrm{CLC}}^{(1,2)}, \\ \tau_d^{(1)} &= -31\,\mathrm{fs}, \\ \tau_d^{(2)} &= -77\,\mathrm{fs}, \end{aligned} \tag{7.19}$$

where τ_{EWS} is given by Eq. (7.10) and $\tau_{\mathrm{CLC}}^{(1,2)}$ are given by Eqs. (7.12) and (7.13), respectively. A theoretical description of the Auger decay is given by Eq. (7.16). Here, the offset t_0 can be associated with the absolute value of the total time delay $\tau_d^{(1,2)}$, the pulse duration is assumed to be $\sigma = 8.59\,\mathrm{fs}$ (corresponding to 20 fs FWHM) and the Auger decay time $\tau_{\mathrm{AE}} = 23\,\mathrm{fs}$ of the SA electron is taken from the literature [161] (Fig. 7.19). The resulting theoretical time delays are

$$\begin{aligned} \Delta t_1^{(\mathrm{theo})} &= 42\,\mathrm{fs}, \\ \Delta t_2^{(\mathrm{theo})} &= 87\,\mathrm{fs}. \end{aligned} \tag{7.20}$$

Consequently, the experimental time delay $\Delta t^{(\mathrm{exp})}$ overlaps with the expected theoretical time shift $\Delta t_{1,2}^{(\mathrm{theo})}$. The dominant term in the theoretical time shift is the offset $t_0 = \tau_d^{(1,2)}$. Even a double Auger decay time of $2\tau_{\mathrm{AE}} = 46\,\mathrm{fs}$ leads only to $\Delta t_{1,2}^{(\mathrm{theo})} = 44\,\mathrm{fs}\,(91\,\mathrm{fs})$, which still overlaps with the experimental time delay $\Delta t^{(\mathrm{exp})}$.

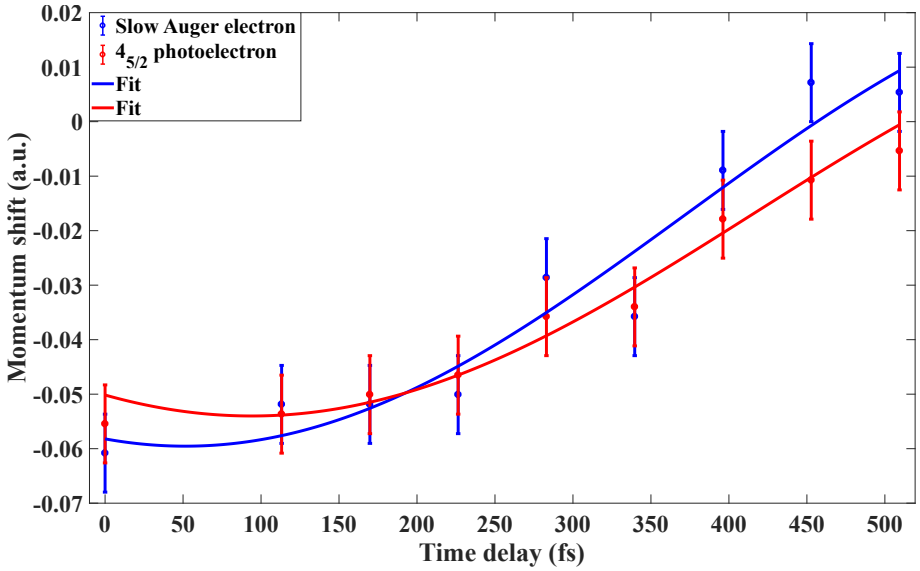

Figure 7.18: THz induced shift of the $4d_{5/2}$ photoelectron and the slow Auger electron as a function of the time delay between the XUV and THz pulse. The time shift between both periodic functions is obtained to $\Delta t^{(\mathrm{exp})} = (45.6 \pm 55.6)\,\mathrm{fs}$.

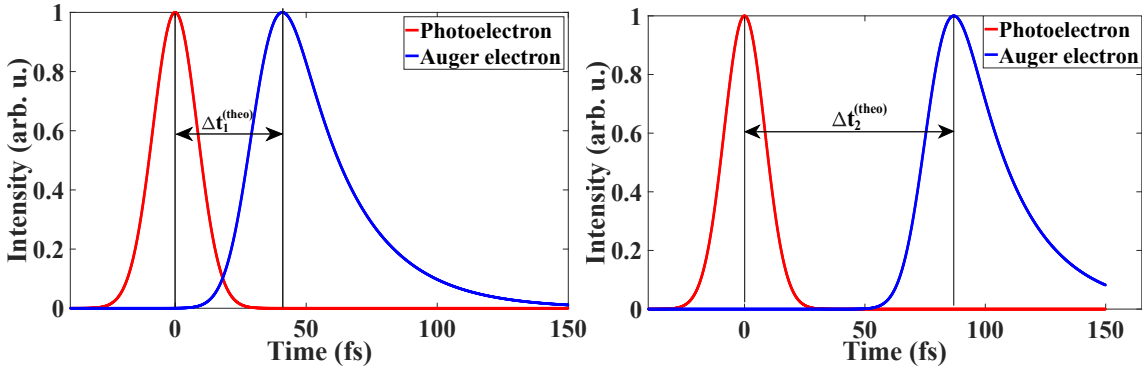

(a) $\sigma = 8.59\,\mathrm{fs}$, $t_0 = \left|\tau_d^{(1)}\right| = 31\,\mathrm{fs}$ (b) $\sigma = 8.59\,\mathrm{fs}$, , $t_0 = \left|\tau_d^{(2)}\right| = 77\,\mathrm{fs}$

Figure 7.19: Calculation of the SA electron emission rate in Xe using Eq. (7.16) assuming $\tau_{\mathrm{AE}} = 23\,\mathrm{fs}$ (a) $t_0 = \tau_d^{(1)}$ resulting to $\Delta t_1^{(\mathrm{theo})} = 42\,\mathrm{fs}$. (b) $t_0 = \tau_d^{(2)}$ resulting to $\Delta t_2^{(\mathrm{theo})} = 87\,\mathrm{fs}$.

Chapter 8

Conclusion and outlook

Within the scope of this thesis, a table-top THz streak camera was successfully implemented to measure the angular photoelectron momentum distribution using a VMIS with a novel capillary gas injection. The geometry of the VMIS was optimized with extensive computer simulations. In particular, the VMIS was designed such that the incoupling of THz radiation between the Repeller and Extractor electrodes is possible. The novel capillary gas injection delivers a high gas load into the interaction volume and at the same time preserves its energy resolution. It was experimentally shown that by applying the proper voltage to the capillary gas injection, a relative detector energy resolution of 3.3% for the $N_{4,5}OO$ Auger electrons in Xe could be achieved. The VMIS is equipped with a high-speed camera allowing for single-shot electron detection in the continuous mode. A post-processing centroiding algorithm was implemented to improve the resolution of the obtained images. A possible application could be a single-shot coincidence experiment of $N_{4,5}OO$ Auger electrons and $4d$ photoelectrons in Xe using a THz streak camera in combination with this VMIS. As already shown, both electrons will exchange kinetic energy due to long-range post-collision interaction leading to an energetic chirp of the Auger electron wavepacket [26]. In this experiment the effect was averaged over several electron pairs. Based on this, a single-shot detection would allow to determine the angular correlation of the Auger electron/ photoelectron pairs.
Strong near single-cycle THz pulses were produced with a new tilted-pulse-front setup and a single achromatic imaging lens in a cLNB crystal by optical rectification. Carrier-envelope phase stable THz pulses were generated with a broadband NIR pump pulse. The temporal profile of the THz pulse was measured with EO sampling and electric field amplitudes up to 3.25 MV/m were obtained. The beam radii ($1/e^2$) of the focused THz radiation were around 1 mm and therefore THz electric fields could be delivered close to the capillary gas injection. The NIR-to-THz conversion efficiency was determined to be 0.06% and is comparable to other uncooled tilted-pulse-front setups.
In this work, also a new HHG source was developed, implemented and characterized with an HHG spectrometer. As a target gas Ne up to a few 100 mbar was supplied to the HHG source. Harmonics up to the 57^{th} order were detected and the 51^{st} harmonic order was selected and guided into the interaction volume by one plane and one focusing Mo/Si-multilayer mirror. The number of XUV photons $N = 5500$ in the interaction volume was measured with a calibrated XUV photodiode resulting to a conversion efficiency of 0.39×10^{-9}.
Two experiments were carried out with a table-top THz streak camera. In the first part, the dynamics of low-energy (LE) photoelectrons, that scatter from the ionic core in Xe, were experimentally investigated. Using intense NIR pulses, the simultaneous absorption of multiple photons leads to LE photoelectrons. Momemtum is transferred to these photoelectrons by the additional superposition with THz pulses. Depending on the time delay between the NIR and THz pulse, the photoelectrons

can be decelerated and may rescatter from the ionic core. In this case, the momentum distribution of the photoelectrons is strongly modulated. Their kinetic energy in the continuum is significantly higher than directly emitted photoelectrons that are not rescattered. An advantage of the current setup is that the ionization and steering of photoelectrons are decoupled and realized by two different light fields. Rescattering can be easily influenced by changing the time delay between both light pulses. The emphasis of future work will be on a better theoretical understanding of the rescattered LE photoelectrons. Ongoing quantum-mechanical calculations, based on solving the TDSE, have to be compared to the experimental data [167, 168] and the literature (e.g. [177]). The current classical model describes only qualitatively the measured photoelectron momentum distribution. However, the initial spatial and momentum distribution of the photoelectrons after the ionization is still not known. A simpler approach to theoretically describe this process would be a two-step semiclassical model: (i) ionization of the photoelectrons by the NIR electric field and (ii) evolution of the photoelectrons in the THz electric field. While the initial conditions for the photoelectrons after the ionization in the first step could be obtained from quantum-mechanical calculations, the evolution of the photoelectrons could be described classically (as already done). Semiclassical models were already used in experiments were phase-dependent photoelectron momentum distributions of orthogonal light fields were studied [171, 178]. The universal LE photoelectron peak [42] was also analyzed with semiclassical models [43, 45]. A development of a semiclassical model in the present experiment is still challenging because the estimation of the Keldysh parameter $\gamma > 3$ suggests that we are in the deep multiphoton regime. Furthermore, a semiclassical or fully quantum-mechanical model could also explain what fraction of photoelectrons is rescattered. According to the literature, the number of rescattered photoelectrons scales with $\lambda_{\mathrm{THz}}^{-4}$, when neglecting the influence of the Coulomb potential [170]. In the current measurements, however, a large fraction of photoelectrons is rescattered, which is due to the Coulomb potential and the slow photoelectrons. A next step could be to investigate by simulations whether THz radiation can be combined with light-induced electron diffraction (LIED). It was already shown that the returning probability of the photoelectron wavepacket carries structural information on the ionized orbital [179]. Moreover, another group already showed that structural information, such as bond lengths of the initial system, can be retrieved by LIED [180].

In the second part, a double Auger decay in Xe was experimentally investigated. The ionization of $4d$ photoelectrons using the 51^{st} harmonic of an HHG source leads to several Auger decay channels. A dominant decay channel is a double Auger decay, where a slow Auger (SA) and a fast Auger electron are emitted. It turned out, that in the presence of THz radiation, a relative time shift between the SA electron and the $4d_{5/2}$ photoelectron momentum distributions was observed. This relative time shift is a result of two contributions. First, the SA electron has a lifetime of $\tau_{\mathrm{AE}} > 23\,\mathrm{fs}$ leading to a later ejection. Second, time delays in the emission of photo- and Auger electrons have to be taken into account. Generally, such a time delay consists of two parts: (i) an intrinsic part (Eisenbud-Wigner-Smith time delay), which is determined by the kinetic energy and the angular momentum of the photoelectron and the ionization state of the ionized target gas and (ii) a measurement induced part (Coulomb-laser-coupling (CLC) time delay), which is a result of the probe field combined with the atomic Coulomb potential. Both contributions

are strongly pronounced for low kinetic energies and the CLC time delay becomes dominant for long wavelengths, i.e. in the THz range. As a result, the SA electron is significantly delayed because its kinetic energy is on the order of 0.2 eV while the induced delay of the $4d_{5/2}$ photoelectron (around 10 eV kinetic energy) can be neglected. The expected total time delay of the SA electron was measured to be

$$\Delta t^{(\mathrm{theo})} = (64.5 \pm 22.5)\,\mathrm{fs}. \tag{8.1}$$

The big error bar is a consequence of the different values of the CLC time delays given by Eqs. (7.12) and (7.13) from the literature [172, 175]. The measured total time delay is

$$\Delta t^{(\mathrm{exp})} = (45.6 \pm 55.6)\,\mathrm{fs} \tag{8.2}$$

and is in good agreement with the expected interval. Numerous groups have also measured time delays in photoionization processes in the attosecond time domain, were photoelectrons were generated in noble gases with XUV radiation and streaked by NIR pulses [50, 52, 181]. In a recent experiment this concept was transferred into the femtosecond regime with THz streaking, where relative time shifts up to 70 fs were measured between LE photoelectrons and $2p$ photoelectrons in Ne [53]. Nevertheless, the question is whether we can transfer those concepts from attosecond streaking to femtosecond streaking using THz wavelengths, which are more than two orders of magnitude larger than NIR laser wavelengths. Therefore, further theoretical analysis are necessary to fully understand the current measurement. In addition, the big error bar of $\Delta t^{(\mathrm{exp})}$ in Eq. (8.1) can be reduced by improving the statistics in the experiment.

Bibliography

1. Muybridge, E. *The Horse in Motion* 1878.
2. Technology, M. I. o. *The Edgerton Digital Collections project* https://edgerton-digital-collections.org/.
3. Maiman, T. H. Stimulated Optical Radiation in Ruby. *Nature* **187,** 493–494 (1960).
4. Strickland, D. *et al.* Compression of amplified chirped optical pulses. *Optics Communications* **55,** 447–449 (1985).
5. Keller, U. *et al.* Femtosecond pulses from a continuously self-starting passively mode-locked Ti:sapphire laser. *Optics Letters* **16,** 1022–1024 (1991).
6. Gaumnitz, T. *et al.* Streaking of 43-attosecond soft-X-ray pulses generated by a passively CEP-stable mid-infrared driver. *Optics Express* **25,** 27506–27518 (2017).
7. Zewail, A. H. Laser Femtochemistry. *Science* **242,** 1645 (1988).
8. McPherson, A. *et al.* Studies of multiphoton production of vacuum-ultraviolet radiation in the rare gases. *Journal of the Optical Society of America B* **4,** 595–601 (1987).
9. Ferray, M. *et al.* Multiple-harmonic conversion of 1064 nm radiation in rare gases. *Journal of Physics B: Atomic, Molecular and Optical Physics* **21,** L31–L35 (1988).
10. Bradley, D. J. *et al.* Direct linear measurement of ultrashort light pulses with a picosecond streak camera. *Optics Communications* **2,** 391–395 (1971).
11. Bradley, D. J. *et al.* Picosecond Electron-Optical Chronography. *Applied Physics Letters* **20,** 219–221 (1972).
12. Drescher, M. *et al.* X-ray Pulses Approaching the Attosecond Frontier. *Science* **291,** 1923 (2001).
13. Hentschel, M. *et al.* Attosecond metrology. *Nature* **414,** 509 (2001).
14. Goulielmakis, E. *et al.* Direct Measurement of Light Waves. *Science* **305,** 1267 (2004).
15. Kienberger, R. *et al.* Atomic transient recorder. *Nature* **427.** 10.1038/nature02277, 817–821 (2004).
16. Glover, T. E. *et al.* Observation of Laser Assisted Photoelectric Effect and Femtosecond High Order Harmonic Radiation. *Physical Review Letters* **76.** PRL, 2468–2471 (1996).
17. Frühling, U. *et al.* Single-shot terahertz-field-driven X-ray streak camera. *Nature Photonics* **3,** 523 (2009).
18. Schütte, B. *et al.* Electron wave packet sampling with laser-generated extreme ultraviolet and terahertz fields. *Optics Express* **19,** 18833–18841 (2011).
19. Drescher, M. *et al.* Time-resolved atomic inner-shell spectroscopy. *Nature* **419.** 10.1038/nature01143, 803–807 (2002).

20. Baltuška, A. *et al.* Attosecond control of electronic processes by intense light fields. *Nature* **421,** 611 (2003).

21. Auger, P. Sûr l'effet photoélectrique composé. *J. Phys. Radium* **6,** 205–208 (1925).

22. Barker, R. B. *et al.* Electron Energy Distributions from Ionizing Collisions of Helium and Neon Ions with Helium. *Physical Review* **151.** PR, 14–19 (1966).

23. Niehaus, A. Analysis of post-collision interactions in Auger processes following near-threshold inner-shell photoionization. *Journal of Physics B: Atomic and Molecular Physics* **10,** 1845 (1977).

24. Schmidt, V. *et al.* Post-Collision Interaction in the Xenon $N_{4,5} - OO$ Auger Spectrum Excited by Photon Impact. *Physical Review Letters* **38.** PRL, 63–66 (1977).

25. Åberg, T. Unified Theory of Auger Electron Emission. *Physica Scripta* **1992,** 71 (1992).

26. Schütte, B. *et al.* Evidence for Chirped Auger-Electron Emission. *Physical Review Letters* **108.** PRL, 253003 (2012).

27. Eppink, A. T.J. B. *et al.* Velocity map imaging of ions and electrons using electrostatic lenses: Application in photoelectron and photofragment ion imaging of molecular oxygen. *Review of Scientific Instruments* **68,** 3477–3484 (1997).

28. Ye, H. *et al. Velocity Map Imaging of Electrons Strong-Field Photoemitted from Si-Nanotip* in *19th International Conference on Ultrafast Phenomena* (Optical Society of America), 09.Wed.P3.37.

29. Ye, H. *et al.* Velocity-Map Imaging for Emittance Characterization of Multiphoton Electron Emission from a Gold Surface. *Physical Review Applied* **9.** PRAPPLIED, 044018 (2018).

30. Rolles, D. *et al.* A velocity map imaging spectrometer for electron–ion and ion–ion coincidence experiments with synchrotron radiation. *Nuclear Instruments and Methods in Physics Research Section B: Beam Interactions with Materials and Atoms* **261,** 170–174 (2007).

31. Kling, N. G. *et al.* Thick-lens velocity-map imaging spectrometer with high resolution for high-energy charged particles. *Journal of Instrumentation* **9,** P05005–P05005 (2014).

32. Ghafur, O. *et al.* A velocity map imaging detector with an integrated gas injection system. *Review of Scientific Instruments* **80,** 033110 (2009).

33. Zherebtsov, S. *et al.* Attosecond imaging of XUV-induced atomic photoemission and Auger decay in strong laser fields. *Journal of Physics B: Atomic, Molecular and Optical Physics* **44,** 105601 (2011).

34. Schütte, B. *et al.* Autoionization following nanoplasma formation in atomic and molecular clusters. *Eur. Phys. J. D* **70** (2016).

35. Suran, V. V. *et al.* Observation of Sr^{2+} in multiple-photon ionization of strontium. *Sov. Tech. Phys. Lett.* **1** (1975).

36. L'Huillier, A. *et al.* Multiply Charged Ions Formed by Multiphoton Absorption Processes in the Continuum. *Physical Review Letters* **48.** PRL, 1814–1817 (1982).

37. Agostini, P. *et al.* Free-Free Transitions Following Six-Photon Ionization of Xenon Atoms. *Physical Review Letters* **42.** PRL, 1127–1130 (1979).

38. Paulus, G. G. *et al.* Plateau in above threshold ionization spectra. *Physical Review Letters* **72.** PRL, 2851–2854 (1994).

39. Yang, B. *et al.* Intensity-dependent scattering rings in high order above-threshold ionization. *Physical Review Letters* **71.** PRL, 3770–3773 (1993).

40. Paulus, G. G. *et al.* Rescattering effects in above-threshold ionization: a classical model. *Journal of Physics B: Atomic, Molecular and Optical Physics* **27,** L703–L708 (1994).

41. Becker, W. *et al.* Effects of rescattering on above-threshold ionization. *Journal of Physics B: Atomic, Molecular and Optical Physics* **27,** L325–L332 (1994).

42. Blaga, C. I. *et al.* Strong-field photoionization revisited. *Nature Physics* **5,** 335 (2009).

43. Wu, C. Y. *et al.* Characteristic Spectrum of Very Low-Energy Photoelectron from Above-Threshold Ionization in the Tunneling Regime. *Physical Review Letters* **109.** PRL, 043001 (2012).

44. Smirnova, O. *et al.* Coulomb and polarization effects in sub-cycle dynamics of strong-field ionization. *Journal of Physics B: Atomic, Molecular and Optical Physics* **39,** S307–S321 (2006).

45. Quan, W. *et al.* Classical Aspects in Above-Threshold Ionization with a Mid-infrared Strong Laser Field. *Physical Review Letters* **103.** PRL, 093001 (2009).

46. Guo, L. *et al.* Scaling of the Low-Energy Structure in Above-Threshold Ionization in the Tunneling Regime: Theory and Experiment. *Physical Review Letters* **110.** PRL, 013001 (2013).

47. Li, M. *et al.* Subcycle nonadiabatic strong-field tunneling ionization. *Physical Review A* **93.** PRA, 013402 (2016).

48. Shvetsov-Shilovski, N. I. *et al.* Semiclassical two-step model for strong-field ionization. *Physical Review A* **94.** PRA, 013415 (2016).

49. Wiese, J. *et al.* Strong-field photoelectron momentum imaging of OCS at finely resolved incident intensities. *New Journal of Physics* **21** (2019).

50. Schultze, M. *et al.* Delay in Photoemission. *Science* **328,** 1658 (2010).

51. Ossiander, M. *et al.* Attosecond correlation dynamics. *Nature Physics* **13,** 280 (2016).

52. Isinger, M. *et al.* Photoionization in the time and frequency domain. *Science* **358,** 893 (2017).

53. Schmid, G. *et al.* Terahertz-Field-Induced Time Shifts in Atomic Photoemission. *Physical Review Letters* **122.** PRL, 073001 (2019).

54. Einstein, A. Über einen die Erzeugung und Verwandlung des Lichtes betreffenden heuristischen Gesichtspunkt. *Annalen der Physik* **322,** 132–148 (1905).

55. Becker, U. *et al. VUV and Soft X-Ray Photoionization* 1996.

56. Jurvansuu, M. *et al.* Inherent lifetime widths of Ar $2p^{-1}$, Kr $3d^{-1}$, Xe $3d^{-1}$, and Xe $4d^{-1}$ states. *Physical Review A* **64.** PRA, 012502 (2001).

57. Uiberacker, M. *et al.* Attosecond real-time observation of electron tunnelling in atoms. *Nature* **446,** 627–632 (2007).

58. Sorokin, A. A. *et al.* Photoelectric Effect at Ultrahigh Intensities. *Physical Review Letters* **99.** PRL, 213002 (2007).

59. Boyd, R. W. *Nonlinear Optics* 3rd ed. (Academic Press, Orlando, FL, USA, 2008).

60. Sommer, A. *et al.* Attosecond nonlinear polarization and light–matter energy transfer in solids. *Nature* **534,** 86 (2016).

61. Franken, P. A. *et al.* Generation of Optical Harmonics. *Physical Review Letters* **7.** PRL, 118–119 (1961).

62. Kerr, J. XL. A new relation between electricity and light: Dielectrified media birefringent. *The London, Edinburgh, and Dublin Philosophical Magazine and Journal of Science* **50,** 337–348 (1875).

63. Brabec, T. *et al.* Intense few-cycle laser fields: Frontiers of nonlinear optics. *Reviews of Modern Physics* **72.** RMP, 545–591 (2000).

64. Keldysh. Ionization in the field of a strong electromagnetic wave. *Soviet Physics JETP* **20,** 1307 (1965).

65. Augst, S. *et al.* Laser ionization of noble gases by Coulomb-barrier suppression. *Journal of the Optical Society of America B* **8,** 858–867 (1991).

66. Popmintchev, T. *et al.* Bright Coherent Ultrahigh Harmonics in the keV X-ray Regime from Mid-Infrared Femtosecond Lasers. *Science* **336,** 1287 (2012).

67. Krause, J. L. *et al.* High-order harmonic generation from atoms and ions in the high intensity regime. *Physical Review Letters* **68.** PRL, 3535–3538 (1992).

68. Corkum, P. B. Plasma perspective on strong field multiphoton ionization. *Physical Review Letters* **71.** PRL, 1994–1997 (1993).

69. Lewenstein, M. *et al.* Theory of high-harmonic generation by low-frequency laser fields. *Physical Review A* **49.** PRA, 2117–2132 (1994).

70. Falcão Filho, E. L. *et al.* Scaling of high-order harmonic efficiencies with visible wavelength drivers: A route to efficient extreme ultraviolet sources. *Applied Physics Letters* **97,** 061107 (2010).

71. Shiner, A. D. *et al.* Wavelength Scaling of High Harmonic Generation Efficiency. *Physical Review Letters* **103.** PRL, 073902 (2009).

72. Kim, I. J. *et al.* Generation of submicrojoule high harmonics using a long gas jet in a two-color laser field. *Applied Physics Letters* **92,** 021125 (2008).

73. M.V. Ammosov N.B. Delone, V. K. Tunnel ionization of complex atoms and of atomic ions in an alternating electromagnetic field. *Soviet Physics JETP* **64** (1986).

74. Yudin, G. L. *et al.* Nonadiabatic tunnel ionization: Looking inside a laser cycle. *Physical Review A* **64.** PRA, 013409 (2001).

75. Antoine, P. *et al.* Theory of high-order harmonic generation by an elliptically polarized laser field. *Physical Review A* **53.** PRA, 1725–1745 (1996).

76. Reiss, H. R. Limits on Tunneling Theories of Strong-Field Ionization. *Physical Review Letters* **101.** PRL, 043002 (2008).

77. Balcou, P. *et al.* Phase-matching effects in strong-field harmonic generation. *Physical Review A* **47.** PRA, 1447–1459 (1993).

78. Jan, R. *et al.* Absorption-limited and phase-matched high harmonic generation in the tight focusing regime. *New Journal of Physics* **16,** 033022 (2014).

79. Paul, A. *et al.* Phase-matching techniques for coherent soft X-ray generation. *IEEE Journal of Quantum Electronics* **42,** 14–26 (2006).

80. Constant, E. *et al.* Optimizing High Harmonic Generation in Absorbing Gases: Model and Experiment. *Physical Review Letters* **82.** PRL, 1668–1671 (1999).

81. Fabre, F. *et al.* Multiphoton above-threshold ionisation of xenon at 0.53 and 1.06μm. *Journal of Physics B: Atomic and Molecular Physics* **15,** 1353 (1982).

82. McIlrath, T. J. *et al.* Above-threshold ionization processes in xenon and krypton. *Physical Review A* **35.** PRA, 4611–4623 (1987).

83. Leuchs, G. *et al.* Photoelectron angular distributions in resonant multiphonon ionization of atoms. *Journal of Soviet Laser Research* **6,** 296–303 (1985).

84. Smith, S. J. *et al.* in *Advances in Atomic and Molecular Physics* (eds Bates, D. *et al.*) 157–221 (Academic Press, 1988).

85. Becker, W. *et al.* Low-energy electron rescattering in laser-induced ionization. *Journal of Physics B: Atomic, Molecular and Optical Physics* **47,** 204022 (2014).

86. Lee, Y.-S. *Principles of Terahertz Science and Technology* (Springer, 2009).

87. Hoffmann, M. C. *et al.* Intense ultrashort terahertz pulses: generation and applications. *Journal of Physics D: Applied Physics* **44,** 083001 (2011).

88. Smith, F. W. *et al.* Picosecond GaAs-based photoconductive optoelectronic detectors. *Applied Physics Letters* **54,** 890–892 (1989).

89. Tani, M. *et al.* Emission characteristics of photoconductive antennas based on low-temperature-grown GaAs and semi-insulating GaAs. *Applied Optics* **36,** 7853–7859 (1997).

90. Dreyhaupt, A. *et al.* High-intensity terahertz radiation from a microstructured large-area photoconductor. *Applied Physics Letters* **86,** 121114 (2005).

91. Beck, M. *et al.* Impulsive terahertz radiation with high electric fields from an amplifier-driven large-area photoconductive antenna. *Optics Express* **18,** 9251–9257 (2010).

92. Cook, D. J. *et al.* Intense terahertz pulses by four-wave rectification in air. *Optics Letters* **25,** 1210–1212 (2000).

93. Karpowicz, N. *et al.* Coherent Terahertz Echo of Tunnel Ionization in Gases. *Physical Review Letters* **102.** PRL, 093001 (2009).

94. Schneider, A. *et al.* Generation of terahertz pulses through optical rectification in organic DAST crystals: theory and experiment. *Journal of the Optical Society of America B* **23,** 1822–1835 (2006).

95. Pan, F. *et al.* Electro-optic properties of the organic salt 4-N,N-dimethylamino-4′-N'-methyl-stilbazolium tasylate. *Applied Physics Letters* **69,** 13–15 (1996).

96. Mutter, L. *et al.* Linear and nonlinear optical properties of the organic crystal DSTMS. *Journal of the Optical Society of America B* **24,** 2556–2561 (2007).

97. Ruchert, C. *et al.* Scaling submillimeter single-cycle transients toward megavolts per centimeter field strength via optical rectification in the organic crystal OH1. *Optics Letters* **37,** 899–901 (2012).

98. Jazbinsek, M. *et al. Handbook of Organic Materials for Optical and (Opto)electronic Devices* (Woodhead Publishing Series, 2013).

99. Xianbin, Z. *et al.* The impact of MgO-doped near-stoichiometric lithium niobate crystals on the THz wave output characteristics. *Journal of Physics: Conference Series* (2011).

100. Pálfalvi, L. *et al.* Temperature dependence of the absorption and refraction of Mg-doped congruent and stoichiometric LiNbO3 in the THz range. *Journal of Applied Physics* **97,** 123505 (2005).

101. Stillhart, M. *et al.* Optical properties of 4-N,N-dimethylamino-4′-N'-methyl-stilbazolium $2,4,6$-trimethylbenzenesulfonate crystals at terahertz frequencies. *Journal of the Optical Society of America B* **25,** 1914–1919 (2008).

102. Brunner, F. D. J. *et al.* A hydrogen-bonded organic nonlinear optical crystal for high-efficiency terahertz generation and detection. *Optics Express* **16,** 16496–16508 (2008).

103. Huang, S.-W. *et al.* High conversion efficiency, high energy terahertz pulses by optical rectification in cryogenically cooled lithium niobate. *Optics Letters* **38,** 796–798 (2013).

104. Yeh, K.-L. *The generation of high field terahertz radiation and its application in terahertz nonlinear spectroscopy* PhD (2009).

105. Fülöp, J. A. *et al.* Design of high-energy terahertz sources based on optical rectification. *Optics Express* **18,** 12311–12327 (2010).

106. Hirori, H. *et al.* Single-cycle terahertz pulses with amplitudes exceeding 1 MV/cm generated by optical rectification in $LiNb)_3$. *Applied Physics Letters* **98,** 091106 (2011).

107. Planken, P. C. M. *et al.* Measurement and calculation of the orientation dependence of terahertz pulse detection in ZnTe. *Journal of the Optical Society of America B* **18,** 313–317 (2001).

108. Shakya, M. M. *et al.* Achieving 280fs resolution with a streak camera by reducing the deflection dispersion. *Applied Physics Letters* **87,** 041103 (2005).

109. Feng, J. *et al.* An x-ray streak camera with high spatio-temporal resolution. *Applied Physics Letters* **91,** 134102 (2007).

110. Itatani, J. *et al.* Attosecond Streak Camera. *Physical Review Letters* **88.** PRL, 173903 (2002).

111. Frühling, U. Light-field streaking for FELs. *Journal of Physics B: Atomic, Molecular and Optical Physics* **44,** 243001 (2011).

112. Frühling, U. *Lichtfeld getriebene Streak-Kamera zur Einzelschuss Zeitstrukturmessung der XUV-Pulse eines Freie-Elektronen Lasers* PhD thesis (2009).

113. Quéré, F. *et al.* Temporal characterization of attosecond XUV fields. *Journal of Modern Optics* **52,** 339–360 (2005).

114. Gagnon, J. *et al.* The accurate FROG characterization of attosecond pulses from streaking measurements. *Applied Physics B* **92,** 25–32 (2008).

115. Henke, B. *et al. X-Ray Interactions With Matter* 2019. http://henke.lbl.gov/optical_constants/.

116. Cunningham, P. D. *et al.* Broadband terahertz characterization of the refractive index and absorption of some important polymeric and organic electro-optic materials. *Journal of Applied Physics* **109,** 043505–043505–5 (2011).

117. Nielsen, K. *et al.* Bendable, low-loss Topas fibers for the terahertz frequency range. *Optics Express* **17,** 8592–8601 (2009).

118. Oksenhendler, T. *et al.* Intracavity acousto-optic programmable gain control for ultra-wide-band regenerative amplifiers. *Applied Physics B* **83,** 491 (2006).

119. Feng, C. *et al.* Complete analog control of the carrier-envelope-phase of a high-power laser amplifier. *Optics Express* **21,** 25248–25256 (2013).

120. Iaconis, C. *et al.* Spectral phase interferometry for direct electric-field reconstruction of ultrashort optical pulses. *Optics Letters* **23,** 792–794 (1998).

121. Trebino, R. *et al.* Measuring ultrashort laser pulses in the time-frequency domain using frequency-resolved optical gating. *Review of Scientific Instruments* **68,** 3277–3295 (1997).

122. Kunitski, M. *et al.* Optimization of single-cycle terahertz generation in LiNbO3 for sub-50 femtosecond pump pulses. *Optics Express* **21,** 6826–6836 (2013).

123. Wu, X. *et al.* Terahertz generation in lithium niobate driven by Ti:sapphire laser pulses and its limitations. *Optics Letters* **39,** 5403–5406 (2014).

124. Fülöp, J. A. *et al.* Design of high-energy terahertz sources based on optical rectification. *Optics Express* **18,** 12311–12327 (2010).

125. Ibrahim, A. *et al.* Ultra-high dynamic range electro-optic sampling for detecting millimeter and sub-millimeter radiation. *Scientific Reports* **6,** 23107 (2016).

126. *Imaging in Molecular Dynamics: Technology and Applications* (Cambridge University Press, Cambridge, 2003).

127. Dick, B. *Molecular Spectroscopy and Photochemistry of Isolated Cold Molecules in the Gas Phase* 2019. http://www-dick.chemie.uni-regensburg.de/IonImag.html.

128. Wiley, W. C. *et al.* Time-of-Flight Mass Spectrometer with Improved Resolution. *Review of Scientific Instruments* **26,** 1150–1157 (1955).

129. Moore, J. H. *et al. Building Scientific Apparatus* 4th ed. (Cambridge University Press, Cambridge, 2009).

130. Dahl, D. A. *et al.* SIMION PC/PS2 electrostatic lens design program. *Review of Scientific Instruments* **61,** 607–609 (1990).

131. Dahl, D. A. simion for the personal computer in reflection. *International Journal of Mass Spectrometry* **200,** 3–25 (2000).

132. *Hamamatsu MCP Assembly, Technical Information* 2013. https://www.hamamatsu.com/resources/pdf/etd/MCP_TMCP0002E.pdf.

133. *Basler: the power of sight* 2018. https://www.baslerweb.com/de/produkte/kameras/flaechenkameras/ace/aca1920-40um/.

134. *Optronis CamRecord CL300x2, CL600x2* 2018. https://www.stemmer-imaging.com/media/uploads/docmanager/65942-Optronis_CL300x2_-_CL600x2_Manual.pdf.

135. Süßmann, F. *et al.* Single-shot velocity-map imaging of attosecond light-field control at kilohertz rate. *Review of Scientific Instruments* **82,** 093109 (2011).

136. Hoshen, J. *et al.* Percolation and cluster distribution. I. Cluster multiple labeling technique and critical concentration algorithm. *Physical Review B* **14.** PRB, 3438–3445 (1976).

137. Dick, B. Inverting ion images without Abel inversion: maximum entropy reconstruction of velocity maps. *Physical Chemistry Chemical Physics* **16,** 570–580 (2014).

138. Montgomery Smith, L. *et al.* Abel inversion using transform techniques. *Journal of Quantitative Spectroscopy and Radiative Transfer* **39,** 367–373 (1988).

139. Vrakking, M. J. *Abel inversion of 2D velocity map images using a Legendre polynomial expansion*

140. Vrakking, M. J. J. An iterative procedure for the inversion of two-dimensional ion/photoelectron imaging experiments. *Review of Scientific Instruments* **72,** 4084–4089 (2001).

141. Garcia, G. A. *et al.* Two-dimensional charged particle image inversion using a polar basis function expansion. *Review of Scientific Instruments* **75,** 4989–4996 (2004).

142. Dribinski, V. *et al.* Reconstruction of Abel-transformable images: The Gaussian basis-set expansion Abel transform method. *Review of Scientific Instruments* **73,** 2634–2642 (2002).

143. Dixit, S. N. *et al.* Theory of photoelectron angular distributions in resonant multiphoton ionization. *Physical Review A* **27.** PRA, 861–874 (1983).

144. Bordas, C. *et al.* Photoelectron imaging spectrometry: Principle and inversion method. *Review of Scientific Instruments* **67,** 2257–2268 (1996).

145. Manzhos, S. *et al.* Photofragment image analysis using the Onion-Peeling Algorithm. *Computer Physics Communications* **154,** 76–87 (2003).

146. Zhao, K. *et al.* Deconvolving two-dimensional images of three-dimensional momentum trajectories. *Review of Scientific Instruments* **73,** 3044–3050 (2002).

147. Roberts, G. M. *et al.* Toward real-time charged-particle image reconstruction using polar onion-peeling. *Review of Scientific Instruments* **80,** 053104 (2009).

148. Natan, A. *Polar Onion Peeling* 2018. https://www.mathworks.com/matlabcentral/fileexchange/41064-polar-onion-peeling.

149. Champenois, E. G. *CPBASEX* 2017. https://github.com/e-champenois/CPBASEX.

150. Sumfleth, M. *Datenauswertung und Analyse zur Rekonstruktion von Relativwinkelverteilungen bei koinzidenter Messung von korrelierten Elektronen in einem VMI-Spektrometer* Master thesis (2018).

151. Werme, L. O. *et al.* The High Resolution $L_{2,3}MM$ and $M_{4,5}NN$ Auger Spectra from Krypton and $M_{4,5}NN$ and $N_{4,5}OO$ Auger Spectra from Xenon. *Physica Scripta* **6,** 141 (1972).

152. Hippler, R. *et al.* Angular distribution of photoelectrons from multiphoton ionisation ($\lambda = 532$ nm) of xenon. *Journal of Physics B: Atomic and Molecular Physics* **16,** L713 (1983).

153. Kaminski, P. *et al.* Wavelength dependence of multiphoton ionization of xenon. *Physical Review A* **70.** PRA, 053413 (2004).

154. Stei, M. *et al.* High resolution spatial map imaging of a gaseous target. *The Journal of Chemical Physics* **138,** 214201 (2013).

155. Pfeiffer, V. *The Vacuum Technology Book* ().

156. Scoles, G. *Atomic and molecular beam methods. Vol. 1 Vol. 1* (Oxford University Press, New York; Oxford, 1988).

157. Becker, U. *et al.* Subshell photoionization of Xe between 40 and 1000eV. *Physical Review A* **39.** PRA, 3902–3911 (1989).

158. Ausmees, A. *et al.* High-resolution study of the Xe $4d_{5/2}$:$4d_{3/2}$ branching ratio. *Physical Review A* **51.** PRA, 855–858 (1995).

159. Sheinerman, S. *et al.* Electron correlation in Xe 4d Auger decay studied by slow photoelectron - Auger electron coincidence spectroscopy. *Journal of Physics B: Atomic, Molecular and Optical Physics* **39,** 1017 (2006).

160. Wiedenhoeft, M. *et al.* Coincident energy and angular distributions in xenon $4d_{5/2}$ inner-shell double photoionization. *Journal of Physics B: Atomic, Molecular and Optical Physics* **41,** 095202 (2008).

161. Penent, F. *et al.* Multielectron Spectroscopy: The Xenon $4d$ Hole Double Auger Decay. *Physical Review Letters* **95.** PRL, 083002 (2005).

162. Ullrich, J. *et al.* Recoil-ion and electron momentum spectroscopy: reaction-microscopes. *Reports on Progress in Physics* **66,** 1463–1545 (2003).

163. Schütte, B. *Laser-based terahertz-field-driven streak camera for the temporal characterization of ultrashort processes* PhD thesis (2011).

164. Rallis, C. E. *et al.* Incorporating real time velocity map image reconstruction into closed-loop coherent control. *Review of Scientific Instruments* **85,** 113105 (2014).

165. Gibson, S. *et al. Open-source Python software package (PyAbel)* 2019. https://zenodo.org/record/3243413#.XTnJ4RTgpaR.

166. Van de Sand, G. *et al.* Semiclassical description of multiphoton processes. *Physical Review A* **62.** PRA, 053403 (2000).

167. Kazansky, A. K. *et al.* Theoretical description of atomic photoionization by an attosecond XUV pulse in a strong laser field: effects of rescattering and orbital polarization. *Journal of Physics B: Atomic, Molecular and Optical Physics* **40,** 2163–2177 (2007).

168. Kazansky, A. K. *et al.* Theoretical description of atomic photoionization by attosecond XUV pulses in a strong laser field: the case of p-shell ionization. *Journal of Physics B: Atomic, Molecular and Optical Physics* **40,** 3413–3424 (2007).

169. Clementi, E. *et al.* Atomic Screening Constants from SCF Functions. II. Atoms with 37 to 86 Electrons. *The Journal of Chemical Physics* **47,** 1300–1307 (1967).

170. Agostini, P. *et al.* Atoms in high intensity mid-infrared pulses. *Contemporary Physics* **49,** 179–197 (2008).

171. Würzler, D. *et al.* Velocity map imaging of scattering dynamics in orthogonal two-color fields. *Journal of Physics B: Atomic, Molecular and Optical Physics* **51,** 015001 (2017).

172. Pazourek, R. *et al.* Time-resolved photoemission on the attosecond scale: opportunities and challenges. *Faraday Discussions* **163,** 353–376 (2013).

173. Serov, V. V. *et al.* Interpretation of time delay in the ionization of two-center systems. *Physical Review A* **87.** PRA, 063414 (2013).

174. Ivanov, M. *et al.* How Accurate Is the Attosecond Streak Camera? *Physical Review Letters* **107.** PRL, 213605 (2011).

175. Derbov, V. L. *et al. Attosecond pulse measurements and time delay in the ionization of Coulomb systems* in *2014 16th International Conference on Transparent Optical Networks (ICTON)* (), 1–7.

176. Wenig, K. *et al.* Electronic decay of core-excited HCl molecules probed by THz streaking. *Structural Dynamics* **6,** 034301 (2019).

177. Marchenko, T. *et al.* Electron angular distributions in near-threshold atomic ionization. *Journal of Physics B: Atomic, Molecular and Optical Physics* **43,** 095601 (2010).

178. Richter, M. *et al.* Streaking Temporal Double-Slit Interference by an Orthogonal Two-Color Laser Field. *Physical Review Letters* **114.** PRL, 143001 (2015).

179. Schell, F. *et al.* Molecular orbital imprint in laser-driven electron recollision. *Science Advances* **4,** eaap8148 (2018).

180. Pullen, M. G. *et al.* Imaging an aligned polyatomic molecule with laser-induced electron diffraction. *Nature Communications* **6,** 7262 (2015).

181. Klünder, K. *et al.* Probing Single-Photon Ionization on the Attosecond Time Scale. *Physical Review Letters* **106.** PRL, 143002 (2011).

182. *Legendre polynomials* 2019. https://en.wikipedia.org/wiki/Legendre_polynomials.

183. Reichert, J. *et al.* Measuring the frequency of light with mode-locked lasers. *Optics Communications* **172,** 59–68 (1999).

184. Saleh, B. E. A. *et al. Fundamentals of photonics* 2007.

185. Hoff, D. *et al.* Tracing the phase of focused broadband laser pulses. **13,** 947 (2017).

Appendix A

Additional data

A.1 Legendre polynomials

A detailed description of the Legendre polynomials $P_l(x)$ is given elsewhere [182]. The first explicit Legendre polynomials are

$$\begin{aligned}
P_0(x) &= 1, \\
P_1(x) &= x, \\
P_2(x) &= \frac{1}{2}(3x^2 - 1), \\
P_3(x) &= \frac{1}{2}(5x^3 - 3x), \\
P_4(x) &= \frac{1}{8}(35x^4 - 30x^2 + 3), \\
P_5(x) &= \frac{1}{8}(65x^5 - 70x^3 + 15x), \\
P_6(x) &= \frac{1}{16}(231x^6 - 315x^4 + 105x^2 - 5), \\
P_7(x) &= \frac{1}{16}(429x^7 - 693x^5 + 315x^3 - 35x), \\
P_8(x) &= \frac{1}{128}(6435x^8 - 12012x^6 + 6930x^4 - 1260x^2 + 35), \\
P_9(x) &= \frac{1}{128}(12155x^9 - 25740x^7 + 18018x^5 - 4620x^3 + 315x), \\
P_10(x) &= \frac{1}{256}(46189x^{10} - 109395x^8 + 90090x^6 - 30030x^4 + 3465x^2 - 63).
\end{aligned} \tag{A.1}$$

A.2 Gaussian optics

Using Maxwell's equations, the wave equation in vacuum can be analytically solved with a complex electric field $E(t, r, z)$. This electric field can be decoupled into a temporal $E_1(t)$ and $E_2(r, z)$ spatial part (assuming both parts are independent). The temporal part is given by

$$E_1(t) = A(t) \exp\left[i(\omega_0 t + \varphi_{\mathrm{CE}})\right], \tag{A.2}$$

which is decomposed into a slowly varying envelope $A(t)$ and a fast oscillating term with a carrier-frequency ω_0 and carrier-envelope phase φ_{CE}. For phase sensitive

measurements, the offset has to be actively stabilized [183]. It is often convenient to describe the pulse envelope with a Gaussian function:

$$A(t) = A_0 \exp\left[-4\ln 2\left(\frac{t}{\tau_{\mathrm{FWHM}}}\right)^2\right], \tag{A.3}$$

with the amplitude A_0 and the full width at half maximum pulse duration τ_{FWHM}. A general class of solutions of the wave equation in the paraxial approximation are Hermite-Gaussian modes [184]. A special case of these modes is the fundamental Gaussian beam TEM_{00} mode, which is given by

$$E_2(r,z) = \frac{w_0}{w(z)} \exp\left(-\frac{r^2}{w^2(z)}\right) \exp\left[-i\left(kz + \frac{kr^2}{2R(z)} - \Phi_G(z)\right)\right], \tag{A.4}$$

where E_0 represents the maximum of the electric field, w_0 the beam waist, $w(z)$ the beam radius at the longitudinal position z, $k = 2\pi/\lambda$ the wavenumber, $R(z)$ the radius of the wavefront and $\Phi_G(z)$ the Gouy phase.
The beam radius can be expressed as

$$w(z) = w_0\sqrt{1 + \left(\frac{z}{z_r}\right)^2}, \tag{A.5}$$

with the Rayleigh length

$$z_r = \frac{\pi w_0^2}{\lambda}. \tag{A.6}$$

For $z \gg z_r$, the beam radius converges to

$$w(z) = w_0\frac{z}{z_r} = \frac{\lambda}{\pi w_0} =: \frac{\Theta}{2}, \qquad z \gg z_r, \tag{A.7}$$

which is defined as the beam divergence (Fig. A.1). At the Rayleigh length, z_r the beam radius already increases to $\sqrt{2}w_0$. The region between $-z_r$ and z_r is defined as the focal length b. In addition to the beam radius, the plot also shows the behavior of the Gouy phase Φ_G, calculated as

$$\Phi_G = \arctan\left(\frac{z}{z_r}\right). \tag{A.8}$$

Over the focal length b, the Gouy phase changes by $\pi/2$. Along the propagation direction, the overall Gouy phase change is π.
Note that this simple equation only holds for monochromatic light. The Gouy phase of a broadband pulse is modified [185]. The radius of the curvature is calculated according to

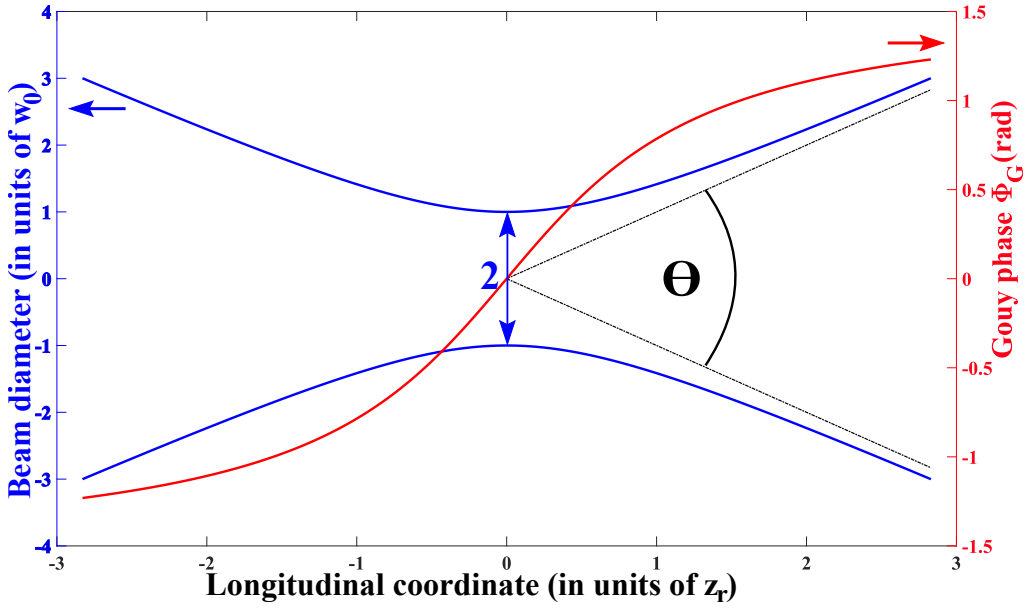

Figure A.1: Beam diameter $2w$ (blue) and Gouy phase Φ_G (red) as a function of the propagation z. In the far-field, the beam divergence is defined as $\Theta = 2\frac{\lambda}{\pi w_0}$.

$$R(z) = z\left[1 + \left(\frac{z_r}{z}\right)^2\right]. \tag{A.9}$$

The intensity $I(r, z)$ is proportional to the absolute squared value of the electric field. Using Eq. (A.4), the intensity can be calculated as

$$I(r, z) = I_0\left[\frac{w_0}{w(z)}\right]^2 \exp\left[-\frac{2r^2}{w^2(z)}\right]. \tag{A.10}$$

In the experiment, usually the total power P_0 can be measured. This value can be obtained by the radial integration of the intensity at a given longitudinal position z:

$$P_0 = \int_0^\infty I(r, z) 2\pi r dr = \frac{I_0}{2}\pi w_0^2. \tag{A.11}$$

Consequently, the intensity in Eq. (A.10) can be expressed as a function of the total power:

$$I(r, z) = \frac{2P_0}{\pi w^2(z)} \exp\left[-\frac{2r^2}{w^2(z)}\right]. \tag{A.12}$$

In contrast, the intensity of a monochromatic wave with the electric field $E(t) = E_0 \exp(i\omega_0 t)$ is given by

$$I_0 = \frac{c\epsilon_0}{2} E_0^2. \tag{A.13}$$

A.3 Auger decay emission rate

The Auger emission rate is calculated by the convolution of the ionizing XUV intensity I_{XUV} with Auger electron decay $\mathrm{AE}(t)$. Using Eqs. (7.14) and (7.15), it follows that

$$\begin{aligned} I_{\mathrm{Auger}}(t) &= I_{\mathrm{XUV}}(t) \circledast \mathrm{AE}(t) = \int_{-\infty}^{\infty} I_{\mathrm{XUV}}(t-t')\mathrm{AE}(t')dt' \\ &= \cancel{\int_{-\infty}^{t_0} I_{\mathrm{XUV}}(t-t')\mathrm{AE}(t')dt'} + \int_{t_0}^{\infty} I_{\mathrm{XUV}}(t-t')\mathrm{AE}(t')dt' \\ &= \int_{t_0}^{\infty} \exp\left[-\frac{(t-t')^2}{2\sigma^2}\right] A_1 \exp\left[-\frac{t'-t_0}{\tau_{\mathrm{AE}}}\right] dt' \\ &= A_1 \exp\left(-\frac{t^2}{2\sigma^2} + \frac{t_0}{\tau_{\mathrm{AE}}}\right) \int_{t_0}^{\infty} \exp \underbrace{\left[-\frac{t'^2}{2\sigma^2} + \frac{tt'}{\sigma^2} - \frac{t'}{\tau_{\mathrm{AE}}}\right]}_{=:f(t')} dt'. \end{aligned} \tag{A.14}$$

The introduced function $f(t')$ is further transformed to

$$\begin{aligned} f(t') &= -\frac{1}{2\sigma^2}\left[t'^2 - 2t'\left(t - \frac{\sigma^2}{\tau_{\mathrm{AE}}}\right) + \left(t - \frac{\sigma^2}{\tau_{\mathrm{AE}}}\right)^2 - \left(t - \frac{\sigma^2}{\tau_{\mathrm{AE}}}\right)^2\right] \\ &= -\frac{1}{2\sigma^2}\left[t' - \left(t - \frac{\sigma^2}{\tau_{\mathrm{AE}}}\right)\right]^2 + \frac{1}{2\sigma^2}\left(t - \frac{\sigma^2}{\tau_{\mathrm{AE}}}\right)^2. \end{aligned} \tag{A.15}$$

Substituting Eq (A.15) into Eq (A.14) leads to

$$\begin{aligned} I_{\mathrm{Auger}}(t) &= A_1 \exp\left[g(t)\right] \int_{t_0}^{\infty} \exp\left[-\frac{1}{2\sigma^2}\left(t' - \left(t - \frac{\sigma^2}{\tau_{\mathrm{AE}}}\right)\right)^2\right] dt', \\ g(t) &= -\frac{t^2}{2\sigma^2} + \frac{t_0}{\tau_{\mathrm{AE}}} + \frac{1}{2\sigma^2}\left(t - \frac{\sigma^2}{\tau_{\mathrm{AE}}}\right)^2. \end{aligned} \tag{A.16}$$

The substitution $u(t') = (t' - (t - \sigma^2/\tau_{\mathrm{AE}}))/(\sigma\sqrt{2})$ leads to

$$I_{\mathrm{Auger}} = A_1 \exp\left[g(t)\right] \sigma\sqrt{2} \int_{u(t_0)}^{\infty} \exp\left(-u^2\right) du. \tag{A.17}$$

The solution of the integral on the right-hand side is given by the complementary error function

$$\mathrm{erfc}(x) := 1 - \mathrm{erf}(x) = \frac{2}{\sqrt{\pi}} \int_{x}^{\infty} \exp\left(-v^2\right) dv. \tag{A.18}$$

From the substitution of Eq. (A.18) into Eq. (A.17) follows

$$
\begin{aligned}
I_{\mathrm{Auger}}(t) &= A_1 \exp[g(t)] \frac{\sigma\sqrt{2\pi}}{2} \left[1 - \operatorname{erf}\left(u(t_0)\right)\right] \\
&= A_1 \exp[g(t)] \frac{\sigma\sqrt{2\pi}}{2} \left[1 - \operatorname{erf}\left(\frac{1}{\sigma\sqrt{2}}\left(t_0 - t + \frac{\sigma^2}{\tau_{\mathrm{AE}}}\right)\right)\right] \\
&= A_1 \frac{\sigma\sqrt{2\pi}}{2} \exp\left[\frac{1}{\tau_{\mathrm{AE}}}\left(t_0 - t + \frac{\sigma^2}{2\tau_{\mathrm{AE}}}\right)\right] \cdot \left[1 - \operatorname{erf}\left(\frac{1}{\sigma\sqrt{2}}\left(t_0 - t + \frac{\sigma^2}{\tau_{\mathrm{AE}}}\right)\right)\right]
\end{aligned}
\tag{A.19}
$$

Appendix B

Acknowledgements

As everybody knows a PhD thesis is always an achievement of several people who contribute to this scientific work. It would not have been possible to carry out my PhD thesis alone. During that time, I always had a lot of people who actively participated in this PhD project.
In the first place, I would like to thank my supervisor Ulrike Frühling who gave me the opportunity to work on such a fascinating project. She always gave me good advice and helped me a lot with her extensive experience.
At this point, I would like to thank Markus Drescher a lot for his supportive discussions and the initial idea to construct such an electron spectrometer.
Special thanks go also to my co-supervisor Franz Kärtner who always had good ideas how to proceed with the measurements and the analysis. Besides that I gained from him a broader perspective on this scientific field, which helped me a lot to continue my work.
Many thanks go to Nikolay Kabachnik and Andrey Kazansky with their great theoretical and computational support. Without them it would not be possible to understand the fundamental physics, which is involved in the multiphoton absorption processes.
Here, I would like to thank all former and actual members of our ufast group for their continuous help and fruitful discussions at any time. I would like to thank in particular Sophie Walther for her tremendous support in the lab during the experiments, Markus Pfau for his detailed design of the HHG chamber, Anastasios Dimitriou for his support of setting up the electron spectrometer and the THz source, Thomas Gebert for his advice and experience when designing the experimental beamline and electron spectrometer and Malte Sumfleth who contributed especially with numerical simulations in his master thesis to this work.
Carrying out the experments would have been impossible without Mark Prandolini who was always helping in the lab and giving very useful advice. In addition, I also thank him a lot for proof-reading this thesis.
I am very glad that I was working in close collaboration with the dynamix group, which was very useful to start research in a new scientific area. Special thanks go to Marek Wieland for his advice and the opportunity of borrowing scientific equipment and Oliver Becker for his technical support in the lab. I also thank a lot the mechanical and electrical workshop under the supervision of Stephan Fleig and Armin Spikofsky, respectively. The realization of the experiment heavily relied on the machining of customized vacuum chambers and other parts as well as specially designed electronic devices.
Manfred Spiwek was a very reliable colleague because he precisely cut the gas inlet tubes for the electron spectrometer.
At the end I would like to thank a lot my family, especially my wife Lara, and friends for always supporting me and their patience during the last years.

Appendix C

List of abbreviations

ATI	Above-threshold ionization
CEP	Carrier-envelope phase
cLNB	congruent $LiNbO_3$ crystal
CMOS	Complementary metal-oxide-semiconductor
CPA	Chirped-pulse amplification
EOS	Electro-optic sampling
FA	Fast Auger
FFT	Fast Fourier Transform
FROG	Frequency-resolved optical gating
FWHM	Full width at half maximum
HHG	High-order harmonic generation
LE	Low-energy
MCP	Microchannel plate
NIR	Near-infrared
OAPM	Off-axis parabolic mirror
ODE	Ordinary differential equation
OR	Optical rectification
pBASEX	polar basis function expansion
PEEK	Polyether ether ketone
POP	Polar onion-peeling
PSD	Position-sensitive detector
SA	Slow Auger
SPIDER	Spectral phase interferometry for direct electric-field reconstruction
SFA	Strong-field approximation
TDSE	Time-dependent Schrödinger equation
TOF	Time-of-flight
THz	Terahertz
VMIS	Velocity-map-imaging spectrometer
XUV	Extreme ultraviolet

Appendix D

Declaration on oath

I hereby declare, on oath, that I have written the present dissertation by my own and have not used other than the acknowledged resources and aids.

Hamburg, October 22nd, 2019

Martin Ranke

List of Figures